2013

Penetration of Composites by Arbitrary Shaped Fragments - A Numerical and Experimental Investigation.

Joseph Jordan
Lehigh University

Penetration of Composites by Arbitrary Shaped Fragments – A Numerical and Experimental Investigation.

by

Joseph B. Jordan

Presented to the Graduate and Research Committee

Of Lehigh University

in Candidacy for the Degree of

Doctor of Philosophy

in

Mechanical Engineering

Lehigh University

January 2013

Approved and recommend for acceptance as a dissertation in partial fulfillment of the requirements for the degree of Doctor of Philosophy.

Date

Dissertation Advisor
Professor C. J. Naito

Accepted Date

Committee Members:

Committee Chair
Professor J. Y. Kazakia

Professor H. F. Nied

Professor W. Z. Misiolek

T. R. Slawson, PhD

TABLE OF CONTENTS

LIST OF TABLES

LIST OF FIGURES

ABSTRACT

Glass fiber reinforced plastic (GFRP) panels are used as a means of providing personnel protection ballistic fragments generated from small arms and mortar and rocket munitions. These panels are often fielded in temporary shelters used for military operations. The effectiveness of these panels against the variety of fragment sizes and shapes are not definitively understood. To address this shortcoming, an investigation consisting of numerical and experimental studies on the terminal behavior of arbitrary shaped fragments versus E-Glass/Phenolic glass fiber-reinforced plastic composites has been conducted. The goals of the work include assessment of the penetration resistance of arbitrary shaped fragments, material characterization of E-Glass/Phenolic GFRP at static, dynamic and ballistic rates, numerical modeling and validation, and numerical quantification of damage mechanisms associated with ballistic fragment impact.

Four hundred ballistic experiments were conducted using 2.85 gram fragments, eight different nose shapes, and three different thicknesses (4, 9, 14 mm) of E-Glass/Phenolic glass fiber reinforced plastic (GFRP) targets. Initial velocity, residual velocity, and ballistic limit velocities were determined for each nose shape and target thickness. These experiments revealed that the ballistic limit and energy absorbed is significantly affected by the nose shape of the fragment simulating projectile (FSP). While all of the fragments are considered blunt nose shapes, the penetration effectiveness was found to be directly correlated to the degree of sharpness. For the 14-mm-thick targets the eight fragment shapes had an average ballistic limit of 726

m/s. The variation in ballistic limit, however, varied by 326 m/s from the least to most efficient nose shape.

The experimental data was fit using Wen's [1, 2] analytical model for projectiles and was found to provide an excellent agreement when using a new empirically derived constant for each of the fragment nose shapes.

Numerical modeling of the fragment-target interaction was examined using the LS-DYNA finite element analysis code and the rate dependent material model MAT162 composite MSC damage model. The 39 material properties and parameters required for the MAT162 model were assessed as part of the research through a comprehensive material characterization study prior to the FEA investigation. The basic material properties where determined from quasi-static testing. Indirect material properties such as erosion criteria were determined by numerically simulating a series of low velocity impact experiments, depth of penetration and ballistic impact experiments conducted. The criteria were varied to provide the best fit with the experimental tests.

When all the material properties and parameters were determined, the model was validated by comparing numerical simulations to experimental data for ballistic impacts into thinner targets. The material properties and validated parameters can be used in future ballistic impact analysis of the E-glass/Phenolic material. The methodology presented for determining the material properties and parameters can be used as a guide for other plain-weave fabric materials. A concluding series of numerical simulations using the right circular cylinder and hemispherical nosed FSP were used to determine the phases of penetration for the different target thicknesses used in the ballistic experiments. The analyses reveal that the thin targets (4 mm) absorbed more energy through dishing and tensile fiber failure and the thicker targets (9 and 14 mm) absorbed more energy by compression-crushing and compression-shear. The simulations support the experimental observations which showed increased penetration efficiency for the sharper nosed fragments when impacting the 9, 14, and 50 mm thick targets. For thin 4 mm thick targets the geometric shape becomes more critical than the degree of bluntness when assessing penetration capability.

CHAPTER 1 - INTRODUCTION

In the current war on terrorism there is a need to field lightweight, cost effective solutions to mitigate indirect fire from rocket, artillery and mortar (RAM) threats. Some glass-fiber-reinforced plastic (GFRP) composites, such as E-glass, R-glass and S2-glass are considered cost effective solutions for mitigating RAM threats. In applications other than aircraft and armor vehicles the weight penalty of these GFRPs is normally acceptable in order to achieve a more cost effective solution. The effort to create optimized solutions of GFRP composites requires a better understanding of their performance versus arbitrary shaped fragments typical of RAM threats. This proposed research effort will be focused on the E-Glass/Phenolic since it is the least expensive of the GFRP materials and its use is the most prevalent in protective structures due to the large square footage requirement.

Typical applications for E-Glass/Phenolic materials are overhead protection applications, such as dining facilities, and living quarters in Iraq and Afghanistan; as well as, side wall and overhead protection for modular re-locatable buildings (MRLB) in the same locations. Another use is for protective panels in modular protective systems. This material has also been used in the past for some light armor applications for vehicles. Examples of each of these are shown in Figure 1.

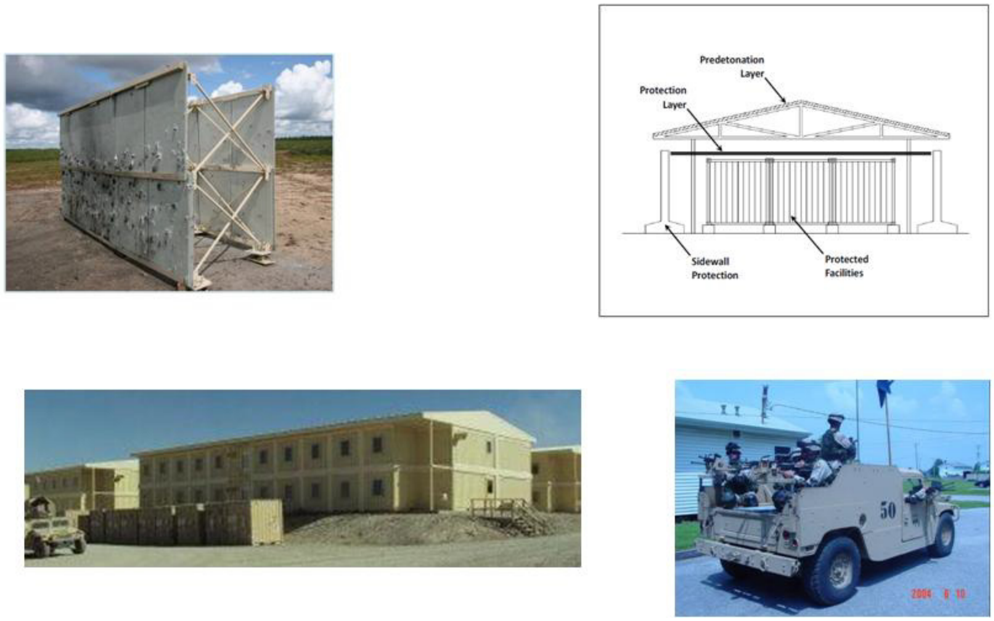

Figure 1. Applications where E-glass/Phenolic material would be used.

1.1 BACKGROUND

A short overview will be given of four topics important in understanding this research effort. These overviews are not in no way considered all in compassing; in fact they are only brief summaries of information that will be useful to the reader in understanding the research.

1.1.1 Penetration Mechanics Overview

The three most significant parameters required for a parametric study of a penetration event are; the mass, velocity and geometry of the fragment or projectile penetrating into the target material. While strength, density and other factors affect penetration efficiency, these three are the primary influence for a parametric study where the material of the projectile and the target remain the same. The influence of changing the mass and the velocity of a fragment can easily been seen by calculating the kinetic energy of the projectile just before impact. As the mass of the fragment (m_f) increases, so does the kinetic energy and penetration efficiency. The fragment mass is also known as the projectile mass (m_p) and can be interchangeably. The velocity is squared in the kinetic energy equation therefore its influence is greater than the increasing mass component. Geometry can be further subdivided into length (L) to diameter (D) ratio (L/D), nose shape, and presented area. The presented area (A_p) of a fragment is that area a tumbling fragment in flight projects at a given time and rotation. For example a flight of a circular cylinder would have a presented area of a circle for a face on impact, a rectangle for a side on impact, and an ellipse for any other orientation. During most of its flight a fragment is tumbling and has numerous orientations and resultant presented areas, an average presented area is used in all calculations for the shape factor. The shape factor (γ) gives a functional relationship between the volume of a fragment and its presented area, $A_p = \gamma \left(\frac{m_f}{\rho_f} \right)^{\frac{2}{3}}$ [3], where ρ_f is the fragment density. Several fragments (100+) are used to determine an average shape factor for a particular munition. As the shape factor increases the penetration efficiency decreases since more of the target material interacts with the projectile. It is well known that as the *L/D* increases the penetration efficiency of the penetrator increases. Typical military rifle bullets have *L/D* in the range of 4.08 to 4.62, while a compact fragment has an *L/D* of unity.

1.1.2 V_{50} Testing Overview

The V_{50} ballistic limit indicates the ballistic penetration resistance of an armor component versus a specific projectile. The V_{50} is an important measure of an armors penetration resistance and it allows a direct comparison to be made between different armor solutions. The V_{50} ballistic limit which is also referred to as the ballistic limit (V_{BL}) is the impact (or strike) velocity where a complete penetration and incomplete penetration are equally likely to occur [4]. The V_{50} test is used since it is the easiest to determine and the least expense to conduct. Most materials exhibit a phenomenon known as a zone of mixed results. The zone of mixed results occurs when the highest velocity for a partial penetration is greater than the lowest velocity for a complete penetration. The range of the "zone of mixed results" is shown in the penetration probability curve shown in Figure 2 [5]. The zone of mixed results stems from the fact that materials are in general not homogeneous. While we can assume materials such as steel are homogenous for the purpose of standard engineering design, they are not homogenous at the microscopic level; there are lattice defeats, and other defects which can influence an impact event which is localized in nature.

Determining the strike velocity at impact is another important aspect in V_{50} testing with fragments due to the larger induced drag as compared to an ogive nose shape of a typical rifle projectile.

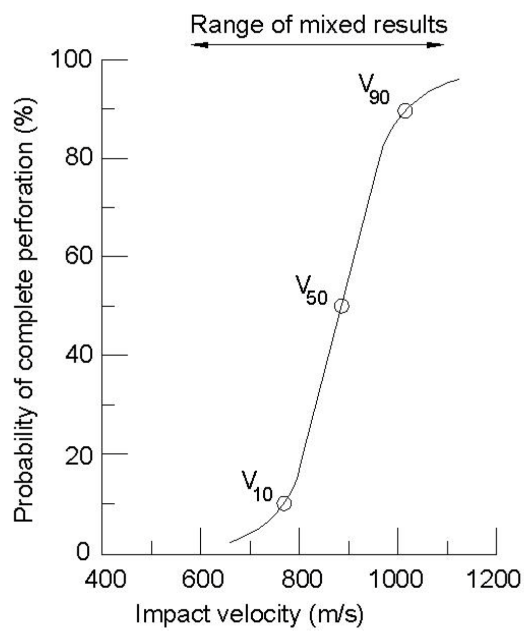

Figure 2. Penetration Probability Curve (adapted from [5])

The velocity is found by taking two velocity measurements as the fragment proceeds downrange prior to impacting the target, then using the equation

$$V_s = V_2 + \left(\frac{L_2}{L_1}\right)(V_2 - V_1) \tag{1}$$

to calculate the impact velocity at the target front face. Where L_1 is the distance between velocity two and the impact face, and L_2 is the distance between velocity one and two. A typical setup is shown in Figure 3. Also shown in Figure 3 are the two velocity screens downrange from the target which give the residual velocity in the event of a complete perforation.

1.1.3 The V_{50} Process

Step one: impact the target at the estimated V_{50} and determine whether or not the impact was a complete penetration (CP) or partial penetration (PP). A witness panel of 0.5 mm thick 2024-T3 aluminum is placed 152.4 mm (6 inches) behind the target to assess whether or not an impact is a CP or PP. A CP is defined as: when any light emanating from a 60 watt light bulb can be seen through the witness panel; a PP is any other impact. *Step two:* change the velocity of the next impact by ± 30 m/s depending on whether or not the shot was CP or PP. For a PP the next shot will be increased, for a CP the next shot will be decreased. *Repeat:* until requirements are met. A typical requirement for the V_{50} is the four shot V_{50}. A four shot V_{50} requires that there are 2 CP and 2 PP within a spread less than or equal to 18 m/s. Six shot and ten shot V_{50} can also be used for assessing the target.

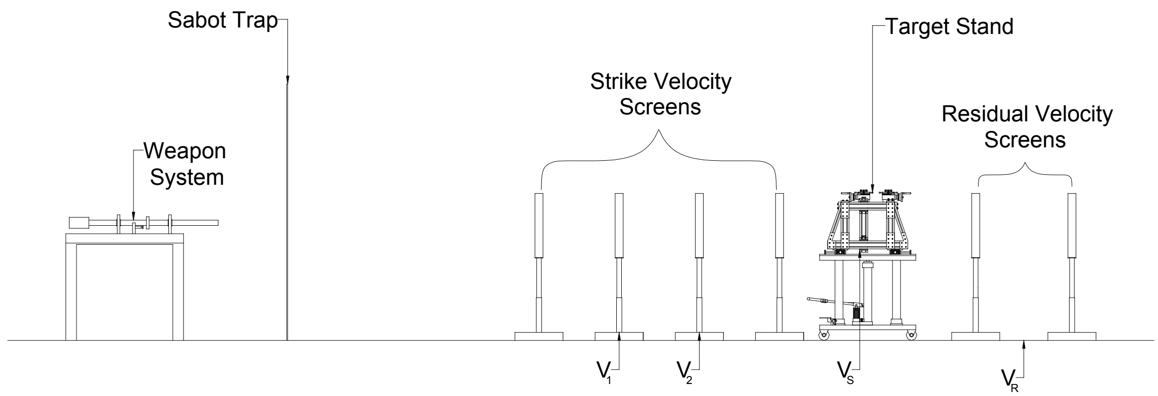

Figure 3. Typical Set-up for Impact and Residual Velocity

1.1.4 Armor Design Overview

In simplified terms the armor design process for defeating RAM threats is as follows: *Step one:* define the threat; which warhead is the threat of interest. *Step two:* determine the required protection level. This will be given as a design fragment. The design fragment will be specified by its mass and velocity. *Step three:* select candidate armor solutions. *Step four:* conduct laboratory testing on candidate armor solutions. Typically this is accomplished by conducting V_{50} ballistic limit testing (as discussed above). *Step five:* live-fire validation of down selected armor candidates. This is typically done in an arena test which is a test with the warhead placed in the center of all candidate armor materials at the stand-off to achieve the desired velocity at impact. *Step six:* conduct weight and cost trade-off analysis to determine which armor solution is to be fielded. Weight and cost are diametrically opposed in armor solutions. Typically the cheaper the solution the heavier it is while the lighter the solution, the more expensive the solution. Expensive military aircraft can absorb the cost of very expensive lightweight armor since weight is typically at a premium for these applications, on the other end of the spectrum expeditionary shelters use the cheapest solution available since reduced cost is the priority and weight is typically not an issue.

1.1.5 Fragment Simulating Projectiles (Design Fragment) Overview

The typical design fragment is specified as a certain fragment-simulating projectile (FSP). In fact, the current protocol for first lot acceptance tests and conformance testing on GFRP composites require that a 30 caliber FSP be used [6]. Ipson and Recht discuss the history and development of the fragment-simulating projectile [7]. The FSP as we know it today was standardized in 1962 with the issuance of a military specification [8]. This standard was updated to include sabot launched FSPs and released as a detailed specification in 2006 [9]. The FSP represents compact or chunky fragments produced by a fragmenting munition. Compact or chunky fragments are defined as fragments in which the ratio of the maximum presented area to the minimum presented area is not far from unity [10]. For a cylindrical shaped fragment the ratio of maximum presented area to the minimum presented area can be replaced by the length to diameter ratio. With a compact fragment being defined as a L/D close to unity. The FSPs L/D range is between 1.15 and 1.17. In addition to the standardized FSP, STANAG 2920 [11] has standardized dimensions and associated masses for right circular cylinders (RCCs), spheres, cubes, and parallelepipeds which can be used as fragment simulating projectiles for testing armor materials. Figure 4 shows a comparison of similar mass fragment simulators defined in STANAG 2920 [11].

For comparison purposes fragments from naturally fragmenting munitions are shown in Figure 5. A current issue of concern is that the usage of composites as protection materials was rare at the time when the FSP was standardized, and this has lead the armor community to question whether or not the standard FSP is appropriate for composite materials.

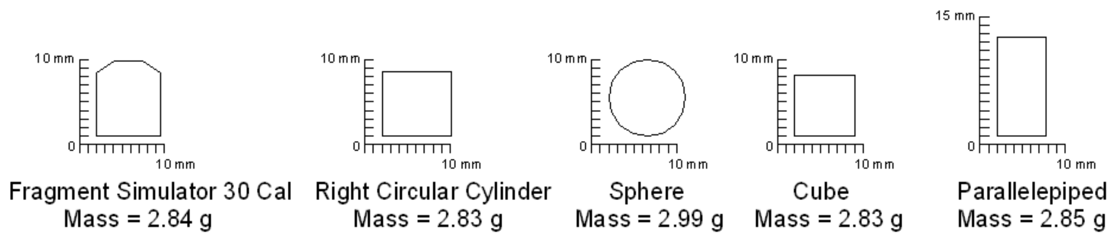

Figure 4. Fragment Simulators of Approximately Equal Mass

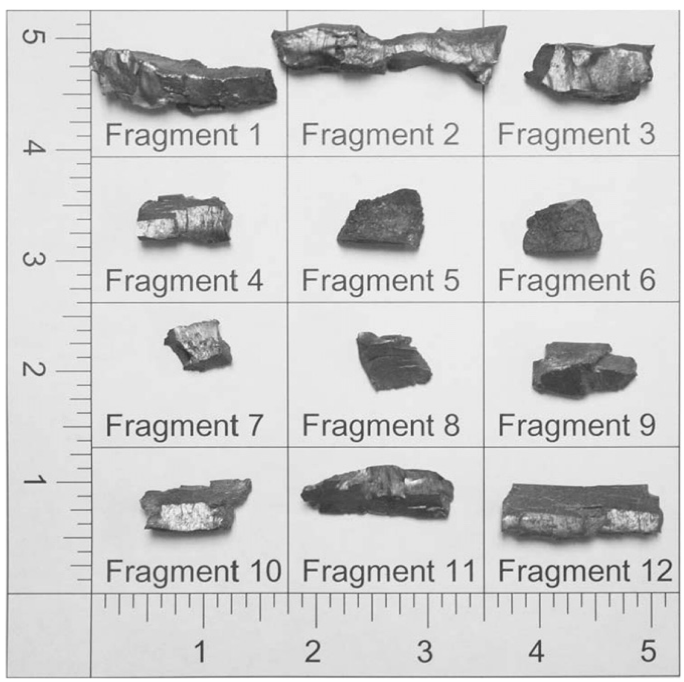

Figure 5. Natural Fragments [10]

While the penetration mechanics overview is only a brief summaries they are important in understanding of the importance of the ballistic limit and the use of fragment simulating projectiles and the two are intimately tied to a material in assessing the materials capability to defeat a given rocket, artillery or mortar threat..

1.2 LITERATURE REVIEW

1.2.1 Ballistic Impacts on Glass-Fiber-Reinforced Plastics

It has been known for some time that the penetration resistance of steels and aluminums is not influenced by the shape of fragments [7]. Metals fail during penetration or perforation by a) fracture due to initial stress wave, b) scabbing (spall failure), c) petalling, and d) plugging [7, 13, 5]. Glass fiber reinforced plastics (GFRPs) such as E-glass and S2-glass fail differently than metals in a penetration event; GFRPs fail as a result of a) shear plugging, b) tensile fiber failure, c) fiber debonding, d) fiber pull-out, e) matrix cracking (interlaminar), and f) interlaminar delamination, or by a combination of these [14]. As a result of the varying failure modes, penetration resistance of GFRPs has been found to be sensitive to projectile shape. Abrate [15] discusses the influence of projectile nose shape on the penetration of composites based on the assumption that the normal pressure on the surface of the projectile is uniform as put forth by Wen [2, 1], and how laminate thickness, projectile diameter, stacking sequence, obliquity and projectile density are all factors affecting the ballistic limit of composites. Wen [15, 1] developed equations for the ballistic limit of projectiles with conical, flat, hemispherical and ogival nose shapes into E-glass/Polyester, S2-glass/Phenolic, and E-glass/Phenolic. Wen used an energy balance approach coupled with an empirical constant to develop his equations. Good correlation was reported between the equations and experimental data using projectiles with length to diameter ratios above 2.5. Ben-Dor et al. [16] generalized Wen's model to determine an optimal nose shape into fiber reinforced plastics. The optimal shape closely matched the performance of the optimal blunt cone penetrator, indicating that the blunt nose was more efficient than the sharp cone and ogive nose shapes. Wen's equations for the conical and the flat-nosed projectiles will be presented in more detail below.

Jenq et al. [17] predicted the ballistic limit based on the principle of conservation of energy for plain woven E-glass/epoxy laminates using the simple relationship

$$\frac{1}{2}m_pV_{BL}^2 = \frac{1}{2}m_pV_s^2 - \frac{1}{2}m_pV_r^2 \tag{2}$$

Where m_p is the mass of the projectile, V_{BL} is the ballistic limit velocity, V_s is the strike velocity and V_r is the residual velocity of the projectile after completely perforating the target. Jenq et al. concluded that the proposed equation was adequate for predicting the ballistic limit of a glass/epoxy target struck by a bullet-like penetrator (hemispherical nose shape). This is a similar technique used by Wen [1] with the exception that the penetrator always perforates the target material in this investigation. Sabet et al. [18] reported excellent results using the same equation for a sharp tipped projectile into E-glass with five different types of reinforcement.

Naik and Doshi [19] conducted a parametric study using analytical methods of the energy absorbing mechanisms, ballistic limit, contact duration, and damage shape and size of E-glass/Epoxy impacted by a flat-nosed cylinder with a length to diameter ratio of 3.77. The analytical model requires the diameter, mass, and velocity of the projectile, along with the target thickness and material properties. They found that the major energy absorbing mechanism is shear plugging. The other two mechanisms reported as absorbing a significant amount of energy were the compression directly under the penetrator and friction between the projectile and target. Other energy absorbing mechanisms such as matrix cracking, delamination, and tension and compression in the yarns were found to have negligible contributions. It is uncertain whether the major and minor mechanisms contributing to the energy absorption would remain the same for nose shapes other than flat and with less efficient penetrators such as one with a length to diameter ratio close to unity.

Gellert et al. [20] conducted an experimental investigation of E-glass/Vinylester target thickness versus three different nose geometries with an average length to diameter ratio of 5.2. It was found that at lower thicknesses, the energy absorbed was independent of nose geometry. Separation of the energy absorption began at a thickness of approximately 9 mm. Energy absorption increased as the conical nose shape increased from 45 degrees to 180 degrees (flat).

Bless et al. [21, 22] conducted experimental studies using fragment simulating projectiles (FSPs) on S2-Glasses with both epoxy and phenolic resins and one of their findings was that the nose shape of the projectile had a dramatic effect on the energy absorption of the composite. The investigation of the nose shape was not the primary purpose of this study, and the fragments were elongated with a length to diameter ratios varying from 1.6 to 2.7.

Investigations using different nose shapes of compact fragments were conducted for Twaron [23] and Carbon/Epoxy [24] composite panels. These investigations revealed that the influence of the nose shape was material dependent as shown by Table 1. In the case of Twaron the conical nose shape was the most ballistically efficient nose shape; however, for the Carbon/Epoxy composite material the conical nose shape was the least ballistically efficient nose shape. The influence of nose shape was significantly less for the carbon/epoxy panels.

While there are a number of articles in the literature on the influence of nose shape on the penetration of projectiles, there is little published concerning the effect of various nose shapes for compact fragment penetration into GFRPs. Compact fragments are defined as fragments in which the ratio of the maximum to the minimum presented area is not far from unity ($L/D \approx 1$) [17]. Previously cited investigations [21, 22] used FSPs with longer length to diameter ratios and approximately twice the mass of typical compact fragments of the same diameter. Other studies such as [23, 24] indicated contradictory results with respect to the performance of various nose shapes of compact fragments. These contradictions could stem from a thickness effect for the targets or from the target material itself.

Table 1. Data from Previous Investigations

Twaron [23]		Carbon/Epoxy[24]	
Projectile Mass = 231 grains Projectile Diameter=12.6mm		FSP Mass = 216 grains FSP Diameter=12.7mm	
Nose Shape	V_{BL} (m/s)	Nose Shape	V_{BL} (m/s)
Hemispherical	159	Conical	166
Flat	100	Flat	154
Ogival	76	Hemispherical	153
Conical	58	FSP	140

1.2.1.1 Wen's Semi-Analytical Model [1]

The basic assumptions of Wen's model are that *"the deformations are localized and that the average pressure provided by the target materials to resist the projectiles can be divided into two parts. One part is the cohesive quasi-static resistive pressure applied normally to the projectile surface due to the elastic-plastic deformations of the FRP laminate materials and the other is the dynamic resistive pressure arising from velocity effects."* The second assumption yields the equation $\sigma = \sigma_s + \sigma_d$. Using two other assumptions; that the quasi-static resistive pressure, σ_s, is equal to the elastic limit in the through thickness direction of the composite, and that the dynamic resistive pressure, σ_d, is equal to

$$\sigma_d = \beta \sqrt{\frac{\rho_t}{\sigma_e}} V_i \sigma_e \tag{3}$$

Where β is an empirical constant, V_i is the impact velocity, is the elastic limit of the material, and ρ_t is the density of the target material. Then the equation for the resistive pressure can be re-written as

$$\sigma = \left[1 + \beta \sqrt{\frac{\rho_t}{\sigma_e}} V_i \right] \sigma_e \tag{4}$$

The geometry for the conical nose shape projectile and the diagram for this projectile impacting on a semi-infinite FRP target are shown in Figure 6. *Theta (θ)* is the included angle of the conical section, *L* is the length of the shank, L_N is the length of the conical section, D is the diameter, a is the radius and P is the depth of penetration into the target. The penetration process is broken down into two cases: 1) where $P \leq L_N$ and 2) where $L_N \leq P$.

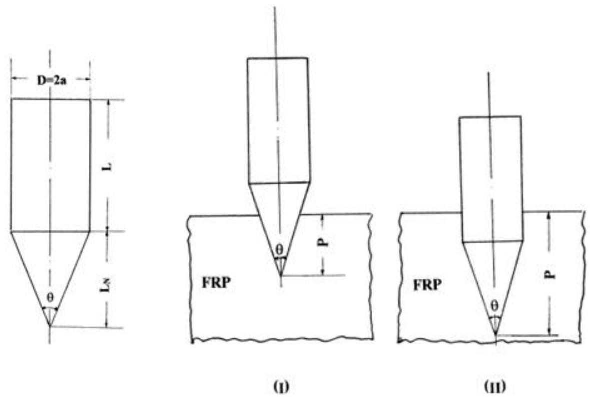

Figure 6. Geometry used for the model [1]

For the first case; the resistive force F equals the resistive pressure, σ, multiplied by the instantaneous cross-sectional area, A, which leads to the following

$$F = \pi P^2 \tan^2 \frac{\theta}{2} \sigma_e \left[1 + \beta \sqrt{\frac{\rho_t}{\sigma_e}} V_i \right] \qquad \text{where} \quad A = \pi P^2 \tan^2 \frac{\theta}{2} \tag{5}$$

For the second case the cross-sectional area, A_o , is constant and the resistive force F equals

$$F = A_0 \sigma_e \left[1 + \beta \sqrt{\frac{\rho_t}{\sigma_e}} V_i \right] \tag{6}$$

From energy conservation one obtains

$$E_k = \int_0^{L_N} F dP + \int_{L_N}^{P} F dP \tag{7}$$

Substituting and integrating yields

$$E_k = \pi a^2 T \sigma_e \left[1 + \beta \sqrt{\frac{\rho_t}{\sigma_e}} V_{BL} \right] \tag{8}$$

After substituting the volume of the target material $\pi a^2 T$ for $\frac{p^2 A_0}{3 L_N}$ and replacing the impact velocity (V_i)with the ballistic limit velocity. By equating the kinetic energy above to $E_k = \frac{1}{2} m_p V_{BL}^2$ and rearranging to solve for V_{BL} the following equation for the ballistic limit is obtained

$$V_{BL} = \frac{\pi \beta \sqrt{\rho_t \sigma_e} D^2 T}{4 m_p} \left[1 + \sqrt{1 + \frac{8 m_p}{\pi \beta^2 \rho_t D^2 T}} \right] \tag{9}$$

The flat faced cylinder is the same as a conical nosed cylinder with theta equal to 180 degrees. If you use the parameters given in the paper i.e. *D*=10.5 mm and *G*=18.7g you can determine that the *L/D*=2.99 for this investigation with the conical nose. Similarly the flat-nosed cylinder used in the paper was calculated to have an *L/D*=2.86. Assuming that the same empirical constant would apply to compact fragments the ballistic limit velocity was calculated. In absence of experimental data to verify the calculations the solutions seem reasonable. The calculated values are shown in Table 2. Note that the lower the ballistic limit the greater the penetration efficiency of the projectile or fragment.

Table 2. Calculated V_{BL} Results

Nose Shape	L/D	Mass (grams)	V_b (m/s)
Conical (from the Paper)	2.99	18.7	100
Flat	2.57	18.7	107
Flat (from the Paper)	2.86	20.4	110
Conical	1	4.74	233
Flat	.66	4.74	265
Flat	1	7.12	200

In summary, while there have been numerous analytical studies for projectiles penetrating composite materials there have been none for compact fragments. In absence of experimental data to verify, the energy balance approach by Wen [1] seems reasonable when used to calculate the ballistic limit for conical and flat-nosed cylinders. The only experimental investigation with more than one nose shape was lacking in the number of shapes investigated, and the mass consistency of the fragments.

1.2.2 Numerical Simulations of Impacts on Glass-Fiber-Reinforced Plastics

Blanas [25] conducted parametric studies of numerical impacts of FSPs against E-glass, S2-glass, and Kevlar targets. He concluded that the results of numerical studies were only marginally acceptable for use in modeling the penetration phenomena of composites. The study was conducted using the composite damage model in DYNA3D an explicit finite element code developed by Lawrence Livermore National Laboratory which was a precursor code to the commercial code LS-DYNA. The composite damage model was developed for use in modeling unidirectional composites. It is a two dimensional model that could model two failure modes; fiber and matrix failure for in-plane stresses. Blanas noted in his report that at that time there was an insufficient knowledge base for high-strain rates of composite materials and that a property degradation model, updating the local material properties of the damaged zone around the failed material as a function of strain rates is needed [25]. The parametric studies showed that the tensile properties of the composite panels controlled the ballistic penetration resistance by fragments, which is contrary to the penetration process of metals where compressive properties and shear banding are dominant. Yen discusses a newly developed material model MAT162 adapted from the composite damage model used by Blanas in [26, 27]. The equations developed by Yen and implemented into LS-DYNA for material model MAT162 will be discussed in detail in a subsequent section.

Deka et al. [14, 28, 29]numerically and experimentally investigated the damage evolution and energy absorption of E-glass/Polypropylene laminated composites versus right circular cylinders. The authors were able to achieve good correlation with experimental data by choosing appropriate damage parameters (m) for the MAT162 constitutive material model. For simplicity $m_1=m_2=m_3=m_4$ (the damage parameters) were kept equal for both of these studies, however each damage parameter represents a different failure mode and should be assigned different values [28]. During the mesh sensitivity study as the mesh was increased from one element through the lamina to 3 elements through the lamina the global stiffness increased and the *m* values had to be reduced by an order of magnitude to match the experimental results. Deka et al. [14] studied multiple impacts into S2-glass composites. During this investigation m_1=m_2 and the other *m* values varied which is more appropriate than the previous studies since m_1 and m_2 both represent fiber tensile/shear failure. The authors observed that the damage parameters m_i and the delamination scaling factor S_d to be the most sensitive in trying to obtain good correlation with experimental data.

Gama [30] recently published a paper on progressive damage modeling of plain weave S2-glass composite using the composite damage model MAT162 in LS-DYNA. The paper discusses elements of the methodology for developing the softening (damage) parameters m_i for MAT162 using a single element. Essentially there are two components to this methodology 1) a quasi-static calibration and validation, and 2) a dynamic validation. An example of how the quasi-static calibration is accomplished: m_3=m_4 were held constant while m_1=m_2 varied from $0 \le m_1 = m_2 \le 100$ while the single element was put into tension, then the stress-strain curves for each of these runs is plotted and compared to experimentally derived stress-strain data, the best fit is chosen for use in future calibrations. Once all of the softening parameters are found in a similar manner a dynamic validation would be done using the softening parameters developed in the quasi-static calibration and validation phase, and compared to dynamic experimental results such as those from a ballistic impact. The delamination scaling factor S_d would then be adjusted to better represent the experimental data.

1.2.2.1 Material Composite MSC Damage Constitutive Model (MAT162)

In Yen's papers [26, 27] he presented the new constitutive model MAT162 which had been implemented in the LS-DYNA finite element code. The constitutive model MAT162 was capable of emulating the seven failure modes for plain weave composite materials; tensile and compressive fiber failure in the warp and fill directions, fiber crushing, in-plane matrix failure (in-plane shear), and through thickness matrix failure (delamination) [26, 31, 32]. The MAT162 model may be used to model the progressive failure analysis for composite materials consisting of woven fabric layers [31, 32]. Material model MAT162 has a damage option that is a generalization of the basic layer failure model of MAT162, which has adopted the damage mechanics approach for characterizing the softening behavior after damage initiation [31, 32].

The plain weave fabric failure criteria for MAT162 are expressed in terms of ply (lamina) level engineering strains (ε_x, ε_y, ε_z, ε_{xy}, ε_{yz}, ε_{zx}) with x, y, z indicating the in-plane warp (longitudinal), in-plane fill (transverse), and out-of-plane (through thickness) directions, with the associated elastic moduli being (E_x, E_y, E_z, G_{xy}, G_{yz}, G_{zx}) [26, 31, 32].

The seven failure modes of plain weave fabric lamina model for the MAT162 models follow. The fiber tensile/shear failures are given by

$$f_1 - r_1^2 = \left(\frac{E_x \langle \varepsilon_x \rangle}{S_{xT}} \right)^2 + \left(\frac{G_{xz} \varepsilon_{xz}}{S_{xFS}} \right)^2 - r_1^2 = 0 \quad (10)$$

$$f_2 - r_2^2 = \left(\frac{E_y \langle \varepsilon_y \rangle}{S_{yT}} \right)^2 + \left(\frac{G_{yz} \varepsilon_{yz}}{S_{yFS}} \right)^2 - r_2^2 = 0 \quad (11)$$

When the tensile/shear failure is predicted in a layer the load carrying capability is completely eliminated in that direction for that layer. The variables not previously defined are: ε is the axial strain, S_{iT} is the axial tensile strength, S_{iFS} is the fiber shear strength, and r_i^2 damage threshold where *i=1, … , 6*. The $\langle \ \rangle$ represent the Macaulay brackets which state that the value must be greater than zero.

The in-plane compressive failure in the warp (longitudinal) and fill (transverse) directions are given by

$$f_3 - r_3^2 = \left(\frac{E_x \langle \varepsilon_x' \rangle}{S_{xC}} \right)^2 - r_3^2 = 0 \qquad \text{where } \varepsilon_x' = -\varepsilon_x - \langle -\varepsilon_z \rangle \frac{E_z}{E_x} \qquad (12)$$

$$f_4 - r_4^2 = \left(\frac{E_y \langle \varepsilon_y' \rangle}{S_{yC}} \right)^2 - r_4^2 = 0 \qquad \text{where } \varepsilon_y' = -\varepsilon_y - \langle -\varepsilon_z \rangle \frac{E_z}{E_y} \qquad (13)$$

For compressive fiber failure the layer is assumed to carry a residual load (residual strength) in the failed direction and is unchanged in the transverse direction.

The fiber crush failure under compressive pressure is given by

$$f_5 - r_5^2 = \left(\frac{E_z \langle \varepsilon_z' \rangle}{S_{FC}} \right)^2 - r_5^2 = 0 \qquad (14)$$

When fiber crush failure has occurred the material is assumed to be elastic for compressive pressures (p<0), and to carry no load for tensile pressures (p>0). S_{FC} is the fiber crush strength.

A plain weave layer can fail due to in-plane shear stress without fiber breakage. This in-plane matrix failure mode is given by

$$f_6 - r_6^2 = \left(\frac{G_{xy}\varepsilon_{yz}}{S_{xy}}\right)^2 - r_6^2 = 0 \tag{15}$$

When the in-plane matrix failure is predicted the in-plane shear stress is reduced to zero and the axial load carrying capacity of an element remains unchanged. S_{xy} is the layer shear strength due to matrix shear failure.

Through thickness matrix failure or delamination is given by

$$f_7 - r_7^2 = S^2\left\{\left(\frac{E_z\langle\varepsilon_z\rangle}{S_{zT}}\right)^2 + \left(\frac{G_{yz}\varepsilon_{yz}}{S_{yz0}+S_{SR}}\right)^2 + \left(\frac{G_{zx}\varepsilon_{zx}}{S_{zx0}+S_{SR}}\right)^2 - r_7^2 = 0 \tag{16}$$

The damage surface due to this equation is parallel to the composite layering plane. S in the equation is a scale factor so that a better correlation with experiments can be attained.

For the MAT162 damage model Yen [26, 27] adopted the damage mechanics approach presented by Matzenmiller et al. [33] for characterizing the softening behavior after damage initiation. The damage functions are converted from the failure criteria presented above by neglecting the Poisson's effect [31]. The elastic moduli are reduced in terms of associated damage parameters ϖ_i :

$$E_i^{'} = (1-\varpi_i)E_i \quad \text{here } \varpi_i = 1-\exp^{\left(\frac{-r_i^{m_j}}{m_i}\right)}, \text{ for } r_i \geq 0 \text{ and I = 1, ...,6, j=1,2,3,4} \quad (17)$$

The variable r_i is the damage thresholds computed from the associated damage functions for fiber and matrix damage, and delamination, and m_j are the material damage parameters; fiber damage in 1-direction (m_1), fiber damage in 2-direction (m_2), fiber crush and shear damage (m_3), and matrix and delamination damage (m_4).

For the MAT162 damage model the strain rate dependent functions for the moduli or strength are

$$\{E_{RT}\} = \{E_0\}\left(1+\{C_{rate}\}\ln\frac{\left\{\dot{\bar{\varepsilon}}\right\}}{\dot{\varepsilon}_0}\right) \quad \text{or} \quad \{S_{RT}\} = \{S_0\}\left(1+C_{rate}\ln\frac{\left\{\dot{\bar{\varepsilon}}\right\}}{\dot{\varepsilon}_0}\right) \quad (18)$$

Where $\{C_{rate}\}$ are the strain constants, $\{E_0\}$ are the modulus values at the reference strain-rate $\dot{\varepsilon}_0$ or the $\{S_0\}$ are the modulus values at the reference strain-rate $\dot{\varepsilon}_0$.

In summary MAT162 is the only constitutive model available that captures the damage softening of plain weave composites. All previous studies were conducted using either S-2 glass or a hybrid of E-glass and Polypropylene fiber materials. Each of the studies only looked at an individual fragment shape in the investigation.

1.3 OBJECTIVES AND APPROACH

1.3.1 Objectives

The primary objective of this numerical and experimental investigation is to determine the terminal behavior of arbitrary shaped fragments versus E-Glass/Phenolic. The secondary objectives are to develop an analytical model(s) (empirical and semi-empirical equations) to predict the performance of these GFRPs versus arbitrary shaped fragments, and to develop the numerical material model parameters and calibrate a numerical model for use in future protection design studies.

1.3.2 Approach

To conduct numerical experiments the materials properties must be fully characterized. To fully characterize the material properties of plain weave E-glass/Phenolic composites the material will be examined under quasi-static, low-velocity impact (LVI) and ballistic loading conditions. This is accomplished through a series of standardized ASTM and Department of Defense test procedures, and through a series of non-standard material property tests. The properties determined in this investigation from standard ASTM Tests are: a) tensile, compressive, and shear strengths, b) elastic and shear moduli, c) density, and d) Poisson's ratio. The material properties determined in this investigation from non-standard testing are punch shear and crush strengths. The LVI test is used to obtain force versus time curves for various loading conditions, and ballistic testing provides depth of penetration and V_{50}

results. The experimental results will be used to optimize and validate the parameters for use in numerical solutions of ballistic impact events.

Ballistic experiments are conducted to determine the dynamic impact response of finite and semi-infinite target thicknesses of E-Glass/Phenolic when penetrated by 8 different nose shaped fragments. V_{50} testing is conducted on 4 mm, 9 mm, and 14 mm finite thick targets. Impact and residual velocity data was acquired for each of the finite thickness targets; these were used to produce impact versus residual velocity curves. Additional ballistic testing referred to as ballistic punch shear testing (BPST) is conducted to determine the ballistic limit for the right circular cylinder (RCC) projectile impacting the 9 and 14 mm targets. The BPST experiments used a specially designed fixture which can easily be replicated in numerical simulations. Depth of penetration experiments are conducted using the RCC into a semi-infinite (50 mm) composite target.

While the nine elastic constants and ten strength parameters [26, 31, 32]of E-Glass/Phenolic are determined by ASTM standard test methods for inclusion into the MAT162 Composite MSC Damage Model, the damage softening (AM), OMGMX, ECRSH, E_LIMT, and EEXPN cannot be found from the ASTM tests. The parameters will be found using numerical parametric studies. The post damage softening parameters AM1-AM4 and the modulus reduction factor OMGMX are determined by simulating low-velocity impact experiments. The penetration erosion parameter ECRSH is found by simulating depth of penetration experiments; while the penetration erosion parameters E_LIMT and EEXPN are determined by simulating ballistic impact experiments.

CHAPTER 2 - AN EXPERIMENTAL INVESTIGATION OF THE EFFECT OF NOSE SHAPE ON FRAGMENTS PENETRATING GFRP

An investigation on the penetration of E-Glass/Phenolic by fragments with eight different nose shapes has been completed. The primary objective of the investigation was to evaluate the ballistic penetration of fragments of equal mass, with L/D of 0.9 to 1.3 and varying nose shapes, into three thicknesses (4, 9, 14 mm) of the GFRP material. The slight variance in L/D was due to the constant mass requirement. Target thickness was varied to examine any sensitivity of the nose shapes to target thickness. Aside from the target thickness, the variables were reduced to the impact velocity and the nose shape of the fragment. The secondary objective was this study is to compare the experimental results for compact fragments with Wen's analytical model [1, 2] and Eq. (2) above presented by Jenq et al.[17]. For Wen's model the data is examined using published values for the experimentally derived β and newly derived β values developed from the experimental data collected in this investigation.

2.1 EXPERIMENTAL SET-UP

The [0/0] E-Glass/Phenolic panels were fabricated using a (5 x 5) plain weave prepreg comprised of OCV Advantex 3011 E-glass and Hexicon SC-1008 phenolic resin. Three nominal thicknesses (4 mm, 9 mm and 14 mm) of composite panels were used in the ballistic testing. The 4 mm thick panel was comprised of 8 plies, the 9 mm thick panel was comprised of 18 plies, and the 14 mm thick panel was comprised of 28 plies. The thinnest target thickness was determined by evaluating the length of the nose for each of the FSPs and ensuring that the target thickness was greater than the length of the longest nose. The 9 mm thickness was chosen based on the separation of energy absorption found by Gellert et al [20], which indicates a transition from thin to intermediate target thickness behavior. The thickest target (14 mm) was considered thick enough to allow all of the FSPs to become fully embedded for a length of time before interacting with the distal side which by definition is a thick target element.

Eight different fragment simulating projectile (FSP) geometries were manufactured for this study, standard 30 caliber FSP, chisel, modified 30 caliber FSP, 120 degree conical, right circular cylinder (RCC), hemispherical, cube, and parallelepiped (Figure 7 and Figure 8a). The FSPs were AISI 4140 steel hardened to Rockwell C 30 ± 1 with a mass of 2.85 g ± 0.03 g. The drawings for all of the FSPs are provided in Appendix A. All FSPs were in the length to diameter (*L/D*) range of $0.9 \leq L/D \leq 1.3$. The *L/D* variance in the FSPs was due to the change in nose shape and the requirement for a constant mass. Table 3 shows the length, nose length (L_N), diameter, *L/D* and L_N/D for each of the FSPs. The *L/D* for the FSPs with non-cylindrical bodies was calculated using an equivalent diameter as indicated by the asterisk in the table. The equivalent diameter was found by taking the cross-sectional area of the shape and determining the equivalent diameter for a circle of the same area.

The nose length to diameter (L_N/D) determines the degree of bluntness for the various nose shapes [34]. Nose length to diameters less than one are considered blunt while $L_N/D > 1$ is considered sharp. The closer the L_N/D value is to zero the blunter the nose shape.

The cube and parallelepiped FSPs were sabot launched from a smooth bore powder gun with a 50 caliber barrel. The sabot design was a serrated four-piece with integral pusher, and is shown in Figure 8b. A sabot stripper was placed 1.5 m downrange from the muzzle. All of the spin stabilized FSPs shown in Figure 7a are fired from a rifled 30 caliber powder gun. The test set-up shown in Figure 9 has four infrared photoelectric velocity screens separated by 76.2 cm and connected to two

Table 3. FSP Length to Diameter Ratios

Fragment Simulating Projectile	*Length, L (mm)*	*Nose Length, L_N (mm)*	*Diameter, D (mm)*	*L/D*	*L_N/D*
Cube	7.11	0	8.03*	0.9	0
Right Circular Cylinder	8.2	0	7.52	1.1	0
Parallelepiped	8.2	0	7.51*	1.1	0
30 Cal FSP	8.48	2.02	7.52	1.1	0.27
120 Degree Conical	9.65	2.29	7.52	1.3	0.3
Modified 30 Caliber FSP	9.12	2.95	7.52	1.2	0.39
Chisel	9.78	3.64	7.52	1.3	0.48
Hemispherical	9.35	3.76	7.52	1.2	0.5

**Equivalent Diameter*

a)

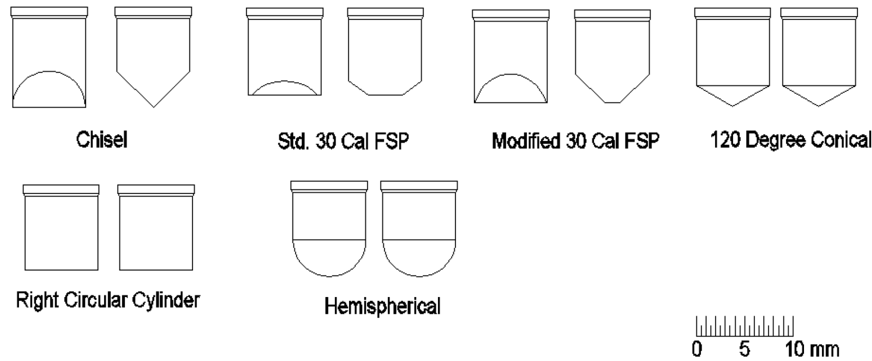

b)

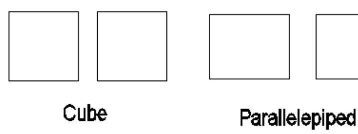

Figure 7. FSP geometries: a) Spin Stabilized Fragments b) Sabot Launched Fragments

a)

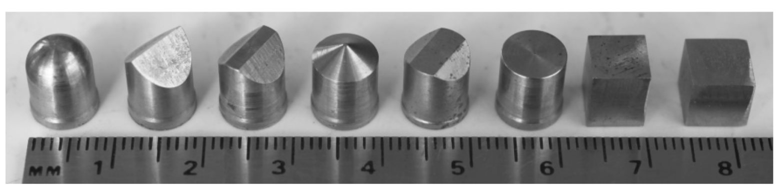

b)

Figure 8. a) Fragment Simulating Projectiles (mm scale), b) 4 Piece Sabot Shown with Cube FSP

chronographs, were used to determine the strike velocities. The residual velocity was recorded using two screens separated by 91.4 cm as shown in Figure 9.

The ballistic limit was determined in accordance with MIL-STD-662F [19] using a four shot ballistic limit with a range of results less than or equal to 18 m/s or a six shot ballistic limit with a range of results less than or equal to 27 m/s.

The strike or impact velocity V_i was determined with respect to the primary velocities using Eq. (1) and in accordance with Eq. (19).

$$V_s = V_2 + \left(\frac{152.4}{76.2}\right)(V_2 - V_1) \tag{19}$$

Both ballistic limit and residual velocity experiments were conducted for each of the FSPs on all three panel thicknesses.

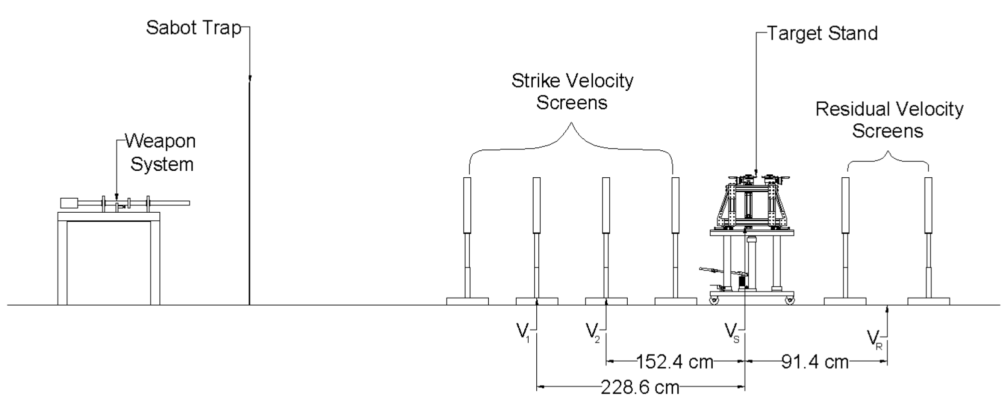

Figure 9. Velocity Measurement Diagram

Once the ballistic limit was determined for each panel, four additional shots were made at approximately 50 m/s intervals above the ballistic limit in order to develop the strike versus residual velocity curves and to investigate energy absorption for the material versus each of the projectiles.

2.2 *EXPERIMENTAL RESULTS*

2.2.1 V_{50} Results

A total of 360 ballistic experiments were conducted in this investigation, and the complete data set is provided in Appendix A. A summary of the ballistic limit data is shown in Table 4 and plotted in Figure 28. As the target material becomes thinner, the data starts to converge for all of the nose shapes; indicating that for thinner targets, the nose shape of the fragment has less influence on the penetration performance. Three error bounds, ±10% and -30%, are plotted relative to the ballistic limit of the standard 30 Cal FSP which is the standard FSP used to qualify composite armor. It can be seen from the data that the projectile nose shape has significant influence on the ballistic limit. The FSP with a hemispherical-shaped nose has the lowest ballistic limit for the 9 mm and 14 mm panel thickness, while the cube-shaped FSP has the highest. For the 9 mm and 14 mm panels, four FSP's are found to have ballistic limits more than 10% below the standard FSP.

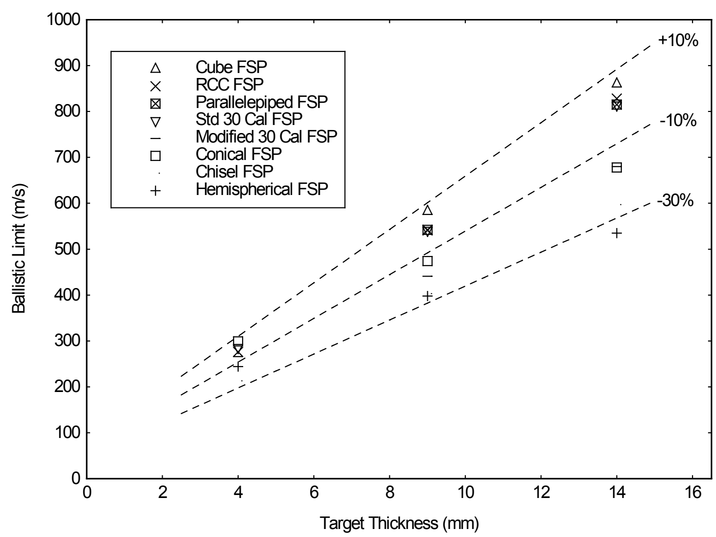

Figure 10. Ballistic Limit versus Target Thickness

Table 4. Ballistic Limit Data

Fragment	*Target Thickness mm*	*V_{BL} m/s*	*Shots in V_{BL} Calculation*	*Error (m/s)*
Cube	14	861	4	8
RCC	14	828	4	3
30 Cal FSP	14	813	4	4
Parallelepiped	14	813	6	13
Modified 30 Cal FSP	14	680	4	9
Conical	14	677	4	7
Chisel	14	598	4	8
Hemispherical	14	535	4	6
Cube	9	583	6	14
Parallelepiped	9	542	6	11
RCC	9	541	4	9
30 Cal FSP	9	541	4	7
Conical	9	474	6	14
Modified 30 Cal FSP	9	441	4	2
Chisel	9	403	4	9
Hemispherical	9	398	4	9
Conical	4	302	4	8
30 Cal FSP	4	284	4	8
RCC	4	276	6	13
Hemispherical	4	244	6	12
Chisel	4	213	6	12
Modified 30 Cal FSP	4	213	6	12

The experimental results indicate that the *L/D* is not as important as the nose shape for fragments, since the chisel and the 120 degree conical had the largest *L/D*, and they were the both less efficient than the hemispherical with a slightly lower *L/D*.

The ballistic data in Table 4 indicates that the rank of penetration efficiency for the FSPs changes within the three thicknesses. Which would indicate that the dominate energy absorbing mechanism must be changing through the thickness and that the three target thicknesses are indicative of thin, intermediate and thick target response. The rank of efficiency for the 9mm target performance aligns exactly with the degree of bluntness for each projectile as shown previously in Table 3, i.e. the blunter the projectile the lower the penetrator efficiency, which has also been observed for projectiles with *L/D*>1 in [20].

2.2.2 V_i-V_r Results

Table 5 shows the impact velocity, residual velocity, impact energy, residual energy, and the energy absorbed for four shots on each target, with each projectile. The energies are based on the kinetic energy of each fragment. The table shows that the energy absorbed directly relates to the penetration performance of each FSPs nose shape. As the penetration efficiency increases for the FSP, the energy absorbed decreases. Of the eight nose shapes tested, the hemispherical nose shape had the lowest ballistic limit and absorbed the least amount of energy.

Table 5. Strike versus Residual Velocity Data

Shot#	*Target Thickness (mm)*	*FSP Mass (g)*	*FSP Shape*	V_I *(m/s)*	V_R *(m/s)*	E_I *(J)*	E_R *(J)*	E_A *(J)*
2011001-6	14	2.84	30 Cal FSP	848	165	1023	39	985
2011001-14	14	2.85	30 Cal FSP	909	273	1178	106	1071
2011001-13	14	2.86	30 Cal FSP	920	286	1208	117	1091
2011001-15	14	2.84	30 Cal FSP	970	404	1335	231	1104
2011002-9	9	2.84	30 Cal FSP	568	153	457	33	424
2011002-6	9	2.85	30 Cal FSP	579	191	477	52	425
2011002-18	9	2.82	30 Cal FSP	644	265	585	99	486
2011002-19	9	2.88	30 Cal FSP	692	376	690	204	486
2011003-6	4	2.84	30 Cal FSP	345	172	169	42	127
2011003-7	4	2.84	30 Cal FSP	381	228	206	74	133
2011003-10	4	2.86	30 Cal FSP	426	286	259	117	142
2011003-8	4	2.86	30 Cal FSP	476	365	324	191	133
2011004-17	14	2.88	Chisel	712	235	730	79	650
2011004-14	14	2.86	Chisel	751	269	806	103	703
2011004-15	14	2.88	Chisel	832	394	998	224	774
2011004-16	14	2.88	Chisel	871	461	1093	307	786
2011005-6	9	2.86	Chisel	481	198	331	56	275
2011005-7	9	2.88	Chisel	539	265	418	101	317
2011005-8	9	2.88	Chisel	569	307	467	136	332

2011005-9	9	2.88	Chisel	618	362	549	189	360
2011006-31	4	2.88	Chisel	246	109	87	17	70
2011006-3	4	2.88	Chisel	291	166	122	40	82
2011006-2	4	2.87	Chisel	374	265	200	100	100
2011006-1	4	2.88	Chisel	419	306	254	135	118
2011007-2	14	2.88	Conical	765	284	845	116	728
2011007-16	14	2.88	Conical	807	297	938	128	810
2011007-14	14	2.88	Conical	774	302	862	131	731
2011007-17	14	2.88	Conical	877	398	1107	228	879
2011008-11	9	2.88	Conical	582	286	488	118	370
2011008-12	9	2.89	Conical	614	332	545	159	386
2011008-13	9	2.88	Conical	639	369	588	196	392
2011008-14	9	2.87	Conical	727	467	758	313	445
2011009-1	4	2.88	Conical	396	240	226	83	143
2011009-22	4	2.88	Conical	465	331	310	158	152
2011009-21	4	2.86	Conical	504	380	364	207	156
2011009-19	4	2.86	Conical	544	435	424	271	153
20110010-3	14	2.88	RCC	852	210	1046	64	982
20110010-2	14	2.88	RCC	870	256	1090	95	996
20110010-8	14	2.88	RCC	912	276	1200	110	1090
20110010-9	14	2.88	RCC	1018	408	1493	240	1254
2011017-11	9	2.88	RCC	650	290	610	121	489
2011017-12	9	2.88	RCC	689	340	685	167	518
2011017-14	9	2.88	RCC	753	426	817	261	555
2011017-13	9	2.86	RCC	772	450	854	290	564
2011019-10	4	2.88	RCC	312	153	140	34	106
2011019-18	4	2.88	RCC	386	230	214	77	138
2011019-19	4	2.88	RCC	442	283	282	116	166
2011019-20	4	2.87	RCC	478	319	328	146	182
2011023-6	14	2.88	Hemisphere	671	309	647	137	510
2011023-3	14	2.88	Hemisphere	768	426	849	260	588
2011023-2	14	2.88	Hemisphere	815	502	956	363	593
2011023-1	14	2.88	Hemisphere	841	527	1017	400	617
2011024-9	9	2.88	Hemisphere	397	39	226	2	224
2011024-6	9	2.88	Hemisphere	410	85	243	10	232
2011024-11	9	2.88	Hemisphere	465	253	311	123	188
2011024-13	9	2.88	Hemisphere	575	355	476	181	294
2011025-7	4	2.87	Hemisphere	269	71	104	7	97
2011025-10	4	2.88	Hemisphere	286	135	118	26	92
2011025-12	4	2.87	Hemisphere	301	152	130	33	97
2011025-21	4	2.87	Hemisphere	408	297	238	127	111
2011026-14	14	2.84	Modified FSP	680	63	658	6	653
2011026-19	14	2.88	Modified FSP	706	140	717	38	679
2011026-20	14	2.88	Modified FSP	777	163	868	75	793
2011026-22	14	2.86	Modified FSP	825	190	974	162	813
2011027-2	9	2.87	Modified FSP	489	101	343	15	328
2011027-17	9	2.86	Modified FSP	528	182	400	48	352
2011027-18	9	2.86	Modified FSP	562	257	453	94	359
2011027-19	9	2.88	Modified FSP	615	337	545	163	382
2011028-4	4	2.84	Modified FSP	267	92	101	12	89
2011028-16	4	2.87	Modified FSP	281	111	113	18	96
2011028-1	4	2.88	Modified FSP	295	135	126	26	99
2011028-10	4	2.86	Modified FSP	325	185	151	49	102

2.2.3 Damage Profiles

To better understand the failure mechanisms for each of the fragment simulating projectile nose shapes, cross-sections were taken for partial penetration events as close as possible to the V_{BL}. Figure 11 shows the displacement profiles for each of the different fragments into 14 mm thick targets. One might expect that the least efficient FSPs would cause more displacement on the distal side of the impact. However, this did not prove to be true; the cube with its flat face was the least efficient FSP, and it had a back face displacement of 3.7 mm, and only the hemispherical and conical FSPs had less displacement than the cube. Gellert et. al [20] reported that the blunter the nose the larger the delamination cone diameter on the exit side. Only the hemispherical nose shape had a lower delamination cone diameter than the flat faced parallelepiped and cube. So no correlation to penetration resistance could be derived from the displacement profiles.

Photographs were taken of the penetration cavities of these cross sections and are shown in Figure 12 and Figure 13. The conical, hemispherical, and the RCC FSPs are symmetrical, and observations will be made for each of the penetration cavities for these fragment simulating projectiles. The remaining FSPs are of an unsymmetrical nature and will require a numerical modeling effort to gain insight into the failure mechanisms produced during their penetration. While it is true that the cube and parallelepiped are symmetric in the through thickness direction it could not be determined with certainty that the cross-section was made on the plane of symmetry, so no observations will be given here, and numerical analysis will be conducted in the future for these shapes as well.

The penetration cavity for the conical FSP reveals that 5 plies towards the impact side were expanded upwards a distance of 2.7 mm from the original surface. On the distal side, there was a bulge 5.6 mm below the original surface which showed expansion across 14 plies. A cavity approximately 10.6 mm deep by 3.5 mm wide was created on the impact side. It appears that the initial failure mode was shear plugging which transitioned into tensile fiber failure and interlaminar delamination failure approximately 8 mm into the target.

The penetration cavity for the hemispherical FSP reveals that 4 plies towards the impact side were expanded upwards a distance of 1.0 mm from the original surface. On the distal side, there was a bulge 2.5 mm below the original surface which showed expansion across 4 plies. A cavity approximately 7 mm deep by 2.2 mm wide was created on the impact side. It appears that the initial failure mode was shear plugging, which transitioned into tensile fiber failure of the last 3 plies.

The penetration cavity for the RCC FSP reveals that 5 plies towards the impact side were expanded upwards a distance of 4.5 mm from the original surface. On the distal side there was a bulge 7.0 mm below the original surface, which showed expansion across 4 plies. A cavity approximately 6.3 mm deep by 2.2 mm wide was created on the impact side. It appears that the initial failure mode was shear plugging, which transitioned into tensile fiber failure and interlaminar delamination failure approximately 9 mm into the target.

For these three symmetrical FSPs the distal side deformation or cone diameter formation at the ballistic limit follows the order of the ballistic limits, i.e., the hemispherical nose shaped FSP has the lowest ballistic limit and the least amount of deformation (2.5 mm) on the distal side of the target. While the blunt nosed FSP (RCC) has the highest ballistic limit, and it also has the highest deformation (7.0 mm) on the distal side of the target.

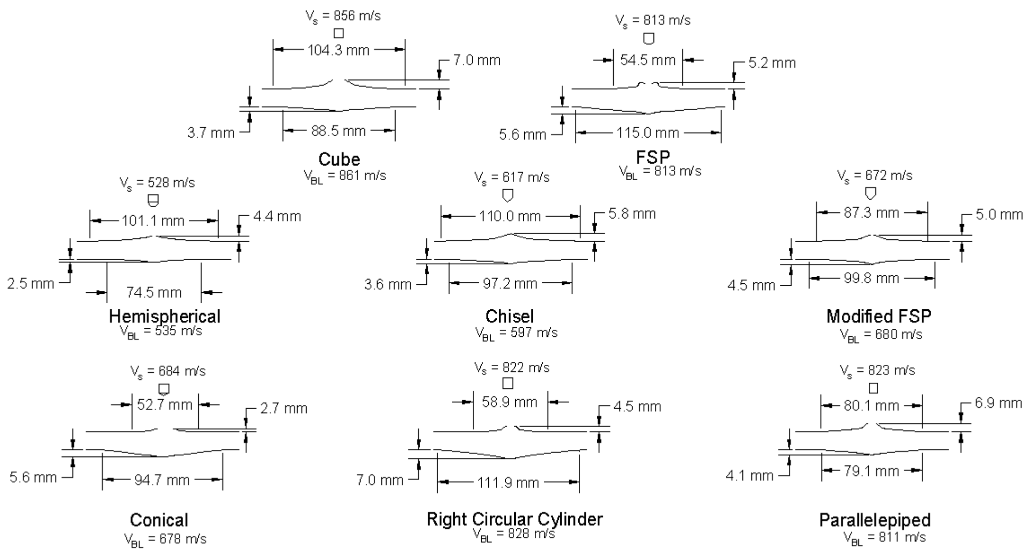

Figure 11. Displacement Profiles for 14mm Thick Targets

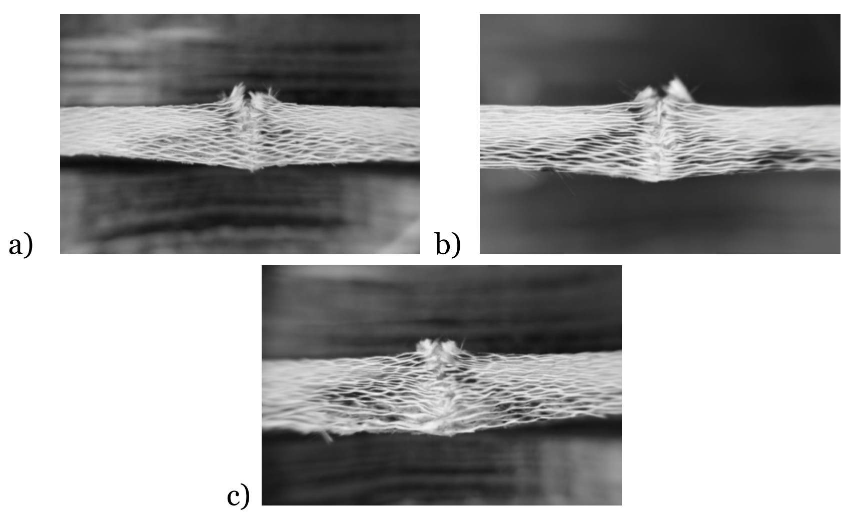

Figure 12. Symmetric Fragments Cross-Sections; a) Conical, b) Hemispherical, c) RCC

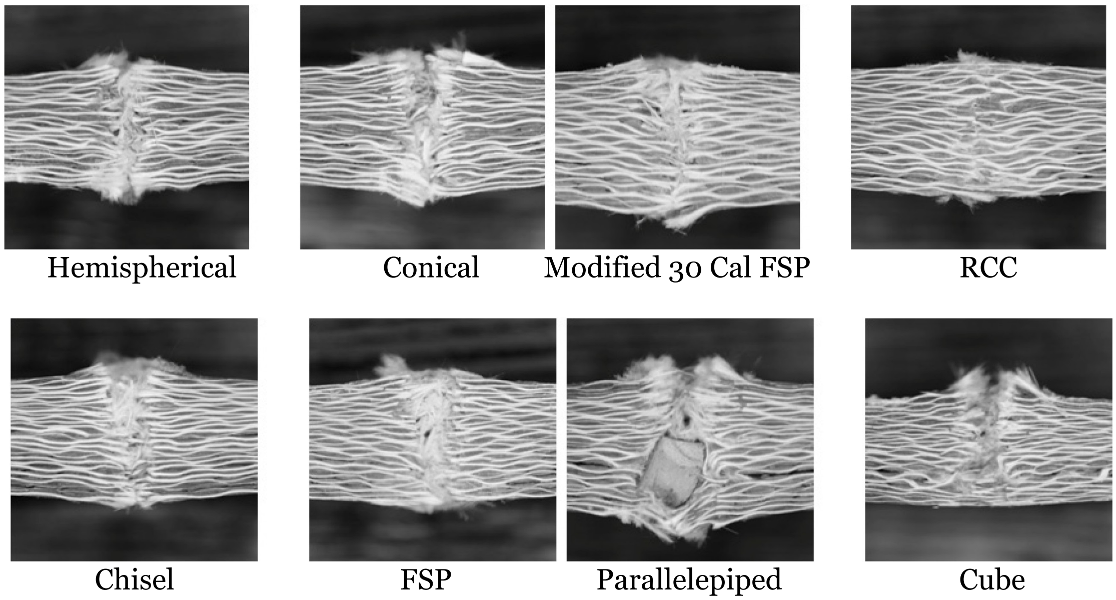

Figure 13. Penetration Cavities Cross-Sections for 14mm Thick Targets

2.3 ANALYTICAL RESULTS

2.3.1 Wen's Analytical Model [1]

The basic assumptions of Wen's model are that "*the deformations are localized and that the average pressure provided by the target materials to resist the projectiles can be divided into two parts. One part is the cohesive quasi-static resistive pressure applied normally to the projectile surface due to the elastic-plastic deformations of the FRP laminate materials and the other is the dynamic resistive pressure arising from velocity effects.*" The simplified ballistic limit equation developed by Wen as presented in [2, 1, 24] is:

$$V_{BL} = \frac{\pi\beta\sqrt{\rho_t\sigma_e}D^2T}{4m_p}\left[1+\sqrt{1+\frac{8m_p}{\pi\beta^2\rho_t D^2 T}}\right] \tag{20}$$

where β is an empirically determined constant. For each nose-shape the β values presented by Wen are Conical-nose $\left(\beta = 2\sin\frac{\theta}{2}\right)$, Flat-nose ($\beta$ = 2), Hemispherical-nose (β = 1.5). In actuality these beta values are not empirical constants as mentioned in [1] but are geometrical shape factors of the nose shape. The parameters for the calculations are; ρ_t is the density of the target (2107 kg/m^3), σ_e is the compression elastic limit of the target (131 MPa), D is the diameter of the projectile or fragment (0.00752m), T is the thickness of the target, and m_p is the mass of the projectile or fragment (0.00285 kg). Figure 14 is a plot of the experimental data points and the curve fit using Eq. (20). The fit to the fragment experiment data was not very good.

New empirical constants were derived by curve fitting the experimental data for all the nose shapes, and are presented in Table 6. The coefficient of determination (R^2) for each of the curve fits to the experimental ballistic limit values is also shown in Table 6. The coefficient of determination values indicate that the goodness of fit for the calculated data points to the experimental data is excellent. Figure 15, is a graphical representation of the comparison between the experimental data and the analytical calculations using the empirically derived β values.

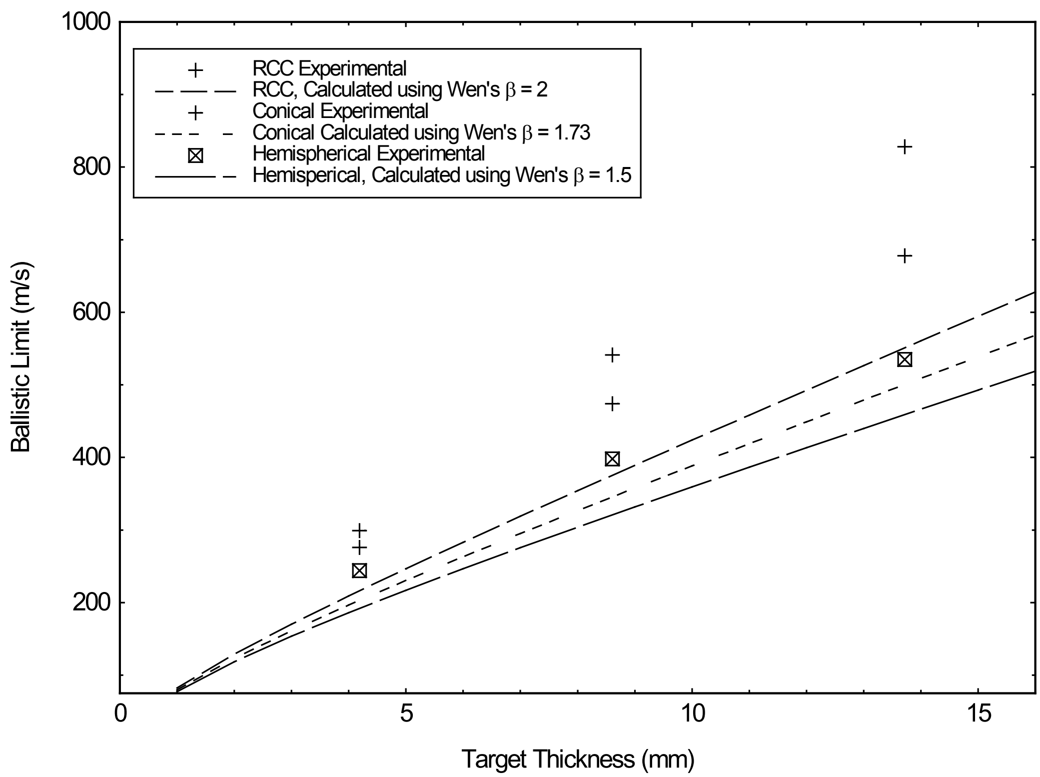

Figure 14. Comparison of Analytical Predictions and Experimental Data

Table 6. Experimentally Derived β

Fragment Simulating Projectile	*β*	*R^2*
Cube	3.59	.992
Right Circular Cylinder	3.37	.999
Parallelepiped	3.34	.999
30 Caliber FSP	3.32	1.00
120 Degree Conical	2.74	.964
Modified 30 Caliber FSP	2.65	.996
Chisel	2.22	.997
Hemispherical	2.02	.964

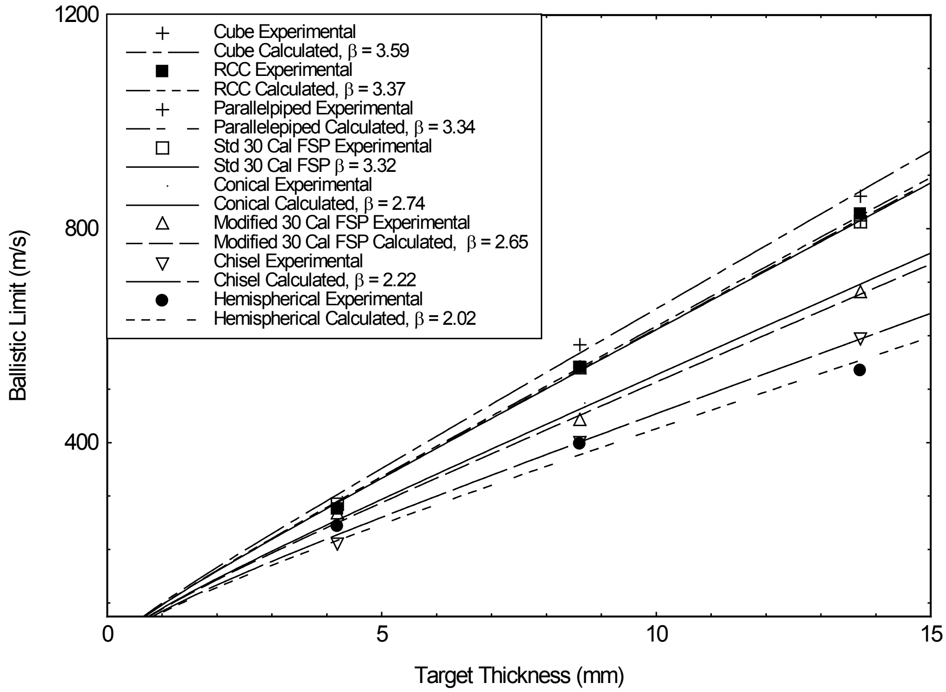

Figure 15. Comparison of Analytical Predictions and Experimental Data for Empirically Derived Betas

2.3.2 Accuracy of Simplified Kinetic Energy Estimation Method

Assuming the penetrator remains rigid and that the mass of the fragment simulating projectile remains constant, Eq. 2 can be further simplified to

$$V_{BL}^2 = V_s^2 - V_r^2 \qquad (21)$$

The ballistic limit data was calculated using Eq. (21) for each shot using the strike and residual velocity data from Table 5. An average for each of the four ballistic limits was compared to the actual ballistic limit velocity obtained experimentally in Table 7. The results show that this equation is marginally accurate for various nose shapes and cross-sectional thicknesses and may be used for rough order of magnitude calculations. It should be pointed out that the use of Eq. (21) only requires one ballistic experiment with a complete penetration, versus a minimum of four experiments for the V_{50} ballistic limit. It is important to note that for all but two cases, the calculated ballistic limit is higher than the actual limit. Due to the unconservative nature of this estimation method, appropriate reductions should be made before using this method for design.

Table 7. Comparison of Experimental Data to Eq. 21

Fragment Simulating Projectile	*Thickness (mm)*	*Actual V_{BL} (m/s)*	*V_{BL} Calculated from Eq. 21*	*%Error*
Chisel	4	213	232	8.9
Chisel	9	403	472	17.1
Chisel	14	597	711	19.1
120 Degree Conical	4	299	325	8.7
120 Degree Conical	9	474	526	11.0
120 Degree Conical	14	678	739	9.0
30 Caliber FSP	4	285	245	-14.0
30 Caliber FSP	9	540	560	3.7
30 Caliber FSP	14	813	848	4.3
Hemispherical	4	244	263	7.8
Hemispherical	9	398	402	1.0
Hemispherical	14	535	633	18.3
Modified 30 Caliber FSP	4	266	260	-2.25
Modified 30 Caliber FSP	9	441	497	12.6
Modified 30 Caliber FSP	14	680	715	5.1
Right Circular Cylinder	4	276	319	15.6
Right Circular Cylinder	9	541	608	12.4
Right Circular Cylinder	14	828	865	4.5

2.4 SUMMARY OF EXPERIMENTAL INVESTIGATION

The results of the investigation showed that the ballistic limit and energy absorbed is significantly affected by the nose shape of the FSP. While all of the fragments are considered blunt nose shapes, the fragments with the sharper nose shapes were the most efficient penetrators (hemispherical, and chisel), and the fragments presenting a flat surface at the nose (cube, RCC and parallelepiped) were the least efficient penetrators. The difference between the ballistic limit for the least efficient nose shape (cube) and the most efficient nose shape (hemispherical) was 326 m/s for the 14-mm-thick target. The investigation also revealed that penetration of thinner targets is not influenced as much by the nose shape of the FSPs.

Beta values for use in Wen's analytical model were derived empirically for all nose shapes. Close agreement was achieved between the analytical equation and the experimental results for FSPs using the empirically derived β values.

The investigation also showed that Jenq's simplified equation is marginally accurate when calculating ballistic limits from strike and residual velocity data for different thickness of materials and for various nose shapes.

CHAPTER 3 - QUASI-STATIC, LOW-VELOCITY IMPACT AND BALLISTIC IMPACT BEHAVIOR OF PLAIN WEAVE E-GLASS/PHENOLIC COMPOSITES

The objective of this chapter is to fully characterize the material properties of plain weave E-glass/Phenolic composites under quasi-static, low-velocity impact (LVI) and ballistic loading conditions. This is accomplished through a series of standardized ASTM and Department of Defense test procedures, and through a series of non-standard material property tests. The properties determined in this investigation from standard ASTM Tests are: a) tensile, compressive, and shear strengths, b) elastic and shear moduli, c) density, and d) Poisson's ratio. The material properties determined in this investigation from non-standard testing are punch shear and crush strengths. The LVI test is used to obtain force versus time curves for various loading conditions, and ballistic testing provides depth of penetration and V_{50} results. The experimental results of this investigation can be used for structural design and to validate numerical solutions of ballistic impact events.

3.1 MATERIAL AND TEST METHODS

3.1.1 E-Glass/Phenolic Material

The [0/0] E-Glass/Phenolic panels were fabricated using a (5 x 5) plain weave prepreg comprised of OCV Advantex 3011 E-glass and Hexicon SC-1008 phenolic resin. Five nominal thicknesses (4 mm, 9mm, 14 mm, 25 mm, and 50 mm) of composite panels were used in this investigation. The 4 mm thick panel was comprised of 8 plies, the 9 mm thick panel was comprised of 18 plies, the 14-mm-thick panel was comprised of 28 plies, the 25 mm thick panel was comprised of 50 plies, and the 50 mm thick panel was comprised of 100 plies. All panels were manufactured in accordance with MIL-DTL-6415B [6].

3.1.2 Quasi-Static Testing

3.1.2.1ASTM Test Methods

The standard ASTM International tests listed in Table 3 were conducted to find the density (ρ), Poisson's ratio (ν), Young's Modulus (E), shear modulus (G), and tensile (F^t), compressive (F^c) and shear strengths (F^s) of the material.

Table 8. Test Standards

ASTM Standard	*Properties*
D792 – 08, Standard Test Methods for Density and Specific Gravity (Relative Density) of Plastics by Displacement [35]	γ, ρ
D3039/D3039M – 08, Standard Test Method for Tensile Properties of Polymer Matrix Composite Materials [36]	ν, E, F^t
D5379/D5379M – 05, Standard Test Method for Shear Properties of Composite Materials by the V-Notched Beam Method [37]	F^s
D6641/D6641M – 09, Standard Test Method for Compressive Properties of Polymer Matrix Composite Materials Using a Combined Loading Compression (CLC) Test Fixture [38]	G, F^c
D7291/D7291M – 07, Through-Thickness "Flatwise" Tensile Strength and Elastic Modulus of a Fiber-Reinforced Polymer Matrix Composite Material [39]	E, F^t

3.1.2.2 Quasi-Static Punch Shear Testing (QS-PST)

A quasi-static punch shear test (QS-PST) methodology was developed by the University of Delaware Center for Composite Materials for studying the damage mechanisms and penetration resistance behavior of thick section composites [10]. QS-PSTs are performed using a steel fixture shown in Figure 16 that consists of a circular bottom support, a matching top cover plate, and a punch. The circular bottom support is an annulus with an outer diameter of 50.8 mm and inner diameter of 12.7 mm that is counterbored to a depth of 19.05 mm with a 25.6 mm concentric hole. The cover plate is an annulus with an outer diameter of 50.8 mm and an inner diameter of 7.62 mm. The cover plate is attached to the bottom support via bolts. A support ring is on each side of the composite material. The upper support ring is a guide for the punch shank and has an outer diameter of 25.4 mm and an inner diameter of 12.72 mm. The bottom support ring has the same outer diameter as the upper (25.4 mm) and the inner diameter is varied to achieve different support span diameters. A two-step cylindrical punch with a 12.7 mm upper diameter punch head and a 7.60 mm lower diameter punch shank slides through the cover plate and the upper support plate to load the 8 ply composite specimens. The upper portion of the punch is adapted to a 133.4 kN load cell that is connected to a universal test machine. QS-PST tests are performed at a cross-head displacement rate of 0.508 mm/min (0.02 in./min), and both the load and cross-head displacement data are collected at approximately 100 Hz. The ratio between the support span diameter and the punch shank diameter is known as SPR. With this fixture, the SPR can range between 1.01 and 1.20. The material is examined at various SPR values in order to extrapolate the true punch shear strength (PSS), which occurs at an SPR of 1.0.

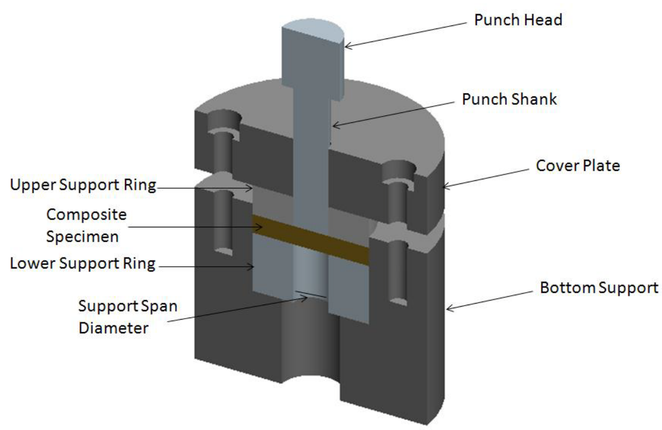

a) QS-PST Fixture b) Cross-Sectional 3D Sketch of the QS-PST Fixture

Figure 16. QS-PST Fixture

3.1.2.3 Punch Crush Strength (PCS) Testing

Two different fixtures are used for the PCS test. One is the QS-PST fixture previously described with a solid lower support ring. The second fixture for the PCS test is the punch crush strength test (PCST) fixture shown in Figure 17. The PCST fixture has an annulus with an outer diameter of 50.8 mm and inner diameter of 12.7 mm, and has a concentric 25.4 mm diameter counterbore to a depth of 19.05 mm. The 25.4 mm counterbored portion of the fixture accommodates the 8 ply specimen, punch, and punch guide. The diameter of the punch (D_p) can be varied between 12.7 mm and 6.37 mm. The PCS test uses the same load cell, data acquisition rates, and cross-head speeds as the QS-PST test. The punch head (12.7 mm diameter) of the QS-PST two-step cylindrical punch is used as a loading block to apply load to the punch for the PCS test.

a) PCST Fixture

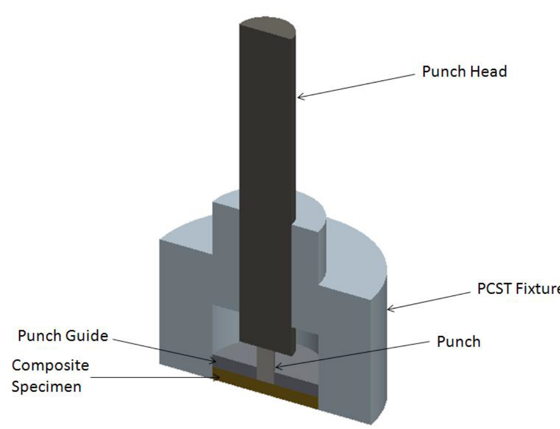

b) Cross-Sectional 3D Sketch of the PCST Fixture

Figure 17. PCST Fixture

3.1.3 Low-Velocity Impact Testing

A Dynatup 9200 drop tower with a 22.3 kN load cell, shown in Figure 18a, is used for the low-velocity impact tests. The LVI test fixture, shown in Figure 18b and Figure 18c, consists of a steel base plate 304 mm by 152 mm by 4 mm, two vertical aluminum support plates 303 mm by 38 mm by 152 mm, a steel support plate 304 mm by 152 mm by 6 mm with a 127 mm by 76 mm central rectangular opening, and a steel cover plate 304 mm by 152 mm by 12.7 mm with a 50.4 mm diameter hole centered on the plate. The 18 ply specimens are aligned and bolted between the steel support plate and the steel cover plate; this provides a perfectly clamped boundary condition. Each of the four bolts is torqued to 1.13 N·m before each experiment. A cylindrical 15.9-mm tip with a hemispherical tip (radius = 7.94 mm) is used for the LVI experiments.

a) b) c)

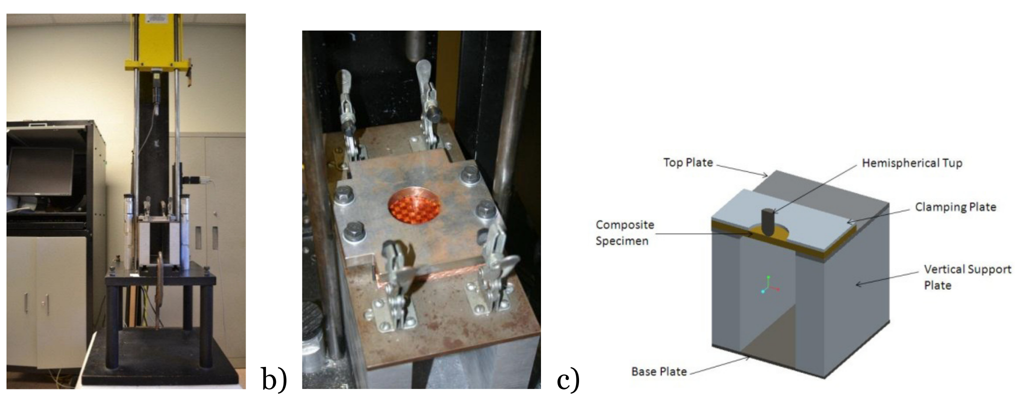

Figure 18. Low-Velocity Impact Experimental Setup

The data provide the contact force ($F(t)$), and the initial velocity (V_o); the instantaneous velocity and displacement of the LVI impact head can be determined following Newton's Second Law of Motion. Assuming rigid body motion and considering the downward motion as positive, this can be expressed as

$$F(t) = -m_p\left(\frac{dV(t)}{dt} - g\right) \tag{22}$$

where m_p is the mass of the drop-weight assembly impacting the specimen. The initial impact velocity can also be determined using the following equation.

$$V_0 = \sqrt{2gH} \tag{23}$$

where g is the acceleration due to gravity, which is equal to 9.81 m/s^2. H is the release height for the drop-weight assembly. To calculate the velocity with respect to time *(t)* Eq. (22) can be written as

$$\int_0^t dV(t) = \int_0^t\left(-\frac{F(t)}{m_p} + g\right)dt \tag{24}$$

Integration of both sides of the equation gives

$$V(t) = V_0 + gt - \frac{p(t)}{m_p} \tag{25}$$

where *p(t)* is the impulse at time *(t)*. Further integration results in Eq. (26).

$$d(t) = V_0 t + \frac{1}{2}gt^2 - \int_0^t \frac{p(t)}{m_p}dt \tag{26}$$

Finally, the total energy can be calculated by integrating the contact force as a function of displacement.

$$W = \int_{h_0}^{h_1} F(h)dh \tag{27}$$

The initial impact energy of the impacting apparatus is calculated using the equation

$$E_I = \frac{1}{2} m_p V_0^2 \tag{28}$$

Equations (25) and (26) are used to calculate the *V(t)* and *d(t)*, respectively. Once the displacement data are obtained from Eq. (26), the force versus displacement curve can be plotted so that the work performed on the specimen can be calculated.

3.1.4 Depth of Penetration (DOP) Ballistic Testing

The depth of penetration (DOP) test set-up was identical to the V_{50} ballistic test set-up with the exception that the DOP test fixture, shown in Figure 19 was placed in front of and clamped to the existing ballistic test fixture. The DOP test fixture is comprised of a solid steel bottom plate with dimensions of 355.6 mm by 254 mm by 25.4 mm thick. The upper frame has the same exterior dimensions with two 76.2 mm by 279.4 mm window openings centered on the plate. The 203.2 mm by 304.8 mm by 50 mm thick 100 ply composite had through holes match drilled down the center and then was clamped together using 18 bolts as shown in Figure 19 and Figure 20. The 100 ply composite plate was a semi-infinite target since it was of sufficient thickness to ensure the distal side had no influence on the penetration.

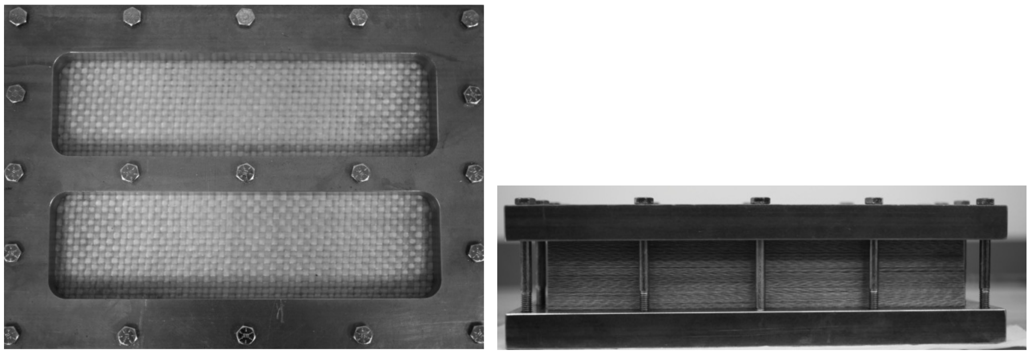

a) Impact Side b) Side View

Figure 19. Depth of Penetration Test Fixture

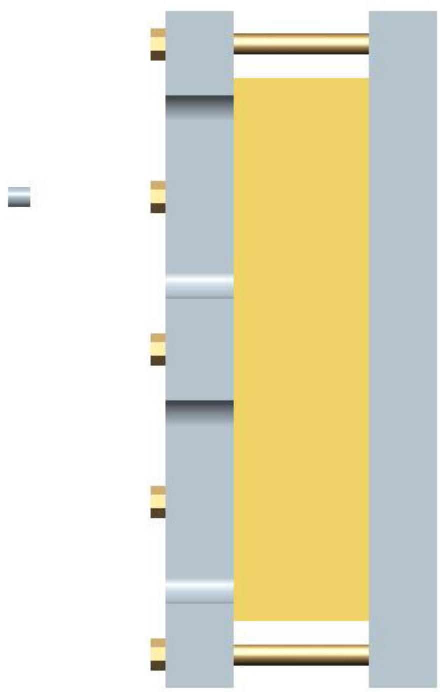

Figure 20. Cross-section of DOP Test Fixture

3.1.5 Ballistic Punch Shear Testing (BPST)

Test Panels of 18 and 28 ply E-Glass/Phenolic composites were cut into 152.4 mm by 152.4 specimens that were bolted between a steel support plate of dimension 178 mm by 178 mm by 50.8 mm thick and a cover plate of the same exterior dimensions with a thickness of 12.7 mm; both plates had a 101.6 mm diameter through hole. Figure 21 and Figure 22 show photographs and cross-sectional views of the BPST fixture.

The 30 caliber (diameter = 7.52 mm) right circular cylinder (RCC) fragment simulating projectile (FSP) was used in these experiments. Both ballistic limit and residual velocity experiments were conducted using the RCC and the two target thicknesses. Once the ballistic limit was determined, additional shots were made at approximately 100 m/s intervals above the ballistic limit in order to develop the strike versus residual velocity curve and to investigate energy absorption for the material versus the FSPs.

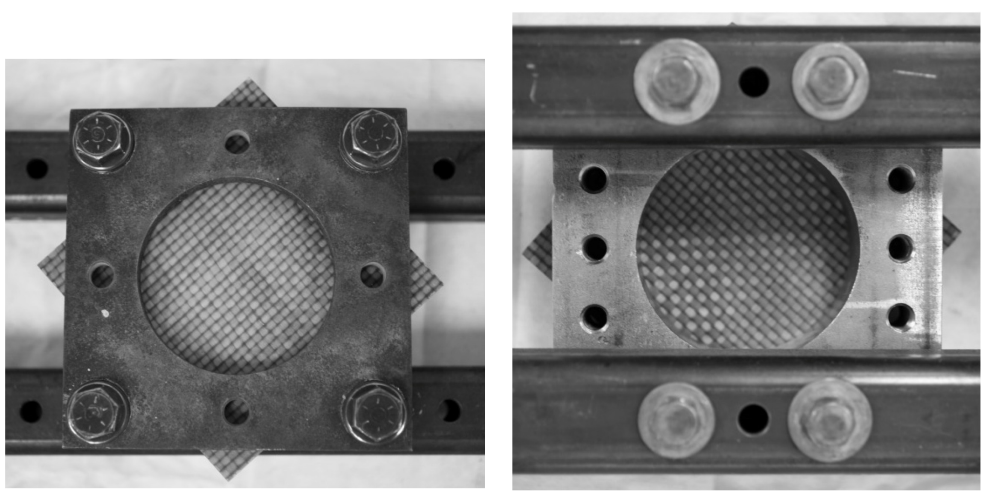

a) Impact Side b) Distal Side

Figure 21. Composite Clamped into the BPST Fixture

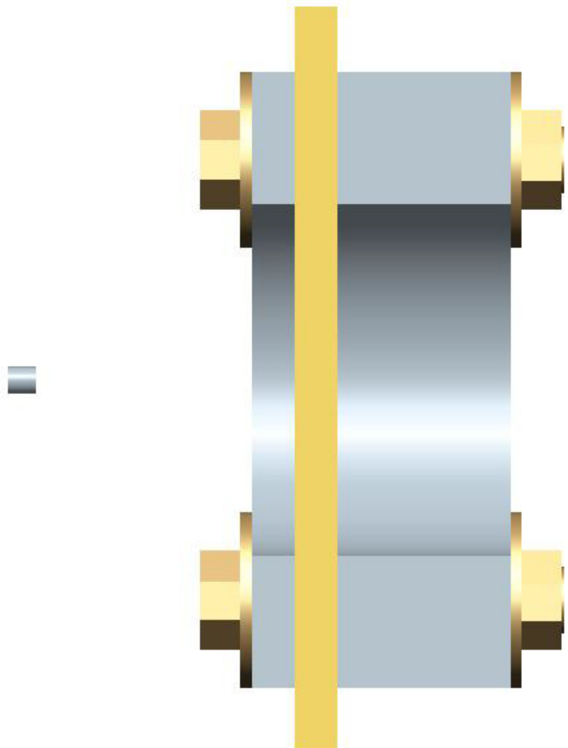

Figure 22. Cross-section of BPST Fixture

3.2 *EXPERIMENTAL RESULTS*

The complete data set from the material property testing is provided in Appendix B and C. A summary of the testing is provided below.

3.2.1 ASTM Test Results

The material properties determined by the standard ASTM tests are shown in Table 9 . The variables are shown using MIL-HDBK-17-1F [40] notation.

Table 9. Laminate Properties from ASTM Tests

Variable	*Description*	*Measured*	*Standard Deviation*
ρ	Mass Density	2107 kg m^{-3}	106 kg m^{-3}
E_1	Young's Modulus – longitudinal direction (warp)	29,151 MPa	3568 MPa
E_2	Young's Modulus – transverse direction (fill)	29,151 MPa	3568 MPa
E_3	Young's Modulus – through-thickness direction	11,000 MPa	1000 MPa
ν_{12}	Poisson's Ratio xy	0.078	0.030
ν_{23}	Poisson's Ratio zx	0.109	0.028
ν_{13}	Poisson's Ratio xz	0.1.09	0.028
G_{12}	In-Plane Shear Modulus xy	1,540 MPa	192 MPa
G_{23}	Out-of-Plane Shear Modulus yz	1,671 MPa	72 MPa
G_{13}	Out-of-Plane Shear Modulus xz	1,671 MPa	72 MPa
F_1^{tu}	Longitudinal Tensile Strength	530.8 MPa	25 MPa
F_1^{cu}	Longitudinal Compressive Strength	130.5 MPa	8 MPa
F_2^{tu}	Transverse Tensile Strength	530.8 MPa	25 MPa
F_2^{cu}	Transverse Compressive Strength	130.5 MPa	8 MPa
F_3^{tu}	Through-thickness Tensile Strength	50.0 MPa	2 MPa
F_{12}^{su}	In-Plane Shear Strength, xy plane	35.2 MPa	0 MPa
F_{23}^{su}	Out-of-Plane Shear Strength, yz plane	26.8 MPa	2 MPa
F_{13}^{su}	Out-of-Plane Shear Strength, xz plane	26.8 MPa	2 MPa
E^c	Compression Modulus	32,574 MPa	1620 MPa

3.2.2 Quasi-Static Punch Shear Test Results

QS-PST experiments were performed at four different SPRs of 1.020, 1.037, 1.053, and 1.171 using 8 ply specimens in order to determine the punch shear strength of the material. Ten specimens were tested at 1.037, 1.053, and 1.171 SPR, and seven specimens were tested at 1.020 SPR. The force-displacement data obtained from the punch shear tests with different SPRs are presented in Figure 23; the maximum force can be determined from these curves. The Punch Shear Strength (PSS) is calculated by dividing the maximum force, F_{max}, by the shear area A_{max}.

$$PSS = \frac{F_{\max}}{A_{\max}} = \frac{F_{\max}}{\pi D_m H_c} \tag{29}$$

where H_c is the laminate thickness and D_m is the mean diameter given by

$$D_m = \frac{D_p + D_s}{2} \tag{30}$$

where D_p is the diameter of the punch, and D_s is the diameter of the support span.

The average values of PSS with standard deviations determined at different SPRs are given in Table 10 and are plotted in Figure 24. Punch shear strength, PSS, tested at SPRs = 1.020, 1.037, and 1.053 have comparable values while those tested at SPR = 1.171 have a lower value.

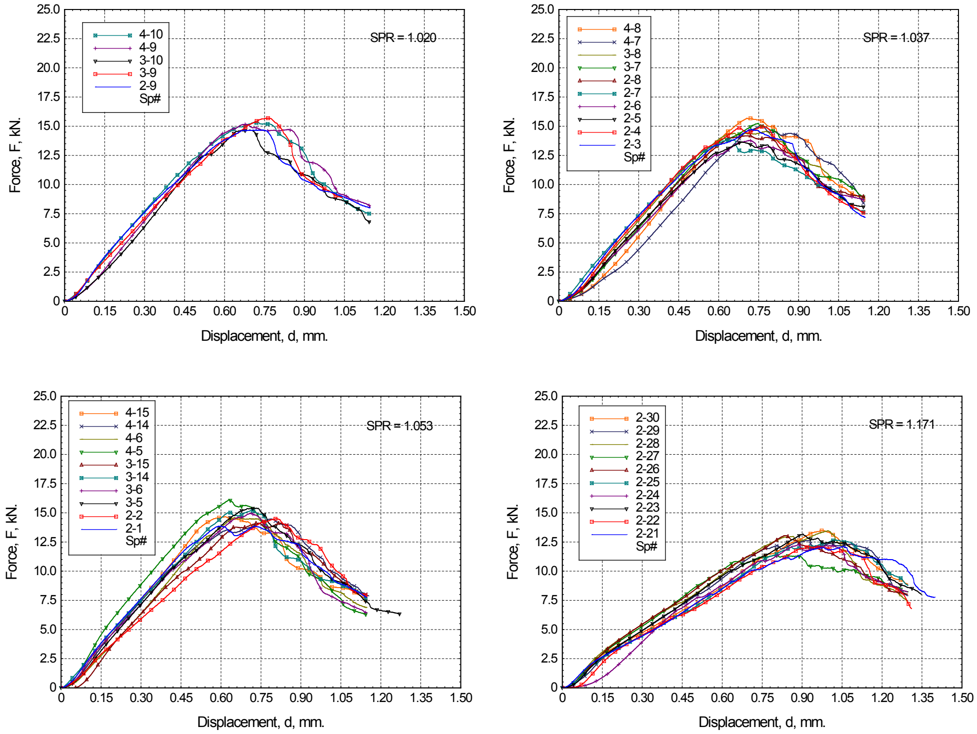

Figure 23. Force versus Displacement Curves for the QS-PST.

Table 10. Average PSS at 4 Different SPR Values

SPR	*Average PSS (MPa)*	*Standard Deviation (MPa)*
1.020	156.05	4.61
1.037	148.73	7.40
1.053	150.14	7.28
1.171	120.15	6.18

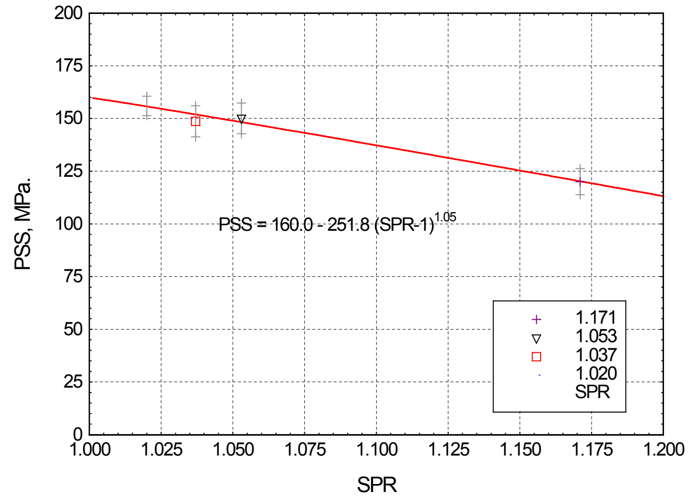

Figure 24. Average PSS and fit to Eq. (31)

The true punch shear strength of the composite is determined at SPR = 1.0. This value is determined by using a trend line of the form

$$PSS = PSS_{SPR=1.00} - A(SPR-1)^{B} \tag{31}$$

where A is an empirical constant. The fit to Eq. (31) is shown in Figure 24, and the value of the punch shear strength for SPR=1.00 is 160 MPa.

3.2.3 Quasi-Static Punch Crush Shear Test Results

Results of punch crush strength testing on 8 ply specimens are presented in Figure 25. It can be seen that the two different fixtures that were used produced different force versus displacement plots. This difference is attributed to the fact that the QS-PST boundary condition is clamped, and the PCST is not clamped. Maximum force can be determined for both test series since they show clear force peaks. Punch crush strength (PCS) is calculated by dividing the maximum force, F_{max}, by the punch crush area A_{max}.

$$PCS = \frac{F_{\max}}{A_{\max}} = \frac{4F_{\max}}{\pi D_p^2} \tag{32}$$

The average values of peak load for specimens tested using the QS-PST fixture are only about 5.5% higher than the values obtained using the PCST fixture. The Punch Crush Strengths predicted by Eq. 32 for the QS-PST and PCST fixtures shown in Table 11 reveal a difference of 48.0 MPa, and the average of the two is 852.0 MPa.

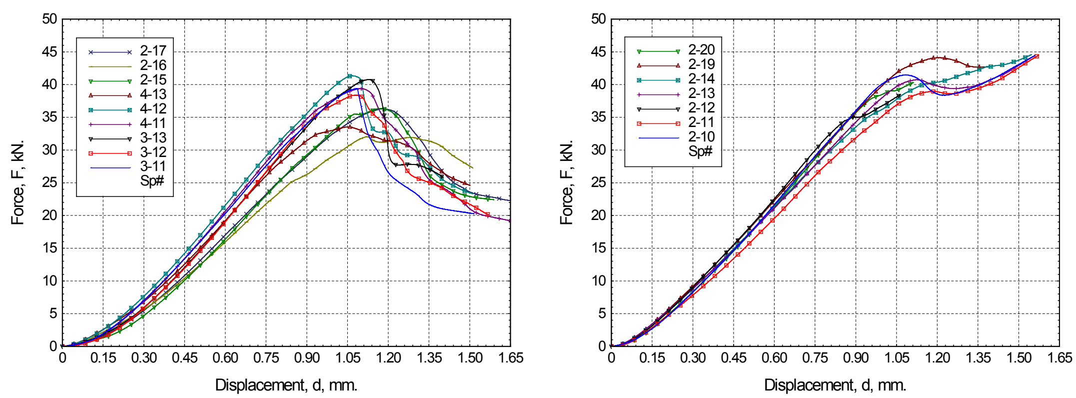

a) PCST Data b) QS-PST Data

Figure 25. Force versus Time Curves for the QS-PST and PCS Test.

Table 11. Average Crush Shear Data

Test	*Average CS (MPa)*	*Standard Deviation (MPa)*
QS-PST	834.26	59.77
PCST	881.91	61.37

3.2.4 LVI Results

LVI tests were conducted on 18 ply specimens at 50 and 70 J energy levels. Five specimens were tested for each energy level. The data from the LVI tests are summarized in Table 12. Force versus time plots at both impact energy levels are shown in Figure 26, while average force versus time and force versus displacement plots are shown in Figure 27. During impact, the force increases with time while loading, and the force decreases with time during unloading. The oscillatory behavior in the beginning of the impact event is due to the natural frequency of the clamped laminate under impact, which diminishes as the impact-contact force rises to a maximum value. Once the maximum force is achieved, unloading begins, and the load becomes zero when the projectile-sliding-mass assembly loses contact with the laminate. Figure 27 show that when the impact energy increases, the peak forces increases; however, the duration of impact remains almost constant at about 8.3 µs.

Table 12. LVI Data Summary

	Test E_I (J)	*V_I (m/s)*	*Actual E_I (J)*	*x_T (mm)*	*x_P (mm)*	*F_{max} (kN)*	*E_T (J)*	*E_D (J)*	*E_E (J)*
	50	3.191	48.86	9.25	5.29	9.99	49.74	39.31	10.43
STD DEV		0.003	0.08	0.08	0.10	0.12	0.08	0.38	0.43
	70	3.770	68.19	11.00	6.51	11.79	69.23	55.53	13.70
STD DEV		0.002	0.07	0.13	0.46	0.08	0.06	0.82	0.79

E_I = Impact Energy = ½ $M_P V_I^2$, V_I = Impact Velocity, x_T = Maximum Dynamic Displacement, x_P = Plastic Deformation at Zero Load, F_{max} = Maximum Force, E_T = Total Integral Energy, E_D = Dissipated Energy, E_E = Elastic or Stored Strain Energy.

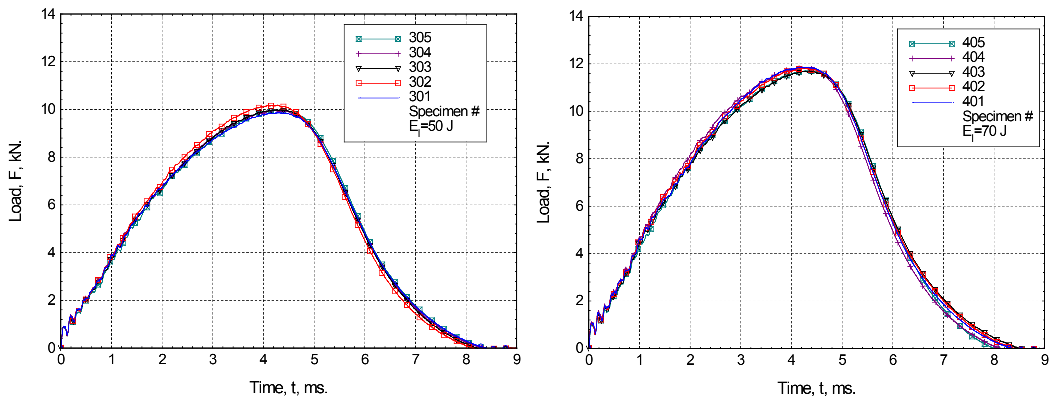

Figure 26. Force versus Time Curves at 50 (left) and 70 (right) Joules

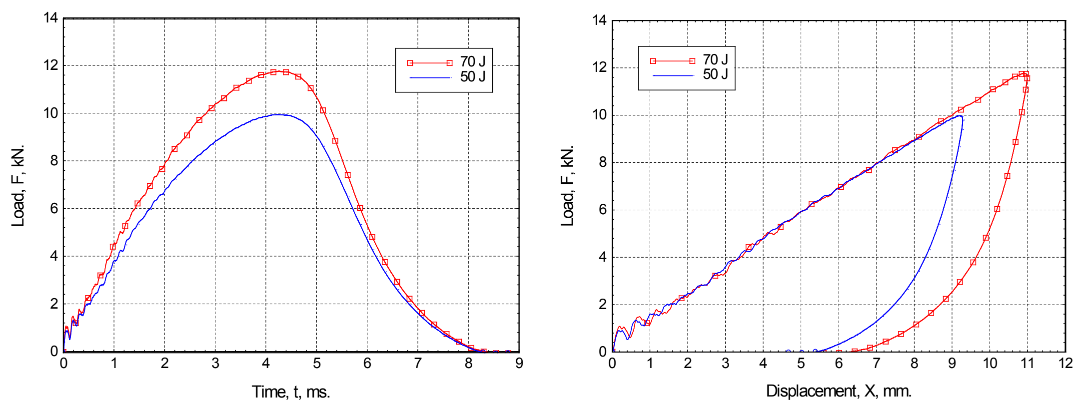

a) Average Load vs. Time b) Average Load vs. Displacement

Figure 27. Average Curves for the LVI Test

3.2.5 DOP Results

The 100 ply panel used for the DOP tests was cross-sectioned so that one side was half the penetration cavity diameter and the other side was offset by the kerf (1 mm). The DOP is measured by using dial calipers to measure the distance from the bottom of the penetration cavity to the bottom of the panel; this distance is subtracted from the 50 mm thickness of the panel to determine the actual DOP. The DOP results are shown in Table 13. The first value (*DOP 1*) was obtained from the cross-section with the penetration cavity halved, and the second value (*DOP 2*) was from the kerf side. Cross sections of shot 1 and shot 2 are shown in Figure 28. It should be noted that the RCC fragment in the figure is not at the deepest depth of penetration; it rebounded during the elastic recovery period of the penetration event. The depth of penetration is plotted versus impact velocity in Figure 29. The experimental data show a linear behavior and are plotted using a first degree polynomial. The linear equation intersects the velocity-axis at 54m/s, which is defined as the critical or threshold impact velocity of penetration. The critical or threshold velocity is the velocity at which no penetration occurs. The anomaly of shot four is due to yaw of the FSP, however the yaw was less than five degrees so it was included in the data set.

Table 13. DOP Test Data

Shot Number	*Impact Velocity, V_I (m/s)*	*DOP 1 (mm)*	*DOP 2 (mm)*
1	491	7.65	7.62
2	615	9.67	9.94
3	736	11.62	11.41
4	831	11.95	11.91
5	937	15.35	15.51
6	987	15.59	13.83

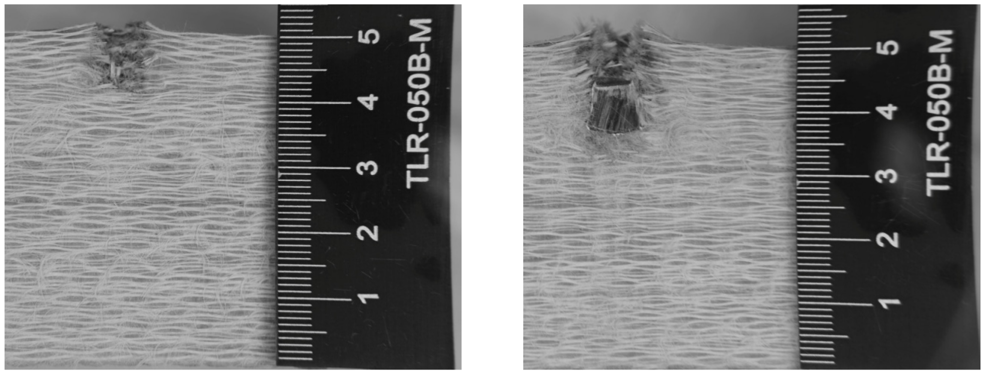

Shot 1 at 491 m/s

Shot 2 at 615 m/s

Figure 28. Penetration Cavity Cross Sections

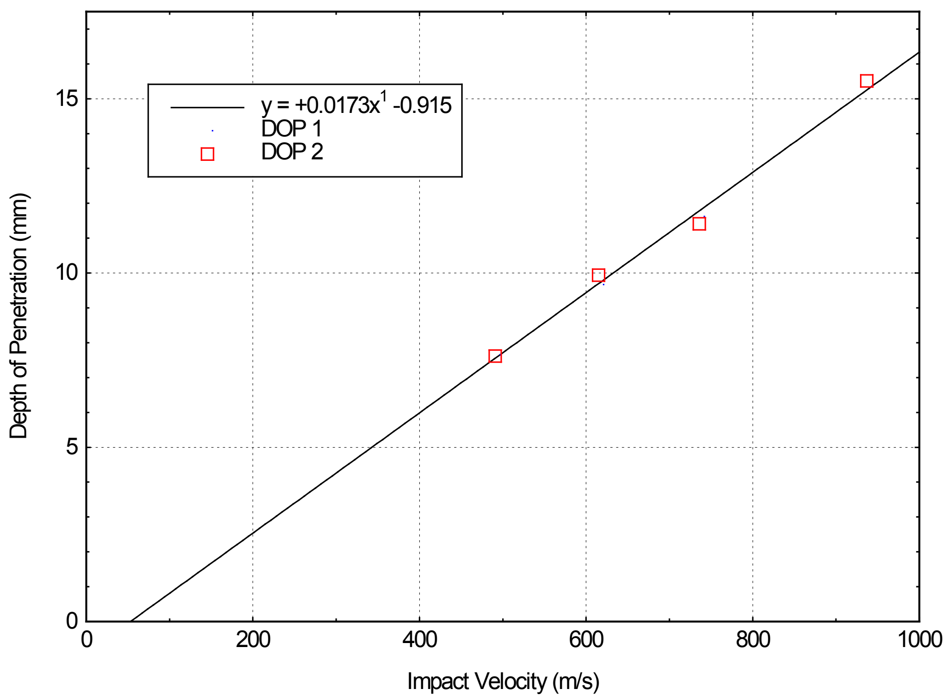

Figure 29. Depth of Penetration versus Impact Velocity

3.2.6 BPST Results

Table 14 shows the impact velocity and residual velocity for all shots into the 28 ply (14 mm) targets. The V_{50} ballistic limit was determined to be 838 m/s using MIL-STD-662F [4] for the 28 ply targets. Table 15 shows the impact velocity and residual velocity for all shots into the 18 ply (9 mm) targets. The V_{50} ballistic limit was determined to be 519 m/s using the same standard for the 28 ply targets.

Table 14. BPST Data for 28 Ply

Shot#	*FSP Mass (g)*	*FSP Shape*	*Impact Velocity (m/s)*	*Residual Velocity (m/s)*
2012-001	2.88	RCC	701	0
2012-002	2.88	RCC	753	0
2012-003	2.88	RCC	741	0
2012-004	2.88	RCC	822	0
2012-005	2.88	RCC	830	0
2012-006	2.88	RCC	839	0
2012-007	2.88	RCC	864	223
2012-008	2.88	RCC	855	240
2012-009	2.88	RCC	821	109
2012-010	2.88	RCC	931	352
2012-011	2.88	RCC	987	440
2012-012	2.88	RCC	1040	458
2012-013	2.88	RCC	1095	547
2012-014	2.88	RCC	1123	568
2012-015	2.88	RCC	1248	681
2012-016	2.88	RCC	1323	758

Table 15. BPST Data for 18 Ply

Shot#	*FSP Mass (g)*	*FSP Shape*	*Impact Velocity (m/s)*	*Residual Velocity (m/s)*
2012-017	2.88	RCC	571	109
2012-018	2.88	RCC	549	74
2012-019	2.88	RCC	557	168
2012-020	2.88	RCC	555	136
2012-021	2.88	RCC	532	26
2012-022	2.88	RCC	536	0
2012-023	2.88	RCC	485	0
2012-024	2.88	RCC	520	140
2012-025	2.88	RCC	489	0
2012-026	2.88	RCC	497	0
2012-027	2.88	RCC	521	45
2012-028	2.88	RCC	499	0
2012-029	2.88	RCC	520	0
2012-030	2.88	RCC	496	0
2012-031	2.88	RCC	512	0
2012-032	2.88	RCC	610	245
2012-033	2.88	RCC	721	364
2012-034	2.88	RCC	837	529

Statistical curve fitting and semi-empirical analytical techniques may also be used to predict the residual velocity versus impact velocity data to determine the ballistic limit velocity.

The Recht and Ipson[7] model is the first penetration model based on the premise that the ejecta of the target absorbed energy during the impact event, and has the form

$$V_R = \alpha\left(V_I^2 - V_{BL}^2\right)^{\frac{1}{2}} \tag{33}$$

where α is a curve fit parameter, and V_{BL} is the ballistic limit velocity. The Lambert-Jonas [41] penetration model, Eq. (33), has a similar general form has Recht and Ipson model and is equal to the Recht and Ipson model when p=2. The Lambert-

Jonas model places a restriction that the residual velocities must equal zero for impacts below the ballistic limit.

$$V_R = \begin{cases} 0 & 0 \le V_I \le V_{BL} \\ \beta \left(V_I^p - V_{BL}^p \right)^{\frac{1}{p}} & V_I > V_{BL} \end{cases} \tag{34}$$

with the constraints that $0 \le \beta \le 1$ and $p > 1$. Haque and Gillespie[42] proposed a penetration model of the form

$$V_R = \left(\left(V_T^{\max} \right)^2 + \beta^* \left(\xi V_I^2 - V_{BL}^2 \right) \right)^{\frac{1}{2}} \tag{35}$$

where $V_t^{\max}$ is the jump velocity at ballistic limit (shown in red in Figure 30b), and β^* & ξ are curve-fit parameters. Each of equations (33-35) are fit to the 28 ply experimental data using an R^2=0.994 or higher and are shown in Figure 30 along with the experimental data. The accuracy of the ballistic limit predication was not as good for the Recht-Ipson and Lambert-Jonas models. The Haque-Gillespie model predicted a ballistic limit 0.20% higher than that of the experimental data calculations, and predicted the jump velocity to be 180 m/s. The jump in velocity in the region of the ballistic limit is very common in experimental data and has been noted previously in the literature [43] and is best described as the velocity at which the residual velocity scatter ceases to exist.

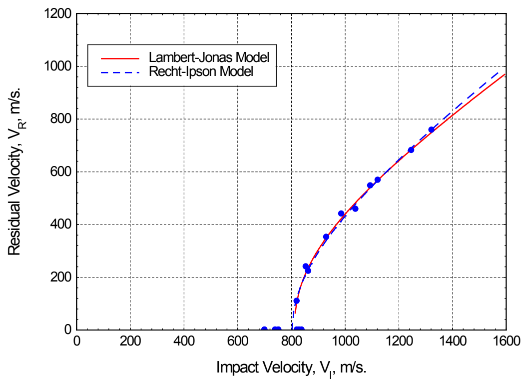

(a) Recht-Ipson & Lambert-Jonas Model Fits

Recht-Ipson: $\alpha = 0.724$, $V_{BL} = 802.6\frac{m}{s}$, $R^2 = 0.994$

Lambert-Jonas: $\beta = 0.724$, $V_{BL} = 811.2\frac{m}{s}$, $p = 2.253$, $R^2 = 0.996$

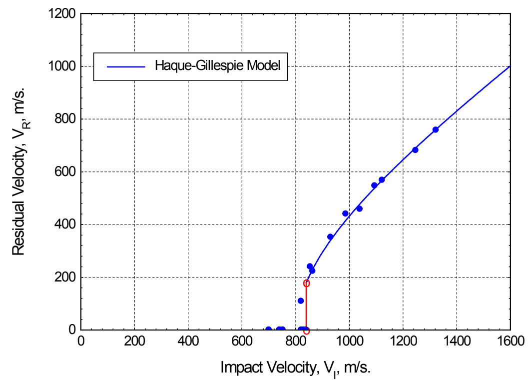

(b) Haque-Gillespie Model Fit

$V_T^{\max} = 179.7\frac{m}{s}$, $\beta^* = 0.524$, $\xi = 0.999$,

$V_{BL} = 839.7\frac{m}{s}$, $R^2 = 0.994$

Figure 30. Strike Velocity versus Residual Velocity

3.3 SUMMARY OF MATERIAL PROPERTY TESTING

Quasi-static, low-velocity impact (LVI) and ballistic loading conditions were used to find the material properties and responses of E-glass/Phenolic composites. Standard ASTM tests were used to find the density, Poisson's ratio, tensile, compressive, and shear strengths, and the elastic and shear moduli of the material. The non-standard quasi-static punch-shear and punch-crush strength tests were used to find the punch shear and crush strengths of the material. The LVI tests were conducted to obtain force versus time curves for various loading conditions. Ballistic testing was conducted using a RCC to find the V_{50} ballistic limit into 9 and 14mm thick composite targets and the depth of penetration of the RCC into a semi-infinite composite target at various velocities. The experimental data presented will be used to determine all of the parameters for the material model MAT162 in LS-DYNA; the subject of a subsequent chapter. Additionally, the experimental results from this investigation can be used for structural design and to validate numerical models for both low-velocity impact and ballistic impact events.

CHAPTER 4 - PROGRESSIVE DAMAGE MODELING OF PLAIN WEAVE E-GLASS/PHENOLIC COMPOSITES

The objective of this chapter is to determine modeling parameters required for LS-DYNA MAT 162 composite MSC damage model [31, 32] using the data generated in Chapter 2. The MAT 162 constitutive material model requires 39 material properties and parameters. Numerical simulations will be used to determine the damage softening parameters AM, OMGMX, ECRSH, E_LIMT, and EEXPN. Post damage softening parameters AM1-AM4 and the modulus reduction factor OMGMX are determined by simulating low-velocity impact experiments. The penetration erosion parameter ECRSH is found by simulating depth of penetration experiments; while the penetration erosion parameters E_LIMT and EEXPN are determined by simulating ballistic impact experiments. Both ECRSH and EEXPN erode elements based on the ratio of the initial volume of the element to the current volume of the element. In the compression case the element is eroded if the volume ratio is smaller than the limit value shown in ECRSH. For element expansion, the element is eroded if the volume ratio is larger than the EEXPN value. E_LIMT is controlled by the fiber tension in both in-plane directions. When tension in both in-plane directions exceeds the value of E_LIMT the element is eroded.

4.1 PARAMETER DEVELOPMENT AND CALIBRATION

4.1.1 LVI Simulations

LVI simulations were run to determine post damage softening parameters AM1- AM4 and the modulus reduction parameter OMGMX. The numerical model used in the simulations is shown in Figure 31. The damage parameters AM are the material damage parameters; fiber damage in 1-direction (AM1), fiber damage in 2-direction (AM2), fiber crunch and shear damage (AM3), and matrix and delamination damage (AM4). The simulations replicated previous experimental tests which were conducted at 50 and 70 J energy levels. The values of AM1-AM4 were initially set the same as those optimized for S2-Glass/Phenolic [44].

Table 16. Initial Values for Variables

Damage Softening Parameters		*Residual Compressive Strength Scale Factor*	
AM_1	1.00	*SFFC*	0.300
AM_2	1.00	*Modulus Reduction*	
AM_3	0.50	*OMGMX*	0.990
AM_4	0.20	*Delamination Scale Factor*	
Coulomb Friction Angle		*S_DELM*	1.20
PHIC	10.0	*Strain Rate Dependent Moduli*	
Strain Rate Dependent Strength		*CERATE2*	0.00
		CERATE3	0.03
CERATE1	0.03	*CERATE4*	0.03

An automatic single surface contact definition is applied between the 8 ply (4 mm thick) composite plate and the impact tup (diameter = 15.9 mm), while a surface to surface contact definition is used between the composite plate and the steel plates. There is mesh refinement at the immediate area of impact tup and composite plate interaction as well as at the clamped boundary condition. The plate element mesh is refined for a distance 3.4 times the tup diameter from the impact centerline. There are

18 elements through the radius of the tup and the corresponding area of the plate has 10 elements through the radius distance. Each ply has three elements through the thickness. A high coefficient of friction is applied between the composite plate and the steel plates to simulate clamped boundary conditions.

OMGMX was varied from 0.990 to 0.994 and the other parameters were kept constant. Figure 32 shows the force time curves for the experiments compared to the numerical simulations at various values of OMGMX. The results show that as OMGMX decreases the predicted peak load increases and the duration of unloading decreases. Simulation results with OMGMX = 0.994 shows the closest match to experimental results. The initial slope and the peak of the curve for OMGMX = 0.994 is in excellent agreement with the experimental data, which indicates that the model is able to capture the physics of the LVI. There is a mismatch between the unloading part of the experimental and simulation force-time graphs due to the linear elastic unloading in the model opposed to unloading with residual plastic strain in the experiments.

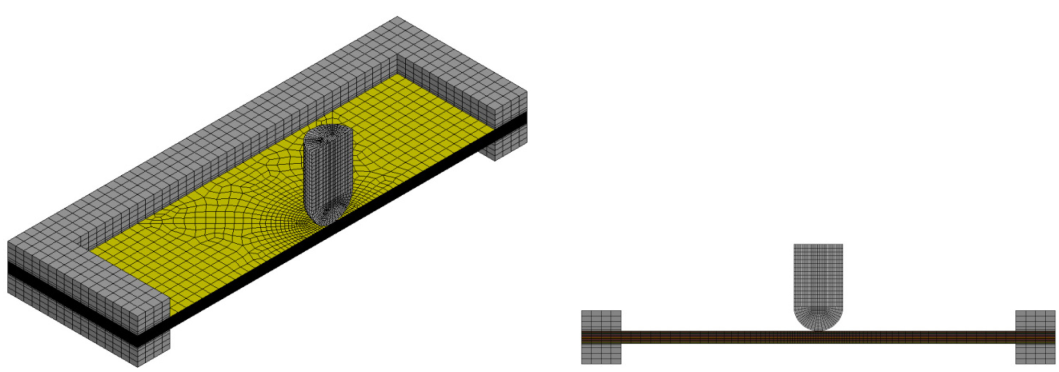

a) Isometric View of the LVI Model b) Cross-Section of LVI Model

Figure 31. LVI Model used in Simulations

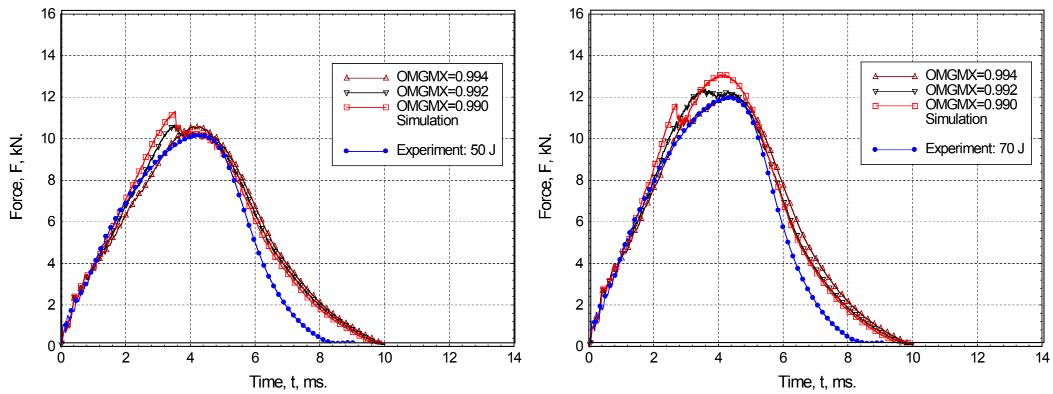

Figure 32. Simulated and Experimental Force versus Time Curves at 50 and 70 Joules.

4.1.2 DOP Simulations

The penetration erosion parameter ECRSH is found by simulating depth of penetration experiments. The numerical model for the depth of penetration experiments is shown in Figure 33. Figure 33a is a top view of the DOP model and Figure 33b shows the RCC cross-sectioned and zoomed in order to observe the mesh. The target solid element mesh is uniform with an in-plane length of 0.5mm. Each layer of the composite target has six elements through the thickness, and each element represents one ply. The RCC has 15 elements through the radius and the corresponding area of the plate has eight elements through the radius distance. A parametric study was conducted where the value of ECRSH was varied from 0.45 to 0.60.

The right circular cylinder simulation velocity was varied from 450 m/s up to 1050 m/s in increments of 150 m/s. The experimental results were compared to the numerical simulations to determine the best data fit. The depth of penetration data was fit using a linear first degree polynomial fit in Figure 34. The critical velocity is 22 m/s for the DOP 1 data. All of the numerical data was fit to the experiment data with the R^2 value shown on the plot. It can be seen from the plot that the optimized value for ECRSH is 0.55. Depth of penetration for ECRSH = 0.55 is shown in Figure 35.

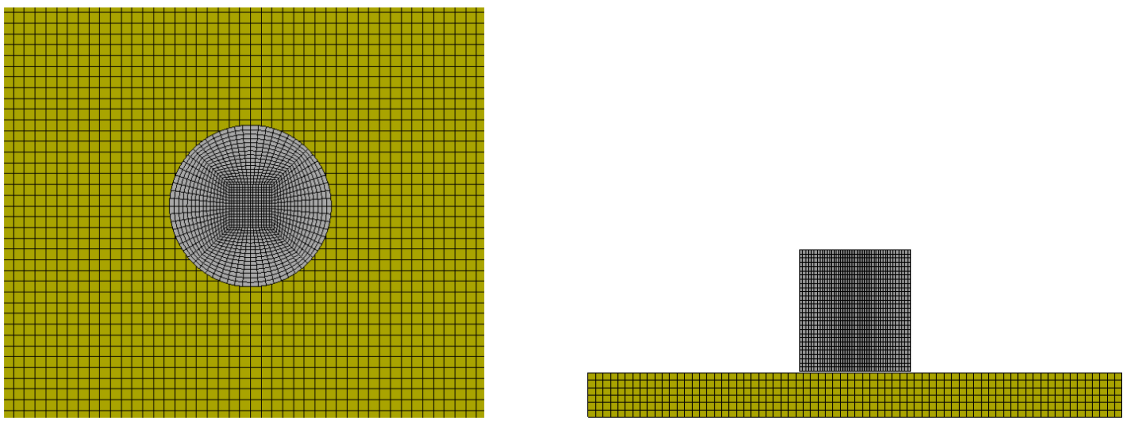

a) Zoomed Top View of the DOP Model

b) Zoomed Cross-Section of DOP Model

Figure 33. Depth of Penetration Model used in Simulations

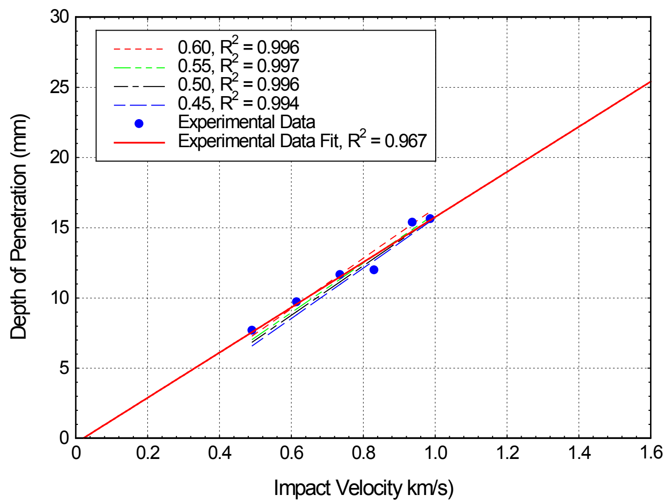

Figure 34. Plot of the DOP Simulations versus DOP Experimental Data at Various ECRSH Values

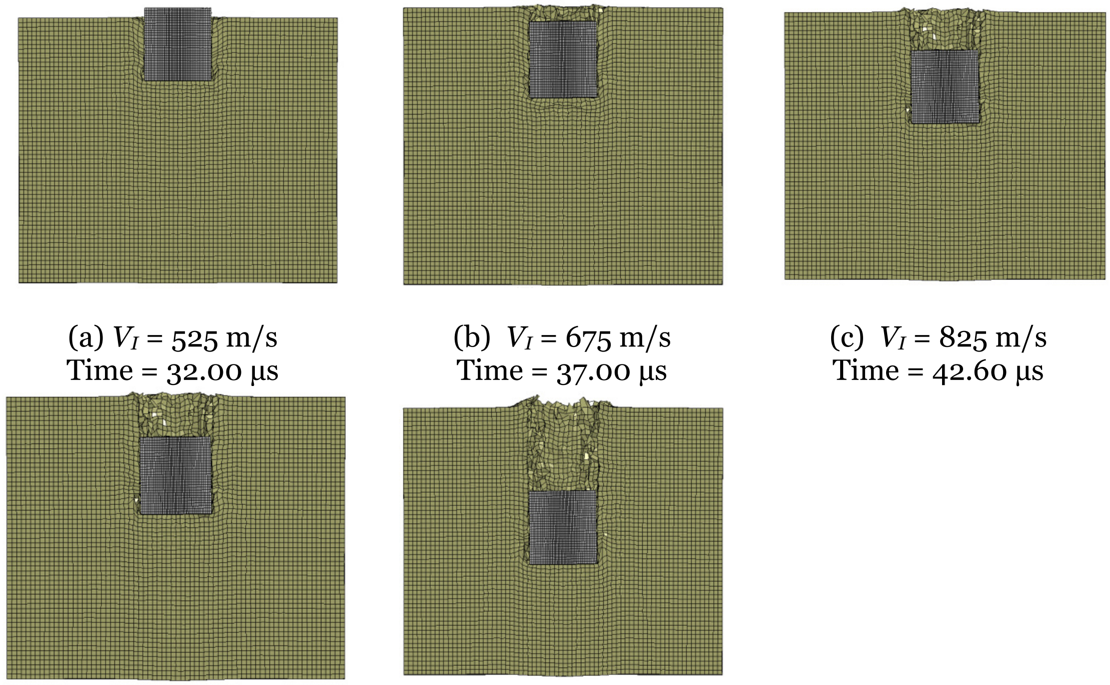

(a) V_I = 525 m/s
Time = 32.00 µs

(b) V_I = 675 m/s
Time = 37.00 µs

(c) V_I = 825 m/s
Time = 42.60 µs

(d) V_I = 975 m/s
Time = 48.00 µs

(e) V_I = 1125 m/s
Time = 64.00 µs

Figure 35. Various Impact Velocities and Time at Maximum Penetration Depth using ESCRSH=0.55

As expected the depth of penetration increases with increased impact velocity. With ECRSH = 0.55, fiber crush (element is erosion) occurs when the volume compression of an element is more than fifty-five percent. When the penetrator velocity becomes low enough, the volume compression is insufficient for element erosion and the penetrator is stopped. Figure 36 shows a photograph of the cross-section at the end of the penetration event compared to the numerical experiment at the maximum depth of penetration. Figure 37 shows the penetration cavity of the experimental and numerical experiments. The model has excellent correlation with the experimental data as shown in Figure 34 through Figure 37 for the case when ECRSH equals 0.55.

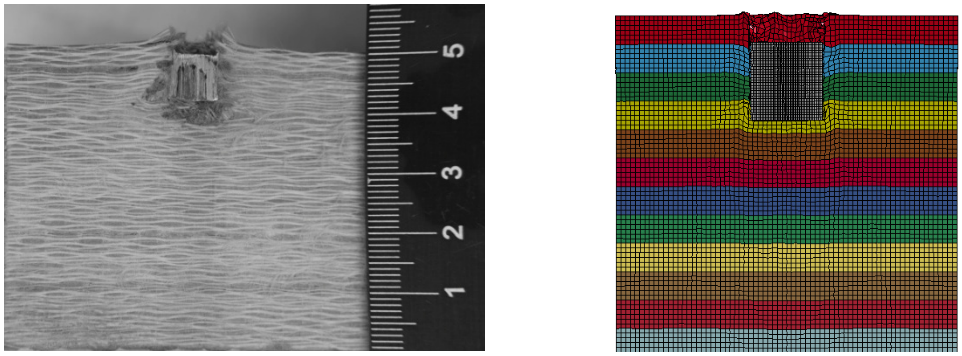

Scale: mm

Each Colored Layer
Represents 3 mm

Figure 36. Comparison of Numerical Results to Experimental Results – With RCC at a Velocity = 736 m/s

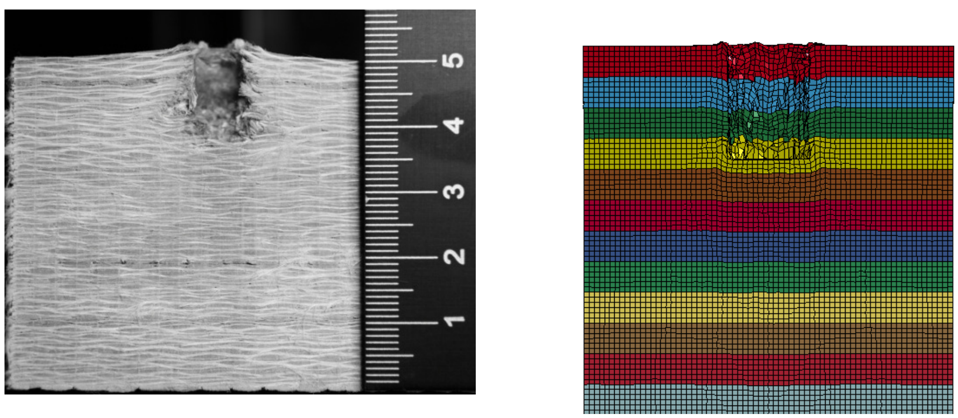

Scale: mm

Each Colored Layer
Represents 3 mm

Figure 37. Comparison of Penetration Cavity for Numerical Results and Experimental Results at a Velocity = 736 m/s

4.1.3 Ballistic Simulations

The penetration erosion parameters ELIMT and EEXPN are determined by simulating ballistic impact experiments. For element expansion, the element is eroded if the volume ratio is larger than the EEXPN value. E_LIMT is controlled by the fiber tension in both in-plane directions. When tension in both in-plane directions exceeds the value of E_LIMT the element is eroded. By setting the two values equal, the E_LIMT erosion criteria is suppressed and the volumetric strain EEXPN controls the element erosion in the calculations. This technique has been used successfully to model ballistic impact events in the literature [30, 45]. The numerical model for the ballistic experiments is shown in Figure 38a, and Figure 38b. Figure 38 is a zoomed section of the ballistics model and Figure 38b is a cross-section of the ballistic model. The plate element mesh is refined 3.4 projectile diameters from the penetration centerline. The RCC has 15 elements through the radius and the corresponding area of the plate has eight elements through the radius distance. Each layer of the composite target has three elements through the thickness, and the outer two elements are half the ply thickness and the inner element is equal to the ply thickness (0.5 mm). A parametric study was conducted where the value of E_LIMT = EEXPN was varied from 3.5 to 4.5.

The right circular cylinder simulation velocity was varied from 800 up to 1300 m/s in increments of 125 m/s. The experimental results were compared to the numerical simulations to determine the best data fit, Figure 39.

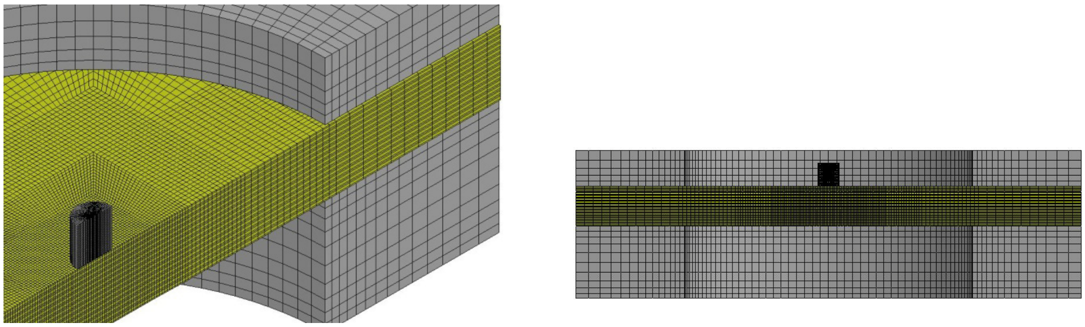

a) Zoomed Isometric View of the Ballistic Model

b) Cross-Section of Ballistic Model

Figure 38. Ballistic Model used in Simulations

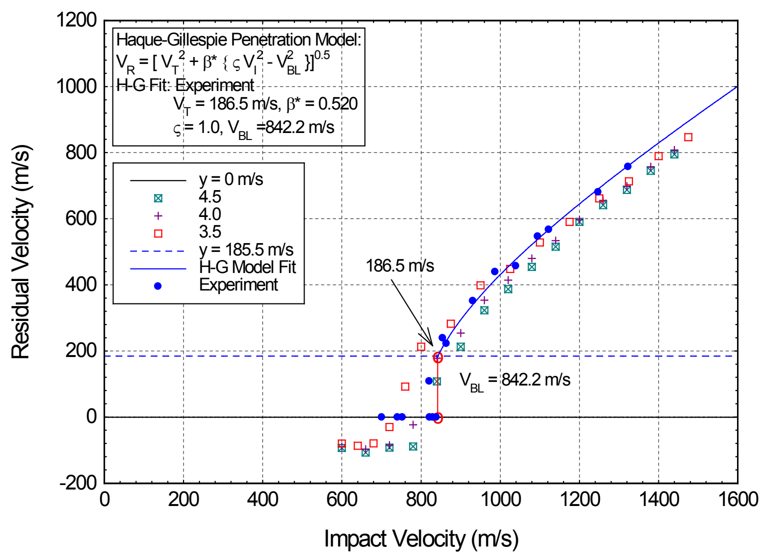

Figure 39. Plot of the Ballistic Simulations versus Ballistic Experimental Data for at Various Parameter Values

Using the data fits in Figure 39 it can be seen that two values closely match the experimental data with some subtle differences. All values of EEXPN = E_LIMT slightly under predict the residual velocity data at higher impact velocities. At values below the impact velocity of 1140 m/s a separation begins to occur between the two best fit values for EEXPN=E_LIMT; for EEXPN = E_LIMT = 4.0 the values are slightly below the experimental data, while EEXPN = E_LIMT = 3.5 begins to over predict the residual velocity data. At lower velocities EEXPN = E_LIMT = 4.0 better predicts the experimental data and was chosen to be the optimized value going forward. Using the optimized value, impacts were simulated using impact velocities from 750 m/s up to 1400 m/s in increments of 150 m/s. The plots in Figure 40 show the delamination damage and penetration depths of the RCC at various times for impact velocities of 750 m/s and 900 m/s respectively. These two velocities represent the damage and displacement of the composite below and above the ballistic limit velocities. The simulation residual velocities are in excellent agreement with the experimental data. Additionally, the rigid body velocities and displacements of the RCC during the penetration event are shown in Figure 41 for each of the eight impact velocities analyzed. The velocity – displacement plots show the dynamics of the penetration event with progressive damage. In the force time history there is significant oscillations due to element erosion. The numerical ballistic limit can be found using the velocity versus displacement plots since the numerical ballistic limit falls between the highest curve going through zero velocity and the lowest curve with residual velocity.

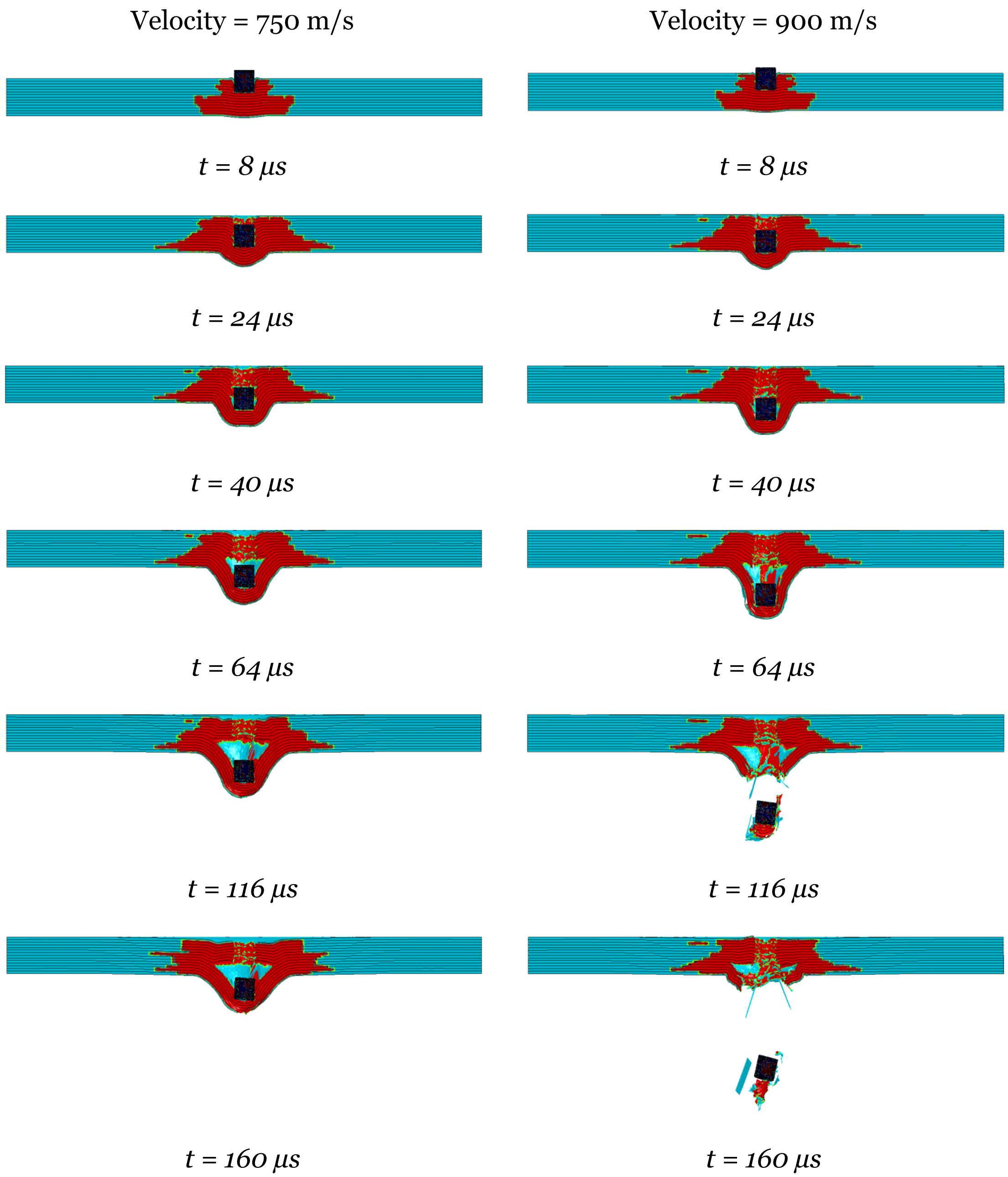

Figure 40. Optimized FEA Simulation of Ballistic Impact

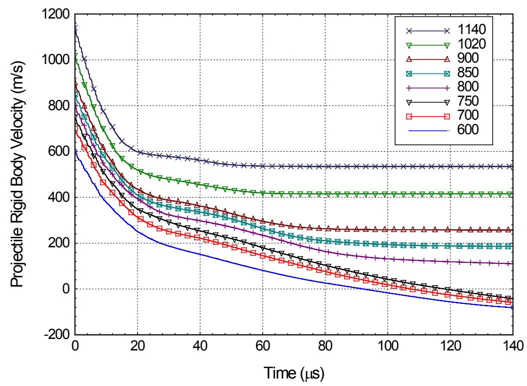

a) Velocity vs. time

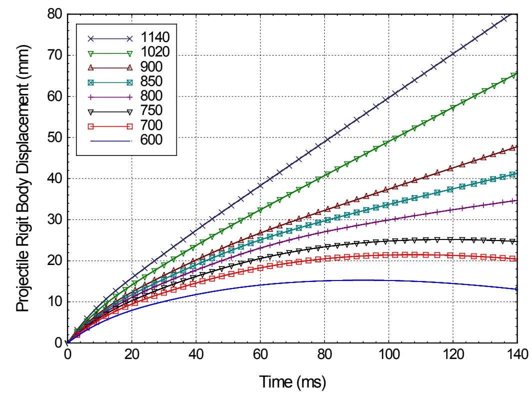

b) Displacement vs. time

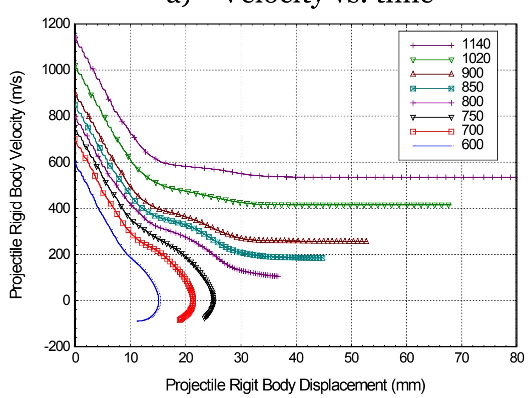

c) Velocity vs. displacement

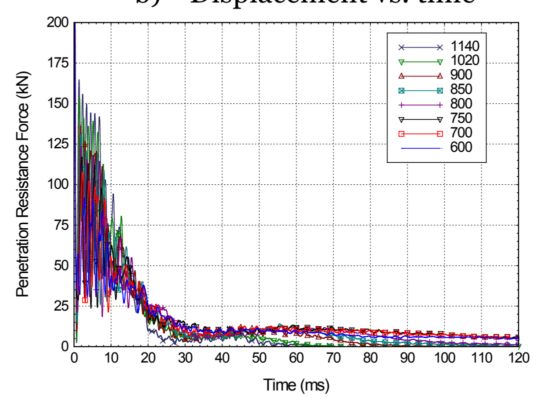

d) Force vs. time

Figure 41. Rigid Body Velocity and Displacement of the RCCs

4.2 VALIDATION CALCULATIONS

The optimized values for a 14 mm thick E-glass/Phenolic composite target have been determined for the MAT162 constitutive material model under ballistic impact conditions and are shown in Table 17. A robust set of MAT162 parameters should be able to predict the ballistic performance of a different thickness of target material without modification to the parameters. If the model can accurately predict the results of a different target thickness without modifications it is considered to be robust and validated.

To test the material model robustness the results of numerical simulations of the RCC impacting an E-glass/Phenolic target which is 9 mm thick are presented next. The simulations were conducted for impact velocities from 450 m/s to 850 m/s incremented by 50 m/s. The simulations are compared to experimental ballistic impact data in Figure 42. The Haque- Gillespie (H-G) fit to the experimental data

Table 17. Optimized MAT162 parameters for E-glass/Phenolic Composite

Damage Softening Parameters		*Residual Compressive Strength Scale Factor*	
m_1	1.00	SFFC	0.300
m_2	1.00	*Modulus Reduction*	
m_3	0.50	OMGMX	0.994
m_4	0.20	*Delamination Scale Factor*	
Coulomb Friction Angle		S_DELM	1.20
PHIC	10.0	*Limit Compressive Volume Strain*	
Limit Tensile Volume Strain		ECRSH	0.55
EEXPN	3.5	*Element Eroding Axial Strain*	
Strain Rate Dependent Moduli		E_LIMT	3.5
		Strain Rate Dependent Strength	
CERATE2	0.00	CERATE1	0.03
CERATE3	0.03		
CERATE4	0.03		

predicts the V_{50}=525 m/s and the H-G fit to the numerical experiments predicts the same value. This shows the robustness of the material model and the optimized data.

The plots in Figure 43 show the delamination damage and penetration depths of the RCC at various times for impact velocities of 450 m/s and 550 m/s respectively. These two velocities represent the damage and displacement of the composite below and above the ballistic limit velocities. The rigid body force and displacement time history results of these validation simulations are shown in Figure 44.

It should be noted that slight dishing of the composite plate can be seen beginning at 40 μs, and this was not evident in the 14 mm thick target. This indicates that a change in damage mechanisms due to thickness is captured in the numerical experiments.

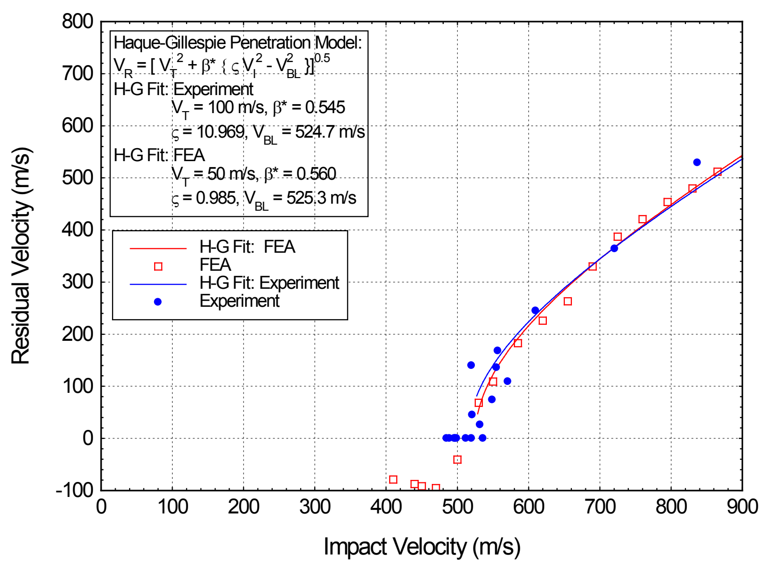

Figure 42. Plot of the Ballistic Simulations versus Ballistic Experimental Data for 18 ply

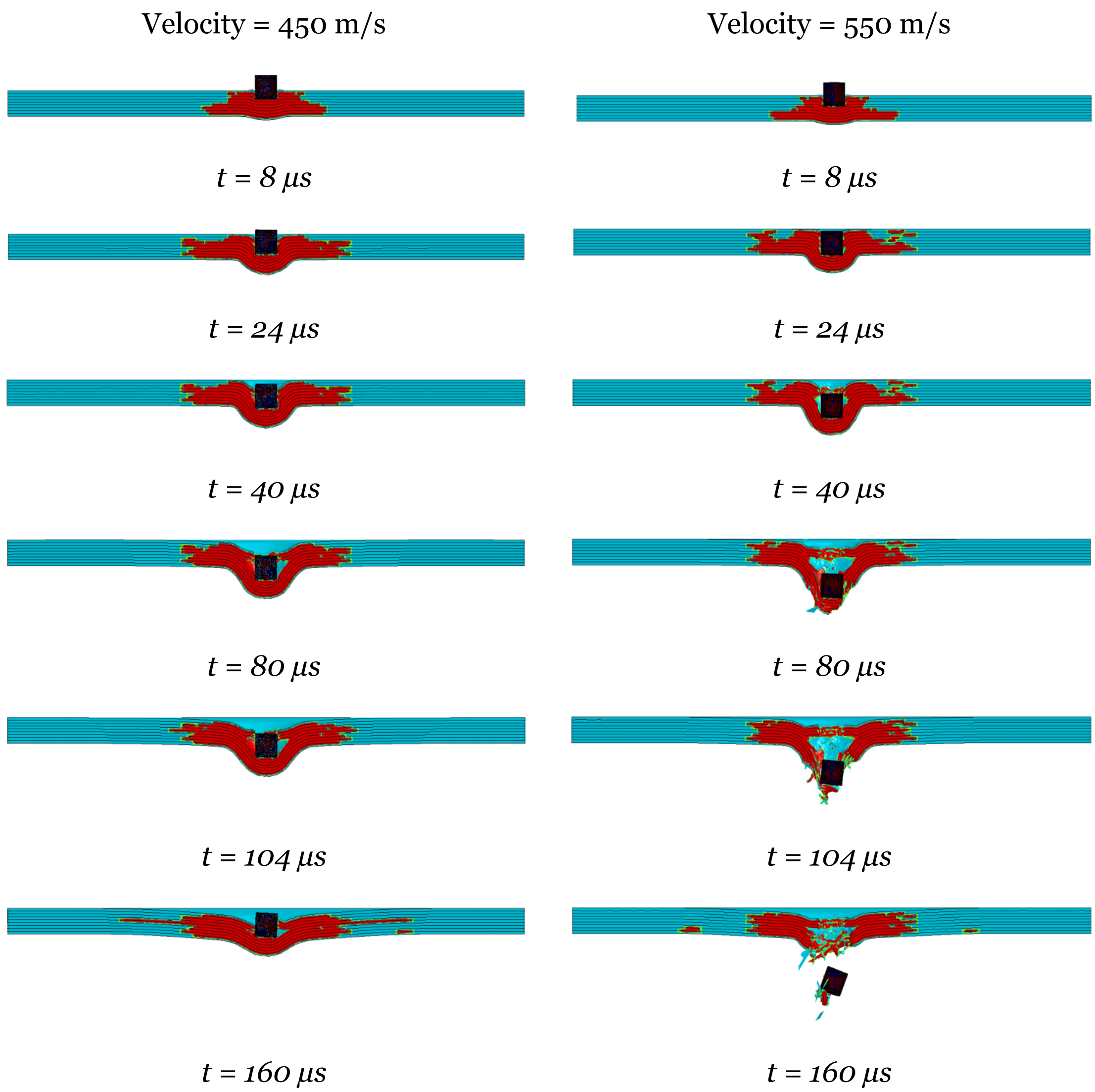

Figure 43. Validation FEA Simulation of Ballistic Impact

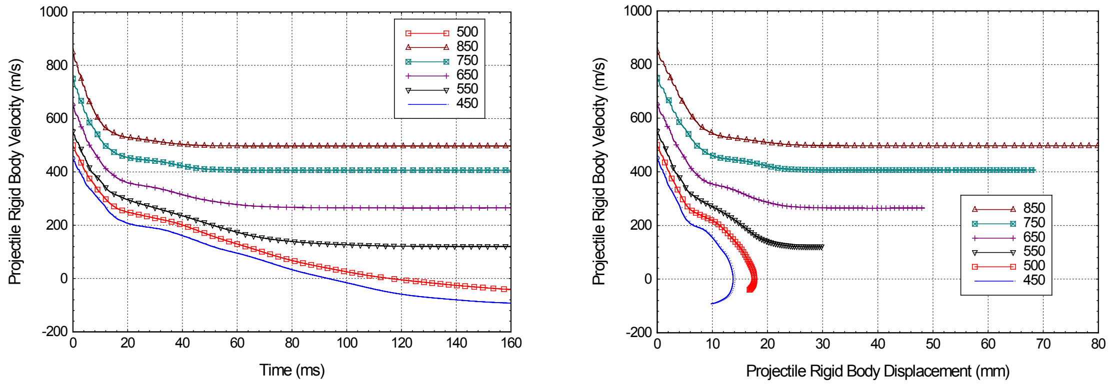

a) Velocity vs. time

b) Velocity vs. displacement

Figure 44. Rigid Body Velocity and Displacement of the RCCs

4.3 SUMMARY OF MAT162 PARAMETER DEVELOPMENT AND VALIDATION

The objective of this chapter was to determine all of the parameters required for the MAT162 constitutive material model in LS-DYNA. The model requires 39 material properties and parameters, and is able to capture the seven different damage modes and post damage softening behavior of composites. In this chapter all of the parameters required to conducted ballistic impact analysis on Advantex 3011 E-glass composite with SC-1008 Phenolic resin using MAT162 were determined and validated. Using the material properties presented in Table 9 (Chapter 2) the unknown MAT162 parameters were determined by conducting parametric simulations of LVI, DOP and ballistic impacts. The modulus reduction parameter OMGMX is found by simulating LVI tests and varying the values of OMGMX to find the best agreement with LVI experimental data. The limit compressive volume strain for element eroding was found by simulating DOP experiments and comparing the results to the experimental data. Then the element eroding criteria EEXPN was determined by simulating ballistic impact experiments. When the optimized values were determined, analysis of ballistic experiments were conducted and compared to the experimental impact versus residual velocity curve. The results of the simulations were in excellent agreement with the experimental data. These optimized MAT162 parameters which are presented in Table 17 for the E-glass/Phenolic composite may be used with confidence to analyze ballistic impact applications.

CHAPTER 5 - A NUMERICAL STUDY ON THE EFFECT OF ARBITRARY SHAPED FRAGMENTS ON THE PENETRATION OF E-GLASS/PHENOLIC

While it is true that experimental data is extremely valuable and allows us to design appropriate armor solutions, experiments do not typically give us much insight into the interaction or mechanisms involved in the penetration event. Therefore we turn to numerical simulations in this chapter to evaluate the failure modes and damage during the penetration and perforation. The failure modes and damage during penetration is also referred to as the phases of penetration. The objectives of this chapter are to determine the influence of composite thickness and arbitrary nose shape on the penetration phases. This is accomplished by describing each of the penetration phases observed in the numerical simulations using the LS-DYNA MAT162 composite MSC damage material model, and then determining the influence of thickness and different nose shapes during penetration. The optimized and validated parameters determined in Chapter 4 for the MAT162 material model will be used for all numerical simulations in this chapter.

5.1 PHASES OF PENETRATION AND INFLUENCE OF TARGET THICKNESS

Greaves [46] reported two phases of penetration for composites based on experimental results and target cross-sections for 12.7 mm thick composites. The first phase was described as the compression and ejection phase and the second phase was broken down into two phases, which were described as delamination, and stretching and bending. The compression and ejection phase was attributed to absorbing the most energy for 12.7 mm thick composites when penetrated by the 30 caliber FSP. According to Greaves the compression and ejection phase ends when the crushing of the material stops and the delamination phase begins.

Haque et al. [47] presented a paper on perforation and penetration of composites, which discusses phases of penetration determined from finite element modeling. In this work the MAT162 material model was used to assess RCC impacts into 53 mm thick S2-glass/Phenolic and the phases of penetration and perforation mechanisms were presented. There were four penetration and perforation mechanisms described; 1) penetration phase, 2) transition phase, 3) perforation phase and 4) retraction phase. The model is in its early stage of development by the presenters, and the penetration phase titles in their present form tend to provide some confusion. The basic mechanisms that were described in the model are excellent and show that the MAT162 model is capable of capturing the appropriate damage mechanisms for ballistic impacts events. The paper indicates that crushing, transverse matrix damage, and delamination occur in the penetration phase. The transition phase consists of compression-shear and initial stages of cone formation on the back side of the target.

While the perforation phase of the model consists of tension-shear and is described as being equivalent to quasi-static test methods. The final phase, retraction phase, adds no value in understanding the ballistic penetration of composites, it does however describe the elastic recovery which occurs after perforation or the FSP being stopped.

The phases of penetration will be investigated first using the RCC impacting the 14mm thick target, and then the 9 mm and 4 mm thick targets at their respective ballistic limit velocity.

5.1.1 Phases of Penetration for the 14 mm Thick Composite

The numerical simulations for the RCC impacting a 14 mm target were examined to determine when the phases introduced above initiated and terminated. By examining the kinetic energy curve from the numerical simulations it was determined that there were four distinct phases of penetration, and that a combination of the two models above would best describe the penetration process. Each of the four phases of penetration initiation and termination times can be determined explicitly by using transitions between the four distinct slopes of the kinetic energy curve; with the change in slope indicating a change in the energy absorbing mechanism. The four phases of penetration will be referred to by the dominate energy absorbing mechanisms of that phase of penetration. Figure 45 shows the kinetic energy curve divided into the four phases of penetration, and images of the projectile/target interaction at the initiation (or termination) of each phase of penetration.

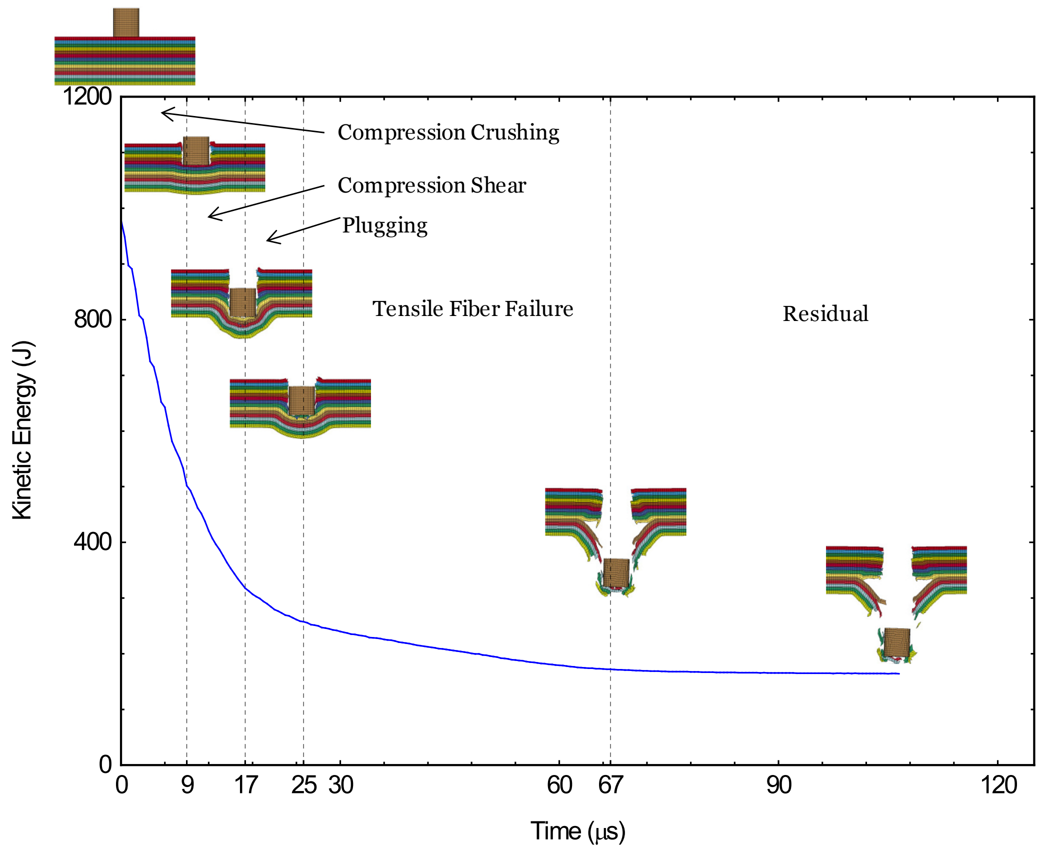

Figure 45. Penetration Phases for RCC Impacting 14mm Thick GFRP Composite

The penetration process into the 14 mm thick composite begins with two compression phases. The first being the compression-crushing phase and it begins at impact and terminates after 9 μs. During the compression-crushing phase the material underneath the projectile is crushed under compression and the matrix area surrounding the projectile is damaged from matrix cracking. The compression-crushing is the dominate energy absorption mechanisms in this phase, which can easily been seen by comparing the matrix strength (50 MPa) to the crush strength (852 MPa) of the composite. While it is known from the experiments that ejection occurs during the penetration and energy is absorbed from this process, this cannot be detected in the numerical experiments due to the erosion criteria. The bulge of the distal side just begins at the end of the crushing phase, this indicates the target is a thick target element as defined by Backman and Goldsmith [34]. The second phase of penetration of the composite is compression-shear and it initiates at the termination of the crushing phase and terminates at 17 μs. Matrix cracking continues to expand during the shear dominated phase, however, the expansion rate for the matrix cracking is decreasing. Cone formation or deformation of the distal side is starting to increase as can be seen in the image at 17 μs. Based on strength considerations the compression-shear phase is dominated by the compression-shear failure of the material surrounding the periphery of the RCC. The third phase of penetration is plugging, it begins when compression-shear ceases and terminates at 25 μs when the velocity of the material under the projectile is equal to the velocity of the composite material at the backside of the target. This would correspond to the termination time of phase one in Greaves model, and the end of the transition phase, phase 2, for the Haque et al. model description. The final phase of penetration of the RCC into the composite is the tensile fiber failure phase which initiates at 25 μs and terminates when the projectile is either stopped by achieving a penetration velocity equal to zero or completely perforates the target, which is the case shown here at 67 μs. The data for these penetration phases are summarized in Table 18. The kinetic energy value at each time of phase change is also shown in the table; this allows the kinetic energy absorbed by the different phases to be calculated along with the % kinetic energy absorbed, and both of these values are shown in Table 18. The table shows that the compression crushing phase at 51% is the dominate energy absorption mechanism for the penetration of the RCC into a 14 mm thick target. The penetration phases developed and used in this discussion are summarized in Table 19.

Table 18. Kinetic Energy for Each Phase of Penetration in the Numberical Simulation of the 14 mm Target Impacted by the RCC at 828 m/s

Target Thickness (mm)		14			
Penetration Phase	Time (µs)	Velocity (m/s)	Projectile KE (J)	KE Absorbed(J)	*% KE Absorbed*
Impact	0.0	828	977		
Compression Crushing	9.0	581	481	496	51
Compression Shear	17.0	457	298	183	19
Plugging	25.0	411	241	57	6
Tensile Fiber Failure	67	338	163	78	8
			Total	814	92
			Projectile KE (J)	KE Remaining (J)	*% KE Remaining*
Residual	82.5	333	158	158	16
			Total	972	99.5

Table 19. Phases of Penetration for the 14 mm target

Projectile Impact

- Phase 1) Compression Crushing
- Phase 2) Compression Shear
- Phase 3) Plugging
- Phase 4) Tensile Fiber Failure

Residual Velocity

5.1.2 Phases of Penetration for the 9 mm Thick Composite

Using the same four penetration phase descriptions described above, and summarized in Table 19, the 9 mm target thickness was examined when impacted by the RCC, and the summary is presented in Table 20. The compression crush stage is still the dominate energy absorption mechanism. The compression shear energy is reduced by 73 % and the tensile failure energy is increased by 47% when compared to the 14 mm thick target summary. The target also displays a small degree of dishing. In penetration mechanics dishing is bending in the target element, and is typical for thin targets, however, Backman and Goldsmith [34] indicated that dishing is not confined to thin targets. There was only slight dishing, and the energy absorbed by it was accounted for in the tensile failure phase. The distal side of the target begins to move at 3 μs, which meets the criteria for an intermediate thick target element as defined by Backman and Goldsmith [34].

Table 20. Kinetic Energy for Each Phase of Penetration in the Numerical Simulation of the 9 mm Target Impacted by the RCC at 541 m/s

Target Thickness (mm)	9				
Penetration Phase	Time (μs)	Velocity (m/s)	Projectile KE (J)	KE Absorbed(J)	*% KE Absorbed*
Impact	0.0	541	417		
Compression Crushing	8.0	382	208	209	50
Compression Shear	13.5	338	163	45	11
Plugging	20.0	316	142	21	5
Tensile Fiber Failure	67.0	235	79	64	15
			Total	339	81
			Projectile KE (J)	KE Remaining (J)	*% KE Remaining*
Residual	84.5	228	74	74	18
			Total	413	98.9

5.1.3 Phases of Penetration for the 4 mm Thick Composite

The 4 mm thick target indicated different energy absorbing mechanisms than the 9 mm and 14 mm targets and required new phases for the penetration model description to describe the penetration process. The first phase, compression-crushing is the same for all thicknesses. This is followed by a plugging phase in the thinner target. The energy absorbing mechanisms previously described remain valid for these two phases. There are two deformation phases in the 4 mm thick target. The first deformation phase is the third phase of penetration, and is the dishing phase. Bending of the target during penetration is defined as dishing. The fourth and final phase is the tensile fiber failure phase described previously. The phases of penetration for the 4 mm thick target plate impacted by the RCC are summarized in Table 21. In Figure 46 and Table 22 the penetration of the 4 mm target is shown with the kinetic energy absorbed and the images at the various penetration phases. The there are two dominate energy absorbing mechanisms for the thinner 4 mm thick composite, the compression crushing and dishing phases with 34 and 33% respectively.

Table 21. Phases of Penetration for the 4 mm target

Projectile Impact
• Phase 1) Compression Crushing
• Phase 2) Plugging
• Phase 3) Dishing
• Phase 4) Tensile Fiber Failure
Residual Velocity

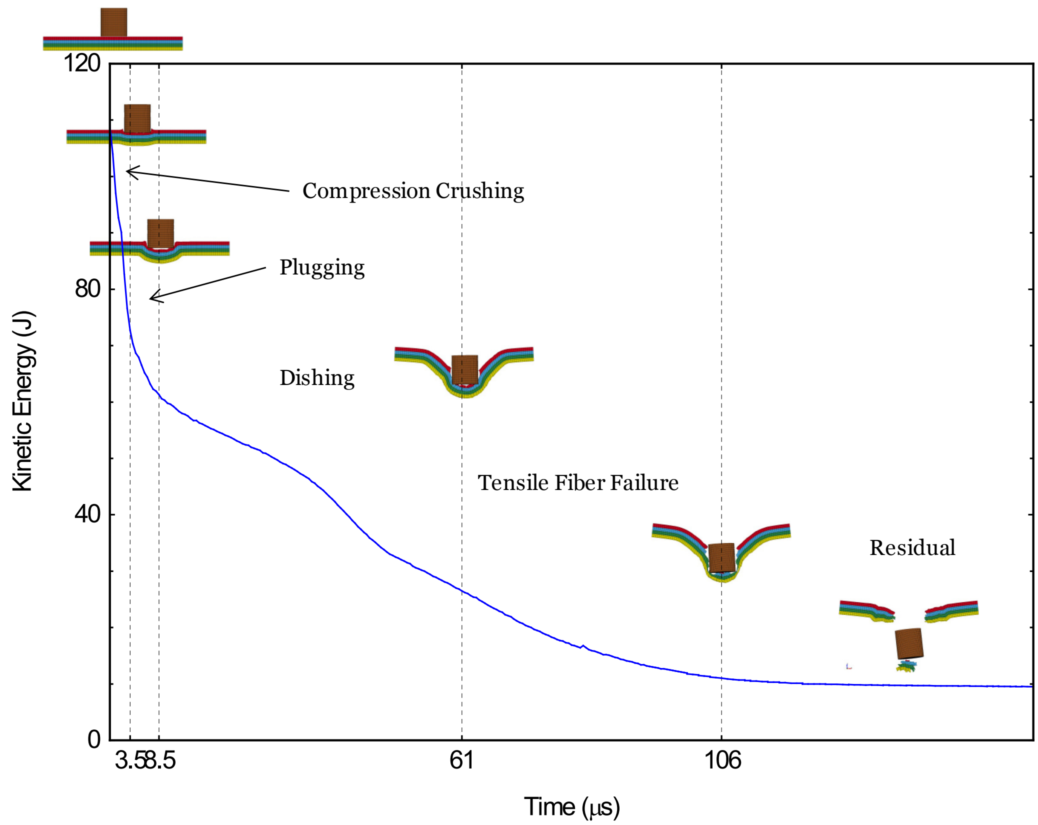

Figure 46. Penetration Phases for RCC Impacting 4mm Thick GFRP Composite

Table 22. Kinetic Energy for Each Phase of Penetration in the Numerical Simulation of the 4 mm Target Impacted by the RCC at 276 m/s

Target Thickness (mm)	4				
Penetration Phase	Time (µs)	Velocity (m/s)	Projectile KE (J)	KE Absorbed(J)	% KE Absorbed
Impact	0.0	276	109		
Compression Crushing	3.5	224	72	37	34
Plugging	8.5	206	60	11	10
Dishing	61.0	131	24	36	33
Tensile Fiber Failure	106	73	8	17	15
			Total	101	92
			Projectile KE (J)	KE Remaining (J)	% KE Remaining
Residual	120.0	64	6	6	5
			Total	107	98.0

5.1.4 Influence of Target Thickness on Penetration Phases

Since all three target thicknesses were used in the phases of penetration investigation the influence of target thickness on the penetration phases was simultaneously investigated. One conclusion that can be drawn from the investigation of target thickness using numerical simulations is that the three target thicknesses investigated represent thin, intermediate and thick targets. The thinnest target (4 mm) displayed a significant amount of energy absorption due to dishing, which indicates this is a thin target. The 9 mm target displayed that the distal side was involved in the majority of the penetration event, and this indicates that the target is exhibiting intermediate thick target element behavior.

5.2 INFLUENCE OF NOSE SHAPE ON PENETRATION PHASES

The influence of nose shape will be determined first by comparing the energy absorbed for the impact of the RCC and hemispherical nose shaped FSP into 14 mm and 4 mm thick composite targets. Then the influence of nose shape impacting semi-infinite targets will be determined by numerically simulating the depth of penetration of five fragments with different nose shapes.

5.2.1 Comparison of Hemispherical and RCC Nose Shapes Penetrating Finite Thick Targets

Initially the penetration phases determined in the previous section were applied to the hemispherical nose shaped FSP impacting the same three thicknesses of targets at its ballistic limit velocity for each thickness. Examination of the summary table for each indicated very similar behavior as the RCC at its respective ballistic limit. So nothing was revealed with respect to the influence of the nose shape, however, it did validate the phases and the influence of target thickness on the penetration phases.

New simulations were analyzed for the hemispherical nose shaped FSP using the same velocity as the RCC in the previous section, and the data for the 14 mm and 9 mm thick targets are summarized in Table 23 and Table 24 respectively.

Table 23. Kinetic Energy for Each Phase of Penetration for 828 m/s Impact into 14 mm Target

	RCC *% KE Absorbed(J)*	*Hemispherical* *% KE Absorbed(J)*
Impact		
Compression Crushing	51	54
Compression Shear	19	13
Plugging	6	6
Tensile Fiber Failure	8	2
Residual	16	25
Total	99.5	99.5

Table 24. Kinetic Energy for Each Phase of Penetration for 276 m/s Impact into 4 mm Target

	RCC *% KE Absorbed(J)*	*Hemispherical* *% KE Absorbed(J)*
Impact		
Compression Crushing	34	20
Plugging	10	8
Dishing	33	25
Tensile Fiber Failure	15	4
Residual	5	42
Total	98.0	99.1

Examining both tables reveals that as the nose shape changes from perfectly blunt to hemispherical the dominate mechanism of energy absorption remains the same for each target thickness unless a severe overmatch of the projectile target interaction is encountered, which is the case for the 4 mm thick target penetrated by the hemispherical nose shape. A severe overmatch in this case refers to the fact that only 58% of the energy is absorbed and 42% remains in the projectile after perforation. The compression-crushing and tensile fiber failure phases are suppressed in the overmatch condition and the residual velocity is high. Since the energy absorption for the target remains similar, the residual energy or residual velocity can be used to assess the efficiency of the FSPs. Where a higher residual energy or velocity indicates better penetration efficiency, this is typical of experimental investigations. Examination of the kinetic energy curves and the energy absorption for each of the penetration phases confirms that the MAT162 model is capable of capturing the influence of nose shape in the simulations for finite thick targets.

5.2.2 Comparison of Arbitrary Shaped Noses on DOP

Depth of penetration simulations are conducted numerically using the cube, chisel, 30 caliber FSP, modified 30 caliber FSP, and the RCC fragment simulated projectiles. Each the FSPs were analyzed for impacts at 400, 600 and 800 m/s. Figure 47 shows the simulated depth of penetration versus impact velocity for the five fragments analyzed, and Figure 48 shows the maximum depth of penetration for each FSP at 600 m/s.

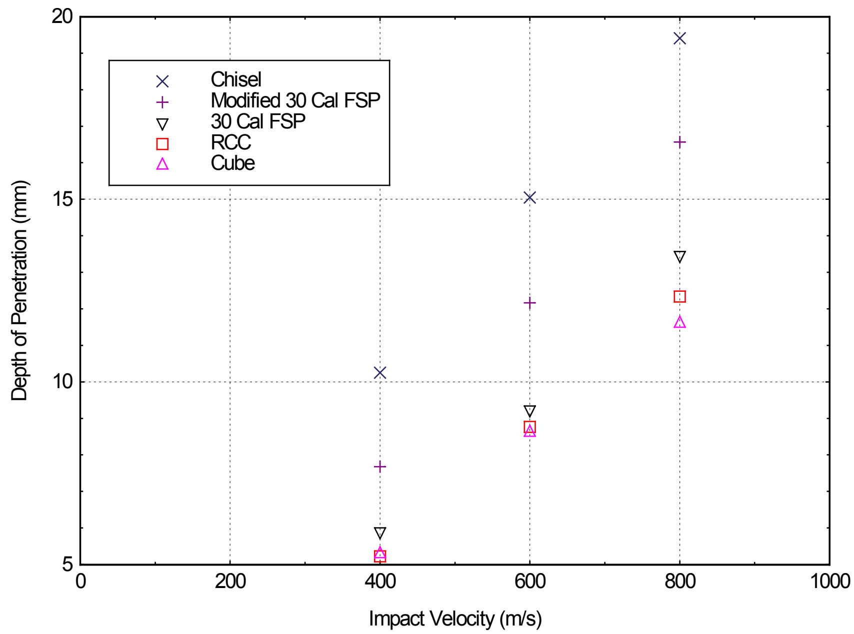

Figure 47. Simulated Depth of Penetration with Respect to Impact Velocity

All of the data is easily fit to linear form as shown in Figure 49. There are some observations from the analyzes worth noting such as; the slope varies by nose shape between 0.0158 < m < 0.0229, with the largest slope being associated with the best penetrator (chisel) and the lowest associated with the worse penetrator (cube). The intersection of the curves with the velocity axis denotes the critical or threshold velocity of penetration for each of the FSPs. The critical or threshold velocity is the velocity at which no penetration occurs. The intersection of the chisel data fit is greater than zero at zero velocity which is impractical, and requires further investigation to determine why this occurred.

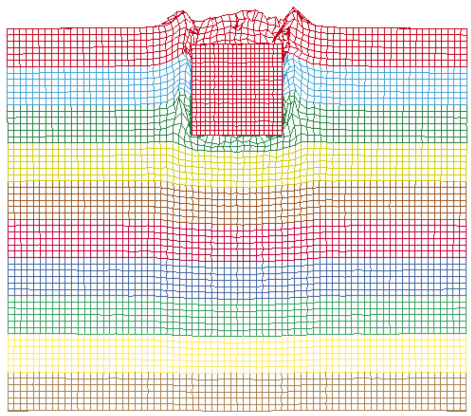

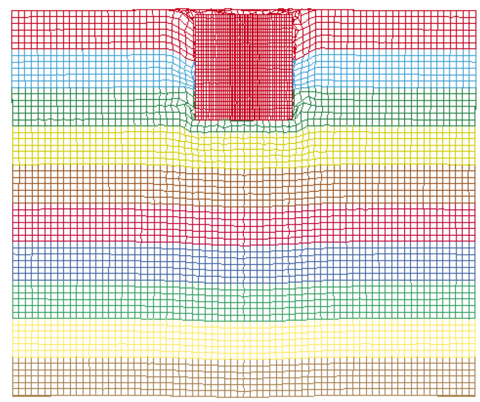

Cube – DOP = 8.6 mm

RCC – DOP =8.8 mm

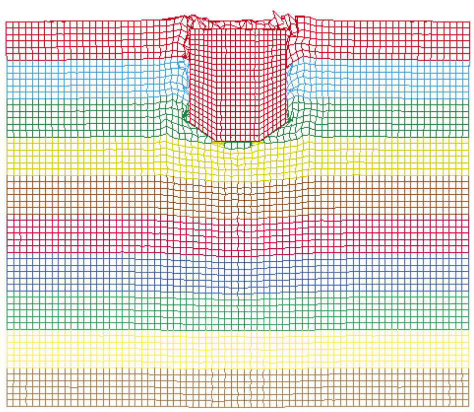

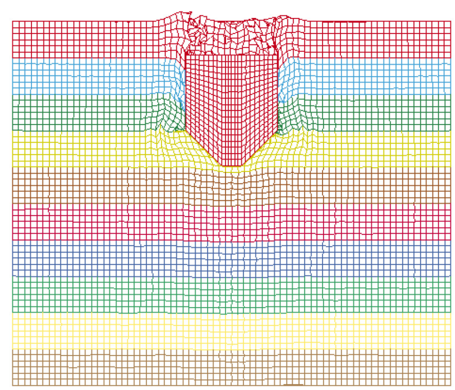

30 Cal FSP – DOP =9.2 mm

Modified 30 Cal FSP – DOP =12.2 mm

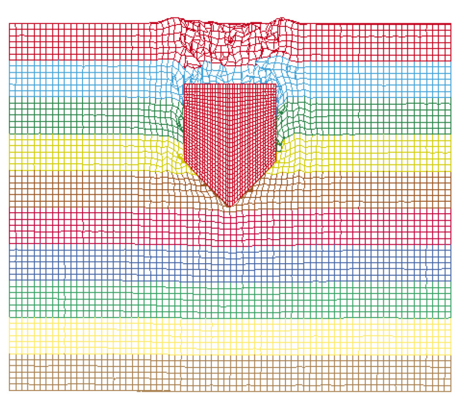

Chisel – DOP = 15.0 mm

Figure 48. DOP Simulations Shown at Maximum Depth for 600 m/s Impact Velocity

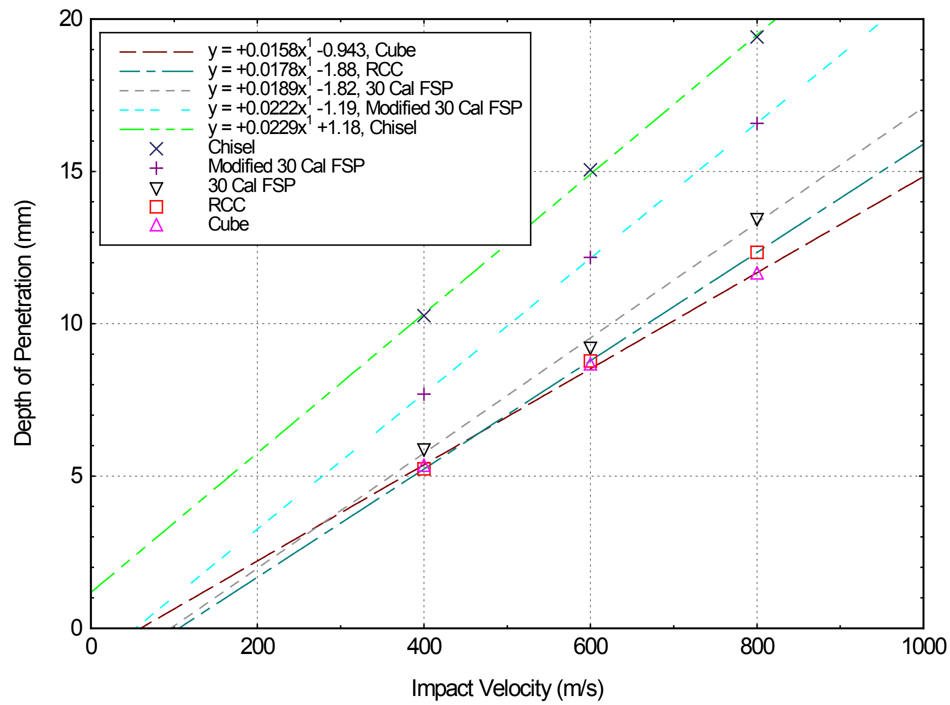

Figure 49. Linear Fits to Numerical DOP Simulations

Figure 50 shows the depth of penetration with respect to time for the 400 m/s and the 600 m/s numerical impacts. It can be seen that at early time the initial slopes of penetration are similar for all nose shapes analyzed. What is not so obvious from the curves in Figure 50 is the fact that the slope of curves is bi-linear and the point at which it varies is linear with impact velocity. The change in slope is due to a change in the energy absorption mechanism, from compression-crushing to compression-shear. Figure 51 is a zoomed in view of the 400 m/s plot shown in Figure 50, and it clearly shows the bi-linear aspect of the penetration.

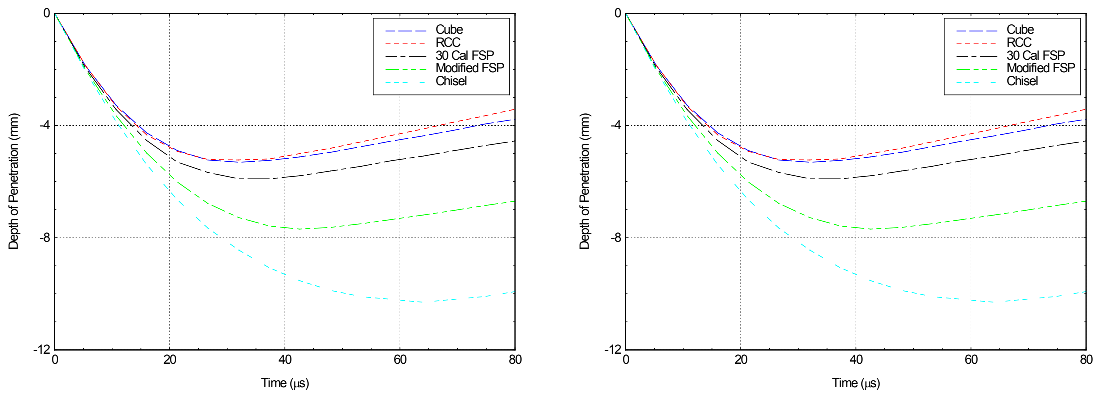

Impact Velocity = 400 m/s   Impact Velocity = 600 m/s

Figure 50. Depth of Penetration with Respect to Time

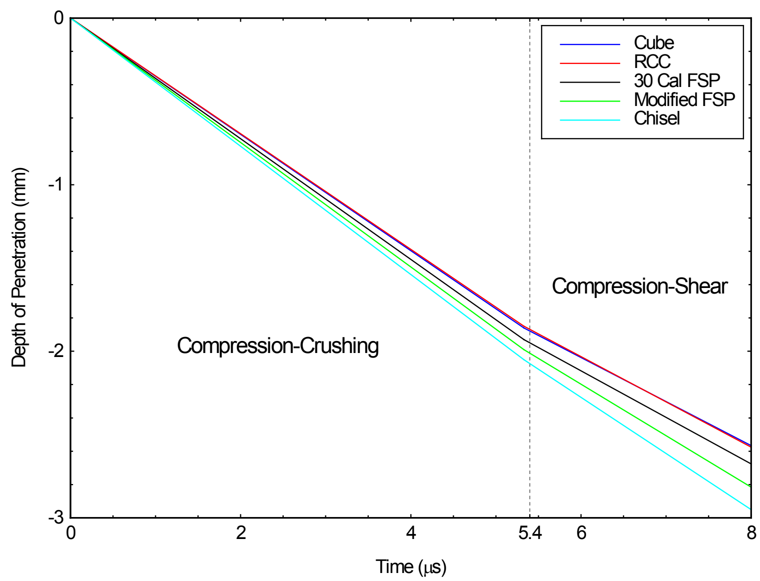

Figure 51. Bi-linear Slopes during Penetration of Semi-Infinite Targets at 400 m/s

The numerical DOP simulations indicated the penetration efficiency of the nose shapes into the semi-infinite thick target (96 mm thick) was identical to the 14 mm thick V_{BL} experiments. The penetration efficiency is summarized for the five fragments analyzed in Table 25, by comparing the depth of penetration at 600 m/s for each fragment to the ballistic limit for each fragment. This validates the thick target determination earlier for the 14 mm thick target.

Table 25. Penetration Efficiency Summary

Fragment	V_{BL} (m/s) for 14 mm	DOP (mm) at 600 m/s
Cube	861	8.6
RCC	828	8.8
30 Caliber FSP	813	9.2
Modified 30 Caliber FSP	680	12.2
Chisel	598	15.0

5.3 SUMMARY OF THE INFLUENCE OF THICKNESS AND NOSE SHAPE ON THE PENETRATION OF GFRP

Phases of penetration for thick and thin targets have been determined and described from the simulation results. These phases were used to evaluate the influence of thickness during FSP impact of composites. The evaluation of thicknesses confirmed that the three target thicknesses used in the ballistic limit experiments are thin, intermediate and thick. Additionally, these simulations have shown that the influence of nose shape and the different energy absorbing mechanisms can be determined for both finite and semi-infinite thick targets using numerical simulations in LS-DYNA when using the MAT162 composite MSC damage material model. The numerical DOP simulations indicated the penetration efficiency of the nose shapes into the semi-infinite thick target (96 mm thick) was identical to the 14 mm thick V_{BL} experiments.

CHAPTER 6 - SUMMARY AND RECOMMENDATIONS

6.1 SUMMARY

The terminal behavior of arbitrary shaped fragments versus E-Glass/Phenolic glass-fiber-reinforced plastic (GFRP) composites has been investigated and the influence of the nose shape has been shown. The 400 ballistic experiments using mass equivalent (2.85 gram) fragments with eight different nose shapes revealed that the ballistic limit and energy absorbed is significantly affected by the nose shape of the FSP. While all of the fragments are considered blunt nose shapes, the fragments with the sharper nose shapes were the most efficient penetrators (hemispherical, and chisel), and the fragments presenting a flat surface at the nose (cube, RCC and parallelepiped) were the least efficient penetrators. The difference between the ballistic limit for the least efficient nose shape (cube) and the most efficient nose shape (hemispherical) was 326 m/s for the 14-mm-thick target. Beta values for use in Wen's analytical model were derived empirically for all nose shapes from the experimental data. Close agreement was achieved between the analytical equation and the experimental results for FSPs using the new empirically derived β values.

Quasi-static, LVI and ballistic loading conditions were used to find the material properties and responses of E-glass/Phenolic composites. Standard ASTM tests were used to find the density, Poisson's ratio, tensile, compressive, and shear strength and the elastic and shear moduli of the material. The non-standard quasi-static punch-shear and punch-crush strength tests were used to find the punch shear and crush shear strengths of the material. The LVI tests were conducted to obtain force versus time curves for various loading conditions. Additional ballistic testing was conducted using a RCC to find the V_{50} ballistic limit using a specific fixture which was replicated during numerical modeling and the depth of penetration of the RCC at various velocities. The experimental data presented was used to determine all of the parameters for the material model MAT162 in LS-DYNA.

The MAT162 constitutive material model 39 material properties and parameters, and is able to capture the seven different damage modes and post damage softening behavior of composites. In this investigation all of the parameters required to conducted ballistic impact analysis on Advantex 3011 E-glass composite with SC-1008 phenolic resin using MAT162 were determined. Using the material properties generated, the unknown MAT162 parameters were determined by conducting parametric simulations of LVI, DOP and ballistic impacts. The modulus reduction parameter OMGMX is found by simulating LVI tests and varying the values of OMGMX to find the best agreement with LVI experimental data. The limit compressive volume strain for element eroding was found by simulating DOP experiments and comparing the results to the experimental data. Then the element eroding axial strain E_LIMT and EEXPN were determined by simulating ballistic impact experiments. When the optimized values were determined, analysis of ballistic experiments were conducted and compared to the experimental impact versus residual velocity curve. The results of the simulations were in excellent agreement with the experimental data. These optimized MAT162 parameters for the E-glass/Phenolic composite may be used with confidence to analyze ballistic impact applications in the future. The methodology presented can be used to find the properties and parameters for any plain weave fabric material.

Computational analysis using validated parameters was conducted for depth of penetration studies, and ballistic impact comparisons and proved that the model is capable of capturing the influence of the various nose shapes. Additionally, the model has given insight to the different failure mechanisms due to thickness. Using the kinetic energy of the projectile, the phases of penetration were developed. These penetration phases showed that the thin target absorbed more energy through dishing and tensile fiber failure and the thicker targets absorbed more energy by compression-crushing and compression-shear. It should be noted that while the compression-shear phase is suppressed in the thin target elements the influence of compression crushing remains high.

The numerical simulations have also captured the influence of thickness for the different nose shaped projectiles. The simulations showed the influence of shape (degree of bluntness) on the penetration event with sharper nosed fragments being more efficient for the 9, 14, and 50 mm. The simulations show that the bulge takes the shape of the fragment nose in the 4 mm target. The sharper geometric shapes load a smaller cross-sectional area of the target and increase the localized stress at the nose. A consequence of this increased localized stress is earlier tensile fiber failure and increased residual kinetic energy. The geometric shape is more critical than the degree of bluntness for thinner targets.

RECOMMENDATIONS FOR FUTURE WORK

The investigation has provided a wealth of data that can be used in future studies of penetration mechanics of nose shapes into composite material. A short coming of existing analytical models in dealing with arbitrary nose shapes is the area of the nose is assumed constant and a geometrical shape factor is used to account for the shape. In this investigation the density, and mass of each FSP is the same, therefore, so is the shape factor. So the analytical models using the shape factor cannot calculate the influence of the nose shape correctly. The alternative is to use an empirical constant, which was done in this investigation. While using empirical constants allows accurate predictions of ballistic penetration events, their use does not provide any insight into the mechanisms of failure or fragment defeat. Therefore, analytical methods should be pursued that explicitly account for the change in shape of the projectile in order to capture the physics of the composite penetration with various nose shapes.

The numerical simulations for semi-infinite targets should be expanded to more nose shapes, and the anomaly of the chisel crossing the velocity axis at a value greater than zero needs to be investigated. This can be done using the experimental data presented and supplementing with new DOP impact data for each nose shape.

Algorithms' for tracking the time when erosion criteria is active should be implemented into the material model MAT162 composite MSC damage. This will allow a check for penetration phase changes.

For completeness of the material properties data for Advantex E-glass/Phenolic, strain rate data and fracture toughness experiments should be conducted.

REFERENCES

[1] H. M. Wen, "Predicting the penetration and perforation of FRP laminates struck normally by projectiles with different nose shapes," *Composite Structures,* vol. 49, no. 3, pp. 321-329, 2000.

[2] H. M. Wen, "Penetration and perforation of thick FRP laminates," *Composites Science and Technology,* vol. 61, pp. 1163-1172, 2001.

[3] R. Saucier, "Shape factor of a randomly oriented cylinder," U. S. Army Research Laboratory, Aberdeen Proving Ground, MD, 2000.

[4] MIL-STD-662F, Department of Defense Test Method Standard V50 Ballistic Test of Armor, 1997.

[5] J. A. Zukas, T. Nicholas, H. F. Swift, L. B. Greszczuk and D. R. Curran, Impact dynamics, Malabar FL: Krieger Publishing Company, 1992.

[6] MIL-DTL-6415B, Detailed Specification - Laminate: Fiberglass-Fabric-Reinforced, Phenolic, 2008.

[7] T. W. Ipson and R. F. Recht, "Ballistic perforation by fragments of arbitrary shape," NWC TP 5927, Naval Weapons Center, China Lake, CA, 1977.

[8] MIL-P-46593(ORD), Military Specification - Projectile, Calibers .22, .30, .50 and 20 MM Fragment-Simulating, 1962.

[9] MIL-DTL-46593B(MR), Detail Specification - Projectile, Calibers .22, .30, .50 and 20 MM Fragment-Simulating, 2006.

[10] T. J. H. University, "The calibration of a collection medium for the determination of particle velocity.," Project Thor Tech Report 50, Ballistics Research Laboratories, Aberdeen Proving Ground, MD, 1962.

[11] STANAG-2920, Ballistic Test Method for Personal Armour Materials and Combat Clothing, 2nd Edition,: NATO Standardization Agency, 2003.

[12] J. B. Jordan, C. J. Naito and B. Z. Haque, "Quasi-static, low velocity impact and ballistic impact behavior of plain weave E-glass/Phenolic composites," *Manuscript submitted for publication,* 2012.

[13] C. E. Anderson, J. S. Wilbeck, P. S. Westine, U. S. Lindholm and A. B. Wenzel, "Course Notes - A short course on penetration mechanics," Southwest Reserach Institute, San Antonio, TX.

[14] L. J. Deka, S. D. Bartus and U. K. Vaidya, "Multi-site impact response of S2-glass/epoxy composite laminates," *Composite Science and Technology,* vol. 69, no. 3, pp. 725-735, 2009.

[15] S. Abrate, "Ch. 19 - Ballistic impacts on composite and sandwich structures," in *Major accomplishments in composite materials and sandwich structures - An anthology of ONR sponsored research*, Springer, 2010.

[16] G. Ben-Dor, A. Dubinsky and T. Elperin, "Optimal nose geometry of the impactor against FRP laminates," *Composite Structures,* vol. 55, pp. 73-80, 2002.

[17] S. T. Jeng, H.-S. Jing and C. Chung, "Predicting the ballistic limit for plain woven glass/epoxy composite laminate," *International Journal of Impact Engineering,* vol. 15, no. 4, pp. 451-464, 1994.

[18] A. Sabet, N. Fagih and H. M. Beheshty, "Effect of reinforcement type on high velocity impact response of GRP plates using sharp timp projectile," *International Journal of Impact Engineering,* vol. 38, pp. 715-722, 2011.

[19] N. K. Naik, A. Asmelash, R. K. Venkateswara and C. Veerraju, "Interlaminar

shear properties of polymer matrix composites: Strain rate effect," *Mechanics of Materials,* vol. 29, pp. 1043-1052, 2007.

[20] E. P. Gellert, S. J. Cimpoeru and R. L. Woodward, "A study of the effect of target thickness on the ballistic perforation of glass-fibre-reinforced plastic composites," *International Journal of Impact Engineering,* vol. 24, pp. 445-456, 2000.

[21] S. J. Bless, D. Hartman, K. Okajima and S. J. Hanchak, "Ballistic penetration of S2 glass laminates," in *3rd TACOM Armor Coordinating Conference for Light Combat Vehicles*, 1987.

[22] S. J. Bless, B. Moshe and K. Hartman, "Penetration through glass-reinforced phenolic," in *International SAMPE Conference*, 1990.

[23] V. Tan, C. T. Lim and C. H. Cheong, "Perforation of high-strength fabric by projectiles of different geometry," *International Journal of Impact Engineering,* vol. 28, pp. 207-222, 2003.

[24] C. Ulven, U. K. Vaidya and M. V. Hosur, "Effect of projectile shape during ballistic perforation of VARTM carbon/epoxy composite panels," *Composite Structures,* vol. 61, pp. 143-150, 2003.

[25] A. M. Blanas, "Finite element modeling of fragment penetration of thin structural composite laminates," Natick TR-92-019, US Army Natick Research, Development and Engineering Center, Natick MA, 1991.

[26] C. F. Yen, "Ballistic impact modeling of composite modeling of composite materials," in *7th International LS-Dyna Users Conference*, 2006.

[27] C. F. Yen, "A ballistic material model for continuous-fiber reinforced

composites," *International Journal of Impact Engineering,* vol. 46, pp. 11-22, 2012.

[28] L. J. Deka, S. D. Bartus and U. K. Vaidya, "Damage evolution and energy absorbtion of E-glass/polypropylene laminates subjected to ballistic impact," *Journal Material Science,* vol. 43, pp. 4399-4410, 2008.

[29] S. D. Bartus, "Simultaneous and sequential multi-site impact response of composite laminates," University of Alabama at Birmingham, PhD thesis, 2007.

[30] B. A. Gama, T. A. Bogetti and J. W. Gillespie, "Progressive damage modeling of plain-weave composites using LS-Dyna composite damage model MAT 162," in *7th European LS-Dyna Users Conference*, 2009.

[31] LS-Dyna, keyword user's manual, version 971, Livermore Software Technology, 2007.

[32] Material Science Corporation, University of Delaware Center of Composite Materials, "A progressive composite damage model for unidirectional and woven fabric composites - User Manual Version 10.0," University of Delaware Center for Composite Materials, LS-DYNA Version 971, 2011.

[33] A. Matzenmiller, J. Lubliner and R. L. Taylor, "A constitutive model for anisotropic damage in fiber-composites," *Mechanics of Materials,* vol. 20, pp. 125-152, 1995.

[34] M. E. Backman and W. Goldsmith, "The mechanics of penetration of projectiles into targets," *International Journal of Engineering Science,* vol. 16, pp. 1-99, 1978.

[35] ASTM, D792 – 08, Standard Test Methods for Density and Specific Gravity

(Relative Density) of Plastics by Displacement, West Conshohocken, PA: American Society for Testing and Materials, 2008.

[36] ASTM, D3039/D3039M – 08, Standard Test Method for Tensile Properties of Polymer Matrix Composite Materials, West Conshohocken, PA: American Society for Testing and Materials, 2008.

[37] ASTM, D5379/D5379M – 05, Standard Test Method for Shear Properties of Composite Materials by the V-Notched Beam Method, West Conshohocken, PA: American Society for Testing and Materials, 2005.

[38] ASTM, D6641/D6641M – 09, Standard Test Method for Compressive Properties of Polymer Matrix Composite Materials Using a Combined Loading Compression (CLC) Test Fixture, West Conshohocken, PA.: American Society for Testing and Materials, 2009.

[39] ASTM, D7291 - 07, Through-Thickness "Flatwise" Tensile Strength and Elastic Modulus of a Fiber-Reinforced Polymer Matrix Composite Material, West Conshohoken, PA: American Society of Test Methods, 2007.

[40] MIL-HDBK-17-1F, Department Of Defense Composite Materials Handbook Volume 1. Polymer Matrix Composites, 2002.

[41] J. P. Lambert and G. H. Jonas, "Towards standardization in terminal ballistics testing: velocity representation," BRL-R-1852 U.S. Army Ballistics Research Laboratory, Aberdeen Proving Grounds, MD, 1976.

[42] B. Z. Haque and J. W. Gillespie Jr, "A new penetration equation satisfying momentum and energy conservation," in *SAMPE 2012*, Baltimore, MD, 2012.

[43] T. Borvik, O. S. Hopperstand, M. Langseth and K. A. Malo, "Effect of target

thickness in blunt projectile penetration of Weldox 460 E steel plates," *International Journal of Impact Engineering,* vol. 28, pp. 413-464, 2003.

[44] B. Z. Haque, S. C. Chowdhury, I. Biswas, P. M. Schweiger, J. W. Gillespie and D. R. Hartman, "Modeling the low velocity impact damage behavior of S-Glass/Phenolic composites," in *SAMPE 2012*, Baltimore MD, 2012.

[45] B. A. Haque, I. Biswas, S. C. Chowdhury, J. W. Gillespie Jr and D. R. Hartman, "Modeling the depth of penetration and ballistic impact on S-Glass/Phenolic thick section composites," in *American Society for Composites 27th Technical Conference*, Arlington, TX, 2012.

[46] L. J. Greaves, "Failure Mechanisms in Glass Fibre," Defense Research Agency, UK, 1992.

[47] B. Z. Haque, J. L. Harrington, I. Biswas and J. W. Gillespie Jr, "Perforation and Penetration of Composites," in *SAMPE 2012*, Baltimore MD, 2012.

[48] C. F. Yen, B. A. Cheeseman, C. P. Hoppel, B. A. Gama and J. W. Gillespie Jr, "Modeling the compressive failure of plain weave composites," in *Proceedings of the American Society for Composites 19th Annual Technical Conference*, Atlanta, GA, 2004.

[49] J. R. Xiao, B. A. Gama and J. W. Gillespie Jr, "Progressive damage and delamination in plain weave S-2 glass/SC-15 composites under quasi-static punch-shear loading," *Composite Structures,* vol. 78, no. 2, pp. 182-196, 2007.

[50] N. A. St John and J. R. Brown, "Flexural and interlaminar shear properties of glass-reinforced phenolic composites," *Composites Part A,* vol. 29A, pp. 939-946, 1998.

[51] W. A. Schmeling, T. W. Ipson and R. F. Recht, "Terminal Ballistics of Irregular Fragments," NWC TP 5597, Naval Warfare Center, China Lake, CA, 1973.

[52] W. A. Schmeling and T. W. Ipson, "Terminal Ballistics of Elongate Fragments," NWC TP 5449, Naval Warfare Center, China Lake CA, 1972.

[53] R. F. Recht and T. W. Ipson, "Ballistic perforation dynamics," *Journal of Applied Mechanics,* pp. 384-390, 1963.

[54] A. T. Nettles, "Basic mechanics of laminated composite plates," NASA Reference Publication 1351, NASA, Marshall Space Flight Center, MSFC AL, 1994.

[55] N. K. Naik and A. V. Doshi, "A constitutive ballistic impact behavior of thick composites; parametric studies," *Composite Structures,* vol. 82, pp. 447-464, 2008.

[56] C. Menna, D. Asprone, G. Caprino, V. Lopresto and A. Prota, "Numerial simulation of impact tests on GFRP composite laminates," *International Journal of Impact Engineering,* vol. 38, pp. 677-685, 2011.

[57] M. Loikkanen, G. Praveen and D. Powell, "Simulation of ballistic impact of composite panels," in *10th International LS-Dyna Users Conference*, 2009.

[58] J. B. Jordan and C. J. Naito, "Calculating fragment impact velocity from penetration data," *International Journal of Impact Engineerinng,* vol. 37, pp. 530-536, 2010.

[59] M. A. Hayat and S. M. A. Suliman, "Mechanical and structural properties of glass reinforced phenolic laminates," *Polymer Testig,* vol. 17, pp. 79-97, 1998.

[60] Z. Hashin, "Failure Criteria for Unidirectional Fiber Composites," *Journal of Applied Mechanics,* vol. 47, pp. 329-334, 1980.

[61] B. Z. Haque and J. W. Gillespie Jr, "A combined theoretical-semiempirical penetration model of ballistic penetration of thick section composites," *Journal of Thermoplastic Composite Material,* pp. 631-659, 2012.

[62] B. A. Gama and J. W. Gillespie Jr, "Punch shear based penetration model of ballistic," *Composite Structures .,* vol. 86, pp. 356-369, 2008.

[63] B. A. Gama and J. W. Gillespie Jr, "Finite element modeling of impact, damage evolution and penetration of," *International Journal of Impact Engineering,* vol. 38, pp. 181-197, 2011.

[64] K. Brown, R. Brooks and N. Warrior, "Numerical simulation of damage in thermoplastic composite materials," in *5th European LS-DYNA Users Conference*, 2007.

[65] J. A. Zukas, T. Nicholas, H. F. Swift, L. B. Greszczuk and D. R. Curran, Impact Dynamics, Malabar FL: Krieger Publishing Company, 1992.

[66] B. Z. Haque, ,. S. C. Chowdhury, I. Biswas, P. M. Schweiger, J. W. Gillespie and D. R. Hartman, "Modeling the Low Velocity Impact Damage Behavior of S-Glass/Phenolic Composites," in *SAMPE 2012*, Baltimore MD, 2012.

APPENDIX A – BALLISTIC DATA AND FSP DRAWINGS

TEST PANEL 20110001

Manufacturer: Sioux Manufacturing Corporation
Test Panel Description: Advantex E-Glass with SC-1008 Phenolic Resin
Width (in): 12 — Plies/Laminates: 28
Height (in): 12 — Weight (lbs): 6.01
Thickness (in): 0.54 — Areal Density (lbs./ft²): 6.01

SET-UP

Relative Humidity (%): -
Temperature (°F): 73
Weapon System: Universal Receiver
Barrel: 7.62 x 51mm
Range to Target (ft): 20
Obliquity (°): 0

Witness Panel: 0.020 in 2024-T3
Target to Witness Panel (in): 6
Velocity Screens: Ohler Model 57
Screen Spacing(s) (ft): 5,5,3
Instrumentation Velocity Distance (ft): 7.5,5
Residual Velocity Distance (ft): 3

AMMUNITION

Projectile: 0.30 Cal FSP
Projectile Weight (grains): 44
Powder: IMR 4227 (wt. in grains)

APPLICABLE STANDARDS/PROCEDURES

(1): MIL-STD-662F
(2):
(3):

VELOCITY DATA (ft/s)

Date	Shot	Powder wt.	FSP wt.	V1	V2	Vs	Vr	Result
6/14/2011	1	18	43.9	2199	2178	2136	0	PP
6/14/2011	2	20.1	43.9	2301	2278	2232	0	PP
6/14/2011	3	25.7	44.3	2926	2896	2836	809	CP
6/14/2011	4	22.6	43.9	2752	2724	2668	0	PP
6/14/2011	5	24.5	44.4	2765	2737	2681	562	CP
6/14/2011	6	23.9	43.9	2864	2837	2783	540	CP
6/14/2011	7	23.6	44.1	2784	2757	2703	684	CP
6/14/2011	8	23.4	44.2	2678	2652	2600	0	PP
6/14/2011	9	23.5	43.7	2693	2665	2609	0	PP
6/14/2011	10	23.7	44.3	2733	2707	2655	824	CP
6/14/2011	11	23.5	43.5	2790	2763	2709	674	CP
6/14/2011	12	23.3	43.9	2721	2693	2665	0	PP
6/14/2011	13	27	44.1	3071	3044	3017	938	CP
6/14/2011	14	28.6	44	3046	3014	2982	896	CP
6/14/2011	15	31.2	43.8	3252	3217	3182	1324	CP

V50 SUMMARY

Number of Shots in Calculation: 4
High Partials: 2668, 2665 ft/s
Low Completes: 2655, 2681 ft/s
Velocity Span Criteria: 60 ft/s
Span Criteria Met? Yes
V_{50} : 2667 ft/s
Range of Results: 26 ft/s
Zone of Mixed Results: 13 ft/s

REMARKS

Zone of Mixed Results

Panel Weights:
#1: 6.01 lbs.
#2: 6.01 lbs.
#3: 5.99 lbs.

TEST PANEL 20110002

Manufacturer: Sioux Manufacturing Corporation
Test Panel Description: Advantex E-Glass with SC-1008 Phenolic Resin
Width (in): 12 | Plies/Laminates: 18
Height (in): 12 | Weight (lbs): 3.84
Thickness (in): 0.339 | Areal Density (lbs./ft²): 3.84

<u>SET-UP</u>

Relative Humidity (%): - | Witness Panel: 0.020 in 2024-T3
Temperature (°F): 73 | Target to Witness Panel (in): 6
Weapon System: Universal Receiver | Velocity Screens: Ohler Model 57
Barrel: 7.62 x 51mm | Screen Spacing(s) (ft): 5,5,3
Range to Target (ft): 20 | Instrumentation Velocity Distance (ft): 7.5,5
Obliquity (°): 0 | Residual Velocity Distance (ft): 3

<u>AMMUNITION</u>

Projectile: 0.30 Cal FSP
Projectile Weight (grains): 44
Powder: IMR 4227 (wt. in grains)

<u>APPLICABLE STANDARDS/PROCEDURES</u>

(1): MIL-STD-662F
(2):
(3):

VELOCITY DATA
(ft/s)

Date	Shot	Powder wt.	FSP wt.	V1	V2	Vs	Vr	Result
6/14/2011	1	10.6	44	1208	1186	1114	0	PP
6/14/2011	2	13.3	44.4	1414	1407	1393	0	PP
6/14/2011	3	14	44	1659	1644	1614	0	PP
6/14/2011	4	15.3	43.9	1524	1515	1497	0	PP
6/14/2011	5	16	44.1	1828	1810	1774	0	CP
6/14/2011	6	16.4	44	1955	1936	1898	628	CP
6/14/2011	7	16.3	44.1	1923	1904	1866	501	CP
6/14/2011	8	16.2	44.4	1888	1870	1834	332	CP
6/14/2011	9	16	43.8	1922	1902	1862	502	CP
6/14/2011	10	16	44.5	1888	1875	1849	412	CP
6/14/2011	11	15.8	44.2	1848	1830	1794	NR	CP
6/14/2011	12	15.6	43.9	1797	1779	1743	0	PP
6/14/2011	13	15.8	43.6	1913	1898	1868	577	CP
6/14/2011	14	15.7	44	1865	1848	1814	350	CP
6/14/2011	15	15.5	44.1	1786	1773	1747	0	PP
6/14/2011	16	15.6	44.5	1829	1812	1778	425	CP
6/14/2011	17	17.1	44.5	1942	1924	1888	559	CP
6/14/2011	18	18.4	43.5	2176	2155	2113	868	CP
6/14/2011	19	19.9	44.5	2342	2318	2227	1234	CP

<u>V50 SUMMARY</u>

Number of Shots in Calculation: 4
High Partials: 1774, 1747 ft/s
Low Completes: 1778, 1794 ft/s
Velocity Span Criteria: 60 ft/s
Span Criteria Met? Yes
V_{50}: 1773 ft/s
Range of Results: 47 ft/s
Zone of Mixed Results: -

<u>REMARKS</u>

Shot 11 did not record residual velocity

Panel Weights:
#1: 3.81 lbs.
#2: 3.86 lbs.
#3: 3.83 lbs.
#4: 3.85 lbs.

TEST PANEL 20110003

Manufacturer: Sioux Manufacturing Corporation
Test Panel Description: Advantex E-Glass with SC-1008 Phenolic Resin

Width (in): 12	Plies/Laminates: 8
Height (in): 12	Weight (lbs): 1.71
Thickness (in): 0.165	Areal Density (lbs./ft^2): 1.71

SET-UP

Relative Humidity (%): -	Witness Panel: 0.020 in 2024-T3
Temperature (°F): 73	Target to Witness Panel (in): 6
Weapon System: Universal Receiver	Velocity Screens: Ohler Model 57
Barrel: 7.62 x 51mm	Screen Spacing(s) (ft): 5,5,3
Range to Target (ft): 20	Instrumentation Velocity Distance (ft): 7.5,5
Obliquity (°): 0	Residual Velocity Distance (ft): 3

AMMUNITION	APPLICABLE STANDARDS/PROCEDURES
Projectile: 0.30 Cal FSP	(1): MIL-STD-662F
Projectile Weight (grains): 44	(2):
Powder: IMR 3031 (wt. in grains)	(3):

VELOCITY DATA
(ft/s)

Date	Shot	Powder wt.	FSP wt.	V1	V2	Vs	Vr	Result
7/8/2011	1	8.1	44.2	839	833	821	0	PP
7/8/2011	2	9.2	43.9	944	938	926	0	PP
7/8/2011	3	9.7	43.9	986	979	965	NR	CP
7/8/2011	4	9.9	43.8	988	981	967	NR	CP
7/8/2011	5	9.4	44.1	896	890	878	0	PP
7/8/2011	6	10.7	44.1	973	966	952	79	CP
7/8/2011	7	12.2	44.1	921	914	900	0	PP
7/8/2011	8	14	44.1	634	630	622	0	PP
7/8/2011	9	13.8	44.1	899	893	881	0	PP
7/8/2011	10	12.6	44	730	725	715	0	PP
7/21/2011	11	8.8	43.9	732	727	717	0	PP
7/21/2011	12	11.2	44	1307	1301	1289	722	CP
7/21/2011	13	8.8	43.9	964	957	943	NR	CP
7/21/2011	14	10.7	43.9	1153	1146	1132	564	CP
7/21/2011	15	12.2	43.9	1265	1260	1250	748	CP
7/21/2011	16	14.3	44.1	1599	1587	1563	1199	CP
7/21/2011	17	13.8	43.8	1629	1613	1581	1176	CP
7/21/2011	18	12.6	44.1	1421	1413	1397	939	CP

V50 SUMMARY	REMARKS
Number of Shots in Calculation: 4	Shot 3-4 did not record residual velocity
High Partials: 926, 900 ft/s	Shot 13 did not record residual velocity
Low Completes: 943, 952 ft/s	
Velocity Span Criteria: 60 ft/s	Panel Weights:
Span Criteria Met? Yes	#1: 1.71 lbs.
V_{50}: 930 ft/s	#2: 1.74 lbs.
Range of Results: 52 ft/s	#3: 1.72 lbs.
Zone of Mixed Results: -	#4: 1.75 lbs.
	#5: 1.71 lbs.

TEST PANEL 20110004

Manufacturer: Sioux Manufacturing Corporation
Test Panel Description: Advantex E-Glass with SC-1008 Phenolic Resin
Width (in): 12 — Plies/Laminates: 28
Height (in): 12 — Weight (lbs): 6.01
Thickness (in): 0.54 — Areal Density (lbs./ft²): 6.01

SET-UP
Relative Humidity (%): -
Temperature (°F): 73
Weapon System: Universal Receiver
Barrel: 7.62 x 51mm
Range to Target (ft): 20
Obliquity (°): 0
Witness Panel: 0.020 in 2024-T3
Target to Witness Panel (in): 6
Velocity Screens: Ohler Model 57
Screen Spacing(s) (ft): 5,5,3
Instrumentation Velocity Distance (ft): 7.5,5
Residual Velocity Distance (ft): 3

AMMUNITION
Projectile: 0.30 Cal Chisel FSP
Projectile Weight (grains): 44
Powder: IMR 4227 (wt. in grains)

APPLICABLE STANDARDS/PROCEDURES
(1): MIL-STD-662F
(2):
(3):

VELOCITY DATA
(ft/s)

Date	Shot	Powder wt.	FSP wt.	V1	V2	Vs	Vr	Result
7/13/2011	1	31	44.3	2079	2059	2019	255	CP
7/13/2011	2	30.3	44.3	1990	1971	1933	0	PP
7/13/2011	3	30.7	44.1	2180	2159	2117	260	CP
7/13/2011	4	30.5	44	2240	2218	2174	454	CP
7/13/2011	5	28.2	44.4	2246	2225	2183	NR	CP
7/13/2011	6	25.4	44.3	1921	1902	1864	0	PP
7/14/2011	7	26.9	44.1	2085	2065	2025	259	CP
7/14/2011	8	25.9	44.4	1934	1916	1880	0	PP
7/14/2011	9	26.4	44.3	2038	2019	1981	0	CP
7/14/2011	10	26.4	44.3	1680	1664	1632	0	PP
7/14/2011	11	26.4	44.2	2043	2023	1983	133	CP
7/14/2011	12	26	44.4	1891	1871	1831	0	PP
7/14/2011	13	26.1	44.3	2000	1981	1943	0	PP
7/14/2011	14	21	44.1	2539	2541	2464	882	CP
7/14/2011	15	23.5	44.5	2807	2781	2729	1293	CP
7/14/2011	16	24.4	44.5	2935	2909	2857	1514	CP
7/14/2011	17	20	44.4	2406	2383	2337	771	CP

V50 SUMMARY
Number of Shots in Calculation: 4
High Partials: 1943, 1933 ft/s
Low Completes: 1981, 1983 ft/s
Velocity Span Criteria: 60 ft/s
Span Criteria Met? Yes
V_{50}: 1960 ft/s
Range of Results: 50 ft/s
Zone of Mixed Results: -

REMARKS
Shot 5 did not record residual velocity

Shot 9 Penetrated the witness plate but did not have sufficient residual velocity to be recorded.

Switched to IMR4227 at Shot 14

Panel Weights:
#1: 5.97 lbs.
#2: 6.01 lbs.
#3: 5.97 lbs.
#4: 5.99 lbs.

TEST PANEL 20110005

Manufacturer: Sioux Manufacturing Corporation
Test Panel Description: Advantex E-Glass with SC-1008 Phenolic Resin
Width (in): 12 — Plies/Laminates: 18
Height (in): 12 — Weight (lbs): 3.84
Thickness (in): 0.339 — Areal Density (lbs./ft^2): 3.84

SET-UP

Relative Humidity (%): -
Temperature (°F): 73
Weapon System: Universal Receiver
Barrel: 7.62 x 51mm
Range to Target (ft): 20
Obliquity (°): 0

Witness Panel: 0.020 in 2024-T3
Target to Witness Panel (in): 6
Velocity Screens: Ohler Model 57
Screen Spacing(s) (ft): 5,5,3
Instrumentation Velocity Distance (ft): 7.5,5
Residual Velocity Distance (ft): 3

AMMUNITION

Projectile: 0.30 Cal Chisel FSP
Projectile Weight (grains): 44
Powder: IMR 4227 (wt. in grains)

APPLICABLE STANDARDS/PROCEDURES

(1): MIL-STD-662F
(2):
(3):

VELOCITY DATA (ft/s)

Date	Shot	Powder wt.	FSP wt.	V1	V2	Vs	Vr	Result
7/13/2011	1	10.5	44.4	1066	1059	1045	0	PP
7/13/2011	2	11.5	44.5	1395	1383	1359	NR	CP
7/13/2011	3	11.5	44.5	1333	1326	1312	0	CP
7/13/2011	4	11.8	44.4	1334	1327	1313	0	CP
7/13/2011	5	11.7	44	1321	1315	1303	0	PP
7/13/2011	6	13.9	44.1	1627	1611	1579	651	CP
7/14/2011	7	14.9	44.4	1820	1803	1769	871	CP
7/14/2011	8	16	44.5	1922	1904	1868	1007	CP
7/14/2011	9	17.1	44.4	2083	2064	2026	1188	CP

V50 SUMMARY

Number of Shots in Calculation: 4
High Partials: 1313, 1303 ft/s
Low Completes: 1313, 1359 ft/s
Velocity Span Criteria: 60 ft/s
Span Criteria Met? Yes
V_{50}: 1322 ft/s
Range of Results: 56 ft/s
Zone of Mixed Results: 0 ft/s

REMARKS

Shot 2 did not record residual velocity

Shot 4 Penetrated the witness plate but did not have sufficient residual velocity to be recorded.

Panel Weights:
#1: 3.82 lbs.
#2: 3.83 lbs.

TEST PANEL 20110006

Manufacturer: Sioux Manufacturing Corporation
Test Panel Description: Advantex E-Glass with SC-1008 Phenolic Resin
Width (in): 12 — Plies/Laminates: 8
Height (in): 12 — Weight (lbs): 1.71
Thickness (in): 0.165 — Areal Density (lbs./ft²): 1.71

SET-UP
Relative Humidity (%): -
Temperature (°F): 73
Weapon System: Universal Receiver
Barrel: 7.62 x 51mm
Range to Target (ft): 20
Obliquity (°): 0
Witness Panel: 0.020 in 2024-T3
Target to Witness Panel (in): 6
Velocity Screens: Ohler Model 57
Screen Spacing(s) (ft): 5,5,3
Instrumentation Velocity Distance (ft): 7.5,5
Residual Velocity Distance (ft): 3

AMMUNITION
Projectile: 0.30 Cal Chisel FSP
Projectile Weight (grains): 44
Powder: IMR 4227 (wt. in grains)

APPLICABLE STANDARDS/PROCEDURES
(1): MIL-STD-662F
(2):
(3):

VELOCITY DATA
(ft/s)

Date	Shot	Powder wt.	FSP wt.	V1	V2	Vs	Vr	Result
7/19/2011	1	8.2	44.5	1406	1396	1376	1005	CP
7/19/2011	2	7	44.3	1241	1236	1226	868	CP
7/19/2011	3	4.1	44.5	969	964	954	546	CP
7/19/2011	4	6.5	44.5	1096	1078	1042	738	CP
7/19/2011	5	3.1	44.3	673	670	664	0	PP
7/19/2011	6	4.3	44.3	916	910	898	490	CP
7/19/2011	7	3.7	44.3	907	901	889	423	CP
7/19/2011	8	3.2	44.5	664	662	658	0	PP
7/19/2011	9	3.4	44.4	669	666	660	0	PP
7/19/2011	10	3.7	44.5	774	770	762	244	CP
7/19/2011	11	3.6	44.5	835	831	823	NR	CP
7/19/2011	12	3.6	44.1	744	740	732	113	CP
7/19/2011	13	3.4	44.5	773	769	761	227	CP
7/19/2011	14	3.4	44.5	759	756	750	263	CP
7/19/2011	15	3.2	44.5	777	773	765	279	CP
7/19/2011	16	3.1	44.2	759	756	750	154	CP
7/21/2011	17	3	44.5	707	704	698	NR	CP
7/21/2011	18	3	44.6	646	644	640	0	PP
7/21/2011	19	3.2	44.3	712	709	703	0	PP
7/21/2011	20	3	44.5	918	912	900	490	CP
7/21/2011	21	2.5	44.6	882	877	867	NR	CP
7/21/2011	22	2	44.4	651	648	642	0	PP
7/21/2011	23	2.2	44.5	663	660	654	0	PP
7/21/2011	24	3.9	44.3	776	773	767	145	CP
7/21/2011	25	3.7	44.4	882	877	867	NR	CP
7/21/2011	26	3.1	44.4	1016	1009	995	616	CP
7/21/2011	27	2.2	44.2	574	572	568	0	PP
7/21/2011	28	3.7	44.3	1021	1014	1000	635	CP
7/21/2011	29	6.4	44.4	1251	1240	1218	882	CP
7/21/2011	30	3.5	44	746	743	737	0	CP
7/21/2011	31	3.2	44.4	820	816	808	358	CP
7/21/2011	32	3.1	44.7	819	815	807	377	CP
7/21/2011	33	2.9	44	859	855	847	401	CP

V50 SUMMARY	REMARKS
Number of Shots in Calculation: 6 High Partials: 703, 664, 660 ft/s Low Completes: 698, 732, 737 ft/s Velocity Span Criteria: 90 ft/s Span Criteria Met? Yes V_{50} : 699 ft/s Range of Results: 77 ft/s Zone of Mixed Results: 5 ft/s	Zone of Mixed Results Switched to IMR3031 at Shot 4 Shot 11 did not record residual velocity Shot 17 did not record residual velocity Switched to IMR4227 at Shot 21 Shot 21 did not record residual velocity Switched to IMR4064 at Shot 24 Shot 25 did not record residual velocity Switched to IMR4198 at Shot 26 Switched to IMR4227 at Shot 27 Switched to IMR4064 at Shot 28 Switched to IMR4227 at Shot 29 Shot 30 Penetrated the witness plate but did not have sufficient residual velocity to be recorded. Panel Weights: #1: 1.74 lbs. #2: 1.71 lbs. #3: 1.72 lbs. #4: 1.72 lbs. #5: 1.71 lbs. #6: 1.71 lbs. #7: 1.71 lbs.

TEST PANEL 20110007

Manufacturer: Sioux Manufacturing Corporation
Test Panel Description: Advantex E-Glass with SC-1008 Phenolic Resin
Width (in): 12 — Plies/Laminates: 28
Height (in): 12 — Weight (lbs): 6.01
Thickness (in): 0.54 — Areal Density (lbs./ft^2): 6.01

SET-UP

Relative Humidity (%): -
Temperature (°F): 73
Weapon System: Universal Receiver
Barrel: 7.62 x 51mm
Range to Target (ft): 20
Obliquity (°): 0

Witness Panel: 0.020 in 2024-T3
Target to Witness Panel (in): 6
Velocity Screens: Ohler Model 57
Screen Spacing(s) (ft): 5,5,3
Instrumentation Velocity Distance (ft): 7.5,5
Residual Velocity Distance (ft): 3

AMMUNITION

Projectile: 0.30 Cal 120° Conical FSP
Projectile Weight (grains): 44
Powder: IMR 4227 (wt. in grains)

APPLICABLE STANDARDS/PROCEDURES

(1): MIL-STD-662F
(2):
(3):

VELOCITY DATA (ft/s)

Date	Shot	Powder wt.	FSP wt.	V1	V2	Vs	Vr	Result
7/22/2011	1	18	44.3	2079	2056	2010	0	PP
7/22/2011	2	22	44.5	2592	2565	2511	932	CP
7/22/2011	3	20	44.5	2313	2287	2235	262	CP
7/22/2011	4	19.5	44.5	2240	2215	2165	0	PP
7/22/2011	5	19.5	44.6	2282	2256	2204	240	CP
7/22/2011	6	19.3	44.5	2318	2293	2243	0	PP
7/22/2011	7	19.5	44.5	2330	2304	2252	NR	CP
7/22/2011	8	19.3	44.4	2269	2246	2200	NR	CP
7/22/2011	9	19.4	44.4	2273	2248	2198	0	CP
7/22/2011	10	19.4	44.5	2298	2274	2226	241	CP
7/22/2011	11	19.3	44.4	2323	2297	2245	0	PP
7/22/2011	12	19.3	44.4	2304	2278	2226	0	PP
7/22/2011	13	21.6	44.4	2624	2596	2540	990	CP
7/22/2011	14	20.6	44.4	2518	2492	2440	590	CP
7/22/2011	15	23	44.5	2730	2702	2646	976	CP
7/22/2011	16	25.2	44.4	2977	2944	2944	1306	CP

V50 SUMMARY

Number of Shots in Calculation: 4
High Partials: 2245, 2243 ft/s
Low Completes: 2198, 2200 ft/s
Velocity Span Criteria: 60 ft/s
Span Criteria Met? Yes
V_{50}: 2222 ft/s
Range of Results: 45 ft/s
Zone of Mixed Results: 45 ft/s

REMARKS

Zone of Mixed Results

Shot 8-9 did not record residual velocity

Shot 10 Penetrated the witness plate but did not have sufficient residual velocity to be recorded.

Panel Weights:
#1: 5.97 lbs.
#2: 5.98 lbs.
#3: 5.97 lbs.
#4: 5.94 lbs.

TEST PANEL 20110008

Manufacturer: Sioux Manufacturing Corporation
Test Panel Description: Advantex E-Glass with SC-1008 Phenolic Resin
Width (in): 12 | Plies/Laminates: 18
Height (in): 12 | Weight (lbs): 3.84
Thickness (in): 0.339 | Areal Density (lbs./ft²): 3.84

SET-UP
Relative Humidity (%): -
Temperature (°F): 73
Weapon System: Universal Receiver
Barrel: 7.62 x 51mm
Range to Target (ft): 20
Obliquity (°): 0
Witness Panel: 0.020 in 2024-T3
Target to Witness Panel (in): 6
Velocity Screens: Ohler Model 57
Screen Spacing(s) (ft): 5,5,3
Instrumentation Velocity Distance (ft): 7.5,5
Residual Velocity Distance (ft): 3

AMMUNITION
Projectile: 0.30 Cal 120° Conical FSP
Projectile Weight (grains): 44
Powder: IMR 4227 (wt. in grains)

APPLICABLE STANDARDS/PROCEDURES
(1): MIL-STD-662F
(2):
(3):

VELOCITY DATA (ft/s)

Date	Shot	Powder wt.	FSP wt.	V1	V2	Vs	Vr	Result
8/2/2011	1	12.8	44.6	1468	1452	1426	0	PP
8/2/2011	2	13.5	44.6	1566	1552	1524	0	CP
8/2/2011	3	13.3	44.5	1442	1433	1415	0	PP
8/2/2011	4	13.6	44.3	1549	1539	1519	0	PP
8/2/2011	5	14.1	44.4	1567	1552	1522	0	PP
8/2/2011	6	14.3	44.3	1630	1619	1597	0	CP
8/2/2011	7	14.1	44.4	1691	1675	1643	478	CP
8/2/2011	8	14.1	44.4	1588	1577	1555	0	PP
8/2/2011	9	14.2	44.4	1646	1635	1613	0	CP
8/2/2011	10	14.1	44.4	1590	1576	1548	0	PP
8/2/2011	11	16.3	44.5	1977	1954	1908	938	CP
8/2/2011	12	18.2	44.6	2080	2058	2014	1088	CP
8/2/2011	13	19.2	44.4	2170	2146	2098	1211	CP
8/2/2011	14	21	44.3	2462	2436	2436	1531	CP

V50 SUMMARY
Number of Shots in Calculation: 6
High Partials: 1555, 1548, 1522 ft/s
Low Completes: 1524, 1597, 1613 ft/s
Velocity Span Criteria: 90 ft/s
Span Criteria Met? Yes
V_{50}: 1556 ft/s
Range of Results: 91 ft/s
Zone of Mixed Results: 31 ft/s

REMARKS
Zone of Mixed Results

Shot 2 Penetrated the witness plate but did not have sufficient residual velocity to be recorded.

Shot 6 Penetrated the witness plate but did not have sufficient residual velocity to be recorded.

Shot 9 Penetrated the witness plate but did not have sufficient residual velocity to be recorded.

Velocity span = 91 which exceeds 90 fps criteria.

Panel Weights:
#1: 3.82 lbs.
#2: 3.81 lbs.
#3: 3.81 lbs.

TEST PANEL 20110009

Manufacturer: Sioux Manufacturing Corporation
Test Panel Description: Advantex E-Glass with SC-1008 Phenolic Resin

Width (in): 12	Plies/Laminates: 8
Height (in): 12	Weight (lbs): 1.71
Thickness (in): 0.165	Areal Density (lbs./ft²): 1.71

SET-UP

Relative Humidity (%): -	Witness Panel: 0.020 in 2024-T3
Temperature (°F): 73	Target to Witness Panel (in): 6
Weapon System: Universal Receiver	Velocity Screens: Ohler Model 57
Barrel: 7.62 x 51mm	Screen Spacing(s) (ft): 5,5,3
Range to Target (ft): 20	Instrumentation Velocity Distance (ft): 7.5,5
Obliquity (°): 0	Residual Velocity Distance (ft): 3

AMMUNITION	APPLICABLE STANDARDS/PROCEDURES
Projectile: 0.30 Cal 120° Conical FSP	(1): MIL-STD-662F
Projectile Weight (grains): 44	(2):
Powder: IMR 4227 (wt. in grains)	(3):

VELOCITY DATA
(ft/s)

Date	Shot	Powder wt.	FSP wt.	V1	V2	Vs	Vr	Result
8/3/2011	1	7.8	44.5	1333	1322	1300	788	CP
8/3/2011	2	4.8	44.5	868	862	850	0	PP
8/3/2011	3	5.3	44.4	986	978	962	0	PP
8/3/2011	4	5.4	44.5	1041	1033	1017	290	CP
8/3/2011	5	5.3	44.5	1028	1020	1004	0	CP
8/3/2011	6	5.1	44.5	913	907	895	0	PP
8/3/2011	7	5.2	44.3	892	885	871	0	PP
8/3/2011	8	5.2	44.5	956	949	935	0	PP
8/11/2011	9	5.3	44.4	845	839	827	0	PP
8/11/2011	10	5.5	44.3	836	830	818	0	PP
8/11/2011	11	6.3	44.5	967	960	946	0	PP
8/11/2011	12	6.5	44.3	1293	1288	1278	746	CP
8/11/2011	13	6.4	44.2	1000	993	979	0	PP
8/11/2011	14	7.8	44.4	1033	1024	1006	266	CP
8/11/2011	15	9.2	44.5	996	989	975	208	CP
8/11/2011	16	11.2	44.2	1189	1179	1159	589	CP
8/11/2011	17	15.8	44.2	1824	1824	1786	1427	CP
8/11/2011	18	13.2	44.3	1419	1412	1398	932	CP
8/11/2011	19	14.4	44.2	1685	1685	1653	1248	CP
8/11/2011	20	13.6	44.4	1554	1544	1524	1087	CP

V50 SUMMARY	REMARKS
Number of Shots in Calculation: 4	Shot 6 Penetrated the witness plate but did not have sufficient residual velocity to be recorded.
High Partials: 979, 962 ft/s	
Low Completes: 1004, 1017 ft/s	
Velocity Span Criteria: 60 ft/s	Panel Weights:
Span Criteria Met? Yes	#1: 1.73 lbs.
V_{50} : 991 ft/s	#2: 1.71 lbs.
Range of Results: 55 ft/s	#3: 1.72 lbs.
Zone of Mixed Results: -	#4: 1.71 lbs.
	#5: 1.72 lbs.

TEST PANEL 20110010

Manufacturer: Sioux Manufacturing Corporation
Test Panel Description: Advantex E-Glass with SC-1008 Phenolic Resin
Width (in): 12 — Plies/Laminates: 28
Height (in): 12 — Weight (lbs): 5.97
Thickness (in): 0.339 — Areal Density (lbs./ft^2): 5.97

SET-UP

Relative Humidity (%): -
Temperature (°F): 73
Weapon System: Universal Receiver
Barrel: 7.62 x 51mm
Range to Target (ft): 20
Obliquity (°): 0

Witness Panel: 0.020 in 2024-T3
Target to Witness Panel (in): 6
Velocity Screens: Ohler Model 57
Screen Spacing(s) (ft): 5,5,3
Instrumentation Velocity Distance (ft): 7.5,5
Residual Velocity Distance (ft): 3

AMMUNITION

Projectile: 0.30 Cal RCC FSP
Projectile Weight (grains): 44
Powder: IMR 4227 (wt. in grains)

APPLICABLE STANDARDS/PROCEDURES

(1): MIL-STD-662F
(2):
(3):

VELOCITY DATA (ft/s)

Date	Shot	Powder wt.	FSP wt.	V1	V2	Vs	Vr	Result
8/15/2011	1	23.5	44.4	2799	2765	2697	0	PP
8/15/2011	2	24.5	44.5	2955	2921	2853	840	CP
8/15/2011	3	24.0	44.5	2896	2862	2794	690	CP
8/15/2011	4	23.7	44.5	2826	2792	2724	0	PP
8/15/2011	5	23.8	44.4	2814	2782	2718	0	CP
8/15/2011	6	23.9	44.5	2818	2785	2719	369	CP
8/15/2011	7	25.5	44.5	2966	2931	2861	362	CP
8/15/2011	8	27.5	44.5	3104	3067	2993	907	CP
8/15/2011	9	31.0	44.5	3468	3425	3339	1338	CP
8/15/2011	10	29.6	44.4	3335	3294	3212	1339	CP

V50 SUMMARY

Number of Shots in Calculation: 4
High Partials: 2724, 2697 ft/s
Low Completes: 2718, 2719 ft/s
Velocity Span Criteria: 60 ft/s
Span Criteria Met? Yes
V_{50}: 2715 ft/s
Range of Results: 22 ft/s
Zone of Mixed Results: 6 ft/s

REMARKS

Zone of Mixed Results

Shot 5 did not record residual velocity

Panel Weights:
#1: 5.96 lbs.
#2: 5.98 lbs.

TEST PANEL 20110017

Manufacturer: Sioux Manufacturing Corporation
Test Panel Description: Advantex E-Glass with SC-1008 Phenolic Resin
Width (in): 12 | Plies/Laminates: 18
Height (in): 12 | Weight (lbs): 3.84
Thickness (in): 0.339 | Areal Density (lbs./ft²): 3.84

SET-UP
Relative Humidity (%): -
Temperature (°F): 73
Weapon System: Universal Receiver
Barrel: 7.62 x 51mm
Range to Target (ft): 20
Obliquity (°): 0
Witness Panel: 0.020 in 2024-T3
Target to Witness Panel (in): 6
Velocity Screens: Ohler Model 57
Screen Spacing(s) (ft): 5,5,3
Instrumentation Velocity Distance (ft): 7.5,5
Residual Velocity Distance (ft): 3

AMMUNITION
Projectile: 0.30 Cal RCC FSP
Projectile Weight (grains): 44
Powder: IMR 4227 (wt. in grains)

APPLICABLE STANDARDS/PROCEDURES
(1): MIL-STD-662F
(2):
(3):

VELOCITY DATA (ft/s)

Date	Shot	Powder wt.	FSP wt.	V1	V2	Vs	Vr	Result
8/25/2011	1	15.5	44.4	1903	1883	1843	404	CP
8/25/2011	2	14..5	44.5	1757	1739	1703	0	CP
8/25/2011	3	15.1	44.5	1811	1791	1751	0	PP
8/25/2011	4	15.5	44.5	1876	1856	1816	NR	CP
8/25/2011	5	15.2	44.3	1790	1772	1736	0	PP
8/25/2011	6	15.5	44.5	1824	1806	1770	0	CP
8/25/2011	7	15.6	44.5	1828	1809	1771	NR	CP
8/25/2011	8	15.8	44.5	1901	1880	1838	295	CP
8/25/2011	9	15.6	44.5	1867	1848	1810	587	CP
8/25/2011	10	17.0	44.5	2035	2013	1969	776	CP
8/25/2011	11	18.5	44.5	2218	2190	2134	950	CP
8/25/2011	12	20.0	44.5	2328	2306	2262	1117	CP
8/25/2011	13	21.5	44.2	2611	2585	2533	1476	CP
8/25/2011	14	21.5	44.5	2544	2519	2409	1396	CP

V50 SUMMARY
Number of Shots in Calculation: 4
High Partials: 1770, 1751 ft/s
Low Completes: 1771, 1810 ft/s
Velocity Span Criteria: 60 ft/s
Span Criteria Met? Yes
V_{50}: 1776 ft/s
Range of Results: 59 ft/s
Zone of Mixed Results: - ft/s

REMARKS
Shot 13 questionable shot location

Panel Weights:
#1: 3.85 lbs.
#2: 3.83 lbs.
#3: 3.82 lbs.

TEST PANEL 20110019

Manufacturer: Sioux Manufacturing Corporation
Test Panel Description: Advantex E-Glass with SC-1008 Phenolic Resin
Width (in): 12 | Plies/Laminates: 8
Height (in): 12 | Weight (lbs): 1.71
Thickness (in): 0.165 | Areal Density (lbs./ft^2): 1.71

SET-UP
Relative Humidity (%): - | Witness Panel: 0.020 in 2024-T3
Temperature (°F): 73 | Target to Witness Panel (in): 6
Weapon System: Universal Receiver | Velocity Screens: Ohler Model 57
Barrel: 7.62 x 51mm | Screen Spacing(s) (ft): 5,5,3
Range to Target (ft): 20 | Instrumentation Velocity Distance (ft): 7.5,5
Obliquity (°): 0 | Residual Velocity Distance (ft): 3

AMMUNITION
Projectile: 0.30 RCC FSP
Projectile Weight (grains): 44
Powder: IMR 4227 (wt. in grains)

APPLICABLE STANDARDS/PROCEDURES
(1): MIL-STD-662F
(2):
(3):

VELOCITY DATA
(ft/s)

Date	Shot	Powder wt.	FSP wt.	V1	V2	Vs	Vr	Result
9/6/2011	1	9.7	44.4	969	960	942	NR	CP
9/6/2011	2	9.0	44.5	948	840	924	NR	CP
9/6/2011	3	8.2	44.5	971	962	944	216	CP
9/6/2011	4	8.6	44.5	970	961	943	318	CP
9/6/2011	5	8.0	44.5	1062	1052	1032	318	CP
9/6/2011	6	5.0	44.2	918	911	897	0	PP
9/6/2011	7	5.3	44.3	891	884	870	0	PP
9/6/2011	8	5.0	44.5	855	848	834	0	PP
9/6/2011	9	5.5	44.5	975	966	948	353	CP
9/6/2011	10	5.3	44.4	1088	1066	1022	501	CP
9/6/2011	11	5.3	44.4	770	764	752	0	PP
9/6/2011	12	5.0	44.4	1048	1039	1021	173	CP
9/6/2011	13	5.0	44.5	1031	1022	1004	NR	CP
9/6/2011	14	4.7	44.3	961	953	937	318	CP
9/6/2011	15	4.6	44.5	874	869	859	0	PP
9/6/2011	16	4.9	44.5	862	856	844	0	PP
9/6/2011	17	10.1	44.5	1070	1060	1040	446	CP
9/6/2011	18	11.1	44.5	1301	1289	1265	756	CP
9/6/2011	19	12.1	44.5	1478	1469	1451	930	CP
9/6/2011	20	13.1	44.3	1601	1590	1568	1046	CP

V50 SUMMARY
Number of Shots in Calculation: 6
High Partials: 897, 870, 859 ft/s
Low Completes: 924, 937, 942 ft/s
Velocity Span Criteria: 90 ft/s
Span Criteria Met? Yes
V_{50}: 905 ft/s
Range of Results: 83 ft/s
Zone of Mixed Results: -

REMARKS
Shot 13 did not record residual velocity

Panel Weights:
#1: 1.73 lb
#2: 1.74 lb
#3: 1.73 lb
#4: 1.72 lb

TEST PANEL 20110023

Manufacturer: Sioux Manufacturing Corporation
Test Panel Description: Advantex E-Glass with SC-1008 Phenolic Resin

Width (in): 12 | Plies/Laminates: 28
Height (in): 12 | Weight (lbs): 6.01
Thickness (in): 0.54 | Areal Density (lbs./ft²): 6.01

SET-UP

Relative Humidity (%): - | Witness Panel: 0.020 in 2024-T3
Temperature (°F): 73 | Target to Witness Panel (in): 6
Weapon System: Universal Receiver | Velocity Screens: Ohler Model 57
Barrel: 7.62 x 51mm | Screen Spacing(s) (ft): 5,5,3
Range to Target (ft): 20 | Instrumentation Velocity Distance (ft): 7.5,5
Obliquity (°): 0 | Residual Velocity Distance (ft): 3

AMMUNITION

Projectile: 0.30 Cal Hemispherical Nose FSP
Projectile Weight (grains): 44
Powder: IMR 4227 (wt. in grains)

APPLICABLE STANDARDS/PROCEDURES

(1): MIL-STD-662F
(2):
(3):

VELOCITY DATA (ft/s)

Date	Shot	Powder wt.	FSP wt.	V1	V2	Vs	Vr	Result
9/6/2011	1	22.6	44.4	2819	2799	2759	1730	CP
9/6/2011	2	21.9	44.4	2734	2714	2674	1648	CP
9/6/2011	3	21.0	44.4	2574	2556	2520	1396	CP
9/6/2011	4	20.1	44.2	2588	2570	2534	1404	CP
9/6/2011	5	19.9	44.2	2536	2518	2482	1394	CP
9/6/2011	6	17.9	44.4	2249	2233	2201	1013	CP
9/6/2011	7	15.4	43.9	1948	1934	1906	452	CP
9/6/2011	8	15.0	44.3	1980	1965	1935	642	CP
9/6/2011	9	14.8	44.4	1906	1892	1864	558	CP
9/6/2011	10	14.3	44.5	1773	1760	1734	0	PP
9/6/2011	11	14.5	44.4	1855	1843	1819	403	CP
9/6/2011	12	14.4	44.5	1816	1803	1777	274	CP
9/6/2011	13	14.4	44.2	1810	1797	1771	253	CP
9/6/2011	14	14.2	44.4	1783	1771	1747	175	CP
9/6/2011	15	14.1	43.6	1801	1788	1762	0	PP

V50 SUMMARY

Number of Shots in Calculation: 4
High Partials: 1762, 1734 ft/s
Low Completes: 1747, 1771 ft/s
Velocity Span Criteria: 60 ft/s
Span Criteria Met? Yes
V_{50}: 1754 ft/s
Range of Results: 37 ft/s
Zone of Mixed Results: 15 ft/s

REMARKS

Zone of Mixed Results

Panel Weights
#1: 5.952 lb.
#2: 6.002 lb.
#3: 5.912 lb.

TEST PANEL 20110024

Manufacturer: Sioux Manufacturing Corporation
Test Panel Description: Advantex E-Glass with SC-1008 Phenolic Resin
Width (in): 12 — Plies/Laminates: 18
Height (in): 12 — Weight (lbs): 3.84
Thickness (in): 0.339 — Areal Density (lbs./ft²): 3.84

SET-UP

Relative Humidity (%): - — Witness Panel: 0.020 in 2024-T3
Temperature (°F): 73 — Target to Witness Panel (in): 6
Weapon System: Universal Receiver — Velocity Screens: Ohler Model 57
Barrel: 7.62 x 51mm — Screen Spacing(s) (ft): 5,5,3
Range to Target (ft): 20 — Instrumentation Velocity Distance (ft): 7.5,5
Obliquity (°): 0 — Residual Velocity Distance (ft): 3

AMMUNITION

Projectile: 0.30 Cal Hemispherical Nose FSP
Projectile Weight (grains): 44
Powder: IMR 4227 (wt. in grains)

APPLICABLE STANDARDS/PROCEDURES

(1): MIL-STD-662F
(2):
(3):

VELOCITY DATA (ft/s)

Date	Shot	Powder wt.	FSP wt.	V1	V2	Vs	Vr	Result
9/7/2011	1	10.5	44.4	1204	1206	1210	0	PP
9/7/2011	2	11.2	44.3	1391	1381	1361	381	CP
9/7/2011	3	10.9	43.8	1362	1354	1338	209	CP
9/7/2011	4	10.6	44.2	1389	1350	1272	NR	-
9/7/2011	5	10.5	44.2	1368	1339	1281	0	PP
9/7/2011	6	10.5	44.5	1355	1352	1346	278	CP
9/7/2011	7	10.3	44.5	1314	1312	1308	0	PP
9/7/2011	8	10.3	44.5	1275	1268	1254	0	PP
9/7/2011	9	10.4	44.4	1325	1317	1301	127	CP
9/7/2011	10	11.9	44.5	1635	1622	1596	NR	CP
9/7/2011	11	13.1	44.5	1638	1600	1524	960	CP
9/7/2011	12	14.3	44.4	1808	1763	1673	NR	CP
9/7/2011	13	15.6	44.4	1929	1915	1887	1165	CP

V50 SUMMARY

Number of Shots in Calculation: 4
High Partials: 1308, 1281 ft/s
Low Completes: 1301, 1338 ft/s
Velocity Span Criteria: 60 ft/s
Span Criteria Met? Yes
V_{50}: 1307 ft/s
Range of Results: 57 ft/s
Zone of Mixed Results: 7 ft/s

REMARKS

Zone of Mixed Results

Shot 4 Bad Hit, FSP at angle during impact

Panel Weights
#1: 3.84 lb.
#2: 3.83 lb.

TEST PANEL 20110025

Manufacturer: Sioux Manufacturing Corporation
Test Panel Description: Advantex E-Glass with SC-1008 Phenolic Resin
Width (in): 12 — Plies/Laminates: 8
Height (in): 12 — Weight (lbs): 1.71
Thickness (in): 0.165 — Areal Density (lbs./ft²): 1.71

SET-UP
Relative Humidity (%): -
Temperature (°F): 73
Weapon System: Universal Receiver
Barrel: 7.62 x 51mm
Range to Target (ft): 20
Obliquity (°): 0
Witness Panel: 0.020 in 2024-T3
Target to Witness Panel (in): 6
Velocity Screens: Ohler Model 57
Screen Spacing(s) (ft): 5,5,3
Instrumentation Velocity Distance (ft): 7.5,5
Residual Velocity Distance (ft): 3

AMMUNITION
Projectile: 0.30 Hemispherical Nose FSP
Projectile Weight (grains): 44
Powder: IMR 4227 (wt. in grains)

APPLICABLE STANDARDS/PROCEDURES
(1): MIL-STD-662F
(2):
(3):

VELOCITY DATA
(ft/s)

Date	Shot	Powder wt.	FSP wt.	V1	V2	Vs	Vr	Result
9/7/2011	1	4.8	44.4	1021	1019	1015	0	PP
9/7/2011	2	4.5	44.1	1073	1070	1064	381	CP
9/7/2011	3	3.8	44.5	1009	1006	1000	209	CP
9/7/2011	4	4.5	44.5	734	733	731	0	PP
9/7/2011	5	4.5	44.3	887	886	884	234	CP
9/7/2011	6	4.4	44.3	846	843	837	0	PP
9/7/2011	7	4.4	44.3	965	963	959	457	CP
9/7/2011	8	4.3	44.5	945	943	939	442	CP
9/7/2011	9	4.1	44.4	834	832	828	87	CP
9/7/2011	10	4.1	44.3	994	992	988	498	CP
9/7/2011	11	4.0	44.3	698	687	665	0	PP
9/7/2011	12	4.1	44.3	707	706	704	0	PP
9/7/2011	13	4.2	44.4	820	818	814	0	PP
9/7/2011	14	4.2	43.9	694	692	688	0	PP
9/7/2011	15	4.3	44.2	832	830	826	0	PP
9/7/2011	16	4.3	44.4	787	779	763	0	PP
9/7/2011	17	4.3	44.4	825	823	819	0	PP
9/7/2011	18	4.4	44.1	755	754	752	0	PP
9/7/2011	19	6.7	44.3	1346	1343	1337	976	CP
9/7/2011	20	7.3	44.3	1305	1297	1281	928	CP

V50 SUMMARY
Number of Shots in Calculation: 6
High Partials: 819, 763, 752 ft/s
Low Completes: 814, 826, 828 ft/s
Velocity Span Criteria: 90 ft/s
Span Criteria Met? Yes
V_{50}: 800 ft/s
Range of Results: 76 ft/s
Zone of Mixed Results: 3 ft/s

REMARKS
Zone of Mixed Results

Shot #2: Switched to IMR3031
Shot #8: Projectile Yaw

Panel Weights
#1: 1.718 lb.
#2: 1.728 lb.
#3: 1.718 lb.
#4: 1.738 lb.

TEST PANEL 20110026

Manufacturer: Sioux Manufacturing Corporation
Test Panel Description: Advantex E-Glass with SC-1008 Phenolic Resin
Width (in): 12 | Plies/Laminates: 28
Height (in): 12 | Weight (lbs): 6.01
Thickness (in): 0.54 | Areal Density (lbs./ft^2): 6.01

SET-UP

Relative Humidity (%): -
Temperature (°F): 73
Weapon System: Universal Receiver
Barrel: 7.62 x 51mm
Range to Target (ft): 20
Obliquity (°): 0
Witness Panel: 0.020 in 2024-T3
Target to Witness Panel (in): 6
Velocity Screens: Ohler Model 57
Screen Spacing(s) (ft): 5,5,3
Instrumentation Velocity Distance (ft): 7.5,5
Residual Velocity Distance (ft): 3

AMMUNITION

Projectile: 0.30 Cal Modified FSP
Projectile Weight (grains): 44
Powder: IMR 4227 (wt. in grains)

APPLICABLE STANDARDS/PROCEDURES

(1): MIL-STD-662F
(2):
(3):

VELOCITY DATA (ft/s)

Date	Shot	Powder wt.	FSP wt.	V1	V2	Vs	Vr	Result
9/8/2011	1	15.7	44.3	2065	2046	2008	0	PP
9/8/2011	2	16.3	44.4	2113	2094	2056	0	PP
9/8/2011	3	16.4	44.3	2005	1985	1945	0	PP
9/8/2011	4	16.5	44.3	2124	2102	2058	0	PP
9/8/2011	5	16.6	44.5	1987	1969	1933	0	PP
9/8/2011	6	16.6	44.3	2181	2159	2115	0	PP
9/8/2011	7	16.7	44.2	2189	2168	2126	0	PP
9/8/2011	8	16.8	44.3	2156	2138	2102	0	PP
9/8/2011	9	17.0	44.0	2107	2086	2044	0	PP
9/8/2011	10	17.5	44.3	2187	2167	2127	0	PP
9/8/2011	11	18.2	44.1	2344	2321	2275	624	CP
9/8/2011	12	18.2	43.9	2301	2278	2232	207	CP
9/8/2011	13	18.0	44.3	2246	2225	2183	0	PP
9/8/2011	14	18.1	44	2293	2271	227	0	PP
9/8/2011	15	18.1	44.1	2264	2244	2204	0	PP
9/8/2011	16	18.2	43.9	2332	2309	2263	458	CP
9/8/2011	17	19.3	44.4	2388	2364	2316	535	CP
9/8/2011	18	20.5	44.4	2624	2599	2549	750	CP
9/8/2011	19	21.7	44.2	2742	2716	2664	1045	CP
9/8/2011	20	22.9	44.2	2787	2760	2706	1102	CP

V50 SUMMARY

Number of Shots in Calculation: 4
High Partials: 2227, 2204 ft/s
Low Completes: 2232, 2263 ft/s
Velocity Span Criteria: 60 ft/s
Span Criteria Met? Yes
V_{50}: 2232 ft/s
Range of Results: 59 ft/s
Zone of Mixed Results: -

REMARKS

Panel Weights
#1: 5.962 lb
#2: 5.89 lb
#3: 5.94 lb
#4: 5.974 lb
#5: 5.954 lb

TEST PANEL 20110027

Manufacturer: Sioux Manufacturing Corporation
Test Panel Description: Advantex E-Glass with SC-1008 Phenolic Resin

Width (in): 12 — Plies/Laminates: 18
Height (in): 12 — Weight (lbs): 3.84
Thickness (in): 0.339 — Areal Density (lbs./ft²): 3.84

SET-UP

Relative Humidity (%): -
Temperature (°F): 73
Weapon System: Universal Receiver
Barrel: 7.62 x 51mm
Range to Target (ft): 20
Obliquity (°): 0

Witness Panel: 0.020 in 2024-T3
Target to Witness Panel (in): 6
Velocity Screens: Ohler Model 57
Screen Spacing(s) (ft): 5,5,3
Instrumentation Velocity Distance (ft): 7.5,5
Residual Velocity Distance (ft): 3

AMMUNITION

Projectile: 0.30 Cal Modified FSP
Projectile Weight (grains): 44
Powder: IMR 4227 (wt. in grains)

APPLICABLE STANDARDS/PROCEDURES

(1): MIL-STD-662F
(2):
(3):

VELOCITY DATA
(ft/s)

Date	Shot	Powder wt.	FSP wt.	V1	V2	Vs	Vr	Result
9/8/2011	1	13.1	44.5	1677	1665	1641	563	CP
9/8/2011	2	12.7	44.3	1643	1630	1604	333	CP
9/8/2011	3	12.3	44.3	1537	1528	1510	275	PP
9/8/2011	4	12.0	44.4	1520	1510	1490	NR	CP
9/8/2011	5	11.8	44.5	1514	1505	1487	NR	CP
9/8/2011	6	11.6	44.4	1472	1463	1445	NR	CP
9/8/2011	7	11.3	44.4	1410	1402	1386	0	PP
9/8/2011	8	11.3	44.2	1391	1383	1367	0	PP
9/8/2011	9	11.5	43.9	1503	1494	1476	0	CP
9/8/2011	10	11.4	44.4	1396	1388	1372	0	PP
9/8/2011	11	11.5	44.1	1394	1387	1373	0	PP
9/8/2011	12	11.8	44.2	1463	1455	1439	0	PP
9/8/2011	13	11.7	44.3	1487	1478	1460	0	CP
9/8/2011	14	11.6	44.2	1478	1469	1451	0	CP
9/8/2011	15	11.5	44.1	1475	1466	1448	0	PP
9/8/2011	16	12.9	44.1	1666	1655	1633	505	CP
9/8/2011	17	14.1	44.2	1790	1771	1733	598	CP
9/8/2011	18	15.3	44.2	1905	1885	1845	842	CP
9/8/2011	19	16.5	44.4	2082	2061	2019	1105	CP

V50 SUMMARY

Number of Shots in Calculation: 4
High Partials: 1448, 1439 ft/s
Low Completes: 1445, 1451 ft/s
Velocity Span Criteria: 60 ft/s
Span Criteria Met? Yes
V_{50}: 1446 ft/s
Range of Results: 12 ft/s
Zone of Mixed Results: 3 ft/s

REMARKS

Zone of Mixed Results

Shot 4-6, 9, 13: did not record residual velocity

Panel Weights
#1: 3.816 lb.
#2: 3.86 lb.
#3: 3.81 lb.
#4: 3.81 lb.

TEST PANEL 20110028

Manufacturer: Sioux Manufacturing Corporation
Test Panel Description: Advantex E-Glass with SC-1008 Phenolic Resin
Width (in): 12 | Plies/Laminates: 8
Height (in): 12 | Weight (lbs): 1.71
Thickness (in): 0.165 | Areal Density (lbs./ft²): 1.71

SET-UP
Relative Humidity (%): - | Witness Panel: 0.020 in 2024-T3
Temperature (°F): 73 | Target to Witness Panel (in): 6
Weapon System: Universal Receiver | Velocity Screens: Ohler Model 57
Barrel: 7.62 x 51mm | Screen Spacing(s) (ft): 5,5,3
Range to Target (ft): 20 | Instrumentation Velocity Distance (ft): 7.5,5
Obliquity (°): 0 | Residual Velocity Distance (ft): 3

AMMUNITION
Projectile: 0.30 Cal Modified FSP
Projectile Weight (grains): 44
Powder: IMR 4227 (wt. in grains)

APPLICABLE STANDARDS/PROCEDURES
(1): MIL-STD-662F
(2):
(3):

VELOCITY DATA
(ft/s)

Date	Shot	Powder wt.	FSP wt.	V1	V2	Vs	Vr	Result
9/9/2011	1	4.4	44.5	969	969	969	1005	CP
9/9/2011	2	4.2	44.0	1007	1001	989	868	CP
9/9/2011	3	4.3	44.1	353	352	350	546	CP
9/9/2011	4	4.2	43.8	891	886	876	738	CP
9/9/2011	5	6.0	44.4	670	667	661	0	PP
9/9/2011	6	6.4	44.2	893	887	875	490	CP
9/9/2011	7	6.2	44.2	960	954	942	423	CP
9/9/2011	8	6.1	44.3	1012	1006	994	0	PP
9/9/2011	9	5.6	44.3	628	625	619	0	PP
9/9/2011	10	5.9	44.2	1089	1081	1065	244	CP
9/9/2011	11	5.8	44.2	886	881	871	NR	CP
9/9/2011	12	5.6	44.1	789	785	777	113	CP
9/9/2011	13	5.7	44.1	909	899	879	227	CP
9/9/2011	14	5.6	44.3	1034	1027	1013	263	CP
9/9/2011	15	5.6	44.2	585	583	579	279	CP
9/9/2011	16	8.6	44.3	939	933	921	154	CP
9/9/2011	17	5.6	44.4	727	722	712	NR	CP
9/9/2011	18	8.4	44.2	727	721	709	0	PP
9/9/2011	19	5.9	44.2	846	841	831	0	PP
9/9/2011	20	11.0	44.1	1106	1096	1076	490	CP
9/9/2011	21	9.7	44	1164	1157	1143	NR	CP
9/9/2011	22	6.1	44.2	968	962	950	0	PP
9/9/2011	23	5.6	44.2	900	895	885	0	PP
9/9/2011	24	4.8	44.2	897	892	882	145	CP
9/9/2011	25	4.6	44.4	787	782	772	NR	CP
9/9/2011	26	7.9	44.2	907	901	889	616	CP
9/9/2011	27	11.9	44.3	1379	1372	1358	0	PP
9/9/2011	28	13.3	44.4	1587	1576	1554	635	CP

V50 SUMMARY
Number of Shots in Calculation: 6
High Partials: 703, 664, 660 ft/s
Low Completes: 698, 732, 737 ft/s
Velocity Span Criteria: 90 ft/s

Shot #5 Switched to IMR4350

Shot #21 Switched to IMR4227

Zone of Mixed Results.

Span Criteria Met? Yes V_{50} : 699 ft/s Range of Results: 77 ft/s Zone of Mixed Results: 5 ft/s	Panel Weights #1: 1.752 lb. #2: 1.718 lb. #3: 1.704 lb. #4: 1.718 lb.

TEST PANEL 20110043

Manufacturer: Sioux Manufacturing Corporation
Test Panel Description: Advantex E-Glass with SC-1008 Phenolic Resin
Width (in): 12 — Plies/Laminates: 28
Height (in): 12 — Weight (lbs): 6.01
Thickness (in): 0.54 — Areal Density (lbs./ft^2): 6.01

SET-UP
Relative Humidity (%): 74 — Witness Panel: 0.020 in 2024-T3
Temperature (°F): 48 — Target to Witness Panel (in): 6
Weapon System: Universal Receiver — Velocity Screens: Ohler Model 57
Barrel: 50 Cal Smooth Bore — Screen Spacing(s) (ft): 5
Range to Target (ft): 20 — Instrumentation Velocity Distance (ft): 7.5
Obliquity (°): 0 — Residual Velocity Distance (ft): N/A

AMMUNITION
Projectile: 0.30 Cal Cube FSP
Projectile Weight (grains): 44
Powder: IMR 4895 (wt. in grains)

APPLICABLE STANDARDS/PROCEDURES
(1): MIL-STD-662F
(2):
(3):

VELOCITY DATA
(ft/s)

Date	Shot	Powder wt.	FSP wt.	V1	V2	Vs	Vr	Result
9/26/2011	1	100.0				2543		PP
9/26/2011	2	110.0				2766		PP
9/26/2011	3	130.0				3266		CP
9/26/2011	4	120.0				3033		CP
9/26/2011	5	115.0				2874		CP
9/26/2011	6	112.0				2859		CP
9/26/2011	7	111.0				2809		CP
9/26/2011	8	110.0				2805		PP
9/26/2011	9	110.0				2755		PP
9/26/2011	10	110.5				2796		PP
9/26/2011	11	110.7				2766		PP
9/26/2011	12	111.0				2821		PP

V50 SUMMARY
Number of Shots in Calculation: 4
High Partials: 2821, 2805 ft/s
Low Completes: 2809, 2859 ft/s
Velocity Span Criteria: 60 ft/s
Span Criteria Met? Yes
V_{50}: 2824 ft/s
Range of Results: 54 ft/s
Zone of Mixed Results: 12 ft/s

REMARKS
Sabot Launched (no spin)

Zone of Mixed Results.

Panel Weights
#1 5.96 lb
#2 5.96 lb
#3 5.94 lb

AFRL #BB09015-17

TEST PANEL 20110044

Manufacturer: Sioux Manufacturing Corporation
Test Panel Description: Advantex E-Glass with SC-1008 Phenolic Resin
Width (in): 12 — Plies/Laminates: 28
Height (in): 12 — Weight (lbs): 6.01
Thickness (in): 0.339 — Areal Density (lbs./ft^2): 6.01

SET-UP

Relative Humidity (%): -
Temperature (°F): 73
Weapon System: Universal Receiver
Barrel: 50 Cal Smooth Bore
Range to Target (ft): 20
Obliquity (°): 0

Witness Panel: 0.020 in 2024-T3
Target to Witness Panel (in): 6
Velocity Screens: Ohler Model 57
Screen Spacing(s) (ft): 5,5,3
Instrumentation Velocity Distance (ft): 7.5,5
Residual Velocity Distance (ft): 3

AMMUNITION

Projectile: 0.30 Cal Parallelepiped FSP
Projectile Weight (grains): 44
Powder: IMR 4227 (wt. in grains)

APPLICABLE STANDARDS/PROCEDURES

(1): MIL-STD-662F
(2):
(3):

VELOCITY DATA (ft/s)

Date	Shot	Powder wt.	FSP wt.	V1	V2	Vs	Vr	Result
9/26/2011	1	105.0				2596		PP
9/26/2011	2	107.0				2769		CP
9/26/2011	3	106.0				2760		CP
9/26/2011	4	105.0				2638		CP
9/26/2011	5	105.0				2750		CP
9/26/2011	6	104.8				2693		CP
9/26/2011	7	104.5				2632		CP
9/26/2011	8	104.0				2678		CP
9/26/2011	9	104.0				2636		PP
9/26/2011	10	104.0				2699		PP
9/26/2011	11					2619		PP
9/26/2011	12					2716		PP

V50 SUMMARY

Number of Shots in Calculation: 6
High Partials: 2716, 2699, 2636 ft/s
Low Completes: 2632, 2638, 2678 ft/s
Velocity Span Criteria: 90 ft/s
Span Criteria Met? Yes
V_{50}: 2667 ft/s
Range of Results: 84 ft/s
Zone of Mixed Results: 84 ft/s

REMARKS

Sabot Launched (no spin)

Zone of Mixed Results.

Panel Weights
#1 5.96 lb
#2 5.92 lb
#3 5.98 lb

AFRL #BB09022-23,31

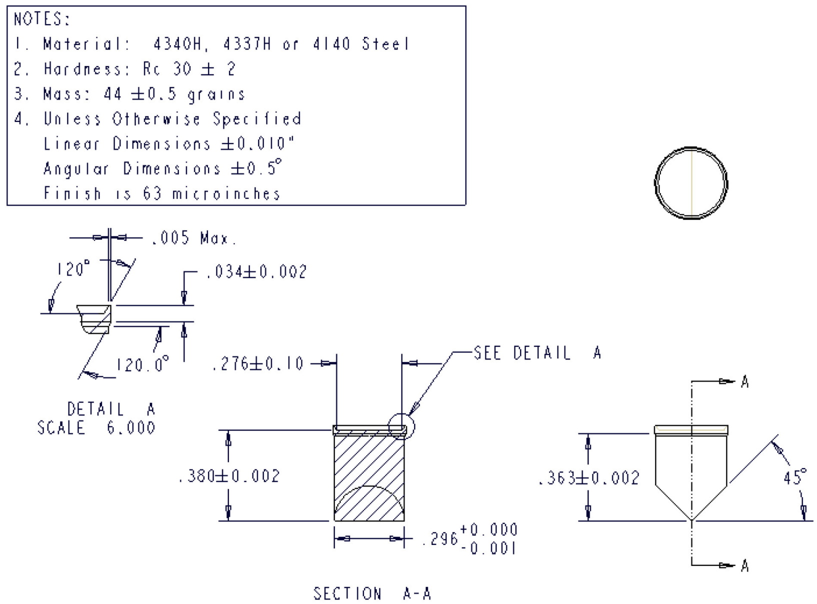

Figure A 1 Fragment-Simulating Projectile – Chisel (44 grain) with Gas Seal

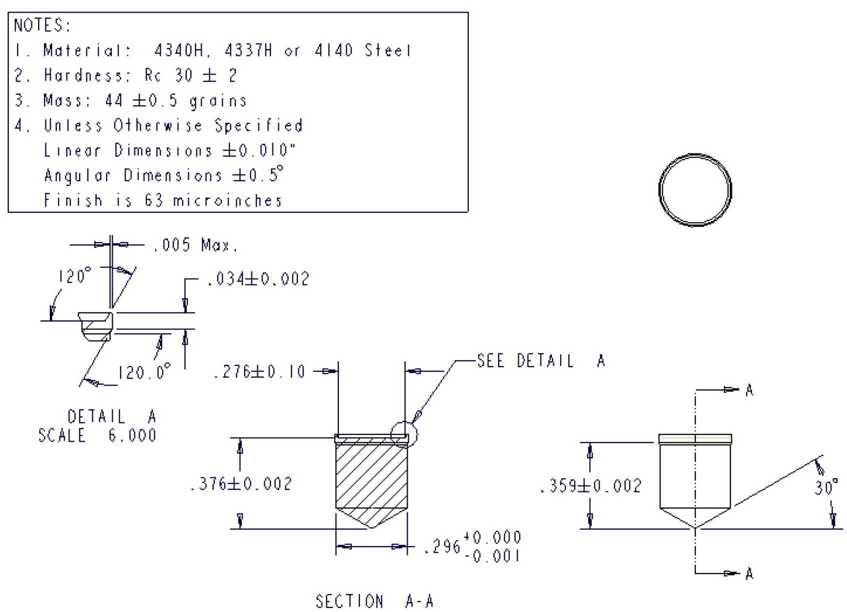

Figure A 2 Fragment-Simulating Projectile – 120 Degree Conical (44 grain) with Gas Seal

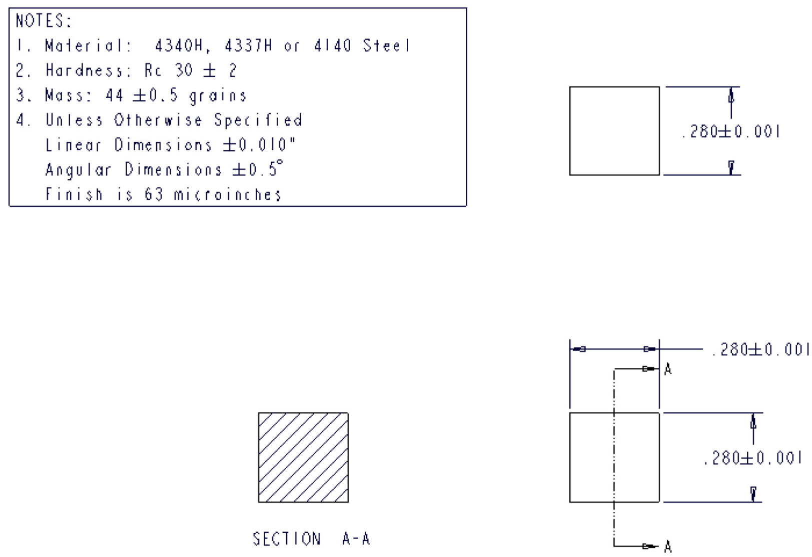

Figure A 3 Fragment-Simulating Projectile – Cube (44 grain) for Sabot

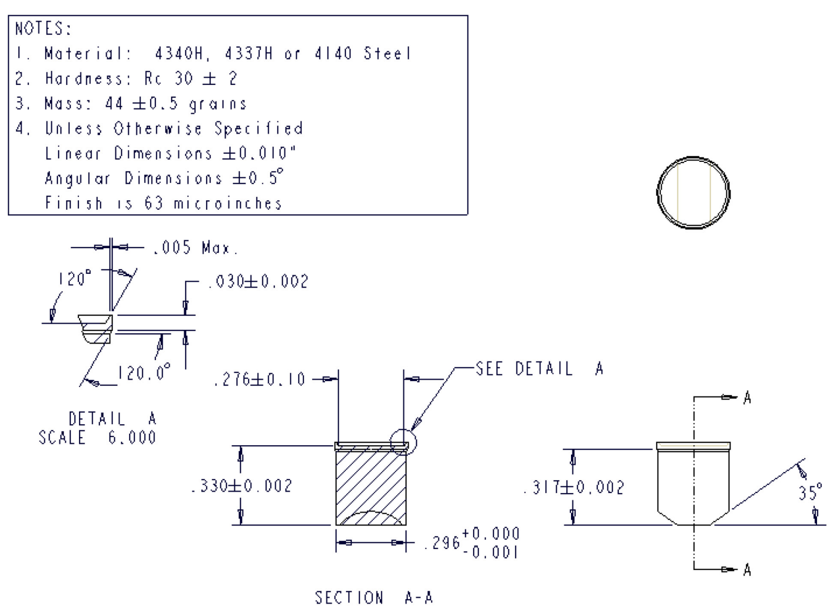

Figure A 4 Fragment-Simulating Projectile – 30 Cal (44 grain) with Gas Seal

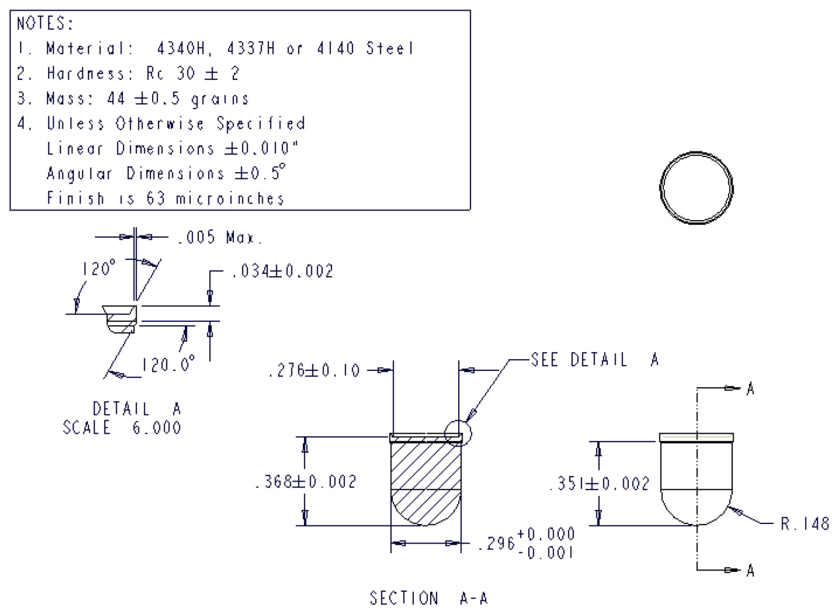

Figure A 5 Fragment-Simulating Projectile – Hemispherical (44 grain) with Gas Seal

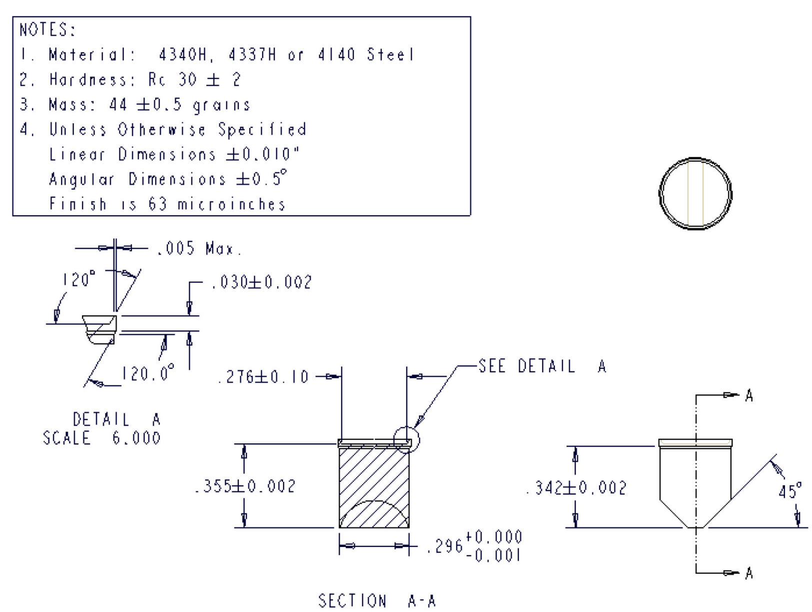

Figure A 6 Fragment-Simulating Projectile – Modified 30 Cal (44 grain) with Gas Seal

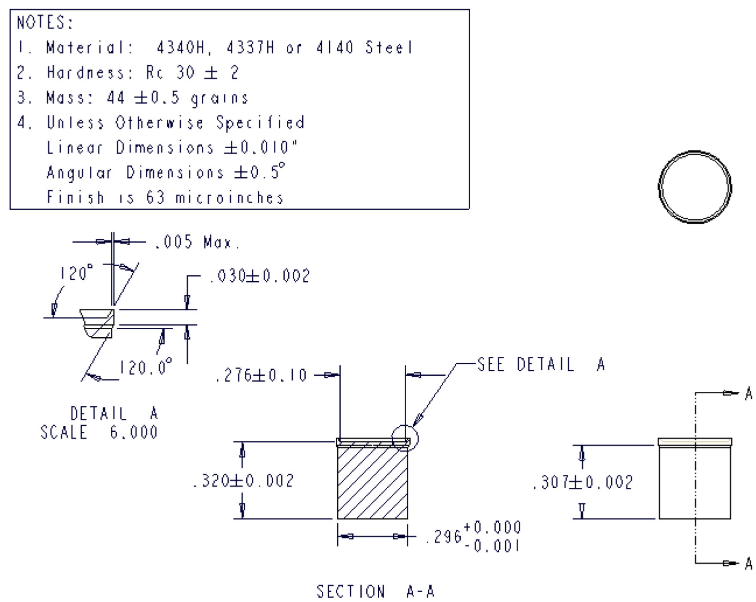

Figure A 7 Fragment-Simulating Projectile – RCC (44 grain) with Gas Seal

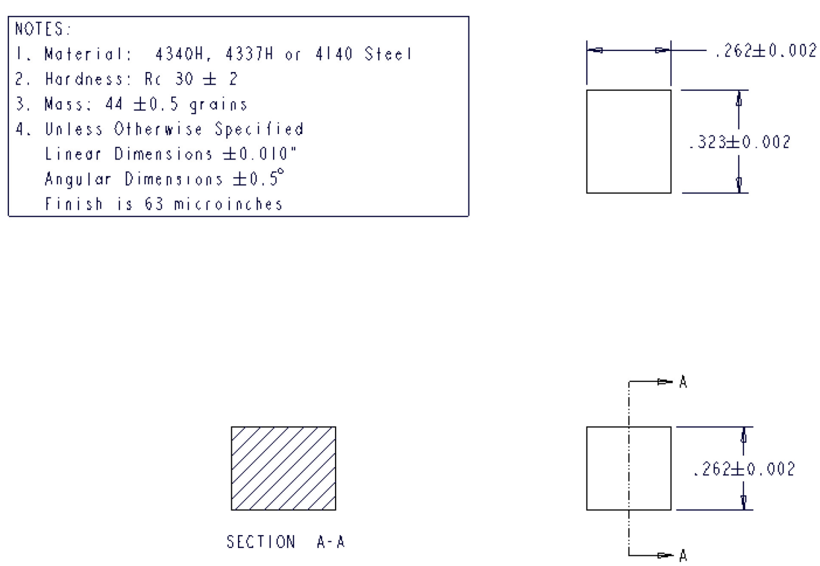

Figure A 8 Fragment-Simulating Projectile – Parallelepiped (44 grain) for Sabot

APPENDIX B – MATERIAL PROPERTY DATA I

Material Property Testing by

University of Dayton Research Institute

D6641/D6641M – 09

Standard Test Method

for

Compressive Properties of Polymer Matrix Composite Materials Using a Combined Loading Compression (CLC) Test Fixture

Data

Table B 1. Specimen Dimensions for Compression Tests

TEST COUPON NUMBER	*THICKNESS (in.)*			Avg Thick (in)	Width (in)			Avg Width (in)	Average X-sectional Area (in^2)	Length (in)	Thickness Variation (in)
	T(a)	*T(b)*	*T(c)*		W(1)	W(2)	W(3)				
110505M-004-C1	0.1496	0.1473	0.1412	0.1460	0.500	0.500	0.501	0.500	0.0736	5.501	0.0084
110505M-004-C2	0.1498	0.1442	0.1487	0.1476	0.500	0.500	0.500	0.500	0.0721	5.501	0.0056
110505M-004-C3	0.1500	0.1438	0.1461	0.1466	0.500	0.501	0.501	0.500	0.0720	5.500	0.0061
110505M-004-C4	0.1451	0.1464	0.1436	0.1450	0.501	0.500	0.500	0.500	0.0732	5.500	0.0028
110505M-004-C5	0.1474	0.1515	0.1498	0.1496	0.497	0.497	0.497	0.497	0.0753	5.501	0.0041
110505M-004-C6	0.1465	0.1461	0.1454	0.1460	0.500	0.500	0.500	0.500	0.0730	5.500	0.0011

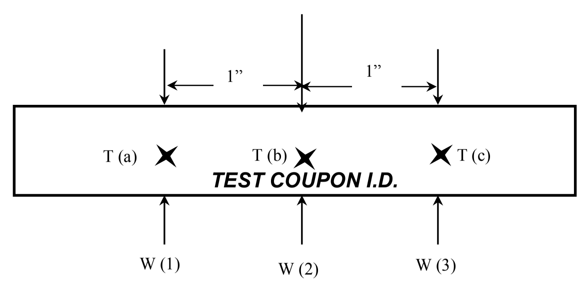

Figure B 1. Sketch of Test Specimens Associated with Table B 1

Table B 2. Summary of Tool Side Compression Data

Test Label	*Area (in²)*	*.Extension at Max Load (in)*	*Max Comp Load (lbf)*	*Comp. Load at =.001 (lbf)*	*Comp. Load at =.002 (lbf)*	*Ultimate Comp. Stress (ksi)*	*Gage Moduli Tool Side (Msi)*	*Comp. Strain at Max Load*
C1	0.0736	0.014	1416	307	678	19.238	5.030	0.093
C2	0.0721	0.009	1368	347	711	18.976	5.041	0.064
C3	0.0720	0.014	1419	400	749	19.714	4.850	0.095
C4	0.0732	0.012	1444	374	732	19.728	4.895	0.086
C5	0.0753	0.012	1280	363	701	17.002	4.859	0.084
Mean	0.0732	0.012	1386	358	714	18.932	4.859	0.084
Std Dev	0.00	0.00	64.95	34.38	27.77	1.13	0.23	0.012
Coeff of Var	1.83	14.35	4.69	9.60	3.89	5.94	4.69	14.350

Table B 3. Summary of Gage Side Compression Data

Test Label	*Area (in²)*	*.Extension at Max Load (in)*	*Max Comp Load (lbf)*	*Comp. Load at =.001 (lbf)*	*Comp. Load at =.002 (lbf)*	*Ultimate Comp. Stress (ksi)*	*Gage Moduli Tool Side (Msi)*	*Comp. Strain at Max Load*
C1	0.0736	0.014	1416	430	792	19.238	4.925	0.093
C2	0.0721	0.009	1368	316	636	18.976	4.427	0.064
C3	0.0720	0.014	1419	263	592	19.714	4.571	0.095
C4	0.0732	0.012	1444	363	707	19.728	4.703	0.086
C5	0.0753	0.012	1280	330	656	17.002	4.323	0.083
Mean	0.0732	0.012	1386	341	677	18.932	4.590	0.084
Std Dev	0.00	0.00	64.95	61.47	76.64	1.13	0.24	0.01
Coeff of Var	1.83	14.35	4.69	18.05	11.33	5.94	5.15	14.35

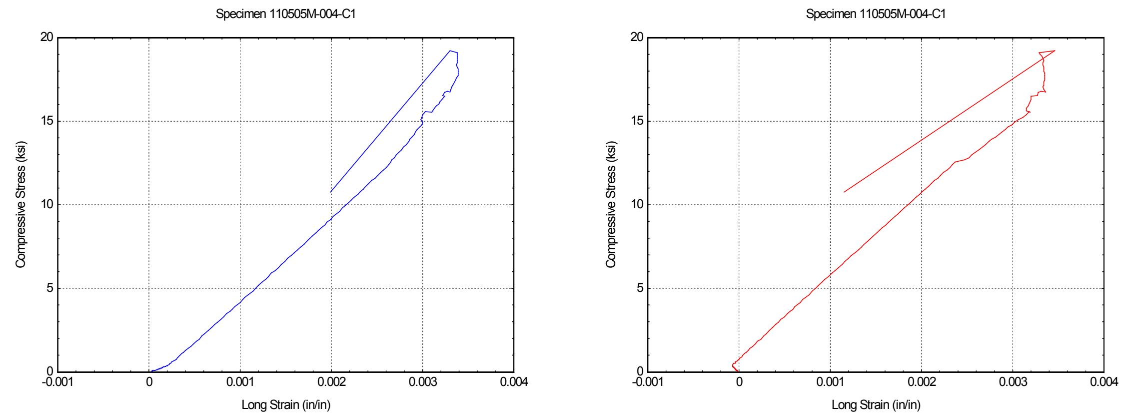

Tool Side

Bag Side

Figure B 2. Compressive Stress for Specimen 110505M-004-C1

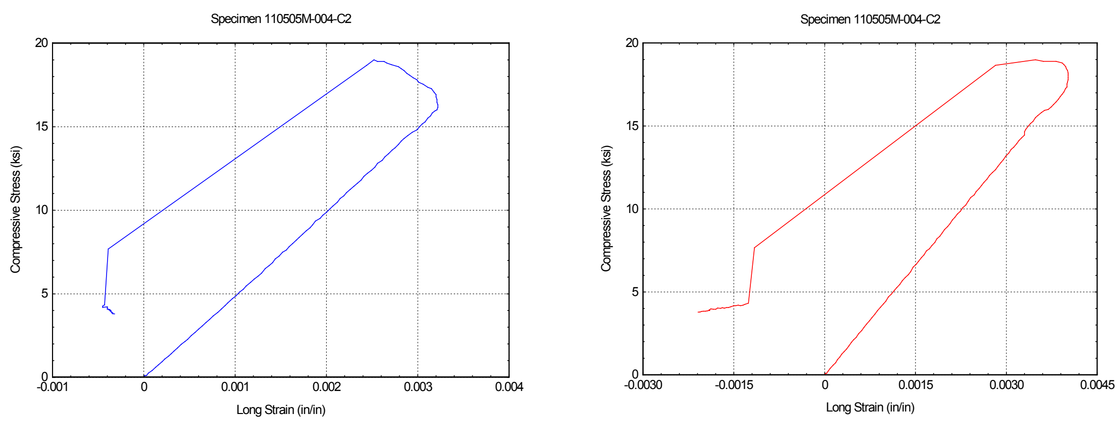

Tool Side

Bag Side

Figure B 3. Compressive Stress for Specimen 110505M-004-C2

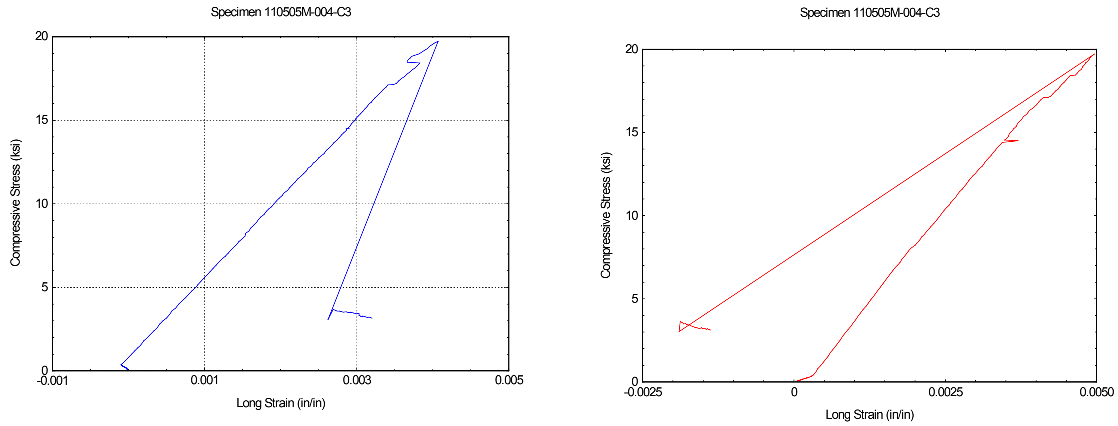

Tool Side

Bag Side

Figure B 4. Compressive Stress for Specimen 110505M-004-C3

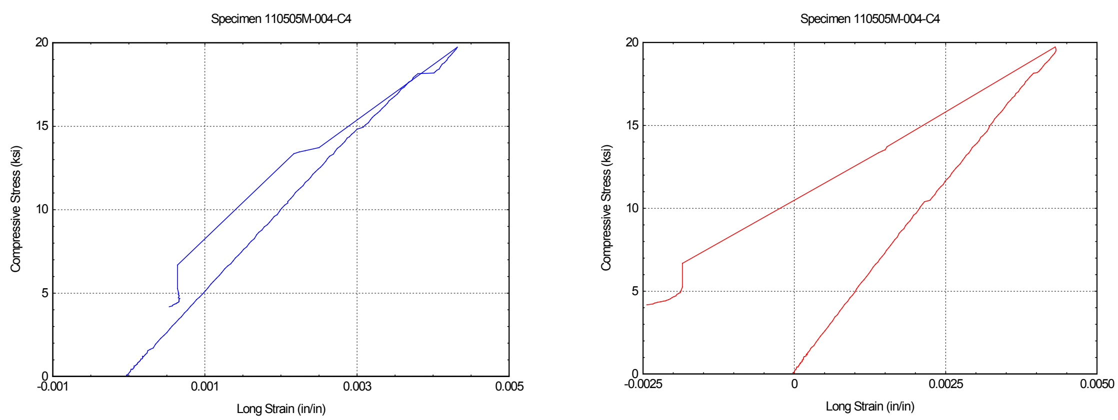

Tool Side

Bag Side

Figure B 5. Compressive Stress for Specimen 110505M-004-C4

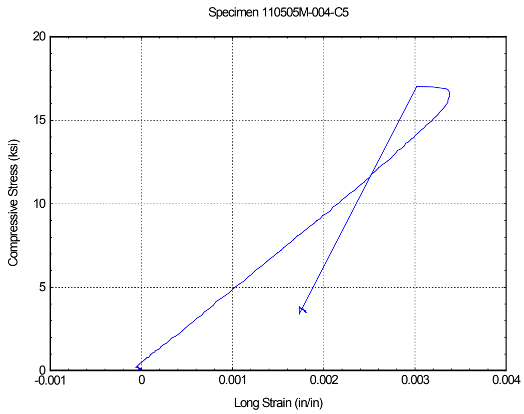

Tool Side

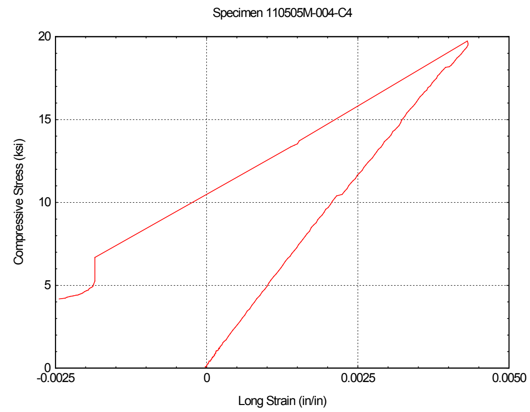

Bag Side

Figure B 6. Compressive Stress for Specimen 110505M-004-C5

D3039/D3039M – 0

Standard Test Method

For

Tensile Properties of Polymer Matrix Composite Materials

Data

Table B 4. Specimen Dimensions for Tensile Tests

TEST ID #	*Test Temp*	*THICKNESS (in.)*			Avg Thick (in)	Width (in)			Cross Sectional Area (in²)			Average X-sectional
		T(a)	*T(b)*	*T(c)*		W(1)	W(2)	W(3)	Point A	Point B	Point C	
T1	RT Dry	0.1485	0.1493	0.1489	0.1460	1.000	0.998	0.999	0.500	0.0736	5.501	0.0084
T2	RT Dry	0.1492	0.1484	0.1483	0.1476	1.002	1.001	1.002	0.500	0.0721	5.501	0.0056
T3	RT Dry	0.1479	0.1475	0.1488	0.1466	1.003	1.003	1.003	0.1483	0.1479	0.1492	0.0061
T4	RT Dry	0.1483	0.1481	0.1491	0.1450	1.003	1.002	1.003	0.500	0.0732	5.500	0.0028
T5	RT Dry	0.1495	0.1494	0.1495	0.1496	1.003	1.004	1.004	0.497	0.0753	5.501	0.0041

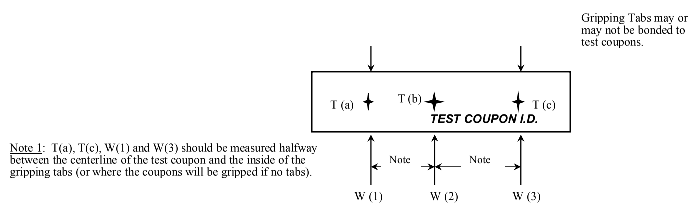

Figure B 7. Sketch of Test Specimens Associated with Table B 4

Table B 5. Summary of Tension Data

Test Label	*Area (in²)*	*Max Load (lbf)*	*Max Tensile Stress (ksi)*	*Tensile Load at =.001 (lbf)*	*Tensile Load at =.003 (lbf)*	*Long. Modulus (Msi)*	*Poisson's Ratio Gage 1*
T1	0.1488	11850	79.640	739	2094	4.555	0.107
T2	0.1489	11850	79.585	563	1887	4.448	0.076
T3	0.1485	10648	71.706	503	1777	4.288	0.018
T4	0.1489	11838	79.501	598	1946	4.527	0.044
T5	0.1500	11176	74.506	402	1398	3.321	0.048
Mean	0.1490	11472	76.987	561	1821	4.228	0.059
Std Dev	0.00	544.51	3.68	124.13	262.43	0.52	0.03
Coeff of Var	0.38	4.75	4.78	22.13	14.42	12.24	57.77

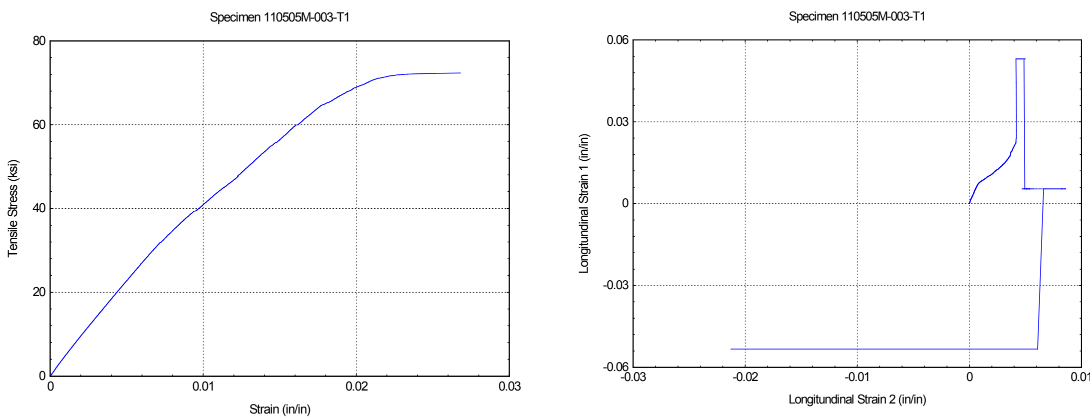

Figure B 8. Tensile Stress-Strain for Specimen 110505M-003-T1

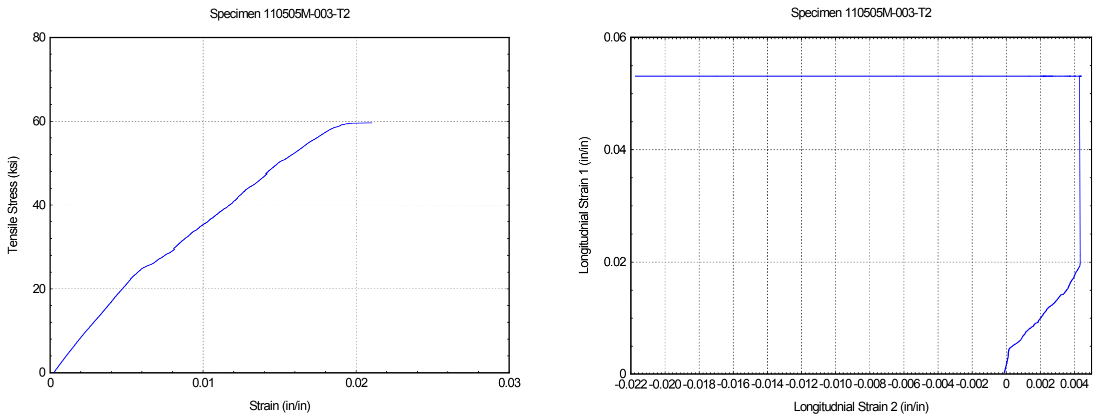

Figure B 9. Tensile Stress-Strain for Specimen 110505M-003-T2

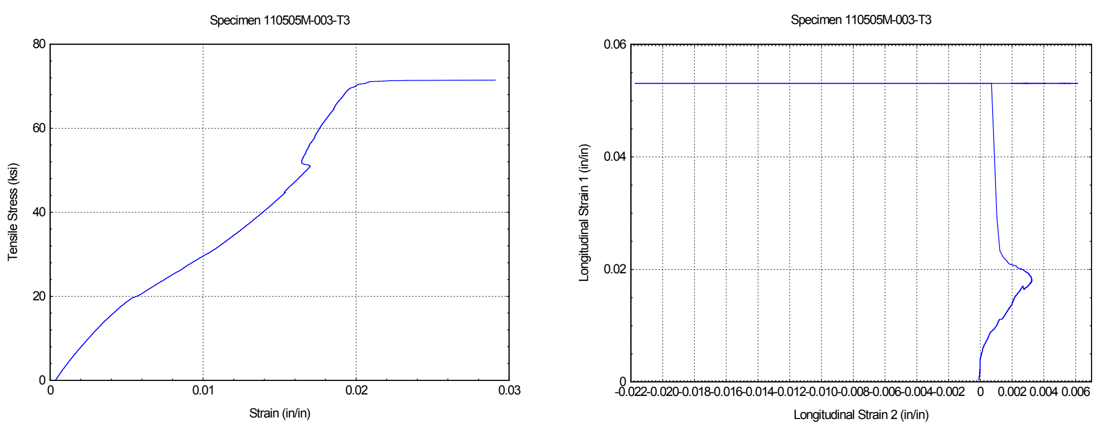

Figure B 10. Tensile Stress-Strain for Specimen 110505M-003-T3

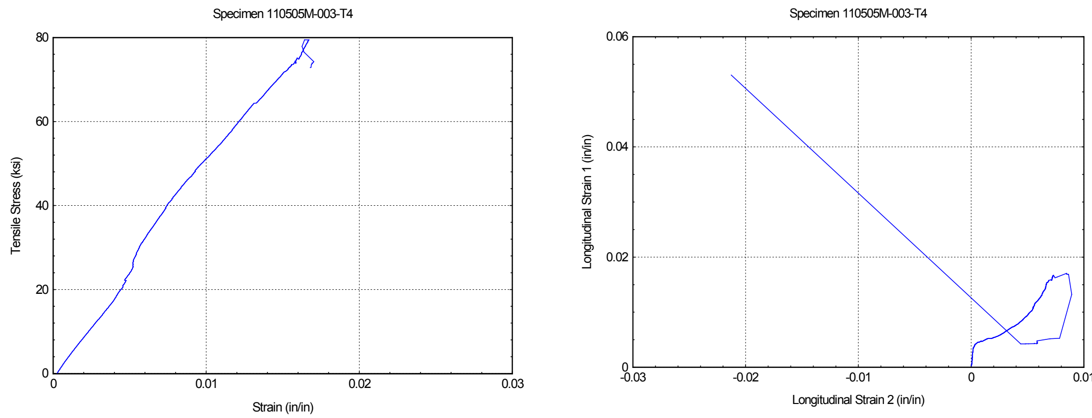

Figure B 11. Tensile Stress-Strain for Specimen 110505M-003-T4

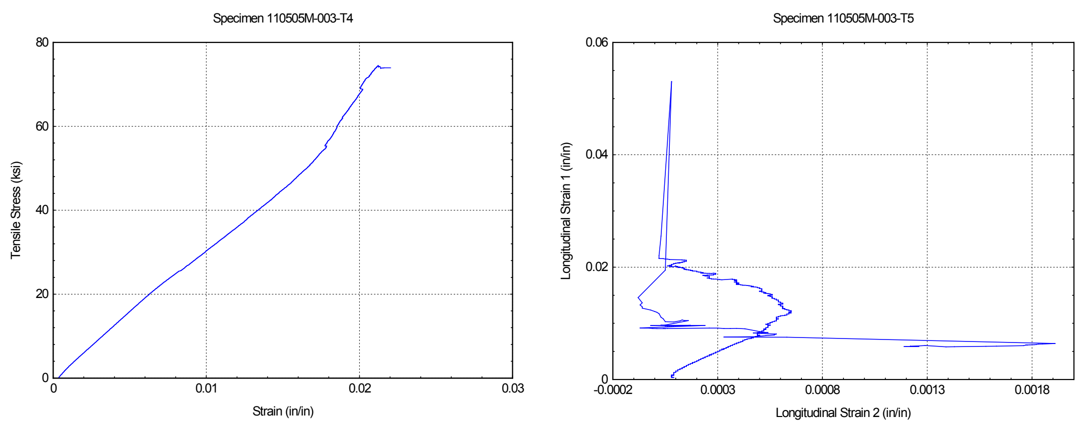

Figure B 12. Tensile Stress-Strain for Specimen 110505M-003-T5

D5379/D5379M – 05

Standard Test Method

For

Shear Properties of Composite Materials by the V-Notched Beam Method

Data

Table B 6. Summary of XY Shear Data

Specimen I.D.	Test	Avg. Thickness (in.)	Avg. Width (in.)	Avg. Cross-Sectional Area (in.^{2})	Max Load (lbs.)	Shear Strength (Ksi)	Shear Chord Modulus (Ksi)
110505M-004-XY-1	RT Dry	0.1492	0.451	0.0670	347	5.180	214.098
110505M-004-XY-2	RT Dry	0.1444	0.454	0.6600	324	4.904	239.585
110505M-004-XY-3	RT Dry	0.1436	0.452	0.0650	340	5.237	179.859
110505M-004-XY-4	RT Dry	0.1560	0.453	0.0710	364	5.128	251.918
110505M-004-XY-5	RT Dry	0.1513	0.452	0.0680	347	5.097	231.030
					Avg. =	5.11	223.298
					Std. Dev. =	0.13	27.91
					CoV =	2.47%	12.50%

Table B 7. Summary of XZ Shear Data

Specimen I.D.	Test	Avg. Thickness (in.)	Avg. Width (in.)	Avg. Cross-Sectional Area (in.^{2})	Max Load (lbs.)	Shear Strength (Ksi)	Shear Chord Modulus (Ksi)
110505M-006-XZ-1	RT Dry	0.1562	0.453	0.0710	250	3.519	162.430
110505M-006-XZ-2	RT Dry	0.1574	0.453	0.0710	282	3.970	202.147
110505M-006-XZ-3	RT Dry	0.1557	0.446	0.0690	248	3.601	174.839
110505M-006-XZ-4	RT Dry	0.1608	0.455	0.0730	312	4.272	419.519
110505M-006-XZ-5	RT Dry	0.1610	0.455	0.0730	298	4.080	253.119
					Avg. =	3.89	242.411
					Std. Dev. =	0.32	104.96
					CoV =	8.23%	43.30%

Table B 8. Specimen Dimensions for XY Shear Tests

TEST COUPON I.D.	*GAGE SECTION. THICKNESS (inch)*	*GAGE SECTION WIDTH (inch)*	*GAGE SECTION AREA ($inch^2$)*	*OVERALL WIDTH (For Info. Only)*	
				OW1 (in.)	*OW2 (in.)*
110505M-004-XY-1	0.149	0.451	0.067	0.752	0.752
110505M-004-XY-2	0.144	0.454	0.066	0.751	0.750
110505M-004-XY-3	0.144	0.452	0.065	0.754	0.753
110505M-004-XY-4	0.156	0.453	0.071	0.752	0.751
110505M-004-XY-5	0.151	0.452	0.068	0.753	0.751
110505M-004-XY-6	0.148	0.455	0.067	0.751	0.749

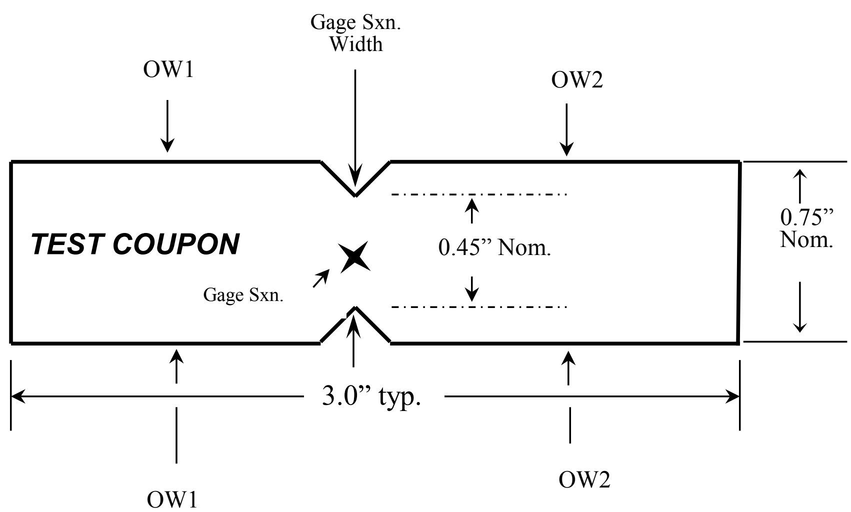

Figure B 13. Sketch of Test Specimens Associated with Table 8

Table B 9. Summary of XY Shear Data at +45° Strain

Test Label	*Area (in²)*	*.Extension at Max Load (in)*	*Max Shear Load (lbf)*	*Shear Load at =.001 (lbf)*	*Shear Load at =.002 (lbf)*	*Ultimate Shear Strength (ksi)*	*Shear Strain at Max Shear Load (in/in)*
XY-1	0.0670	0.068	347	87	131	5.180	0.457
XY-2	0.0660	0.072	324	70	124	4.904	0.485
XY-3	0.0650	0.071	340	102	142	5.237	0.478
XY-4	0.0710	0.066	364	65	108	5.128	0.441
XY-5	0.0680	0.061	347	80	130	5.097	0.407
Mean	0.0674	0.068	344	81	127	5.109	0.454
Std Dev	0.00	0.00	14.55	14.64	12.22	0.13	0.031
Coeff of Var	3.416	6.931	4.225	18.072	9.625	2.473	6.931

Table B 10. Summary of XY Shear Data at -45° Strain

Test Label	*Area (in²)*	*.Extension at Max Load (in)*	*Max Shear Load (lbf)*	*Shear Load at =.001 (lbf)*	*Shear Load at =.002 (lbf)*	*Ultimate Shear Strength (ksi)*	*Shear Strain at Max Shear Load (in/in)*
XY-1	0.0670	0.068	347	78	125	5.180	0.457
XY-2	0.0660	0.072	324	73	128	4.904	0.485
XY-3	0.0650	0.071	340	96	134	5.237	0.478
XY-4	0.0710	0.066	364	85	133	5.128	0.441
XY-5	0.0680	0.061	347	80	132	5.097	0.407
Mean	0.0674	0.068	344	82	130	5.109	0.454
Std Dev	0.00	0.00	14.55	8.52	3.74	0.13	0.031
Coeff of Var	3.416	6.931	4.225	10.349	2.875	2.473	6.931

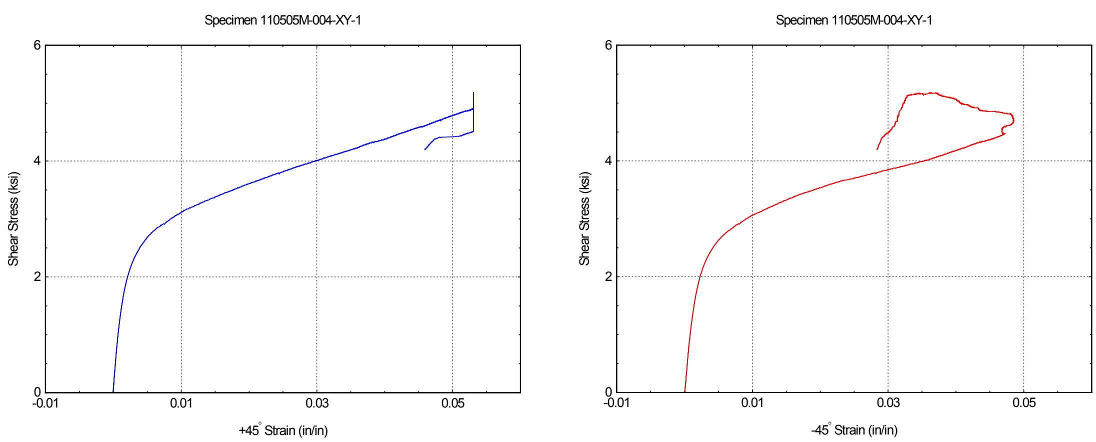

+45°

-45°

Figure B 14. XY Shear vs. Strain for Specimen 110505M-004-XY-1

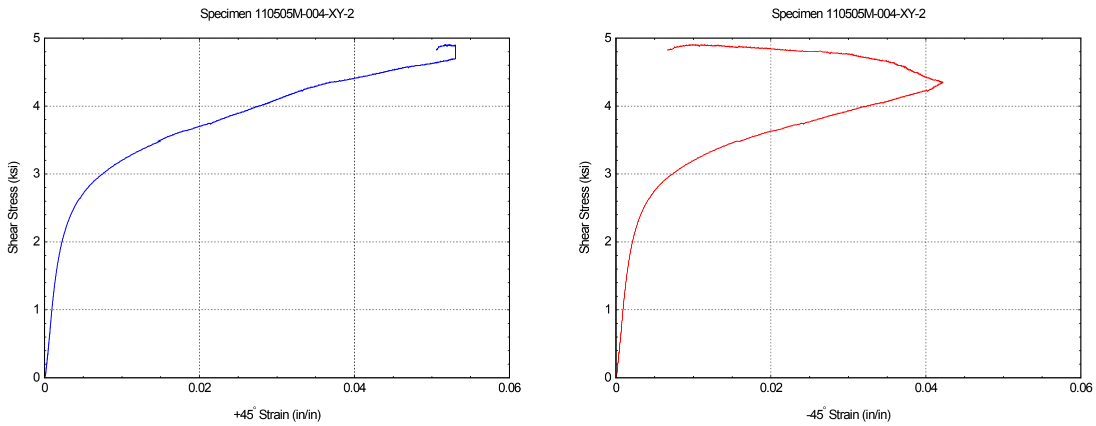

+45°　　　　-45°

Figure B 15. XY Shear vs. Strain for Specimen 110505M-004-XY-2

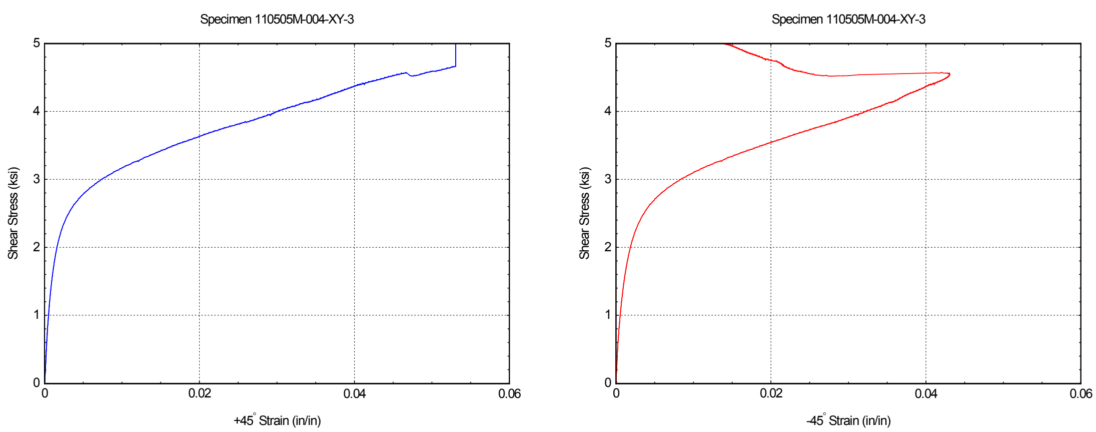

+45°　　　　-45°

Figure B 16. XY Shear vs. Strain for Specimen 110505M-004-XY-3

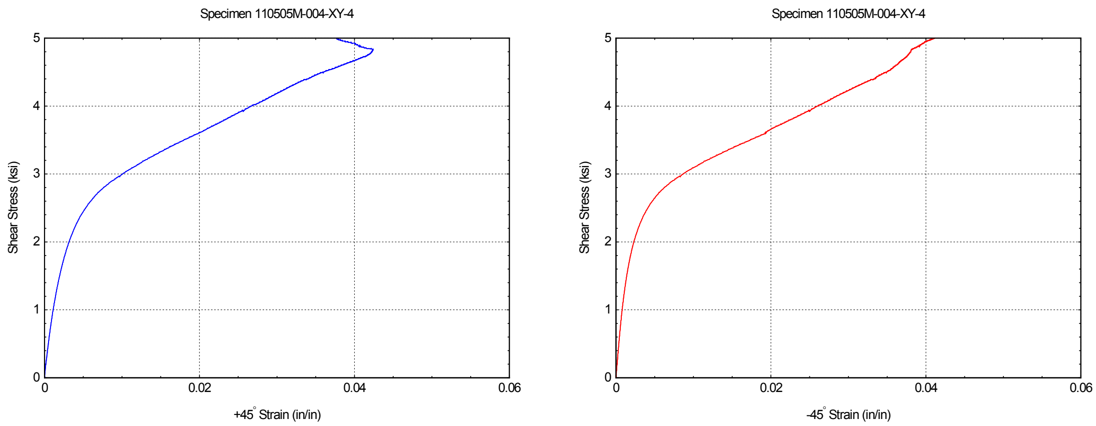

+45° -45°

Figure B 17. XY Shear vs. Strain for Specimen 110505M-004-XY-4

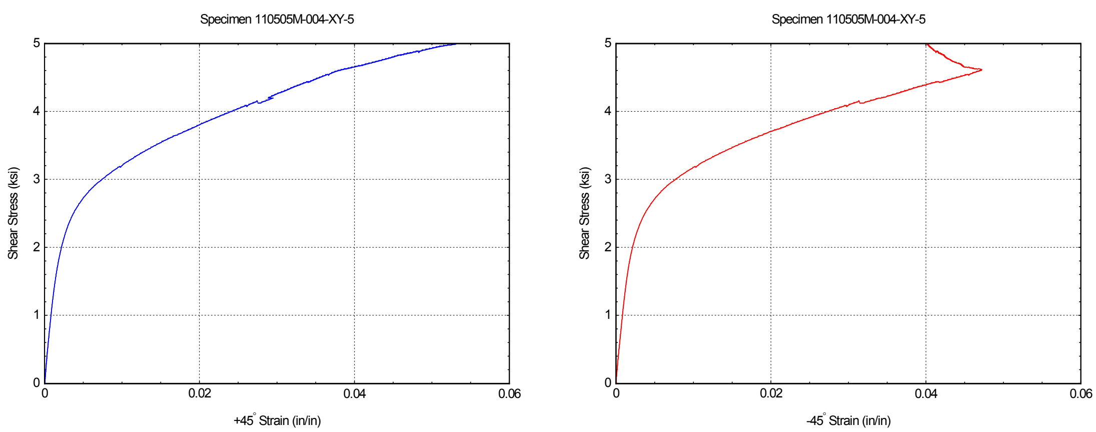

+45° -45°

Figure B 18. XY Shear vs. Strain for Specimen 110505M-004-XY-5

Table B 11. Specimen Dimensions for XZ Shear Tests

Test Coupon I.D.	*Gage Section. Thickness (inch)*	*Gage Section Width (inch)*	*Gage Section Area (inch²)*	*Overall Width (For Info. Only)*	
				OW1 (in.)	*OW2 (in.)*
120125P-006-XZ-1	0.1562	0.453	0.071	0.753	0.752
120125P-006-XZ-2	0.1574	0.453	0.071	0.753	0.752
120125P-006-XZ-3	0.1557	0.446	0.069	0.752	0.752
120125P-006-XZ-4	0.1608	0.455	0.073	0.752	0.751
120125P-006-XZ-5	0.1610	0.455	0.073	0.752	0.751
120125P-006-XZ-6	0.1562	0.455	0.071	0.752	0.752

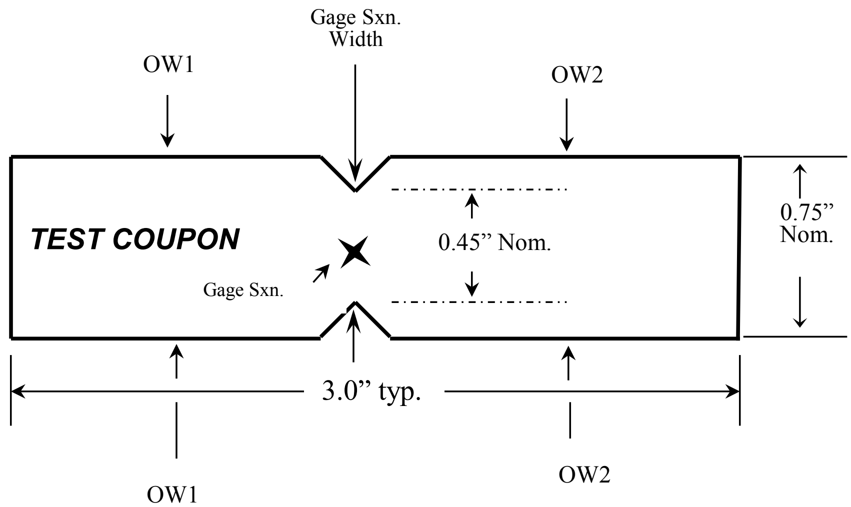

Figure B 19. Sketch of Test Specimens Associated with Table B 11

Table B 12. Summary of XZ Shear Data at +45° Strain

Test Label	*Area (in^2)*	*.Extension at Max Load (in)*	*Max Shear Load (lbf)*	*Shear Load at =.001 (lbf)*	*Shear Load at =.002 (lbf)*	*Ultimate Shear Strength (ksi)*	*Shear Strain at Max Shear Load (in/in)*
XZ-1	0.0710	0.093	250	47	72	3.519	0.596
XZ-2	0.0710	0.099	282	39	62	3.970	0.637
XZ-3	0.0690	0.098	248	41	68	3.601	0.630
XZ-4	0.0730	0.033	312	87	157	4.272	0.210
XZ-5	0.0730	0.100	298	66	98	4.080	0.638
Mean	0.0714	0.085	278	56	91	3.888	0.542
Std Dev	0.00	0.03	28.37	20.59	39.32	0.32	0.186
Coeff of Var	2.340	34.37	10.21	36.87	43.08	8.23	34.368

Table B 13. Summary of XZ Shear Data at -45° Strain

Test Label	*Area (in^2)*	*.Extension at Max Load (in)*	*Max Shear Load (lbf)*	*Shear Load at =.001 (lbf)*	*Shear Load at =.002 (lbf)*	*Ultimate Shear Strength (ksi)*	*Shear Strain at Max Shear Load (in/in)*
XZ-1	0.0710	0.093	250	53	81	3.519	0.596
XZ-2	0.0710	0.099	282	57	90	3.970	0.637
XZ-3	0.0690	0.098	248	48	73	3.601	0.630
XZ-4	0.0730	0.033	312	111	181	4.272	0.210
XZ-5	0.0730	0.100	298	60	92	4.080	0.638
Mean	0.0714	0.085	278	66	104	3.888	0.542
Std Dev	0.00	0.03	28.37	25.88	43.89	0.32	0.19
Coeff of Var	2.340	34.37	10.21	39.36	42.39	8.23	34.37

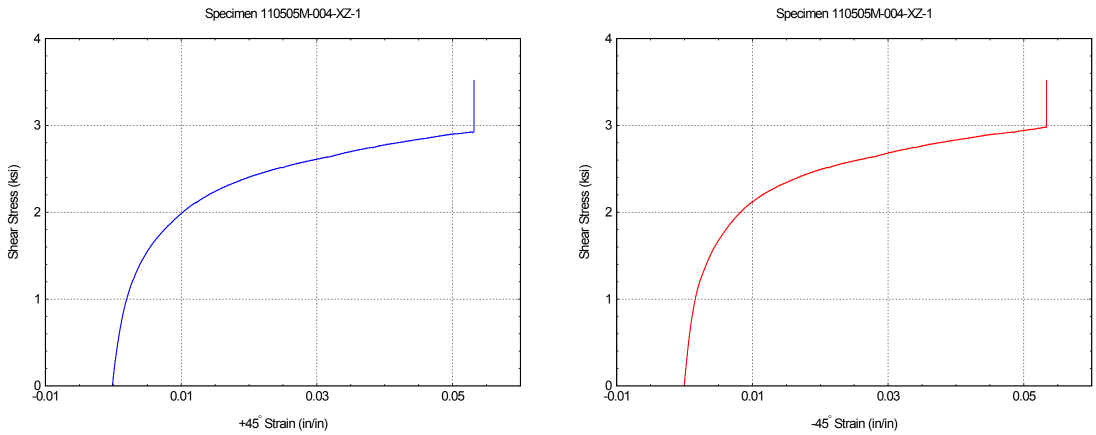

+45°

-45°

Figure B 20. XZ Shear vs. Strain for Specimen 110505M-004-Xz-1

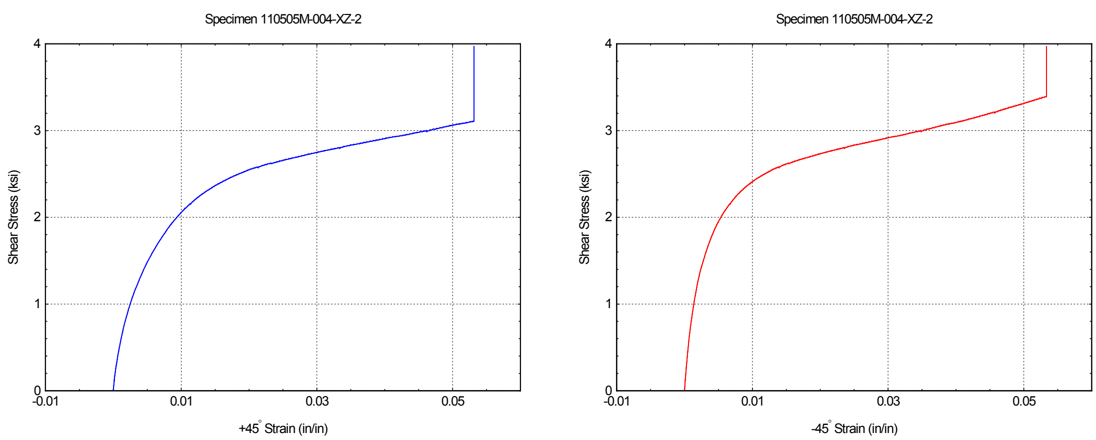

+45°

-45°

Figure B 21. XZ Shear vs. Strain for Specimen 110505M-004-Xz-2

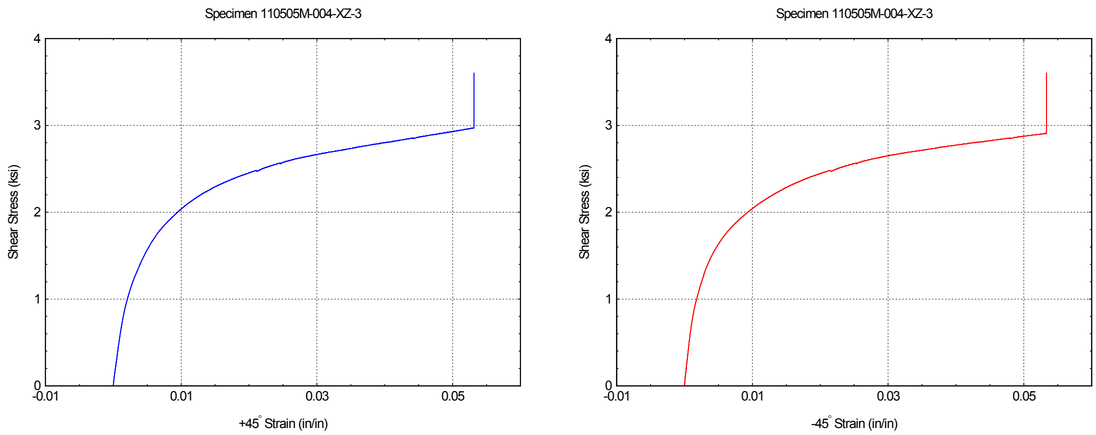

+45°   -45°

Figure B 22. XZ Shear vs. Strain for Specimen 110505M-004-Xz-3

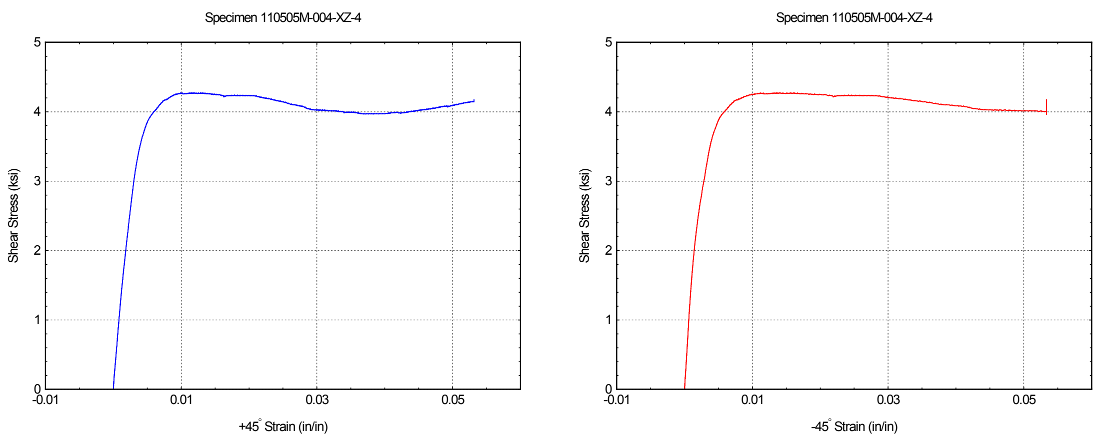

+45°   -45°

Figure B 23. XZ Shear vs. Strain for Specimen 110505M-004-Xz-4

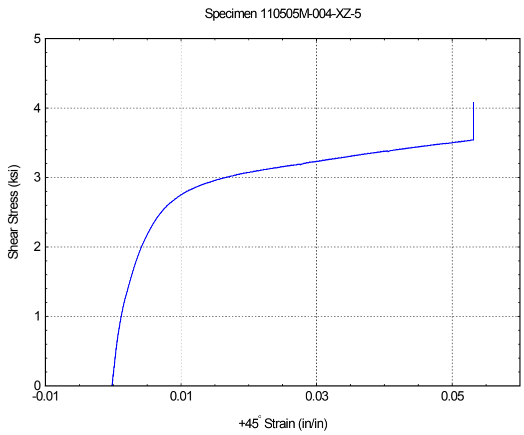

+45°

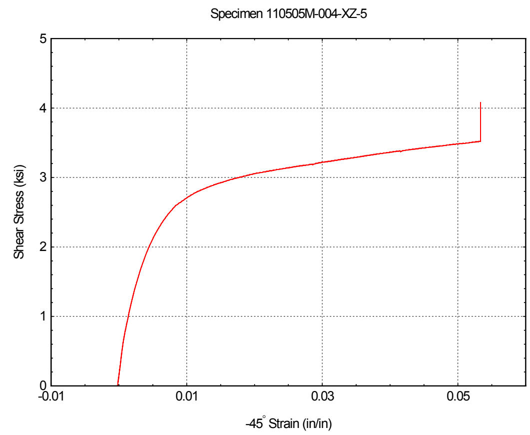

-45°

Figure B 24. XZ Shear vs. Strain for Specimen 110505M-004-Xz-5

D792 – 08

Standard Test Methods

For

Density and Specific Gravity (Relative Density) of Plastics by Displacement

Data

Table B 14. 110505M-003 Laminate Physical Properties

Specimen Number	*Wc* (wt. in air) (x.xxxx g)	*W* (wt. in water) (x.xxxx g)	*Md* Spec. Grav. (x.xxx)	*Wc* (spec. wt.) (x.xxxx g)
1	4.2619	2.3084	2.175	4.2619
2	4.3633	2.3566	2.167	4.3633
3	4.4706	2.4115	2.165	4.4706
		Avg:	2.169	4.3653

Table B 15. 110505M-004 Laminate Physical Properties

Specimen Number	*Wc* (wt. in air) (x.xxxx g)	*W* (wt. in water) (x.xxxx g)	*Md* Spec. Grav. (x.xxx)	*Wc* (spec. wt.) (x.xxxx g)
1	4.3049	2.3292	2.172	4.3049
2	4.2784	2.3039	2.160	4.2784
3	4.2192	2.2766	2.165	4.2192
		Avg:	2.166	4.2675

Table B 16. 110505M-006 Laminate Physical Properties

Specimen Number	*Wc* (wt. in air) (x.xxxx g)	*W* (wt. in water) (x.xxxx g)	*Md* Spec. Grav. (x.xxx)	*Wc* (spec. wt.) (x.xxxx g)
1	3.8618	1.9156	1.978	3.8618
2	4.2336	2.1105	1.988	4.2336
3	3.8202	1.9075	1.991	3.8202
		Avg:	1.986	3.9719

APPENDIX C – MATERIAL PROPERTY DATA II

Quasi-Static and Low Velocity Impact Testing of E-Glass/Phenolic Composite

by

University of Delaware Center of Composite Materials

NOMENCLATURE

SPR	Support span to punch diameter ratio
D_S	Support span diameter
D_P	Punch diameter
AD	Areal density
H_C	Specimen thickness
ρ_C	Specimen density
#L	Number of layers in a laminate
F	Penetration resistance force / impact contact force
F_{max}	Maximum force
X	Displacement
x_{max}	Maximum displacement
x_P	Permanent displacement after unloading to F = 0.
E_I	Impact energy = $(1/2)m_P V_I^2$
E_T	Total integral energy
E_D	Dissipated energy
E_E	Elastic energy, $E_T - E_D$
v_f	Fiber volume fraction
V_I	Impact velocity

The main objectives of this section are to determine (i) the punch shear strength (PSS) and the punch crush strength (PCS) of PW E-Glass/Phenolic composites, and to (ii) determine the low velocity impact (LVI) behavior of E-Glass/Phenolic composites at two different impact energy levels. The PSS and PCS of composites are two important parameters needed for the LS-DYNA progressive composite damage model MAT162.

SUMMARY

In order to accomplish the main objectives, quasi-static punch shear test (QS-PST), quasi-static crush shear test and LVI experiments are conducted following the QS-PST experimental methodology developed at UD-CCM and using the modified ASTM LVI test methods. Some additional testing has been performed on the E-Glass /

Phenolic composites to compare the new results with previous results to ensure the accuracy of the original test results. These additional tests include Fiber Volume Fraction (FVF), Tension Tests (TT), Through Thickness Tension Tests (TTTT), and Through Thickness Compression Tests (TTCT). The average results for all of these experiments are summarized in the tables below.

Table C 1. Average Fiber Volume Fraction of PW E-Glass/Phenolic

Specimen ID	*ρ_c (g/cm^3)*	*V_f(%)*
Average	2.057	65.8
STDEV	0.012	0.633
COV%	0.006	0.010

Table C 2. Average PSS Test Parameters and Results, Punch Diameter $D_P = 7.595$-mm

Specimen #	*D_s (mm)*	*SPR*	*PSS (MPa)*	*Stdev (MPa)*
2-9, 3-9-10, 4-9-10	7.747	1.020	156.05	4.61
2-3-8, 3-7-8, 4-7-8	7.874	1.037	148.73	7.40
2-1-2, 3-5-6, 3-14-15, 4-5-6, 4-14-15	8.001	1.053	150.14	7.28
2-21-30	8.890	1.171	120.15	6.18

Table C 3. Average Peak Load and Descending PCS Values for Specimens (Renumbered) Tested using HSCT Fixture

Specimen # (Actual)	*Specimen # (Renumbered)*	*Peak Load (kN)*	*PCS (Descending)*
Average	N/A	37.217	834.26
STDEV	N/A	3.13518	59.77
COV%	N/A	0.084241	7.16

Table C 4. Peak Load and Descending PCS Values for Specimens (Renumbered) Tested using Mini QS-PST Fixture

Specimen # (Actual)	*Specimen # (Renumbered)*	*Peak Load (kN)*	*PCS (MPa) (Descending)*
Average	N/A	39.956	881.98
STDEV	N/A	2.779	61.37
COV%	N/A	0.070	6.96

Table C 5. Summary of LVI Experimental Data for Laminate 300 & 400, $H_C = 8.97$-mm

Date	*Material*			*Density, g/cm³*		*FVF*		
5/10/2012	PW E-Glass/Phenolic			2.00		65.8%		
E_I (J)	*V_I (m/s)*	*E_I (J)*	*x_T (mm)*	*x_P (mm)*	*F_{max} (kN)*	*E_T (J)*	*E_D (J)*	*E_E (J)*
50	3.191	48.86	9.25	5.29	9.99	49.74	39.31	10.43
70	3.770	68.19	11.00	6.51	11.79	69.23	55.53	13.70

Table C 6. Average Slope, Poisson's Ratio, & Elastic Modulus for Axial Tension Test

Specimen #	*Load Range (kN)*	*Strain Range (με)*	*A (mm²)*	*M_3*	*M_1*	*ν_{12} (kN/kN)*	*E_{11} (GPa)*
Average	N/A	1000-3000	102.24	2.636E6	52.605E6	0.056	25.00
STDEV	N/A	0	0.641	0.295E6	24.307E6	0.033	2.809
COV%	N/A	0	0.006	0.112	0.462	0.529	0.109

Table C 7. Average Poisson's Ratio & Elastic Modulus for Through Thickness Compression Test

Specimen #	*ν_{31}, kN/kN*	*E_{33}, GPa.*
Average	0.100	7.438
STDEV	0.026	1.227
COV%	0.261	0.165

Table C 8. Average Failure Load and Strength for Through Thickness Tension Test

Specimen #	*Failure Load (N)*	*X-Section Area (mm²)*	*Stress (MPa)*
Average	631.986	482.415	1.312
STDEV	80.168	7.068	0.184
COV%	0.127	0.015	0.140

Quasi-Static Test Methodology

Specimens of 8 layer plain weave (PW) E-glass/phenolic laminates are core drilled to a diameter of 25 mm for Quasi Static Punch Shear Testing (QS-PST), and machined using a wet saw to 101.6 mm × 152.4 mm dimensions for low velocity impact (LVI) testing.

The thickness, dimensions, and mass of the composite laminates are measured to calculate the density and the areal-density of the composite materials. Density of the composite panels is measured following ASTM D2584 standard. The areal-densities of the composite materials are calculated from the measured density and thickness of the composite panels using the following equation.

$$AD = \rho_c H_c \tag{C 1}$$

where ρ_c is the average composite density, and H_c is the average thickness of the composite laminates. Average material and geometric properties of all composite laminates are shown in Table C 9.

Table C 9. Geometric & Mass Properties of PW E-Glass/Phenolic Composite Materials used in Different Test Methods

Test Method	*H, mm*	ρ *, g/cm³*	*# of Specimens*	*Comments*
PSS	4.04	2.05	35	Mini QS-PST Test
PCS-I	4.04	2.04	10	Hydrostatic Crush Test
PCS-II	4.06	2.04	7	Mini QS-PST Test

Fiber Volume Fraction

The fiber volume fraction determines the reinforcing fiber content of a composite material. The ASTM D3171 standard is used to determine fiber volume fraction. For that purpose round samples of 25 mm diameter are cut out of test specimens. The samples are weighed in air and water to determine the total weight and the density of each specimen. Then the specimens are placed in an oven at 562° C for about 180 minutes in order to burn out the phenolic resin and to relieve the glass fibers from the phenolic matrix. The glass fibers are weighed again and the fiber volume fraction of the material is determined using the following equation.

$$V_f = 100\left(\frac{M_f}{M_i}\right)\left(\frac{\rho_c}{\rho_f}\right) \tag{C 2}$$

Where V_f is the fiber volume fraction in percent, ρ_c is the density of the specimen, ρ_f is the density of the reinforcement, M_i is the initial mass of the specimen in grams, and M_f is the mass of the fibers in grams after burn off.

Table C 10. Fiber Volume Fraction of PW E-Glass/Phenolic Composite Materials used in Different Test Methods

Specimen ID	*M_f, gm*	*M_i, gm*	*V_c, cm³*	*ρ_c, g/cm³*	*ρ_r, g/cm³*	*V_f*
3-1	3.281	4.013	1.949	2.059	2.550	66.0
3-2	3.254	3.986	1.931	2.064	2.550	66.1
3-3	3.314	4.049	1.963	2.062	2.550	66.2
3-4	3.339	4.066	1.964	2.071	2.550	66.7
4-1	3.325	4.078	2.002	2.038	2.550	65.1
4-2	3.339	4.101	1.986	2.065	2.550	65.9
4-3	3.308	4.064	1.972	2.061	2.550	65.8
4-4	3.323	4.106	2.014	2.039	2.550	64.7
Average	3.310	4.058	1.972	2.057	2.550	65.8

Punch Shear Strength Test

A quasi-static punch shear test (QS-PST) methodology has been developed for studying the energy dissipating damage mechanisms and penetration resistance behavior of thick section composites. QS-PSTs are performed using a custom made steel fixture which consists of a circular bottom support plate, a matching top cover plate, and a punch (Figure C 1). The Mini QS-PST fixture has a bottom support plate of diameter 50.8 mm (2-in) with a centered hole of diameter 25.4 mm (1-in) bored 19.05 mm (0.75-in) deep, and is capable of housing many support rings of various diameters. There is also a 12.7 mm diameter through hole in the support plate which provides access from the rear side of the support plate. Around the perimeter of the support plate there are eight bolt holes to secure the cover and the support plate while clamping the composite specimen between them. The inner hole diameter of the cover plate is 7.61+0.01 mm through which a two-step cylindrical punch of shank diameter 7.60 mm can slide through. The ratio between the support span diameter and the punch head diameter is termed as "*SPR*", a value which can vary in the range $1.02 < SPR = \frac{D_s}{D_p} < 1.20$ for the 7.60 mm punch.

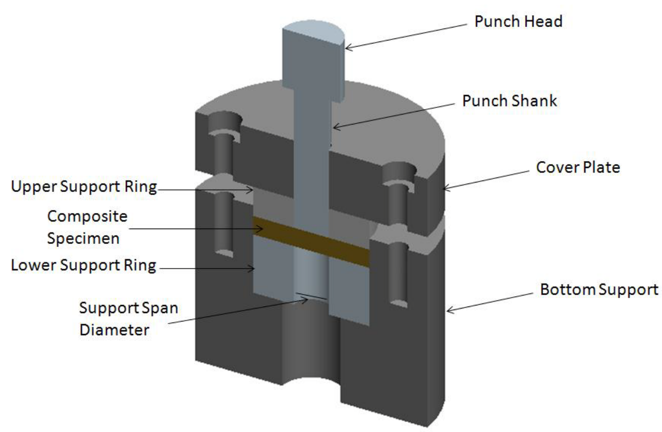

a) QS-PST Fixture b) Cross-Sectional 3D Sketch of the QS-PST Fixture

Figure C 1. Mini QS-PST Fixture

An Instron 4484 universal testing machine with a 133.4 kN load cell is used in QS-PST where the tests are performed at a cross-head displacement rate of 0.508 mm/min (0.02-in/min). The load and cross-head displacement data are acquired using the Blue Hill control and data acquisition software using a data collection rate of 100 data per second. The punch shank is loaded by a driving nose which consists of an adapter threaded to fit the 133.45 kN load cell used in these experiments. Threaded into the lower end of the adapter there is a larger punch with a 12.7 mm (0.5 inch) diameter with rounded edges. This punch is aligned with the 7.59 mm (0.299 inch) punch shank before testing. By using different diameter support span-to-punch ratios (SPRs), one can test specimens under shear-dominated loading.

QS-PST experiments are performed at four different SPRs of 1.020, 1.037, 1.053, and 1.171 in this study using the PSS specimens presented in Table C 9. A typical force-displacement data obtained from the tests is presented in Figure C 1 for SPR of 1.053. The maximum force (F_{max}) can be determined from the force-displacement data. Punch Shear Strength is calculated by dividing the F_{max} by the shear area (A_{shear}).

$$PSS = \frac{F_{\max}}{A_{\max}} = \frac{F_{\max}}{\pi D_m H_c} \quad \text{(C 3)}$$

where H_c is laminate thickness, and D_m is the mean diameter given as:

$$D_m = \frac{D_p + D_s}{2} \tag{C 4}$$

where D_p is the diameter of the punch, and D_s is the diameter of the support span.

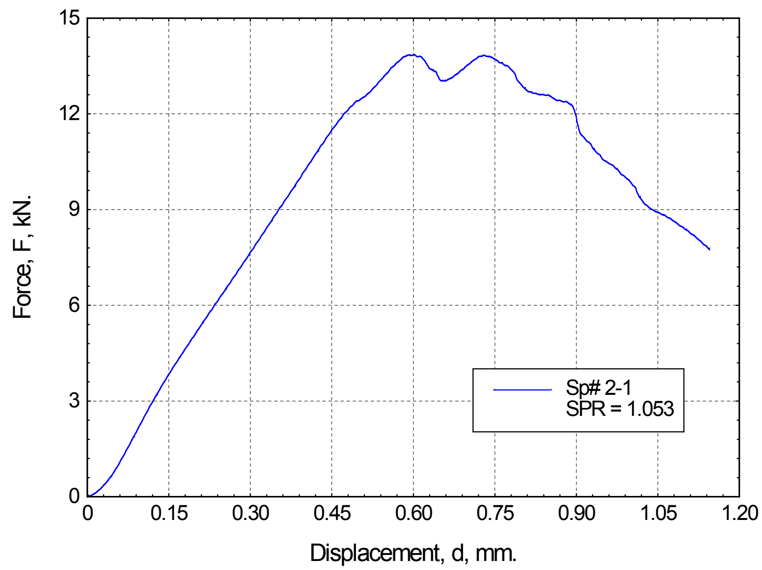

Figure C 2. Force vs. Displacement Plot of a Specimen Tested at SPR = 1.053

Punch Crush Strength

Similar to QS-PST, crush testing is performed on the round PCS-I & PCS-II (Table C 9) specimens of 25.01 mm in diameter and 25.00 mm thickness. Two separate fixtures have been used to produce different results. The first fixture is the Mini QS-PST fixture used for punch shear testing previously shown in Figure C 1, with a solid support span, SPR = 0. The other fixture is the hydrostatic crush test (HSCT) fixture shown in Figure C 3. This fixture is similar to the Mini QS-PST fixture, and consists of a circular test fixture of 50.8 mm in diameter with a central 12.7 mm hole from the top that is 25.4mm deep which guides the loading block. From the bottom of the fixture there is a 25.4 mm central hole 19.05mm deep which accommodates the specimen, punch and punch guide. The diameter of the punch can be varied between 12.7mm and 6.37mm.

a) PCST Fixture

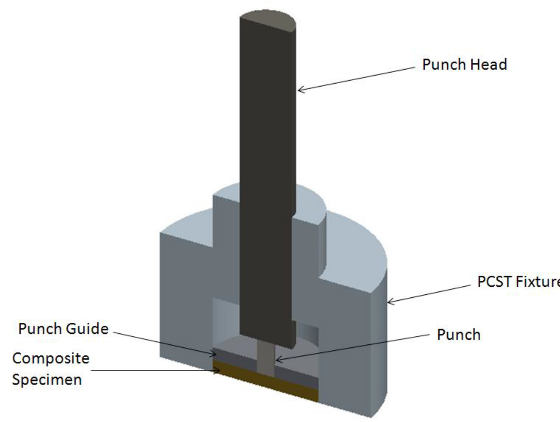

b) Cross-Sectional 3D Sketch of the PCST Fixture

Figure C 3 PCST Fixture

Typical force vs. displacement data obtained from Mini-QS-PST & HSCT tests is presented in Figure C 4. In both cases the maximum force is can be determined from the curve peak for each. Punch Crush Strength (PCS) is calculated by dividing the F_{max} by the shear area (A_{shear}).

$$PCS = \frac{F_{\max}}{A_{\max}} = \frac{4F_{\max}}{\pi D_p^2} \tag{C 5}$$

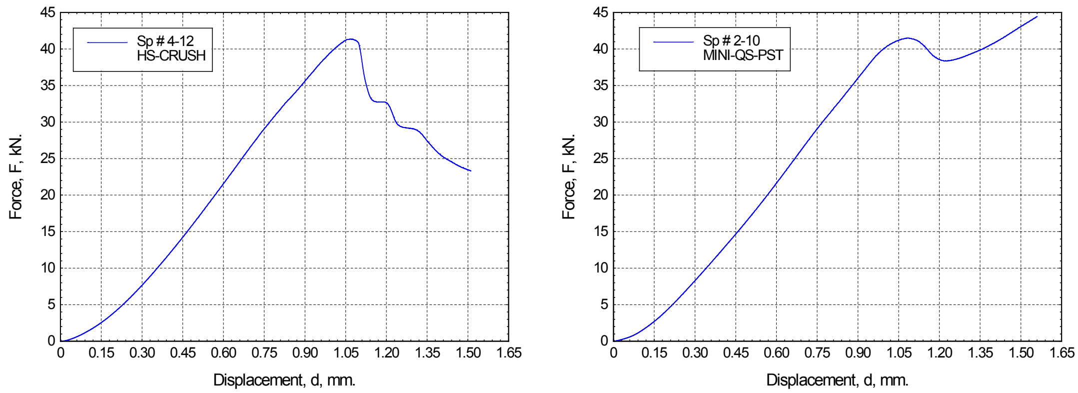

(a) Hydro Static Crush Test Fixture Results

(b) Mini QS-PST Fixture Results

Figure C 4. Force vs. Displacement Plots for two Different Crush Test Methods

Low Velocity Impact (LVI) Test

A Dynatup 9200 drop tower with a 22.3 kN load cell, shown in Figure C 5 is used in the low velocity impact tests. The load cell data as a function of time is stored in a computer via the AD converter and LVI data acquisition software. The Impulse Data Acquisition software is also used to set up the test method, and to read parameters such as displacement, velocity, impact energy, and impact force. The method used for data collection was to set the signal source to the tup in order to extract data. The filter is set to 100 kHz, and the max load or load range to 22.2 kN. Also, the tup calibration factor is set to 14.3 kN, and the duration of data collection to 10 ms (819.2 kHz) for an assumed impact duration of 5 ms. The trigger setting set to receive data from the velocity flag. The flag activates an electronic sensor which measures the velocity of the tup shown in (Figure C 1b). It is adjusted by setting the bottom of the flag parallel to the bottom of the flag reader.

The impact energy is varied by adjusting the height of the drop weight assembly or by varying the drop mass. The height is measured from the top of the specimen in the fixture to the bottom of the tup and can be changed continuously. To achieve average results, multiple specimens at each energy level are tested. The two impact energy levels of 50 and 70 Joules are tested. The standard LVI test fixture has been modified to have a perfectly clamped boundary condition. Shown in Figure C 5 and Figure C 6, the modified LVI test fixture consists of a thin steel base plate 304 mm × 152 mm × 4 mm, two vertical aluminum support plates 303 mm × 38 mm × 152 mm, a thin steel support plate 304 mm × 152 mm × 6 mm with a 127 mm × 76 mm central rectangular opening, and three guide pins attached to the plate to align the specimen being tested.

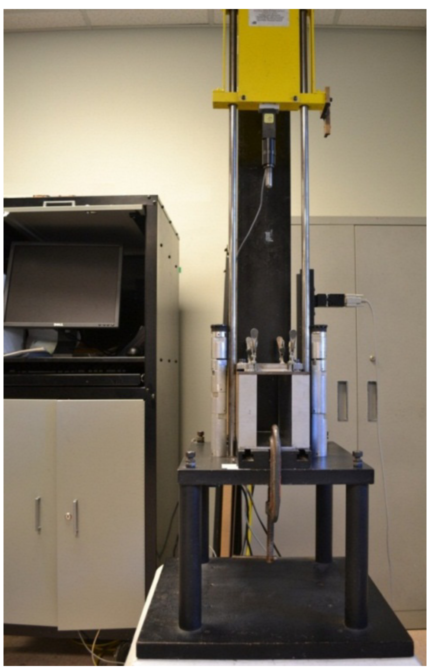

(a) Drop Tower

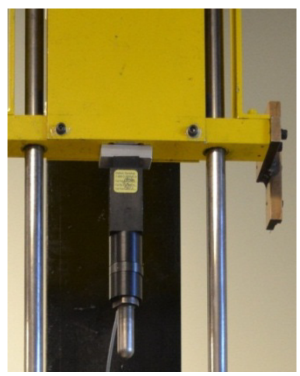

Top

Bottom

(b) Top: Slider with Load Cell and Hemispherical Tup; Bottom: Velocity Sensor

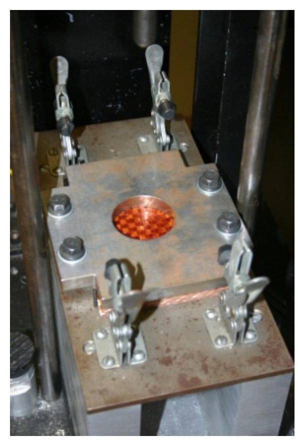

(c) Modified LVI Test Fixture

Figure C 5. Low Velocity Impact experimental Set-Up

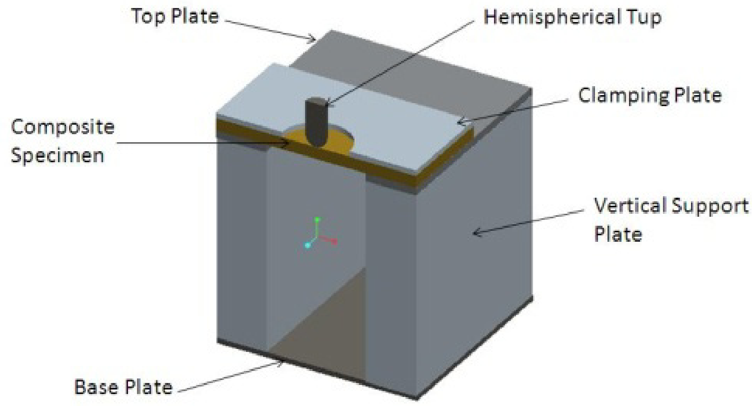

Figure C 6. Sketch of LVI Experimental Set-Up

The data provide the contact force, *F(t)*, and the initial velocity, V_o. The instantaneous velocity and displacement of the LVI impact head can be determined following Newton's Second Law of Motion. Assuming rigid body motion and considering the downward motion as positive, this can be expressed as

$$F(t) = -m_p\left(\frac{dV(t)}{dt} - g\right) \tag{C 6}$$

where m_p is the mass of the drop-weight assembly impacting the specimen. The initial impact velocity can also be determined using the following equation.

$$V_0 = \sqrt{2gH} \tag{C 7}$$

where g is the acceleration due to gravity, which is equal to 9.81 m/s^2. H is the release height for the drop-weight assembly. To calculate the velocity at time, t, Eq. (C 6) can be written as

$$\int_0^t dV(t) = \int_0^t \left(-\frac{F(t)}{m_p} + g \right) dt \qquad \text{(C 8)}$$

Integration of both sides of the equation gives

$$V(t) = V_0 + gt - \frac{p(t)}{m_p} \qquad \text{(C 9)}$$

where *p(t)* is the impulse at time *(t)*. Further integration results in Eq. (C 10).

$$d(t) = V_0 t + \frac{1}{2} g t^2 - \int_0^t \frac{p(t)}{m_p} dt \qquad \text{(C 10)}$$

Finally, the total energy can be calculated by integrating the contact force as a function of displacement.

$$W = \int_{h_0}^{h_1} F(h) dh \qquad \text{(C 11)}$$

The initial impact energy of the impacting apparatus is calculated using the equation

$$E_I = \frac{1}{2} m_p V_0^2 \qquad \text{(C 12)}$$

Equations (C 9) and (C 10) are used to calculate the *V(t)* and *d(t)*, respectively. Once the displacement data are obtained from Eq. (C 10), the force versus displacement curve can be plotted so that the work performed on the specimen can be calculated.

Results

Punch Shear Strength (PSS) Results

Punch Shear Tests have been conducted to determine the Punch Shear Strength of the PW E-Glass/Phenolic composite specimens. Specimens are tested at four different SPRs. Ten specimens are tested at 1.037, 1.053 & 1.171 SPR and seven specimens are tested at 1.020 SPR to produce reliable and repeatable results. The load-displacement plots of all ten specimens tested at SPR = 1.037 is presented in Figure C 7. Peak force ranges between 12.5 kN and 15.5 kN for this set of tests. Looking at displacement data, failure is in the range between 0.6 mm and 0.8 mm for all specimens tested at this SPR. Variation in the dimensions, material properties, and inconsistencies in the material may play a major role in the variability of results.

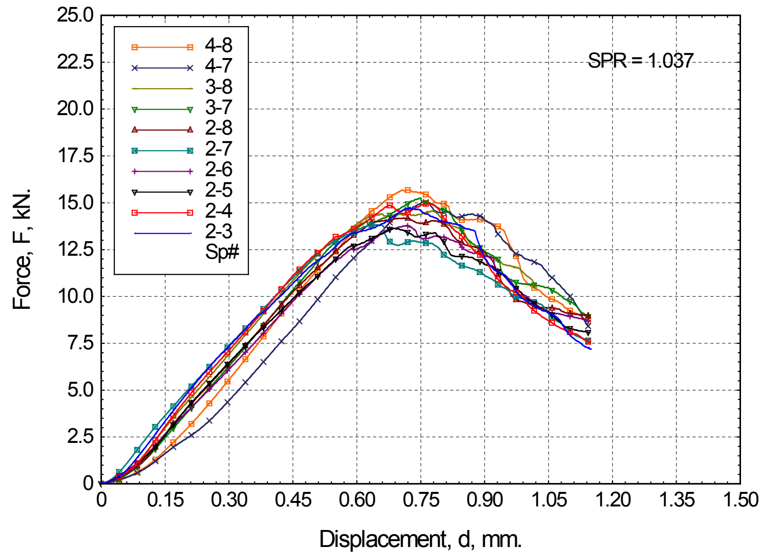

Figure C 7. Force vs. Displacement of 10 Specimens at SPR=1.037

Data from all tests is summarized and presented in Table C 11.

Table C 11. Average PSS Test Parameters and Results, Punch Diameter $D_P = 7.595$-mm

Specimen #	D_S (mm)	SPR	PSS (MPa)	Stdev (MPa)
2-9, 3-9-10, 4-9-10	7.747	1.020	156.05	4.61
2-3-8, 3-7-8, 4-7-8	7.874	1.037	148.73	7.40
2-1-2, 3-5-6, 3-14-15, 4-5-6, 4-14-15	8.001	1.053	150.14	7.28
2-21-30	8.890	1.171	120.15	6.18

A comparison of the results for the various SPRs at which specimens were tested is presented in Figure C 8. The punch shear strength for SPRs = 1.020, 1.037 & 1.053 have comparable values while those tested at SPR = 1.171 has a lower value. The estimated punch shear strength of the composite can be determined at SPR 1.000, and this value is found to be 160.00 MPa, and can be used as an average value in the MAT162 simulations.

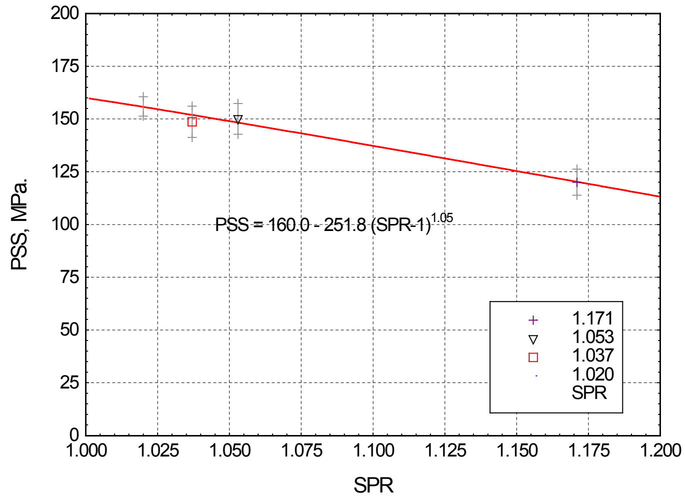

Figure C 8. Average PSS and Standard Deviations of PW E-Glass/Phenolic Composites as a Function of Test SPRs

Punch Crush Strength (PCS) Results

Results of punch crush testing are presented in Figure C 9. It can be seen that the two different fixtures used produced different Force vs. Displacement graphs. The hydrostatic crush fixture returned data similar to that of PSS testing, which produced a clear indication of peak force before failure. The punch crush tests performed using the Mini QS-PST fixture with SPR = 0 produced results with a more linearly increasing curve which shows a decrease in the slope at failure. The difference in the two curves is likely due to the clamped boundary conditions which the Mini QS-PST fixture produces.

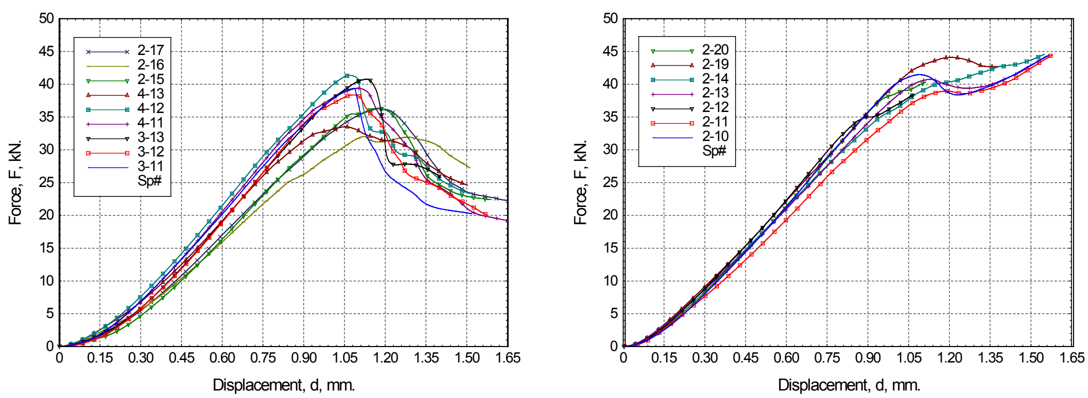

(a) HS Crush Test Fixture (b) Mini QS-PST Fixture

Figure C 9. Force-Displacement of all Crush Test Specimens

The values for peak load and the calculated Punch Crush Strength (PCS) are given in Table C 12. The specimens are renumbered according to the descending order of the Punch Crush Strength values. The specimen # 2-16 (10) was not considered since the value of PCS is much less than the other values. Figure C 10 shows the PCS variation with the new specimen numbers and the average values of SPC for both test fixtures.

The average values for peak load for specimens tested using the Mini QS-PST fixture are only about 5.5% higher than the values obtained via the HSCT fixture.

Table C 12. Peak Load and Descending PCS Values for Specimens (Renumbered) Tested using HSCT Fixture

Specimen # (Actual)	*Specimen # (Renumbered)*	*Peak Load (kN)*	*PCS (Descending)*
4-12	1	39.37	912.60
3-13	2	38.37	899.55
4-11	3	40.75	869.89
3-11	4	39.41	869.10
3-12	5	41.34	846.96
2-15	6	33.53	802.28
2-17	7	36.34	801.09
2-18	8	32.04	766.69
4-13	9	36.29	740.20
2-16	10	34.73	707.38
Average	N/A	37.217	834.26
STDEV	N/A	3.135	59.77
COV%	N/A	0.084	7.16

Table C 13. Peak Load and Descending PCS Values for Specimens (Renumbered) Tested using Mini QS-PST Fixture

Specimen # (Actual)	Specimen # (Renumbered)	Peak Load, (kN)	PCS (MPa) (Descending)
2-19	1	41.48	973.88
2-10	2	38.96	915.76
2-13	3	35.04	899.55
2-14	4	40.75	888.87
2-20	5	40.27	862.38
2-11	6	44.12	860.01
2-12	7	39.07	773.41
Average	N/A	39.956	881.98
STDEV	N/A	2.779	61.37
COV%	N/A	0.070	6.96

The Punch Crush Strengths predicted by Mini-QS-PST and HSCT Fixtures show a difference of 48.0 MPa, and the average of the two is found to be 852.0 MPa. The average value of Punch Crush Strength, SFC = 870 MPa is used as the MAT162 input for simulations as an upper bound.

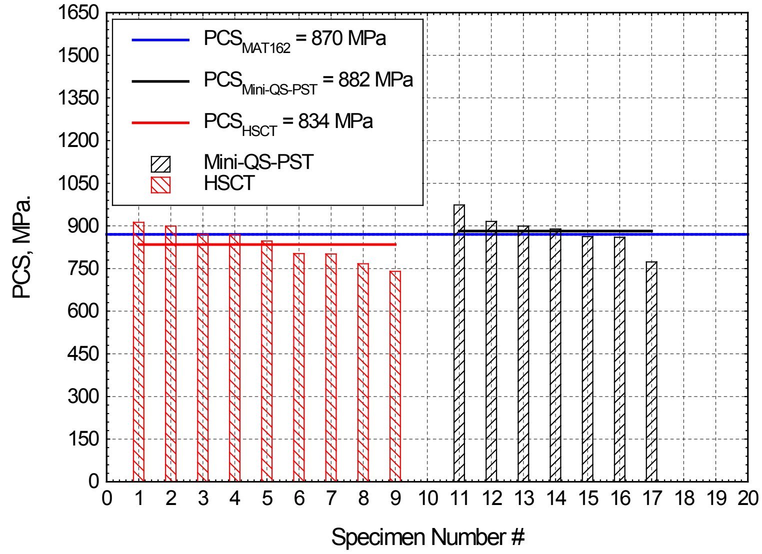

Figure C 10. PCS bar graph for HSCT and Mini-QS-PST

Low Velocity Impact Test Results

Five specimens from two laminates (#300 & #400) are tested at two different impact energy levels (50J, & 70J).

Table C 14. Summary of LVI Experimental Data for Laminate 300 & 400, $H_C = 8.97$-mm

Date	Material			Density, g/cm³	FVF			
5/10/2012	PW E-Glass/Phenolic			2.00				
E_I (J)	V_I (m/s)	E_I (J)	x_T (mm)	x_P (mm)	F_{max} (kN)	E_T (J)	E_D (J)	E_E (J)
50	3.191	48.86	9.25	5.29	9.99	49.74	39.31	10.43
70	3.770	68.19	11.00	6.51	11.79	69.23	55.53	13.70

Table C 14 summarizes the results of LVI experiments presented in Figure C 11. In Figure C 11 each plot represents an average response of 5 specimens. With the increase in impact energy or impact velocity, the peak forces increases. However, the duration of impact remains almost constant. Oscillatory behavior in the beginning of the impact event is due to the natural frequency of the clamped laminate under impact, which diminishes as the impact-contact force raises to a maximum value. At this point, unloading occurs and the load becomes zero when the projectile-sliding-mass assembly loses contact with the laminate. At the end of unloading, a permanent dynamic displacement is observed where F = 0. Maximum dynamic displacement and permanent dynamic displacement is tabulated in Table C 14. Total integral energy, energy dissipated and elastic energies are also calculated and presented in Table C 14 for each impact energy.

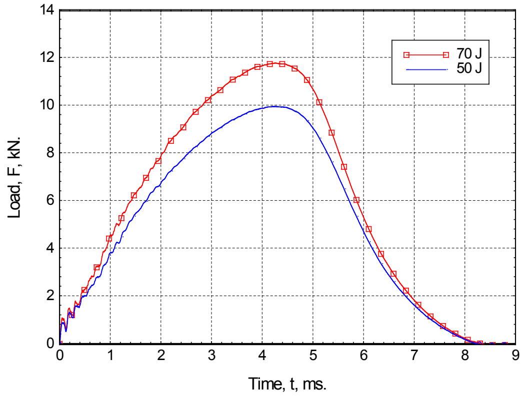

(a) Average Load vs. time

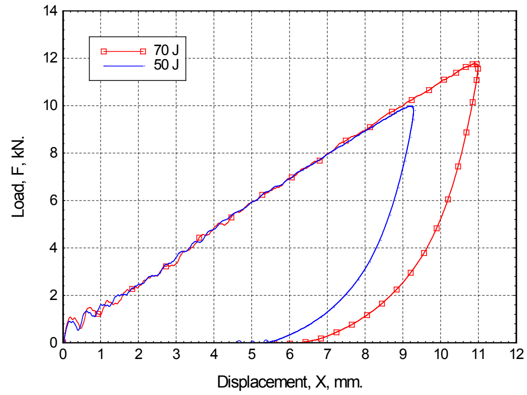

(b) Average Load vs. Displacement

Figure C 11. Summary of LVI Experiments on 300 & 400 PW E-Glass/Phenolic Specimens

Tension Test Results

A tension test (TT) methodology has been developed for studying the stress and strain behavior of E-Glass / Phenolic composites. Specimens from two different panels of the same material are tested in the TT fixture shown below in Figure C 12.

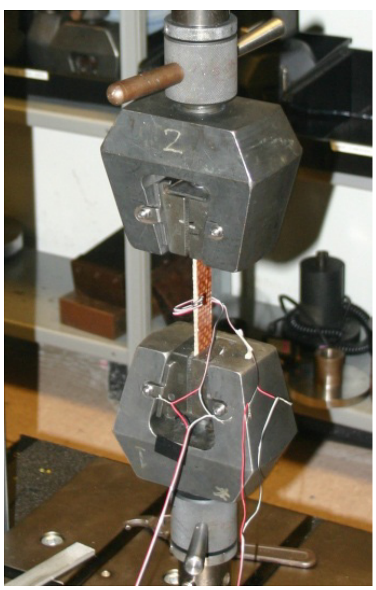

(a) The TT Fixture with the Specimen and Strain Gauge Attached

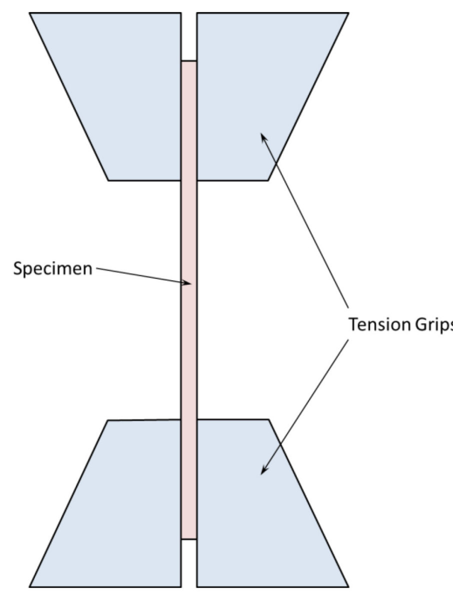

(b) Schematic Diagram of the TT Fixture

Figure C 12. Tension Test Fixture

Specimens are prepared using a slot grinder to cut the specimens into 25.4 mm x 304.8 mm (1 x 12 in) strips. CEA-06-250UT-350 biaxial strain gages are bonded to the tool side of specimens 201-606. Larger CEA-06-250UT-350 biaxial strain gages are attached to specimens 701-703.

Table C 15. Mass and geometry of specimens

Specimen #	*Mass*	*Avg. Width (mm)*	*Avg. H_C (mm)*	*Cross-Sectional Area (mm^2)*
201	42.301	25.094	4.034	101.229
202	42.433	25.138	4.056	101.960
203	42.203	24.994	4.082	102.026
204	42.404	25.028	4.094	102.465
205	42.415	25.052	4.052	101.511
206	42.470	25.454	4.038	102.783
Average	42.371	25.127	4.059	101.996

Table C 16. Mass and geometry of specimens

Specimen #	*Mass*	*Avg. Width (mm)*	*Avg. H_C (mm)*	*Cross-Sectional Area (mm^2)*
701	63.9615	25.292	4.080	103.191
702	64.2055	25.424	4.022	102.255
703	64.0872	25.378	4.000	101.512
Average	64.0847	25.3646667	4.034	102.3195627

Initial testing for specimen #201 was performed using an Instron 1331 testing machine which uses hydraulically controlled displacement and gripping devices. All other tests were carried out on an Instron 5985 which uses mechanically controlled displacement and gripping devices. Load vs. Displacement information is obtained. The differences between the two testing machines may be noticed in the below graphs.

Strain data for specimen #202 was lost due to technical problems with the testing machine and is no longer available.

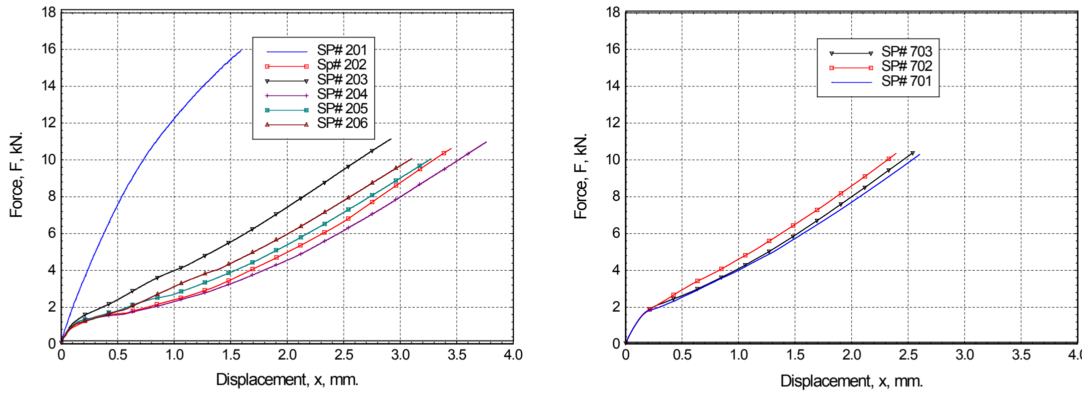

(a) Load vs. Displacement SP#201-206 (b) Stress vs. Displacement SP#701-703

Figure C 13. TT Load vs. Displacement

Load vs. micro-strain and stress vs. strain information is plotted below for the corresponding directions provided.

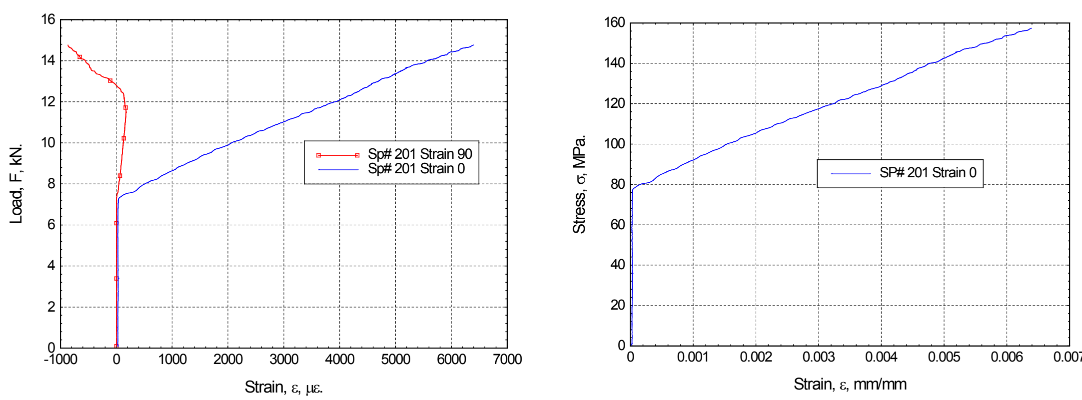

(a) Load vs. Strain (0, 90) (b) Stress vs. Strain (0)

Figure C 14. TT Load vs. Micro-Strain and Stress vs. Strain graphs

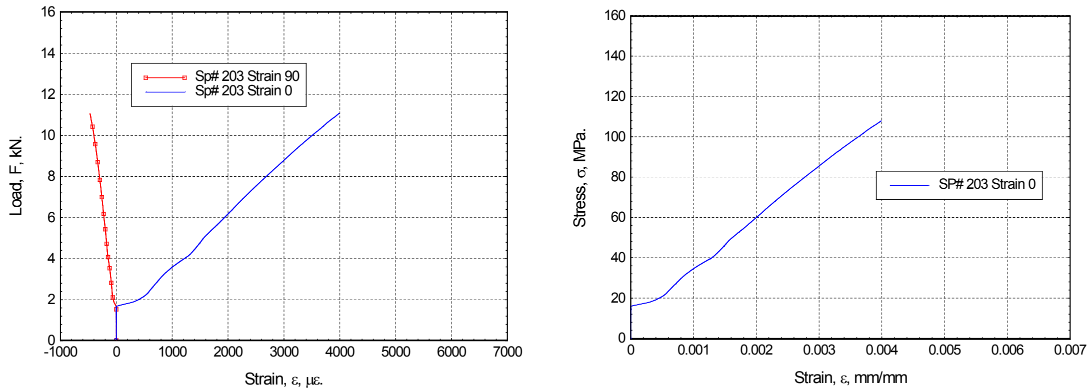

(a) Load vs. Strain (0, 90) (b) Stress vs. Strain (0)

Figure C 15. TT Load vs. Micro-Strain and Stress vs. Strain graphs

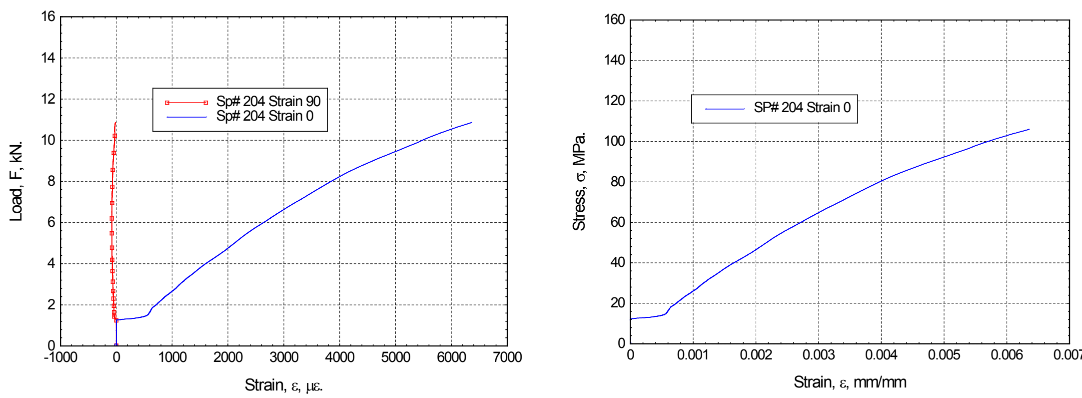

(a) Load vs. Strain (0, 90) (b) Stress vs. Strain (0)

Figure C 16. TT Load vs. Micro-Strain and Stress vs. Strain graphs

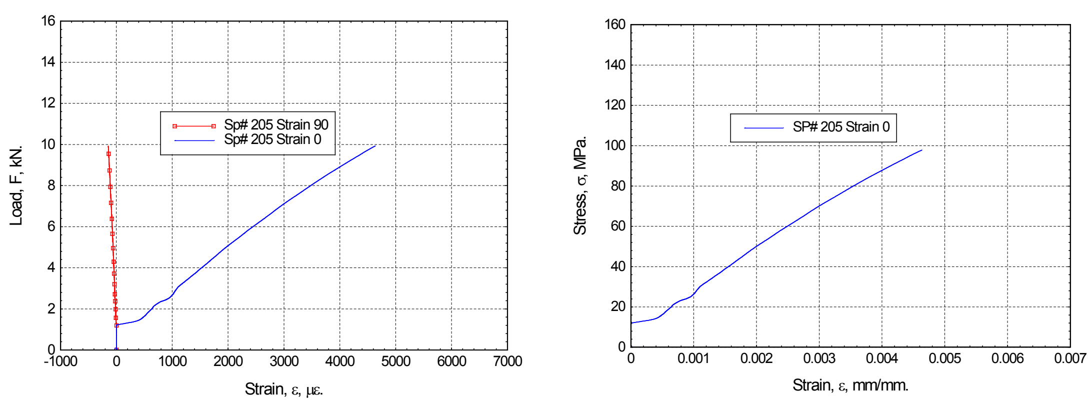

(a) Load vs. Strain (0, 90) (b) Stress vs. Strain (0)

Figure C 17. TT Load vs. Micro-Strain and Stress vs. Strain graphs

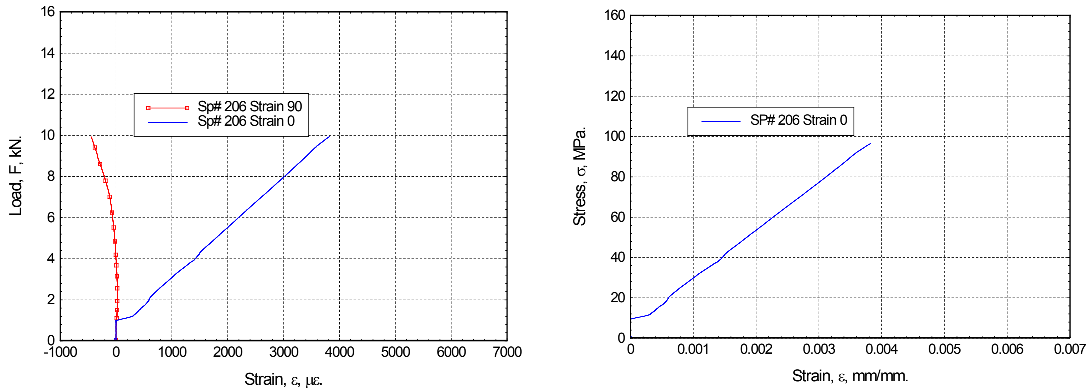

(a) Load vs. Strain (0, 90) (b) Stress vs. Strain (0)

Figure C 18. TT Load vs. Micro-Strain and Stress vs. Strain graphs

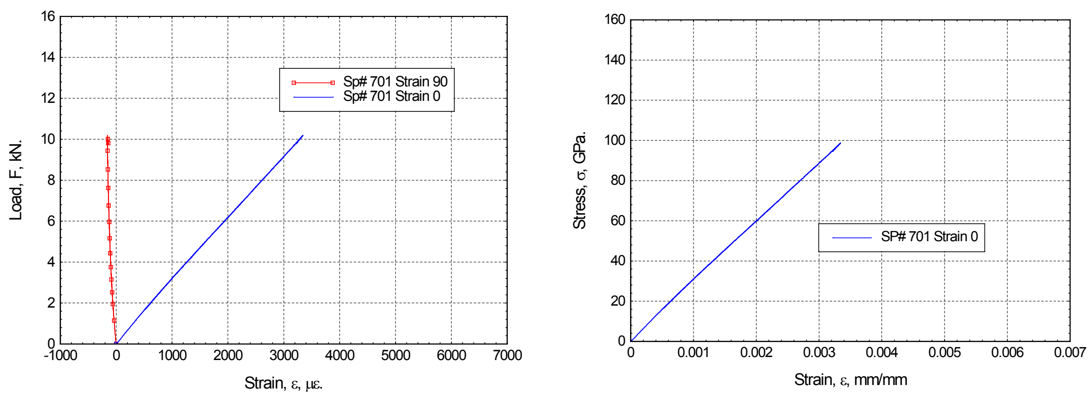

(a) Load vs. Strain (0, 90) (b) Stress vs. Strain (0)

Figure C 19. TT Load vs. Micro-Strain and Stress vs. Strain graphs

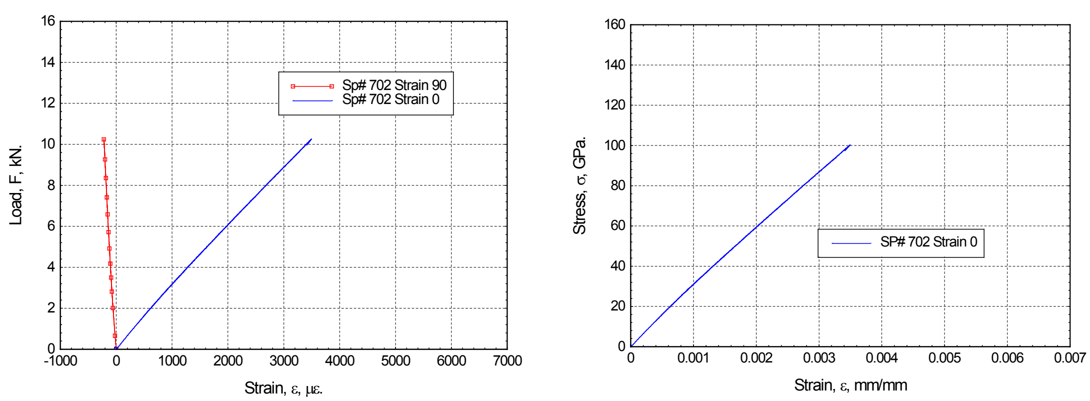

(a) Load vs. Strain (0, 90) (b) Stress vs. Strain (0)

Figure C 20. TT Load vs. Micro-Strain and Stress vs. Strain graphs

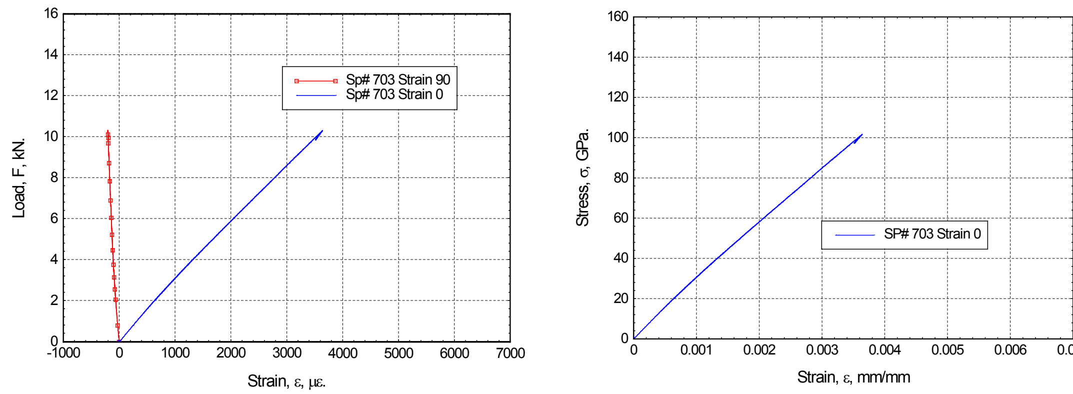

(a) Load vs. Strain (0, 90) (b) Stress vs. Strain (0)

Figure C 21. TT Load vs. Micro-Strain and Stress vs. Strain graphs

After examining the data, tests are either accepted or rejected based on the linearity of the strain curves. Non-linear strain curves result from malfunctioning strain gages. It can be noted that strain gages, especially the smaller gages, were difficult to properly bond to the specimens.

Table C 17 Summary of Data Quality

Specimen #	*Accept / Reject*	*Comments*
201	Reject	90 Strain Gauge Not Acceptable
202	Reject	Data Lost
203	Accept	Data Acceptable
204	Reject	90 Strain Gauge Not Acceptable
205	Reject	Data Not Acceptable
206	Reject	90 Strain Gauge Not Acceptable, Data may still be useful
701	Accept	Data Acceptable
702	Accept	Data Acceptable
703	Accept	Data Acceptable

The slope of the load vs. micro-strain curves are calculated for the respective surfaces using a linear curve fit for the initial linear portion of the strain curve. These values are shown in the tables below along with Poisson's ratio. Poisson's ratio is calculated by dividing the slope in the 90 direction by the slope in the 0 direction and taking the absolute value as shown in Eq. (C 13). The elastic modulus, E, was calculated by dividing the calculated slope of the load vs. micro-strain curve in the zero direction by the cross-sectional area of the specimen as shown in Eq. (C 14).

$$\nu_{12} = \left| \frac{M_0}{M_{90}} \right| \tag{C 13}$$

$$E = \left| \frac{M_0}{A} \right| \tag{C 14}$$

Table C 18. Slope Poisson's Ratio, & Elastic Modulus

Specimen #	*Load Range (kN)*	*Strain Range (με)*	*A (mm²)*	M_0 *(N/A)*	M_{90} *(N/A)*	ν_{12}	E_{11} *(GPa)*
201	N/A	N/A	101.229	N/A	N/A	N/A	N/A
202	N/A	N/A	101.960	N/A	N/A	N/A	N/A
203	4-10	1000-3000	102.026	2.651 x 10^6	24.031 x 10^6	0.110	25.984
204	N/A	N/A	102.465	N/A	N/A	N/A	N/A
205	2-8	1000-3000	101.511	2.158 x 10^6	64.607 x 10^6	0.033	21.259
206	2-8	1000-3000	102.783	2.449 x 10^6	26.025 x 10^6	0.094	23.827
701	2-10	1000-3000	103.191	2.979 x 10^6	87.161 x 10^6	0.034	28.869
702	2-10	1000-3000	102.255	2.851 x 10^6	51.605 x 10^6	0.055	27.881
703	2-10	1000-3000	101.512	2.728 x 10^6	62.199 x 10^6	0.044	26.874
Average	N/A	1000-3000	102.249	2.558 x 10^6	59.873 x 10^6	0.056	25.009

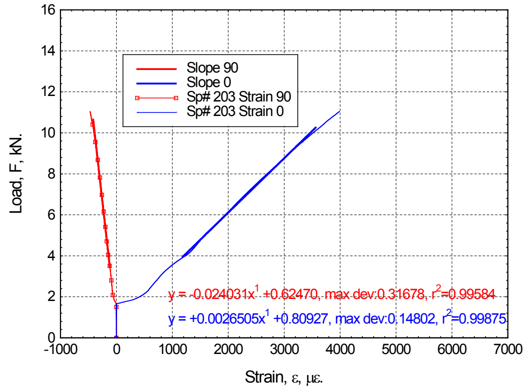

(a) Load vs. Strain (0, 90) Sp# 203

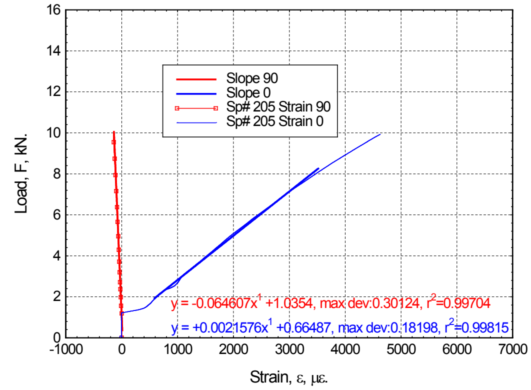

(b) Load vs. Strain (0, 90) Sp# 205

Figure C 22. TT Load vs. Micro-Strain with Slope Calculation

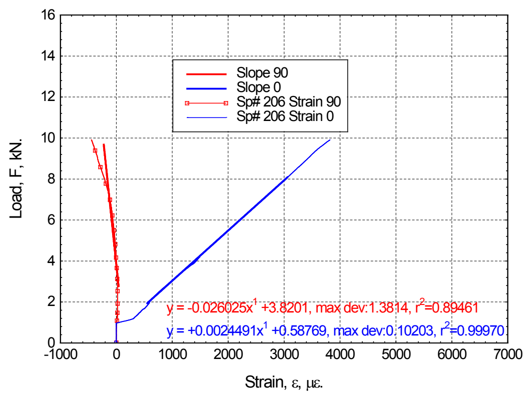

(a) Load vs. Strain (0, 90) Sp# 206

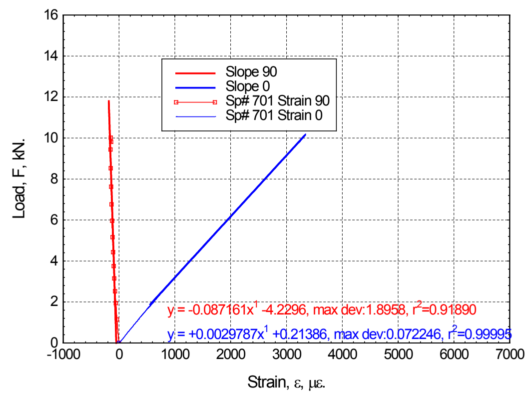

(b) Load vs. Strain (0, 90) Sp# 701

Figure C 23. TT Load vs. Micro-Strain with Slope Calculation

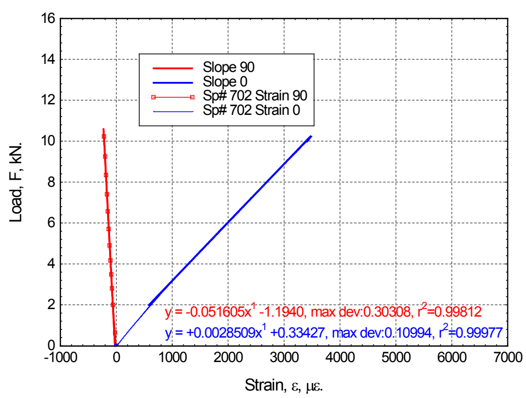

(a) Load vs. Strain (0, 90) Sp# 702

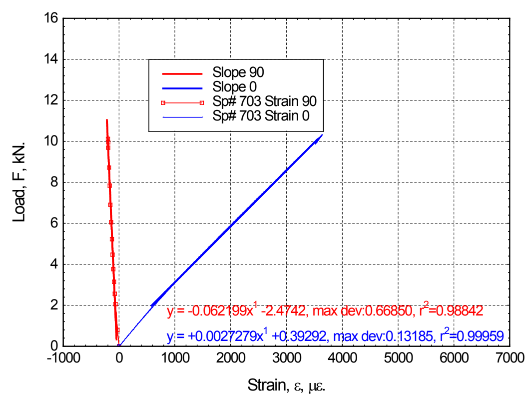

(b) Load vs. Strain (0, 90) Sp# 703

Figure C 24 TT Load vs. Micro-Strain with Slope Calculation

Table C 19. Mass and geometry of specimens

Specimen #	*Mass (gm)*	*Avg. Width (mm)*	*Avg. Length (mm)*	*H_C (mm)*	*Cross-sectional area (mm^2)*
601	38.582	24.884	25.346	24.940	630.710
602	31.815	25.444	25.078	24.926	638.085
603	31.280	25.020	25.150	24.944	629.253
604	32.268	25.410	25.344	24.934	643.991
605	31.604	25.072	25.128	25.018	630.009
606	31.220	25.126	25.312	24.940	635.989
607	31.778	25.198	25.168	25.000	634.183
Average	32.649	25.165	25.218	24.957	634.603

Through Thickness Compression Testing

A through thickness compression test (TTCT) methodology has been developed for studying the stress and strain behavior of E-Glass / Phenolic composites under compression. Seven specimens from the same panel were tested in the TTCT fixture shown below in Figure C 25.

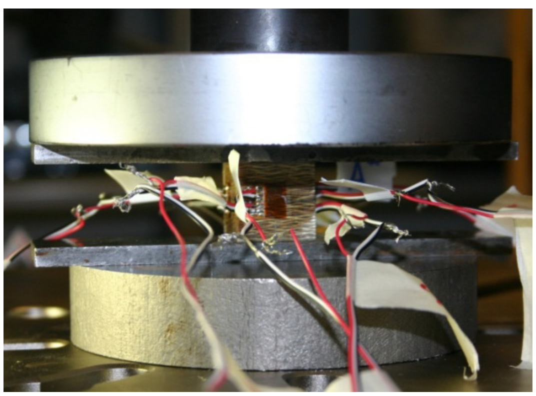

(a) The TTCT Fixture with the Specimen and Strain Gauges attached.

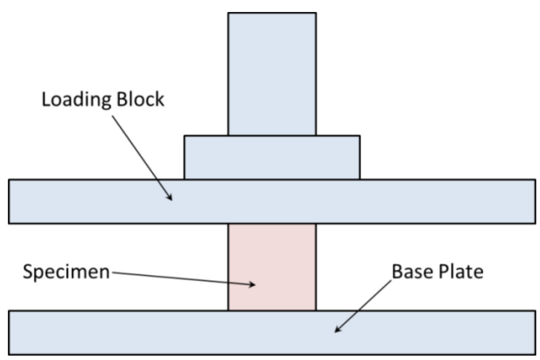

(b) Schematic Diagram of the TTCT Fixture.

Figure C 25 Through Thickness Compression Testing Images

Specimens are prepared using a slot grinder to cut and grind the specimens into 25.4 mm (1 in) cubes. CEA-06-250UT-350 biaxial strain gages are attached to all four through-thickness sides of specimens 601-604. Larger CEA-06-250UT-350 biaxial strain gages are attached to two through-thickness sides (left/right) of specimens 605-607.

Table C 20. Mass and geometry of specimens

Specimen #	*Mass (gm)*	*Avg. Width (mm)*	*Avg. Length (mm)*	*H_C (mm)*	*Cross-sectional area (mm²)*
601	38.582	24.884	25.346	24.940	630.710
602	31.815	25.444	25.078	24.926	638.085
603	31.280	25.020	25.150	24.944	629.253
604	32.268	25.410	25.344	24.934	643.991
605	31.604	25.072	25.128	25.018	630.009
606	31.220	25.126	25.312	24.940	635.989
607	31.778	25.198	25.168	25.000	634.183
Average	32.64957	25.165	25.218	24.957	634.603

Specimens are loaded to the maximum capacity of the 250 kN. Load cell and no failure occurs.

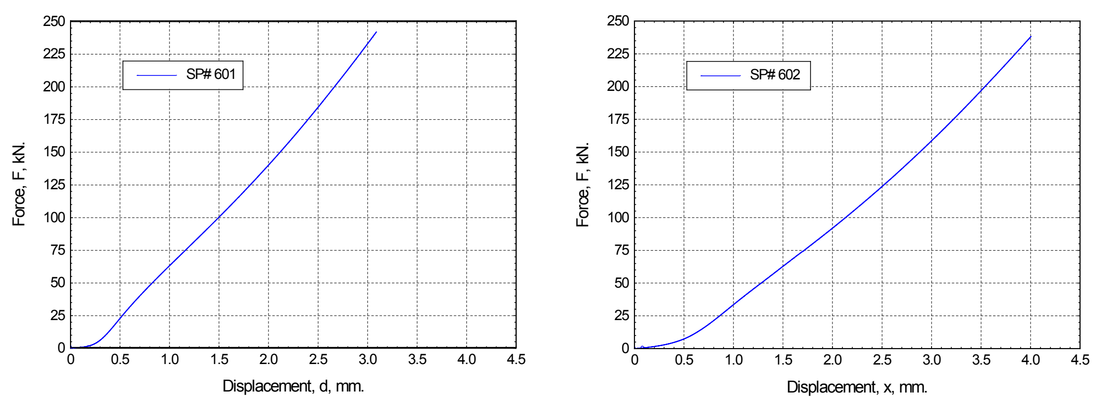

(a) Load vs. Displacement, SP# 601 (b) Load vs. Displacement, SP# 602

Figure C 26. TTCT Load vs. Displacement

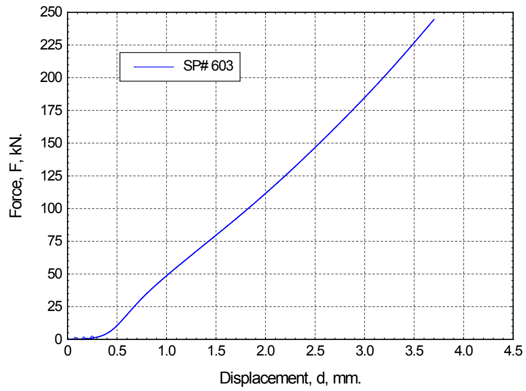

(a) Load vs. Displacement, SP# 603

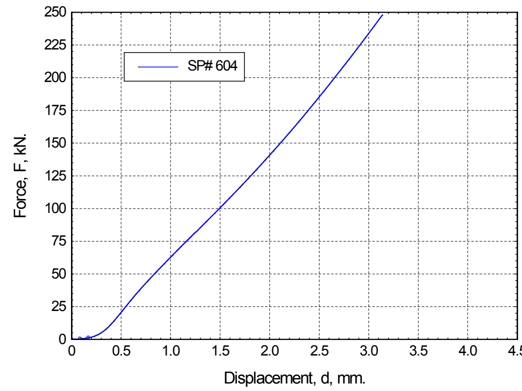

(b) Load vs. Displacement, SP# 604

Figure C 27. TTCT Load vs. Displacement

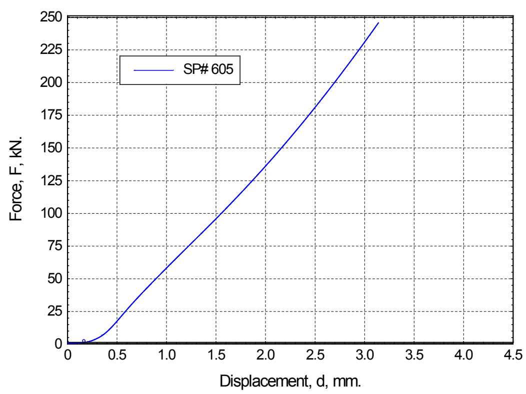

(a) Load vs. Displacement, SP# 605

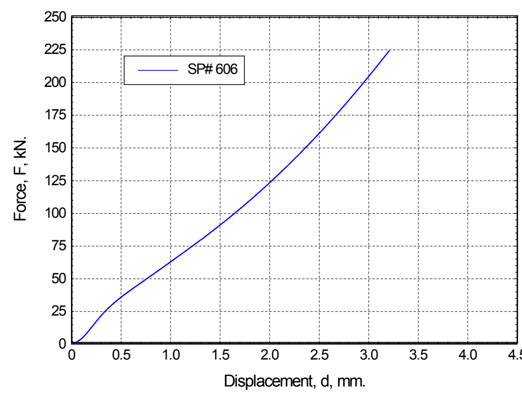

(b) Load vs. Displacement, SP# 606

Figure C 28. TTCT Load vs. Displacement.

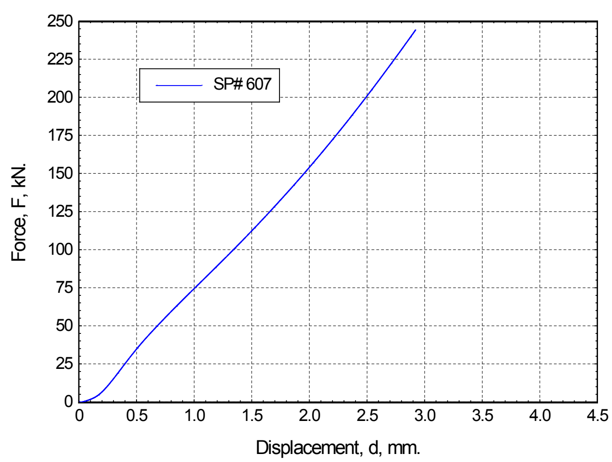

(a) Load vs. Displacement, SP# 607

Figure C 29. TTCT Load vs. Displacement.

Load vs. micro-strain is plotted for the front/back, and left/right faces for comparison of specimens 601-604.

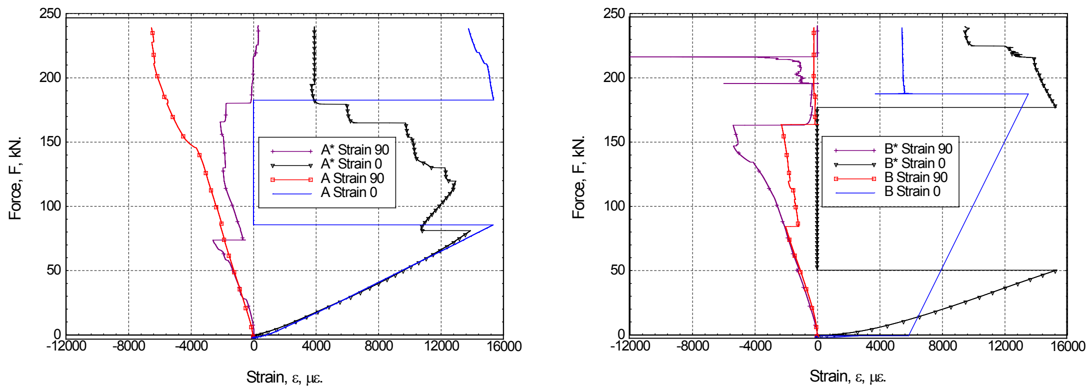

(a) Load vs. Micro-Strain (Left/Right) (b) Load vs. Micro-Strain (Front/Back)

Figure C 30. TTCT Load vs. Micro-Strain SP# 601

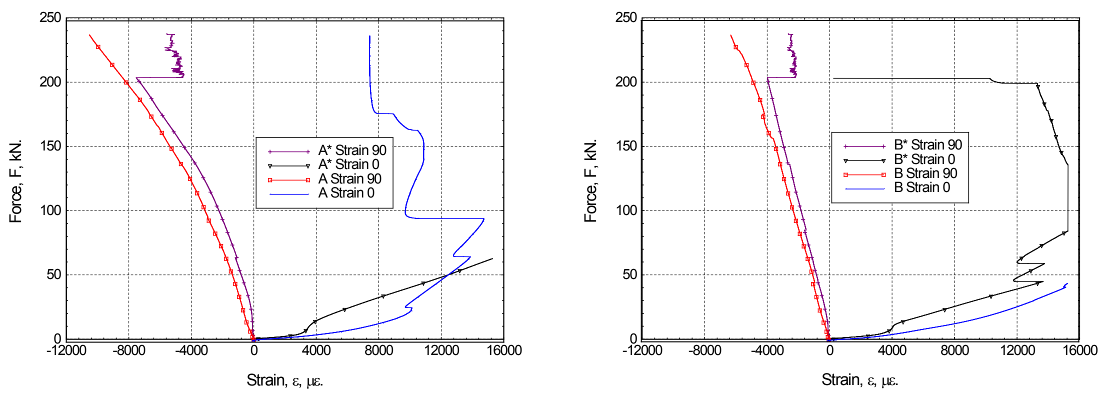

(a) Load vs. Micro-Strain (Left/Right) (b) Load vs. Micro-Strain (Front/Back)

Figure C 31. TTCT Load vs. Micro-Strain SP# 602

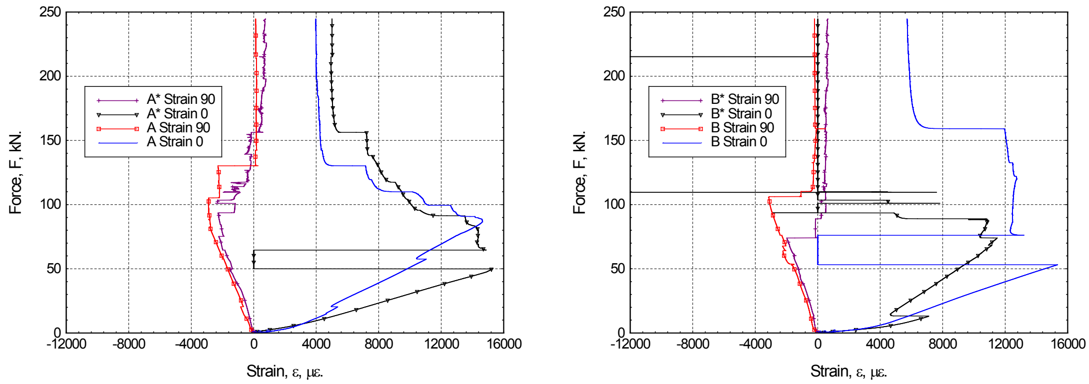

(a) Load vs. Micro-Strain (Left/Right) (b) Load vs. Micro-Strain (Front/Back)

Figure C 32. TTCT Load vs. Micro-Strain SP# 603

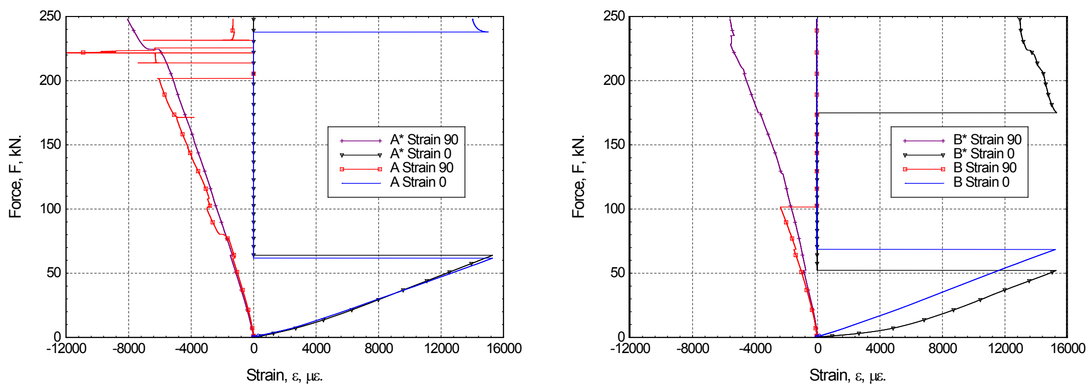

(a) Load vs. Micro-Strain (Left/Right) (b) Load vs. Micro-Strain (Front/Back)

Figure C 33. TTCT Load vs. Micro-Strain SP# 604

Load vs. micro-strain is plotted for the left/right faces for comparison of specimens 605-607.

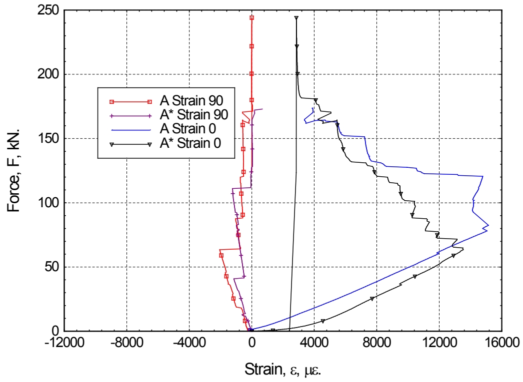

(a) Load vs. Micro-Strain Sp# 605

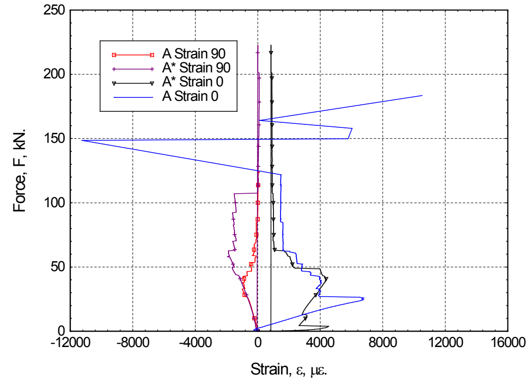

(b) Load vs. Micro-Strain Sp# 606

Figure C 34. TTCT Load vs. Micro-Strain

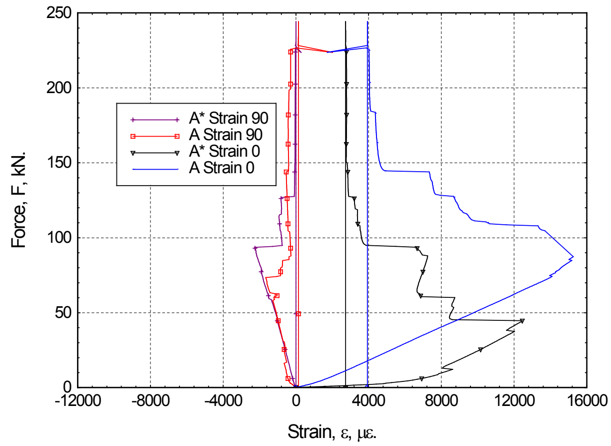

(a) Load vs. Micro-Strain Sp# 607

Figure C 35. TTCT Load vs. Micro-Strain

Slope of the load vs. micro-strain curves are calculated for the respective surfaces using a linear curve fit for the initial linear portion of the strain curve. These values are shown in the tables below along with Poisson's ratio. Poisson's ratio is calculated by dividing the slope in the 90 direction by the slope in the 0 direction and taking the absolute value as shown in Eq. (C 15). The 0 direction is defined as direction 3 and the 90 direction is defined as direction 1. The elastic modulus (*E*) was calculated by dividing the calculated slope of the load vs. micro-strain curve in the zero direction by the cross-sectional area of the specimen as shown in Eq. (C 16).

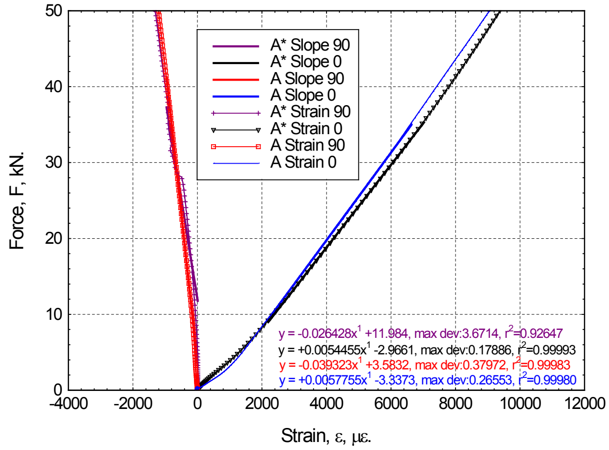

Figure C 36. TTCT Load vs. Micro-Strain Slope Calculation SP# 601

$$\nu_{31} = \left| \frac{M_3}{M_1} \right| \tag{C 15}$$

$$E_{33} = \left| \frac{M_3}{A} \right| \tag{C 16}$$

Table C 21. Slope Poisson’s Ratio, & E (Left/Right) SP# 601

Face	*Load Range (kN)*	*A (mm²)*	*M_3 (N/ε)*	*M_1 (N/ε)*	*ν_{31} (kN/kN)*	*E_{33} (GPa)* .
A	10-35	630.710	5.776 x 10⁶	39.323 x 10⁶	0.147	9.158
A*	10-35	630.710	5.446 x 10⁶	26.428 x 10⁶	0.206	8.635
Average	10-35	630.710	5.611 x 10⁶	32.876 x 10⁶	0.177	8.896

Table C 22. Slope Poisson's Ratio, & E (Front/Back) SP# 601

Face	*Load Range (kN)*	*A (mm²)*	*M_3 (N/ε)*	*M_1 (N/ε)*	*ν_{31} (kN/kN)*	*E_{33} (GPa).*
B	10-35	630.710	N/A	N/A	N/A	N/A
B*	10-35	630.710	3.933×10^6	39.241×10^6	0.100	6.236
Average	10-35	630.710	3.933×10^6	39.241×10^6	0.100	6.236

Table C 23. Slope Poisson's Ratio, & E (Left/Right) SP# 602

Face	*Load Range (kN)*	*A (mm²)*	*M_3 (N/ε)*	*M_1 (N/ε)*	*ν_{31} (kN/kN)*	*E_{33} (GPa).*
A	10-35	638.085	N/A	N/A	N/A	N/A
A*	10-35	638.085	N/A	N/A	N/A	N/A
Average	10-35	638.085	N/A	N/A	N/A	N/A

Table C 24. Slope Poisson's Ratio, & E (Front/Back) SP# 602

Face	*Load Range (kN)*	*A (mm²)*	*M_3 (N/ε)*	*M_1 (N/ε)*	*ν_{31} (kN/kN)*	*E_{33} (GPa).*
B	10-35	638.085	N/A	N/A	N/A	N/A
B*	10-35	638.085	N/A	N/A	N/A	N/A
Average	10-35	638.085	N/A	N/A	N/A	N/A

Table C 25. Slope Poisson's Ratio, & E (Left/Right) SP# 603

Face	*Load Range (kN)*	*A (mm²)*	*M_3 (N/ε)*	*M_1 (N/ε)*	*ν_{31} (kN/kN)*	*E_{33} (GPa).*
A	10-35	629.253	N/A	N/A	N/A	N/A
A*	10-35	629.253	N/A	N/A	N/A	N/A
Average	10-35	629.253	N/A	N/A	N/A	N/A

Table C 26. Slope Poisson's Ratio, & E (Front/Back) SP# 603

Face	*Load Range (kN)*	*A (mm²)*	*M_3 (N/ε)*	*M_1 (N/ε)*	*ν_{31} (kN/kN)*	*E_{33} (GPa).*
B	10-35	629.253	N/A	N/A	N/A	N/A
B*	10-35	629.253	N/A	N/A	N/A	N/A
Average	10-35	629.253	N/A	N/A	N/A	N/A

Table C 27. Slope Poisson's Ratio, & E (Left/Right) SP# 604

Face	*Load Range (kN)*	*A (mm²)*	*M_3 (N/ε)*	*M_1 (N/ε)*	ν_{31} *(kN/kN)*	*E_{33} (GPa).*
A	10-35	643.991	4.218×10^6	46.990×10^6	0.090	6.550
A*	10-35	643.991	4.457×10^6	44.093×10^6	0.101	6.921
Average	10-35	643.991	4.338×10^6	45.542×10^6	0.096	6.735

Table C 28. Slope Poisson's Ratio, & E (Front/Back) SP# 604

Face	*Load Range (kN)*	*A (mm²)*	*M_3 (N/ε)*	*M_1 (N/ε)*	ν_{31} *(kN/kN)*	*E_{33} (GPa).*
B	10-35	643.991	4.485×10^6	49.916×10^6	0.090	6.964
B*	10-35	643.991	N/A	N/A	N/A	N/A
Average	10-35	643.991	4.485×10^6	49.916×10^6	0.090	6.964

Table C 29. Slope Poisson's Ratio, & E (Left/Right) SP# 605

Face	*Load Range (kN)*	*A (mm²)*	*M_3 (N/ε)*	*M_1 (N/ε)*	ν_{31} *(kN/kN)*	*E_{33} (GPa).*
A	10-35	630.009	4.941×10^6	-22.449×10^6	0.220	7.906
A*	10-35	630.009	N/A	N/A	N/A	N/A
Average	10-35	630.009	4.941×10^6	-22.449×10^6	0.220	7.906

Table C 30. Slope Poisson's Ratio, & E (Left/Right) SP# 606

Face	*Load Range (kN)*	*A (mm²)*	*M_3 (N/ε)*	*M_1 (N/ε)*	ν_{31} *(kN/kN)*	*E_{33} (GPa).*
A	5-25	635.989	3.080×10^6	-40.808×10^6	0.075	4.843
A*	5-25	635.989	N/A	N/A	N/A	N/A
Average	5-25	635.989	3.080×10^6	-40.808×10^6	0.075	4.843

Table C 31. Slope Poisson's Ratio, & E (Left/Right) SP# 607

Face	*Load Range (kN)*	*A (mm²)*	*M_3 (N/ε)*	*M_1 (N/ε)*	ν_{31} *(kN/kN)*	*E_{33} (GPa).*
A	10-35	634.183	5.578 x 10^6	-80.874 x 10^6	0.069	8.796
A*	10-35	634.183	N/A	N/A	N/A	N/A
Average	10-35	634.183	5.578 x 10^6	-80.874 x 10^6	0.069	8.796

After examining the data, tests are either accepted or rejected based on the linearity of the strain curves. Non-linear strain curves result from malfunctioning strain gages. It can be noted that strain gages, especially the smaller gages, were difficult to properly bond to the specimens. Graphs of the excepted data are displayed below.

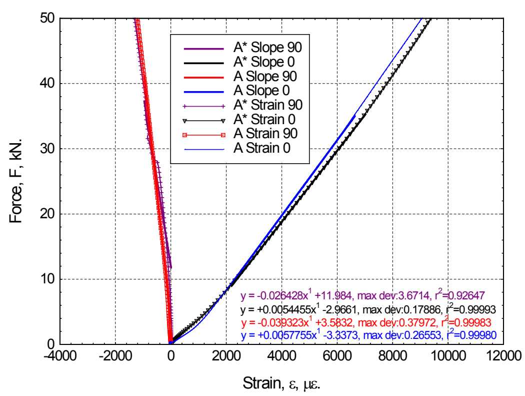

(a) Load vs. Micro-Strain (Left/Right)

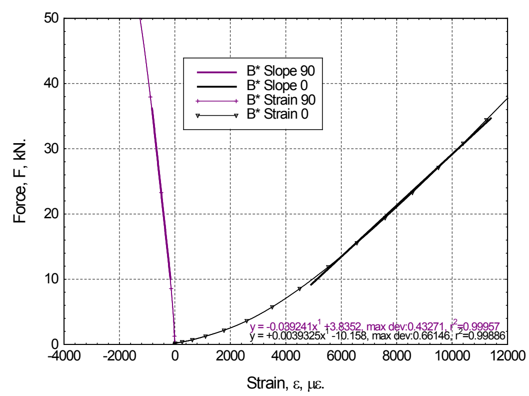

(b) Load vs. Micro-Strain (Front/Back)

Figure C 37. TTCT Load vs. Micro-Strain SP# 601

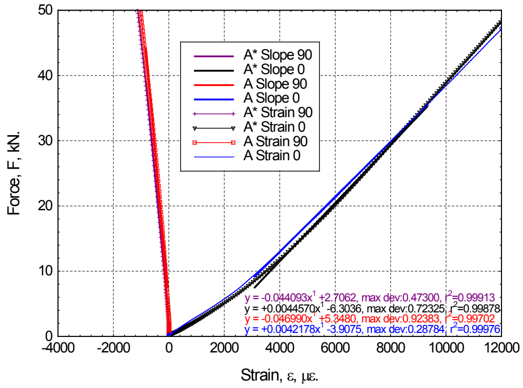

(a) Load vs. Micro-Strain (Left/Right)

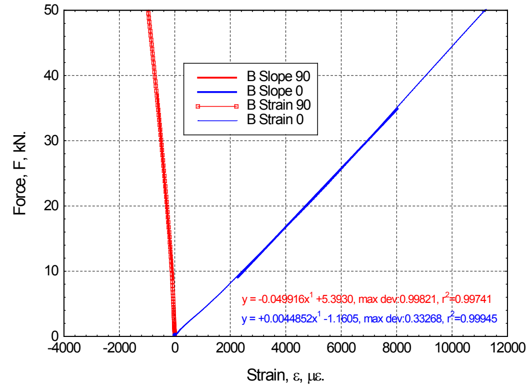

(b) Load vs. Micro-Strain (Front/Back)

Figure C 38. TTCT Load vs. Micro-Strain SP# 604

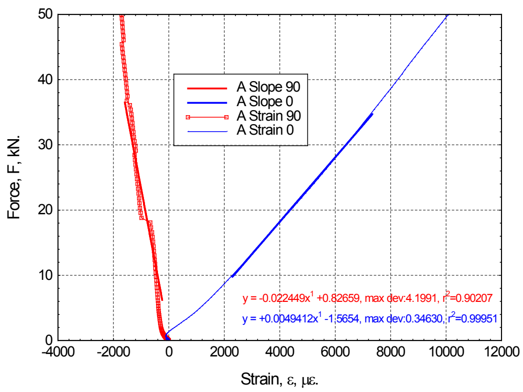

(a) Load vs. Micro-Strain (Left/Right)

Sp# 605

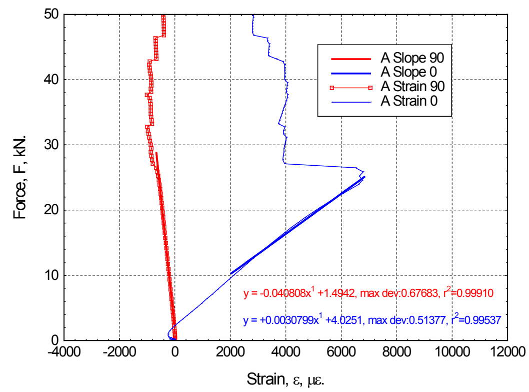

(b) Load vs. Micro-Strain (Left/Right)

Sp# 606

Figure C 39. TTCT Load vs. Micro-Strain SP# 605 & SP# 606

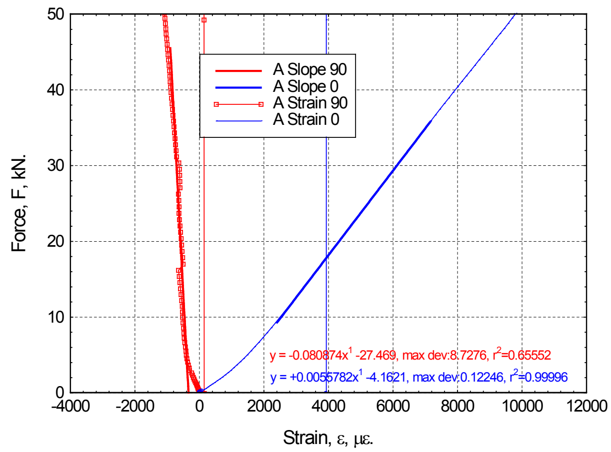

Figure C 40. TTCT Load vs. Micro-Strain SP# 607

Average values for the elastic modulus and Poisson's ratio of the excepted tests are displayed in the table below. Specimens 601 face A*, 605 face A, and 606 face A are rejected due to inaccurate calculations of Poison's Ratio and Elastic Modulus.

Table C 32. Average Poisson and Moduli

Specimen #	*Face*	ν_{31} *(kN/kN)*	E_{33} *(GPa)*
601	A	0.147	9.158
601	B*	0.100	6.236
604	A	0.090	6.550
604	A*	0.101	6.921
604	B	0.090	6.964
607	A	0.069	8.796
Average	N/A	0.100	7.438

Through Thickness Tension Testing

A through thickness tension test (TTTT) methodology has been developed for studying the failure behavior of E-Glass / Phenolic composites under tension along the direction of the plies. 6 specimens from the same panel were tested in the TTTT fixture shown below in Figure 1-1.

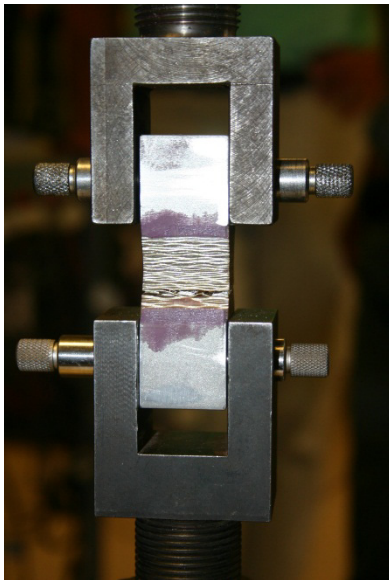

(a) The TTTT Fixture with Specimen

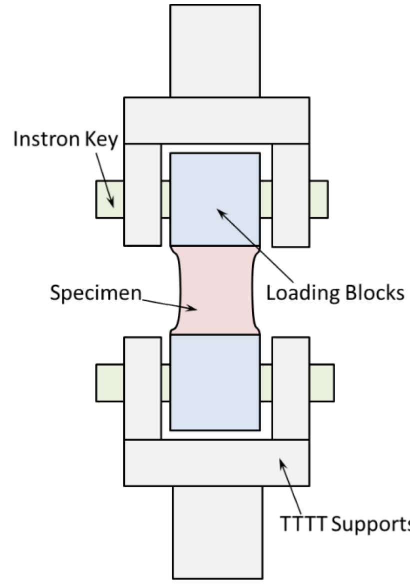

(b) Schematic Diagram of the TTTT Fixture

Figure C 41. Images of TTTT Fixture.

Specimens are prepared using a slot grinder to grind the specimens into 1-in. cubes. The cubes are then ground on the front and back face of the specimen to notch a 0.1in deep groove with a 0.25-in. radius forming a 0.8-in gage section along the front and back faces of the specimen. These specimens are then bonded to 1-in^3 aluminum blocks with a hole through the left and right faces with a two part Hysol EA 9309.3 NA QT System.

Table C 33. Geometry of Specimens.

Specimen #	*Gage Width W_1 (mm)*	*Width, W_2 (mm)*	*X-Section Area (mm^2)*
1	19.476	25.034	487.562
2	19.476	25.074	488.341
3	19.424	24.800	481.715
4	19.434	24.822	482.391
5	18.756	25.008	469.050
6	19.380	25.048	485.430
Average	19.324	24.964	482.415

All specimens failed in the gage section of the specimen. Below are the Load vs. Displacement, and the Stress vs. Strain curves for all tests completed.

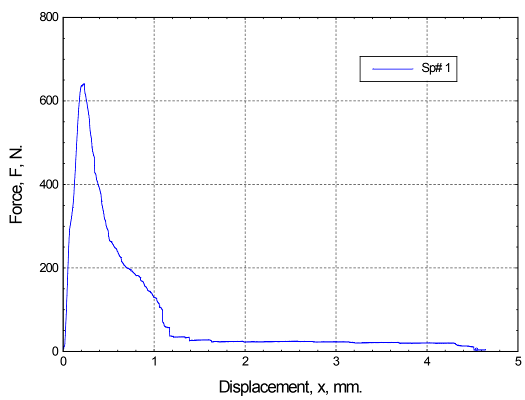

(a) Load vs. Displacement

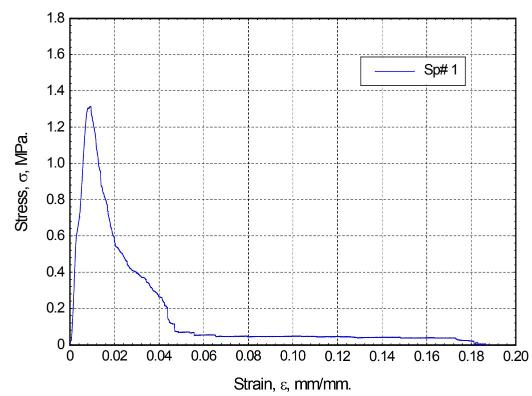

(b) Stress vs. Strain

Figure C 42. TTTT Load vs. Displacement and Stress vs. Strain Curves.

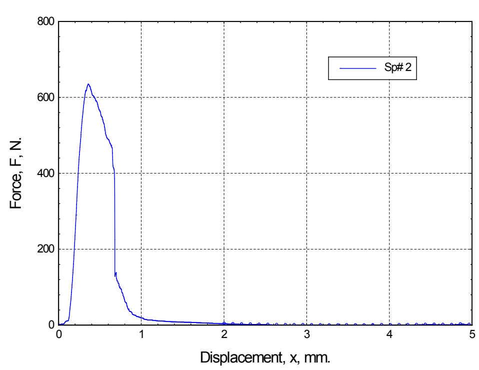

(a) Load vs. Displacement

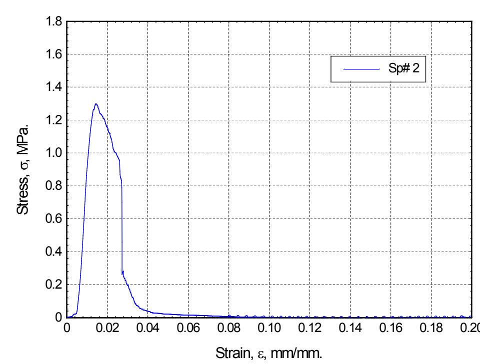

(b) Stress vs. Strain

Figure C 43. TTTT Load vs. Displacement and Stress vs. Strain Curves.

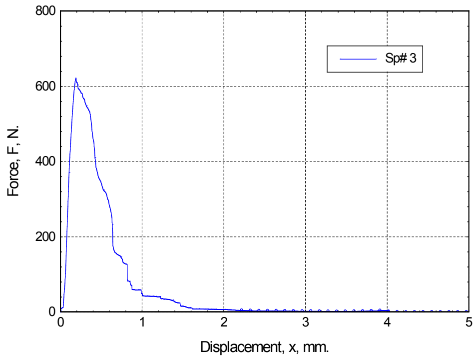

(a) Load vs. Displacement

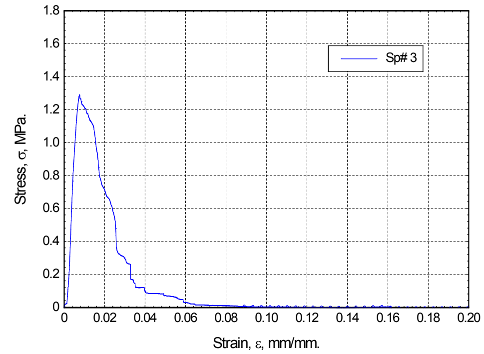

(b) Stress vs. Strain

Figure C 44. TTTT Load vs. Displacement and Stress vs. Strain Curves.

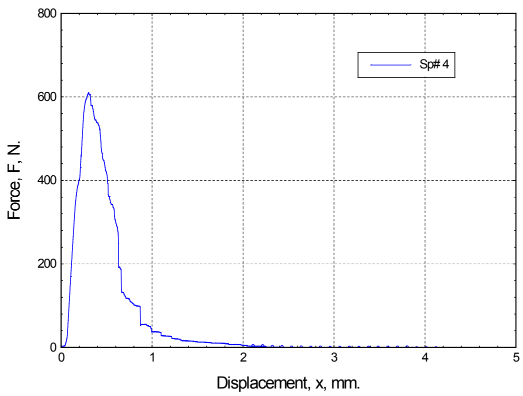

(a) Load vs. Displacement

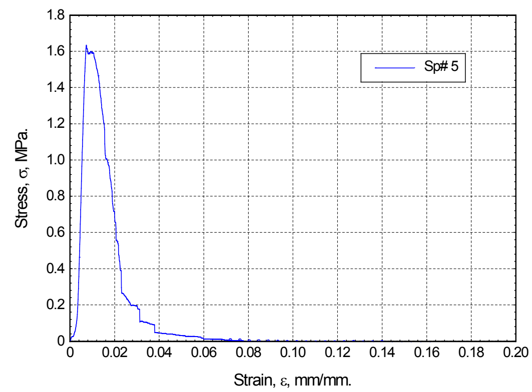

(b) Stress vs. Strain

Figure C 45. TTTT Load vs. Displacement and Stress vs. Strain Curves.

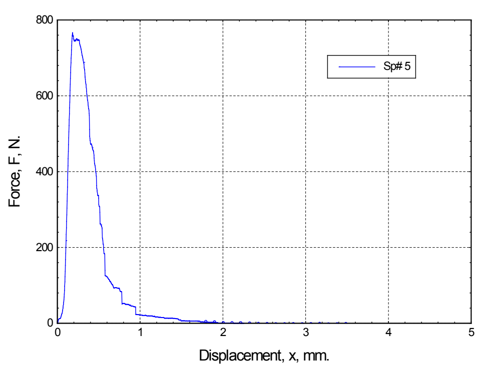

(a) Load vs. Displacement

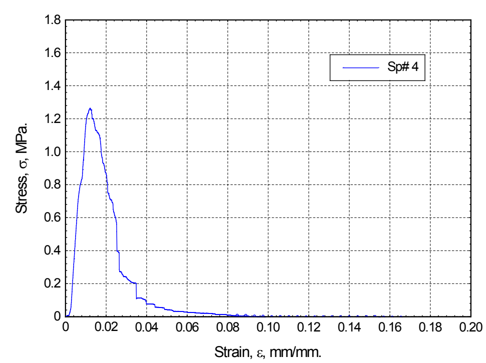

(b) Stress vs. Strain

Figure C 46. TTTT Load vs. Displacement and Stress vs. Strain Curves.

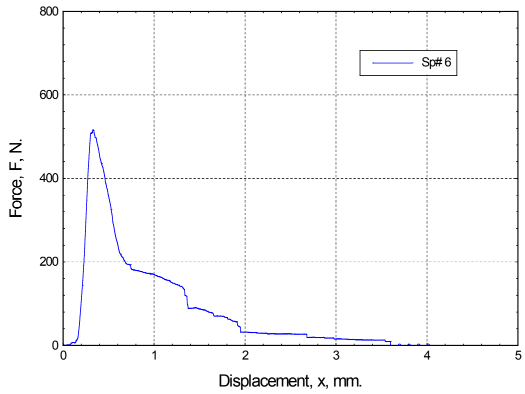

(a) Load vs. Displacement

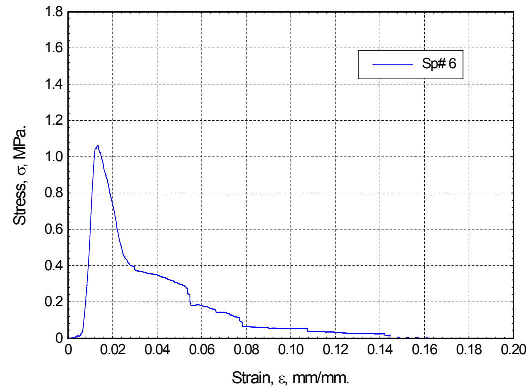

(b) Stress vs. Strain

Figure C 47. TTTT Load vs. Displacement and Stress vs. Strain Curves

Table C 34. Through Thickness Failure Loads and Tensile Stresses

Specimen #	*Failure Load (N)*	*X-Section Area (mm^2)*	*Stress (MPa).*
1	641.305	487.562	1.315
2	635.176	488.341	1.301
3	621.808	481.715	1.291
4	610.284	482.391	1.265
5	766.722	469.050	1.635
6	516.619	485.430	1.064
Average	631.986	482.415	1.312

VITA

Joseph Jordan was born at Patrick Air Force Base, Florida on August 22, 1962. He graduated from the University of Central Florida with a Bachelor of Science in Mechanical Engineering in 1991. He became a registered engineer in the state of Florida in 1998. He received a Master of Science in Mechanical Engineering at Lehigh University in 2009. He has worked the last 15 years conducting research in ballistic and fragmentation protection, and the last three years he has been conducting research for the U.S. Army Engineering Research and Development Center, Geotechnical and Structures Laboratory, Survivability Engineering Branch.